Performance assessment of a solar power plant with parabolic trough collectors assigned for ambient conditions in Morocco

Résumé : Le Maroc a lancé un ambitieux programme des énergies renouvelables pour produire de l'électricité. L'intérêt pour l'énergie solaire figure en tête des priorités de ce programme. Par conséquent, ce travail analyse la simulation des performances d'une centrale solaire à concentrateurs cylindro-paraboliques (CCP) sous les conditions ambiantes marocaines. Dans la première partie, un aperçu a été présenté de la centrale thermique à cycle combiné solaire intégré (CCSI) d'Ain Béni Mathar (ABM). L'intérêt a été porté à la partie solaire afin d'évaluer son impact sur les performances globales de la centrale. La deuxième partie vise à évaluer les performances thermiques du champ solaire de la centrale d'ABM. À ce propos, un modèle physique qui reproduit le comportement dynamique des CCP a été considéré. Les équations du bilan énergétique du système étudié ont été résolues à l'aide du logiciel COMSOL Multiphysics. La troisième partie présente une comparaison entre les modèles analytiques et les réseaux de neurones artificiels (RNA). Les modèles visent à prédire la production d'énergie électrique d'une centrale solaire cylindro-parabolique à la sortie du générateur électrique et, plus particulièrement, la production horaire d'énergie. Dans la dernière partie, deux modèles d'intelligence artificielle sont étudiés : le modèle RNA et le système d'inférence adaptatif neuro-flou, pour estimer la production quotidienne d'énergie électrique de la centrale solaire d'ABM. Les résultats obtenus montrent que les modèles d'intelligence artificielle sont beaucoup plus performants que les modèles analytiques pour prédire les performances des centrales solaires. Les travaux ont conclu que les modèles analytiques sont lents mais explicatifs et bien adaptés à la conception puisqu'ils peuvent anticiper les changements structurels du système simulé. D'une autre part, les modèles d'intelligence artificielle sont rapidement calculables et bien adaptés au contrôle de systèmes physiques qui nécessitent des réactions rapides à des situations changeantes. Ce travail de recherche vise principalement à poser un tremplin dans la recherche de la prévision des performances d'une centrale solaire à concentration, mais aussi à soutenir la recherche visant à comprendre la valeur de l'intelligence artificielle dans la conception et l'optimisation des centrales solaires à concentration.

Mots clés : Modèle analytique, réseaux de neurones artificiels, production d'énergie, centrale solaire, collecteur cylindro-parabolique.

Abstract: Morocco initiated an ambitious renewable energies plan to produce electricity. Interest in solar energy comes at the top of the priorities of this plan. Therefore, this work analyses performance simulation of a solar power plant with parabolic trough collectors (PTC) under Moroccan ambient conditions. In the first part, an overview of the integrated solar combined cycle (ISCC) of Ain Béni Mathar (ABM) was presented. Interest was given to the solar part to evaluate its impact on the power plant's overall performance. The second part aims to assess the thermal performances of the ISCC power plant's solar field at ABM. Thus, a physical model that reproduces the dynamical behavior of the PTC was considered. Energy balance equations of the studied system were solved using COMSOL Multiphysics software. The third part presents a comparison between analytical and artificial neural networks (ANN) models. The models aim to predict the electric energy production of a parabolic trough solar power plant at the electric generator's output and, more especially, the hourly energy production. In the last part, two artificial intelligence models are investigated ANN and adaptive neuro-fuzzy inference system to estimate the daily electric energy generation of the solar power plant at ABM. The obtained results show that the artificial intelligence models perform much better than the analytical models to predict solar power plant performances. The work concluded that analytical models are slow but explanatory and well suited to design since they can anticipate structural changes in the simulated system. On the other hand, artificial intelligence models are quickly computable and well suited for controlling physical systems that require fast reactions to changing situations. This research work is primarily meant to set a stepping stone in the research of performance prediction of a concentrating solar power plant, but also to support the research towards understanding the value of artificial intelligence in concentrating solar power plant design and optimization.

Keywords: Analytical model, Artificial Neural Networks, Energy production, Solar Power Plant, Parabolic trough collector.

Anass ZAAOUMI

Performance assessment of a solar power plant with parabolic trough collectors assigned for ambient conditions in Morocco

Année : 2021   N° thèse : 224/ST2I

École Nationale Supérieure d'Informatique et d'Analyse des Systèmes
Centre d'Études Doctorales en Sciences des Technologies de l'Information et de l'Ingénieur

Université Mohammed V de Rabat

THÈSE DE DOCTORAT

PERFORMANCE ASSESSMENT OF A SOLAR POWER PLANT WITH PARABOLIC TROUGH COLLECTORS ASSIGNED FOR AMBIENT CONDITIONS IN MOROCCO

Présentée par

Anass ZAAOUMI

Le 01/07/2021

- **Formation doctorale :** Sciences de l'Ingénieur - Génie Énergétique

Structure de recherche : Équipe de Recherche en Thermique et Energie (ERTE)

JURY

Professeur Mohamed ASBIK PES, ENSAM, Université Mohammed V de Rabat	**Président**
Professeur Abdellah BAH PES, ENSAM, Université Mohammed V de Rabat	**Directeur de thèse**
Professeur Mohamed ALAOUI PES, ENSAM, Université Mohammed V de Rabat	**Co-Encadrant de thèse**
Professeur Moha CHERKAOUI PES, Ecole Nationale Supérieure des Mines de Rabat	**Rapporteur**
Professeur Mhamed MOUQALLID PES, ENSAM, Université Moulay Ismail de Meknès	**Rapporteur**
Professeur Mohamed ROUGUI PES, ENSAM, Université Mohammed V de Rabat	**Rapporteur**
Professeur Patrick SEBASTIAN Maître de Conférences HDR, Université de Bordeaux, France	**Examinateur**
Professeur Mugur Ciprian BALAN Professor, Faculty of Mechanical Engineering, Technical University of Cluj-Napoca, Romania	**Examinateur**

Acknowledgments

This work was carried out within the Center of Energy, Thermal and Energy Research -Team (ERTE), at ″École Nationale Supérieure d'Arts et Métiers de Rabat″ (ENSAMR), Mohammed V University in Rabat (UM5R), and the Technical University of Cluj-Napoca (Romania), as part of the Eugen Ionescu scholarship program managed by the AUF (Agence universitaire de la francophonie).

I would first like to thank my supervisor Mr **Abdellah BAH**, Professor at ENSAMR who accepted to supervise this research work. He has been an inspiring mentor and honest scientist. During these years of research and training, he has always been on my side, helping me to grow by both encouraging and correcting me. I also would like to thank him for his immense guidance, precious help, encouragement, permanent availability, kindness, sympathy, and support. I have learned many things from him, both professionally and personally.

My sincere gratitude goes to my co-supervisor Mr **Mohammed ALAOUI**, Professor at ENSAMR who co-directed my research. I thank him very much for his advice, his availability, and above all, his personal qualities, which favored the conditions and the quality of the work.

Also, my deepest thanks go to Mr **Mohamed ASBIK**, Professor at ENSAMR for his support. This work could not have been accomplished without his respective contributions, the fantastic discussions we had, and his sense of humor. I express my profound gratitude to him for his kindness, his attentive listening, his efficiency, and his availability along with this work. I owe a lot to him for improving and finalizing this thesis.

I would like to thank Mr **Mugur C. BÃLAN**, Professor at Technical University of Cluj-Napoca (Romania), for welcoming me to his laboratory during my doctoral internship as part of the Eugen Ionescu scholarship (2017/2018 and 2018/2019). Being able to benefit from his knowledge was a real chance for me. He is exceptional with great human and scientific qualities. He was able to make himself available and communicate his enthusiasm when mine was down.

I also warmly thank Mr **Abdellah MECHAQRANE**, Professor at the Faculty of Sciences and Technologies, Sidi Mohamed Ben Abdellah University in Fez for his valuable help. I express

Résumé

Le Maroc a lancé un ambitieux programme des énergies renouvelables pour produire de l'électricité. L'intérêt pour l'énergie solaire figure en tête des priorités de ce programme. Par conséquent, ce travail analyse la simulation des performances d'une centrale solaire à concentrateurs cylindro-paraboliques (CCP) sous les conditions ambiantes marocaines.

Dans la première partie, un aperçu a été présenté de la centrale thermique à cycle combiné solaire intégré (CCSI) d'Ain Béni Mathar (ABM). L'intérêt a été porté à la partie solaire afin d'évaluer son impact sur les performances globales de la centrale. La deuxième partie vise à évaluer les performances thermiques du champ solaire de la centrale d'ABM. À ce propos, un modèle physique qui reproduit le comportement dynamique du CCP a été considéré. Les équations du bilan énergétique du système étudié ont été résolues à l'aide du logiciel COMSOL Multiphysics. La troisième partie présente une comparaison entre les modèles analytiques et les réseaux de neurones artificiels (RNA). Les modèles visent à prédire la production d'énergie électrique d'une centrale solaire cylindro-parabolique à la sortie du générateur électrique et, plus particulièrement, la production horaire d'énergie. Dans la dernière partie, deux modèles d'intelligence artificielle sont étudiés : le modèle RNA et le système d'inférence adaptatif neuro-flou, pour estimer la production quotidienne d'énergie électrique de la centrale solaire d'ABM.

Les résultats obtenus montrent que les modèles d'intelligence artificielle sont beaucoup plus performants que les modèles analytiques pour prédire les performances des centrales solaires. Les travaux ont conclu que les modèles analytiques sont lents mais explicatifs et bien adaptés à la conception puisqu'ils peuvent anticiper les changements structurels du système simulé. D'une autre part, les modèles d'intelligence artificielle sont rapidement calculables et bien adaptés au contrôle de systèmes physiques qui nécessitent des réactions rapides à des situations changeantes. Ce travail de recherche vise principalement à poser un tremplin dans la recherche de la prévision des performances d'une centrale solaire à concentration, mais aussi à soutenir la recherche visant à comprendre la valeur de l'intelligence artificielle dans la conception et l'optimisation des centrales solaires à concentration.

Mots clés : Modèle analytique, réseaux de neurones artificiels, production d'énergie, centrale solaire, collecteur cylindro-parabolique.

Abstract

Morocco initiated an ambitious renewable energies plan to produce electricity. Interest in solar energy comes at the top of the priorities of this plan. Therefore, this work analyses performance simulation of a solar power plant with parabolic trough collectors (PTC) under Moroccan ambient conditions.

In the first part, an overview of the integrated solar combined cycle (ISCC) of Ain Béni Mathar (ABM) was presented. Interest was given to the solar part to evaluate its impact on the power plant's overall performance. The second part aims to assess the thermal performances of the ISCC power plant's solar field at ABM. Thus, a physical model that reproduces the dynamical behavior of the PTC was considered. Energy balance equations of the studied system were solved using COMSOL Multiphysics software. The third part presents a comparison between analytical and artificial neural networks (ANN) models. The models aim to predict the electric energy production of a parabolic trough solar power plant at the electric generator's output and, more especially, the hourly energy production. In the last part, two artificial intelligence models are investigated ANN and adaptive neuro-fuzzy inference system to estimate the daily electric energy generation of the solar power plant at ABM.

The obtained results show that the artificial intelligence models perform much better than the analytical models to predict solar power plant performances. The work concluded that analytical models are slow but explanatory and well suited to design since they can anticipate structural changes in the simulated system. On the other hand, artificial intelligence models are quickly computable and well suited for controlling physical systems that require fast reactions to changing situations. This research work is primarily meant to set a stepping stone in the research of performance prediction of a concentrating solar power plant, but also to support the research towards understanding the value of artificial intelligence in concentrating solar power plant design and optimization.

Keywords: Analytical model, Artificial Neural Networks, Energy production, Solar Power Plant, Parabolic trough collector.

Table of Contents

Chapter 3:   Thermal Performance simulation analysis of a solar field for parabolic trough collectors assigned for ambient conditions in Morocco ... 55

Chapter 4:   Estimation of the energy production of a parabolic trough solar thermal power plant using analytical and artificial neural networks models   91

Chapter 5:   Estimation of Daily Energy Production of a Solar Power Plant Using Artificial Intelligence Techniques 117

List of Tables

List of Figures

Nomenclature

Symbols

a_0	Correction coefficient (1/K)
a_1	Correction coefficient (W/m²K)
a_2	Correction coefficient (W/m²K²)
A	Cross sectional area, (m²)
A_c	Aperture area in a loop, (m²)
A_p	Solar field aperture area (m²)
b	Interaction coefficient, (-)
Bi	Biot number, (-)
c	Accommodation coefficient, (-)
C_p	Heat capacity, (J/kg.K)
D	Tube diameter, (m)
DNI_d	Daily direct normal irradiation (W/m²)
DNI_h	Hourly direct normal irradiation (W/m²)
E_h	Hourly electrical production (MWh)
E_{h-1}	Previous hourly electrical production (MWh)
f	Focal distance of the collector (m)
f_1	Factor between 0 and 1 to account for any additional reduction in energy absorption by the solar field loops
f_{clean}	Mirror cleanliness factor
$f_{dustEnv}$	Factor related to the light absorption of dust on the receiver glass cover
$f_{EndLoss}$	End effect loss
fr	Friction factor, (-)
$f_{RowShad}$	Row shading
h	Heat transfer coefficient, (W/m²K)
H	Height of the parabolic trough (m)
HL	Heat loss, (W/m)
k	Thermal conductivity, (W/mK)
k_1	Correction coefficient that takes into account thermal losses (W/m²K)
k_2	Correction coefficient that takes into account thermal losses (W/m²K²)
k_L	The correction coefficient, due to the longitudinal angle of incidence (α_L)
k_T	The correction coefficient, due to the transversal angle of incidence (α_T)

L	Length (m)
l_{Space}	The space between rows in the solar field (m)
m	Mass in segment, (kg)
n	Number of the day
N_L	Loops number
net_j	Network
Nu	Nusselt number, (-)
O_j	Output
P	Pressure, (Pa)
Pr	Prandlt number, (-)
Q_{loss}	The heat loss from the heat collector element (W/m)
Q_u	The useful thermal power supplied to the HTF (W)
Q_{ele}	The electrical power produced (W)
Q_{HTF}	The useful heat stored in the heat transfer fluid per unit plane surface area of PTC (Wh/m^2)
Qu (AM I)	The useful heat stored in the HTF calculated using AM I (Wh)
Qu (AM II)	The useful heat stored in the HTF calculated using AM II (Wh)
Q_x	Heat flow coming to the segment, (W)
$Q_{x+\Delta x}$	Heat flow leaving the segment, (W)
R	Coefficient of correlation
Ra	Rayleigh number, (-)
Re	Reynolds number, (-)
T	Temperature, (K)
t_h	Ambient temperature (ºC)
t_k	Predicted output
$\bar{t}$	Predicted mean output
V	Velocity, (m/s)
W	Width, (m)
w	Hour angle, (°)
w_h	Wind speed (m/s)
W_{ij}	Weight
$W_{Sca,total}$	The total aperture width of a single SCA (m)
y	Day angle (°)
y_k	Measured output

16

$\bar{y}$ Measured mean output

Abbreviations

ABM	Ain Beni-Mathar
AM	Analytical model
ANN	Artificial neural networks
DNI	Direct normal irradiation
EQT	Equation of time (min)
HCE	Heat Collection Element
HTF	Heat transfer fluid
HRSG	Heat Recovery Steam Generators
IAM	Incident angle modifier
ISCC	Integrated Solar Combined Cycle
MAE	Mean absolute error
MLP	Multi-layers perceptron
MLT	Mean local time (min)
PTC	Parabolic trough collector
PTSTPP	Parabolic trough solar thermal power plant
RMBE	Relative mean bias error
RRMSE	Relative root mean square error
RMSE	Root mean square error
SCA	Solar Collector Assemblies
SNL	Sandia National Laboratories

Greek letters

α_{abs}	Absorbance of the selective coating on the metallic pipe of the absorber tube
α_{gl}	Absorbance of the glass envelope
α_L	Longitudinal angle of incidence (°)
α_S	Angle of solar azimuth (°)
α_T	Transversal angle of incidence (°)
α_t	Azimuth angle of the collector (°)

γ	Interception factor / Ratio of specific heats for the annulus gas
γ_S	Angle of the solar altitude (°)
γ_{st}	The projection of the γ_S on the transversal plane of the collector (°)
γ_t	Tilt angle of the collector (°)
δ	Declination angle of the sun (°) / Molecular diameter of annulus gas (cm)
ε_{gl}	Glass envelope emissivity
η	Global thermal efficiency of the PTC
η_g	Global efficiency (thermal-electrical)
$\eta_{opt}(\theta)$	Optical efficiency
$\eta_{opt,0}$	Peak optical efficiency
η_{track}	Tracking error
λ	Longitude (°)
ρ_{cl}	Reflectivity of the parabolic collector / Density, (kg/m^3)
φ	Latitude (°)
φ_h	Air relative humidity (%)
ω	Hour angle of the sun (°)
θ	Incidence angle (°)
θ_z	Zenith angle (°)
τ	Time (hour)
τ_{env}	Transmissivity of the receiver's glass envelope
$\tau_{h,d}$	Time (hour of the day)
$\tau_{h,y}$	Time (hour of the year)
$K(\theta)$	Incident angle modifier
Δt	Temperature difference between the mean temperature of the heat transfer fluid of the collector (342 °C) and the temperature of the exterior environment (K)
$\dot{m}$	Mass flow rate, (kg/s)

Subscripts

a	Absorber
ai	Absorber interior diameter
ae	Absorber exterior diameter
amb	Ambient
an	Annulus
av	Average

conv	Convection
d	Time step (day)
diff	Diffusion
g	Glass envelope
h	Time step (hour)
h-1	Previous time step (hour)
Loop	Loop
Space	Space between rows in the solar field
sky	Sky
sol	Solar radiation
std	Standard
rad	Radiation
u	useful
w	Wind
x	length

Introduction

In Morocco, energy demand, climate change, and sustainable development have gained great importance in development programs. Over the past decade, several regulatory and institutional measures have effectively addressed environmental concerns in development projects. The reform process initiated by the kingdom of Morocco has paid particular attention to protecting the environment, public health, and sustainable development promotion. Consequently, measures have been taken to strengthen the legal and institutional frameworks to give the country relevant environmental policy and appropriate mechanisms for its implementation.

In 2009, Morocco initiated a green energy dynamic by launching an ambitious program to develop renewable energies and energy efficiency. This vision of Morocco's kingdom is based on a strategy focused on the development of renewable sources of energy such as solar, wind, hydro and biomass. This would diversify and pave the way for Morocco of tomorrow. Thanks to the combination of initiatives and intelligence, Morocco is embarking on a new sustainable energy era. The program consists of installing 6000 MW of renewable power by 2020 (2000 MW for wind energy, 2000 MW for solar energy, and 2000 MW for hydroelectric energy). The installed power will be dedicated to meeting the national demand for electricity and increase the share of renewable energies to 42%. Owing to this program, renewable energies are placed at the heart of the energy and economic policies carried out by Morocco. By 2030, about 52% of electric power intended for national consumption will be of renewable origin (4560 MW solar, 4200 MW wind, and 3100 MW hydropower). Indeed, Morocco intends to position itself as a major player in electricity production from solar photovoltaic and concentrated solar power, which will be the engines of sustainable economic development capable of boosting a new model of growth.

Concentrating solar power plants are one of the most promising technologies to produce electric power. They provide sustainable energy to numerous countries around the world. Four technologies were developed, including the parabolic trough, solar tower, solar dish, and linear Fresnel systems. The parabolic trough collectors are actually the most commercialized and mature solar technology for solar harnessing. They are usually used for a solar steam generation due to their relatively high temperatures (up to 400°C). This technology can also

be employed in other industrial applications at low temperatures, such as desalination and sterilization processes.

Simulation and prediction of the solar parabolic trough power plant's performance are significant for the integration of this technology into the Moroccan markets, and this will be the subject of our study in this thesis. Modeling, simulation, and prediction of the parabolic trough technology performance are needed to determine this system's behavior. To achieve these tasks, it is necessary to know the solar radiation data to estimate the energy produced by this system and understand better the technical operating parameters of this system.

In this regard, the manuscript consists of an introduction, five main chapters and a general conclusion with perspectives. In the first chapter, various concentrating solar power plants are described and compared. A short literature review has been conducted concerning the different methods used for the estimation of parabolic trough solar power plant performances. An overview of the integrated solar combined cycle of Ain Béni Mathar is discussed in the second chapter. Particular interest is given to the solar field for evaluating its impact on the power plant's overall performance. Indeed, existing similar worldwide power plants with parabolic trough technology are reviewed and compared. The third chapter aims to assess the thermal performances of the ISCC power plant's solar field at ABM. Thus, the Schott PTR-70 2008 solar receiver is mathematically modeled using energy balance equations which have been solved by COMSOL Multiphysics software. Next, the model is validated with empirical data from the literature, so the comparison is satisfactory. Results analyze the plant's daily and annual thermal performances and compare simulated and actual plant operating results. The penultimate chapter presents a comparison between analytical and artificial neural network (ANN) models. The models predict the electric energy production of a parabolic trough solar power plant at the generator's output and, more especially, the hourly energy production of the power plant. Several ANN models are presented that vary the number and types of input variables and the number of neurons in the hidden layer. Then, the best ANN model obtained is compared with two proposed analytical models. In the last part, two artificial intelligence models are investigated artificial neural networks and adaptive neuro-fuzzy inference system (ANFIS) to estimate the daily electric energy generation of a solar power plant in Ain Beni-Mathar. Six input variables (daily direct normal irradiation, day of the month, daily average ambient temperature, daily average wind velocity, daily average relative humidity, and previous daily electric production) served as the inputs of the ANN and ANFIS models.

Chapter 1: Background

This chapter offers an overview of different concentrated solar power (CSP) technologies and provides a comparison between them. It discusses also the limitations of CSP technologies and offers possible solutions. Finally, a short literature review of different methods used for the estimation of parabolic trough solar power plant performances.

1.1 Introduction

Solar energy is a useful energy resource available in plenty in the country like Morocco. Harvesting this energy for maximum power generation in the area is of interest to the researchers. There are several techniques for harnessing solar energy. Solar thermal energy allows the creation of thermal energy from solar radiation. Photovoltaic solar energy converts radiation into electricity using photovoltaic cells. Concentrated solar power (CSP) system follows and concentrates the sun's rays to heat a heat transfer fluid that will produce electricity by operating a turbine. This last technology interests us for the following of this study. Indeed, CSP has various advantages. The fluid temperatures circulating inside the system are higher than in fixed solar collectors, so the thermodynamic efficiency is higher. The losses on the mirrors' surface are limited so that the thermal efficiency will be better than in fixed solar thermal systems. The technology is also cheaper because it requires less material and is less complicated to develop. Finally, these systems are economically viable.

As a renewable energy source, CSP technology offers specific advantages due to its ability to integrate energy storage. Using solar heat as an energy source in CSP makes low-cost energy storage possible, as heat can be readily stored with thermal energy storage (TES), which requires heating of a storage material and containing it in an insulated tank [1]. CSP is also advantageous because of its amenability to hybridization. It is considered as an ideal technology to hybridize with other energy technologies for power generation. CSP shares technology with conventional power generation and can be readily integrated with other energy types into a synergistic system, which has many potential benefits including increased dispatchability and reliability, improved efficiency, reduced capital costs through equipment sharing, and the opportunity for flexible operation by alternating between energy sources, which can lead to improved overall efficiency through synergy of the different energy sources [1].

In order to design and establish CSP projects, it is necessary to simulate the operating behavior, calculate energy conversion efficiencies as well as annual performance values, like net electricity production, in advance [2]. This is done via running a performance model of the entire plant over certain periods of time, ranging from typical days, weeks or months up to whole years. However, depending on the required modeling detail, this performance evaluation over longer periods of time can be a rather demanding task, especially, when thinking of detailed physical models of solar thermal power plants on system level. Due to the fact that the performance evaluation of solar thermal power plants is strongly related to the environmental boundary conditions that significantly change over time, the consideration of transients during operation is crucial and classic steady-state models of power plants, which are typical for the evaluation of conventional fossil-fired systems, are usually not sufficient. Therefore, a new field of modeling has emerged in the past few years, specifically tailored to the needs of concentrated solar power. Specific modeling and simulation tools have been developed, which differ in detail, concept and availability [2].

This chapter presents different CSP technologies and discus the limitations of solar processes. Interest was given to the performance prediction of CSP plant as one of the most promising solution. Besides, explores a short literature review of different methods used for the estimation of parabolic trough solar power plant performances.

1.2 Concentrating Solar Power Plants

This part aims to provide a brief explanation of the key component blocks in a CSP plant (i.e., the solar field including the receiver, the thermal energy storage system (TESS) and the power block). The process in a CSP plant is summarized by the schematics shown in figure 1.1.

A CSP plant consists of three main subsystems: a solar field to capture and concentrate the solar radiation, an absorber, and a heat-to-electricity system. In current power plants, a back-up and/or storage system is installed to improve performance and increase the capacity factor, i.e., its annual operating time. The absorber absorbs the solar radiation concentrated by the solar field reflectors and converts it into heat that is transferred to the heat transfer fluid (HTF). The HTF feeds the conversion system, which is the thermodynamic cycle, with the heat source. The storage sub-system allows compensating the intermittence of the solar flow.
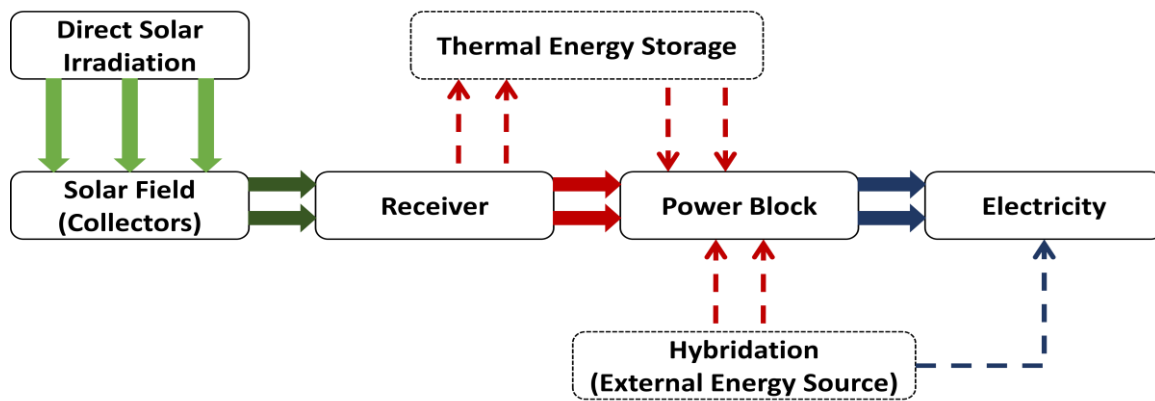
Figure 1.1: Process flow chart of CSP plant

As solar energy is not very dense, it is necessary to concentrate it to increase the density of photon flux on a given surface in order to reach temperature levels that ensure the production of electricity at interesting efficiencies. Currently, four types of concentrated thermodynamic solar power plants are used for electricity production (Line focusing: Parabolic Trough and Linear Fresnel, Point focusing: Solar Tower and Parabolic Dish). Each of these processes differs in terms of geometry, operating temperature, optical and thermal performance and cost.

1.2.1 Parabolic Trough technology

Parabolic trough collectors (PTCs) are the most widespread CSP technology and covers roughly 85% of the global CSP installations to date. The technology can be seen both in schematics (left) and under real operation (right) in figure 1.2.

This system consists of parallel rows of collectors in series. Each collector consists of a mirror, a collector tube (receiver), a metal structure, and a system for tracking the sun's position. The mirrors have a cylindrical-parabolic shape that concentrates the sun's rays on a horizontal collector tube. The concentration ratio for a parabolic cylinder receiver varies between 70 and 80 [3]. The receiver, made of glass, contains a metal tube under a vacuum. In this pipe, the HTF circulates, which is, for this type of solar collector, generally oil. The metal structure must be able to withstand the high temperatures of the tubes and be resistant to the wind that can hit the mirrors. Finally, the mirrors are orientable on a horizontal axis in an east/west direction. It is the sun tracking system that allows choosing the orientation of the mirrors. PTCs system supplies its heat to the working fluid through a heat exchanger. If the working fluid is water, the generated steam can usually reach 100 bar and 370°C. More details could be found in [4]–[7].
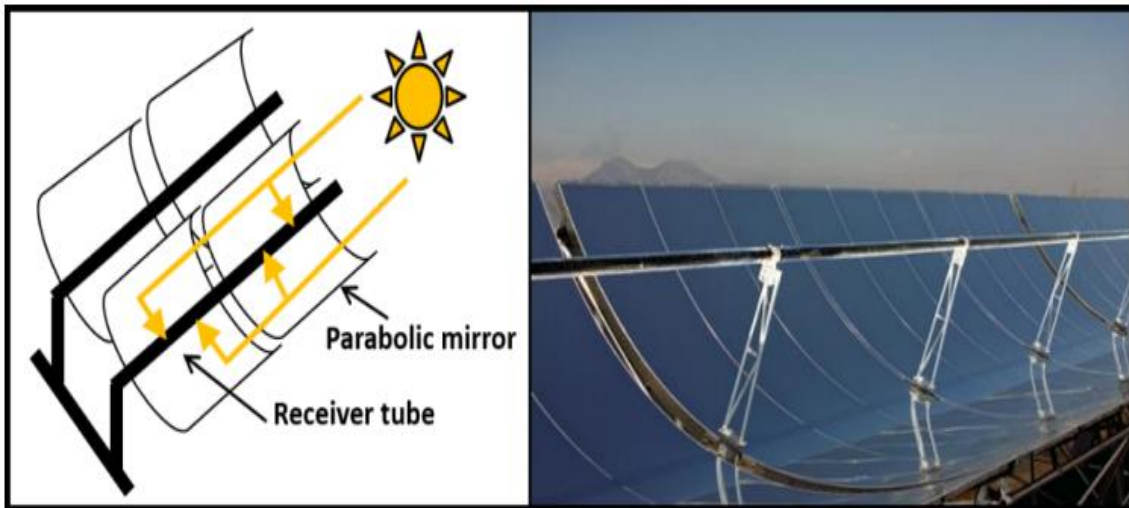
Figure 1.2: Parabolic Trough Collectors. Schematics (left) and real operation (right) [6].

1.2.2 Linear Fresnel technology

Linear Fresnel Reflectors are a CSP technology that is not very widespread but tend to develop. This system is composed of collectors in parallel. Each collector consists of several mirrors, a collector tube, a metal structure, and a system for tracking the sun's position (figure 1.3). The principle is identical to the parabolic trough collectors: the mirrors concentrate the solar radiation on a horizontal tube. However, unlike parabolic trough collectors, the mirrors (the reflectors) are flat, and several mirrors share the same receiver. The receiver, therefore, collects its heat on several rows of mirrors and is fixed. In this receiver, the HTF circulates, which is, for this technology, generally water. The mirrors are located relatively close to the ground, allowing economic gains in the metal structure that supports the mirrors. Finally, the mirrors can rotate along an axis, depending on the sun's position, thanks to the tracking system. More details could be found in [4]–[7].
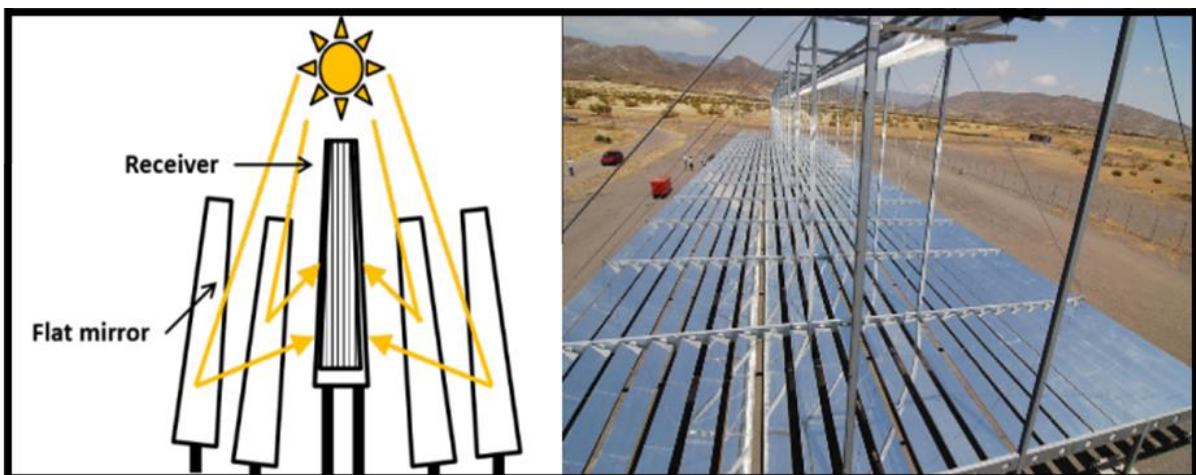
Figure 1.3: Linear Fresnel Collectors: Schematics (left) and real operation [8].

1.2.3 Solar power towers (Central receiver systems) technology

Tower power plants were developed for large-scale production facilities, developing high power and working at high temperatures [9]. The operating principle of the power plant is described in figure 1.4. This type of power plant consists of a field of heliostats and an absorber placed at the top of a tower in the center of the solar field. The heliostats have two degrees of freedom (solar height and azimuth) and redirect the solar radiation to the absorber's focus during the sun's path. A HTF circulates in the absorber and stores the thermal energy produced. One of the major advantages of such a process is a concentration factor that can be between 300 and 1000 [10]. More details could be found in [4]–[7].
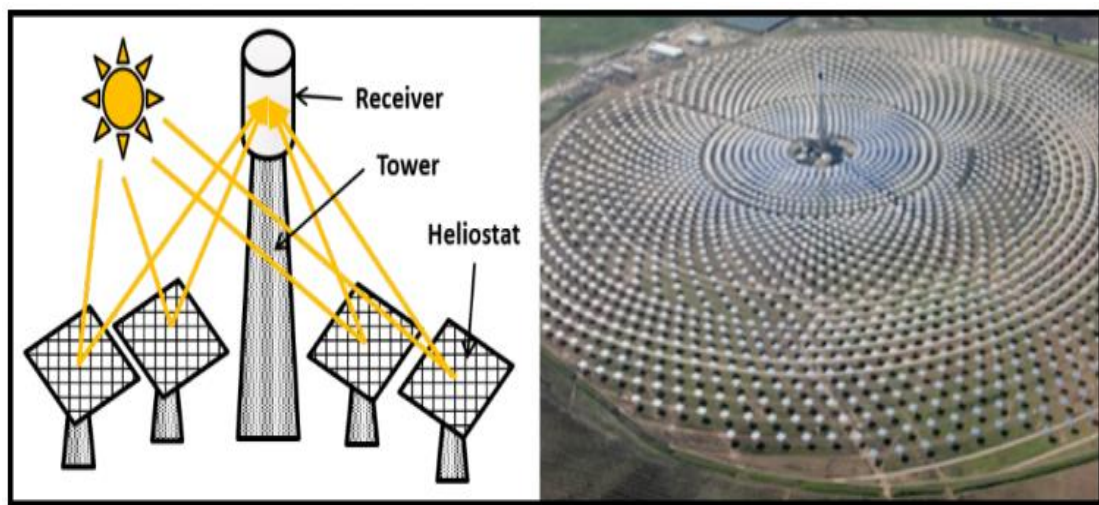
Figure 1.4: Solar Tower Plant: Schematics (left) and under real operation (right) [11].

1.2.4 Solar power towers (Central receiver systems) technology

A parabolic concentrator consists of a parabolic-shaped reflector that reflects solar radiation onto a receiver mounted on the focal point. The components of the system are shown in figure 1.5. The parabolic concentration allows the highest concentration ratios to be achieved of 1000 to 3000, and operating temperatures can reach 1500°C. However, the temperature is limited by the motor, from 700°C to 850°C, depending on the heat engines, which are located at the focal point of the parabola. These concentrators are mounted on a structure with a tracking system having two degrees of freedom. The collected flux is usually used directly by a heat engine mounted on the receiver moving with the dish structure. The Stirling cycle is generally used for the conversion of thermal energy into mechanical energy [10]. More details could be found in [4]–[7].
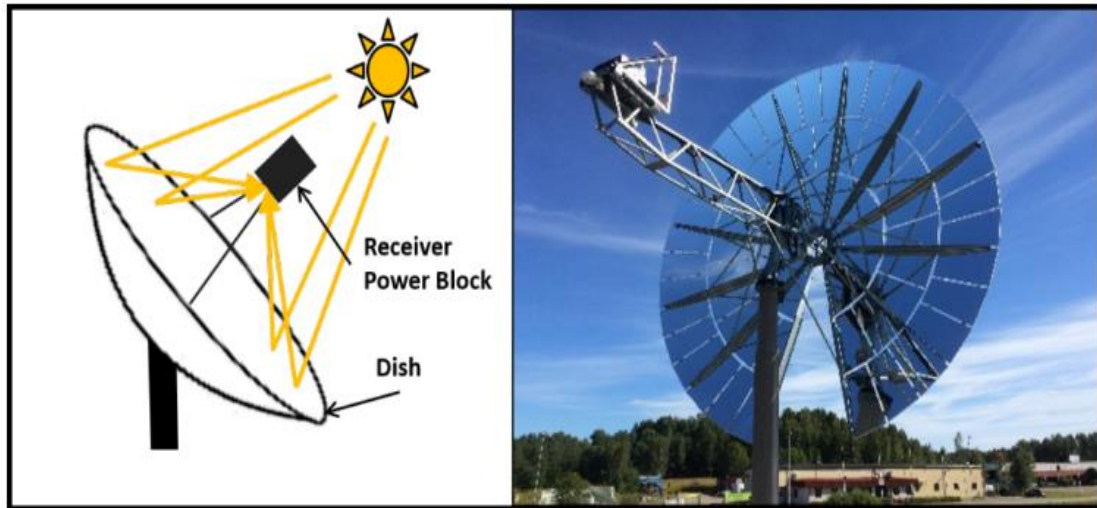
Figure 1.5: Parabolic Dish Systems: Schematics (left) and under real operation.

1.2.5 CSP technologies comparison

Appropriate CSP technology could be selected according to the capacity of the solar power plant. Linear Fresnel and parabolic trough collector are suitable for a low-temperature steam generation (less than 400°C). Solar towers are most suitable in higher temperature range (>450°C). Table 1.1 summarizes the main characteristics of the different CSP technologies [12]–[17].

CSP Technology	Operating temperature [°C]	Relative cost	Land occupancy	Solar concentration ratio	Storage integration possibility	Advantages	Disadvantages
PTC	20-400	Low	Large	70-80	Possible	Relatively low installation cost	The relatively large area occupied, and low thermodynamic efficiency
LFR	50-300	Very low	Medium	>60	Possible	Large experimental feedback. Installation cost is low than PTC	Low thermodynamic efficiency
SPT	300-1000	High	Medium	>1300	Possibility of storage high with low cost	Operating temperature high which led to high thermodynamic efficiency	Occupied space area is large. Installation cost is relatively high. Heat losses are more.
PDC	120-1500	Very high	Small	>1000	Difficult	Occupied area is comparatively small, high operating cost, high thermodynamic efficiency	Installation cost is comparatively high, less experimental work

Table 1.1: Comparison of different CSP technologies.

1.3 Limitations of CSP technologies

Figure 1.6 illustrates the annual direct radiation received on the earth's surface. A very strong disparity is visible between the poles and the solar belt. The belt represents the places where the annual direct radiation is higher than 2000 kWh.m^{-2}.year^{-1}. But whatever the geographical location, solar energy has the inherent characteristics to its very nature: Intermittent availability, discontinuity, and low energy density [18]. Intermittency can be predictable (daily or seasonal fluctuations) and unpredictable (clouds ...). The demand can thus be in phase opposition with the period of high availability. Moreover, the use of an energy source is in fact all the easier as it is dense and regular. These problems, which are found in the main types of renewable energies, constitute the handicaps of these primary energy sources compared to fossil fuels.
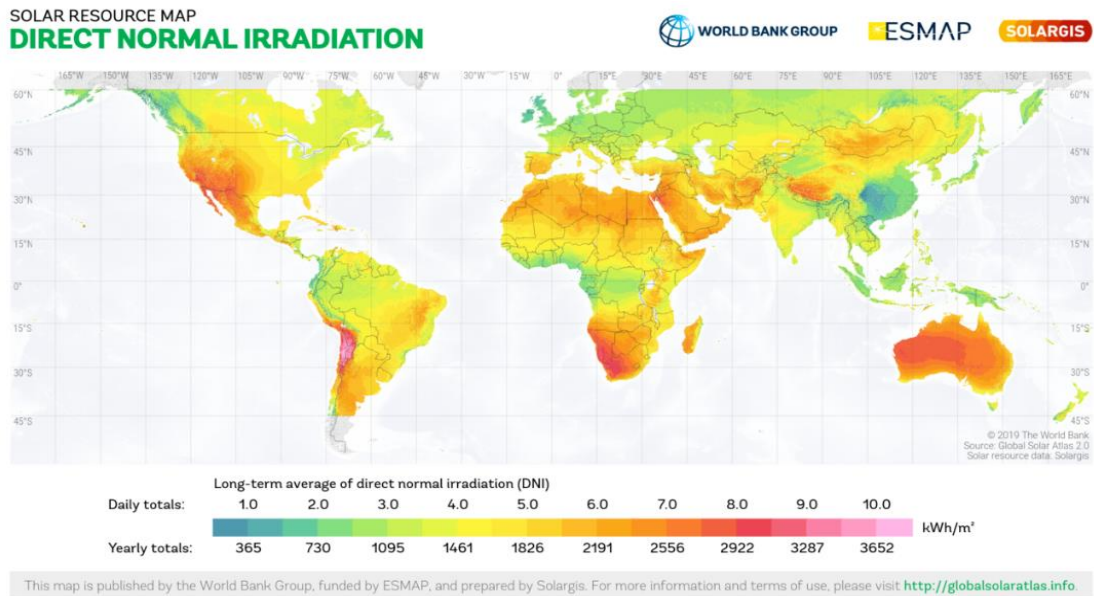
Figure 1.6: Global Map of Direct Normal Radiation [19].

The main approaches being considered to overcome this limitation are as follows:

- Hybridization: The hybridization of power plants can be a solution; a fuel supplement can compensate for the decrease or absence of solar radiation. Usually, the fuel used is gas, oil, or coal. This solution is not optimal in the long term when the goal is to produce clean and decarbonized energy using only renewable energy. Solar power plants with hybrid renewable systems are emerging, such as the Termosolar Borges plant in Spain (Solar and biomass) [20].

- Storage: Energy storage would allow stabilizing the production of CSP plants by storing energy during periods of high production and releasing it during periods of low production. However, the storage of large quantities of energy, low cost, and high efficiencies are the main challenges at the present time.

- Prediction: Development of models for predicting the production of CSP plants energy is important, since it can contribute to a better understanding of the operation of these plants. These models may help engineers, managers of plants, decisions makers and other professionals [2] For example, plant managers can anticipate the transient effects caused by variation of solar irradiance in order to find opportunities, such as the implementation of appropriated control strategies that would allow avoiding losses of plant efficiency. Consequently, opportunities such as this can contribute to increase the overall efficiency of the plant, reducing the cost of electricity generation, making this power plant concept more feasible and competitive. It is in this direction that our research work falls.

The next section presents a short literature review of different models developed for the prediction of parabolic trough solar power plant performances.

1.4 Prediction of parabolic trough solar power plant performances – A short literature review.

The solar field (SF) of PTCs is the key component of a CSP plant. So, it is very important to use proper models to accurately predict its behavior. Many research works have been carried out to study the thermal performances and heat transfer characteristics of PTCs. Generally, published studies could be divided into two main categories: testing models and performance models [21]. Performance models are usually used to estimate the thermal power or the thermal efficiency of a single module, a parabolic solar collector loop, or the entire solar field. Well-known specific PTC parameters such as optical and thermal properties are required to simulate its thermal behavior. Those parameters information could be determined by performing a testing model [21].

A recent literature review shows that most studies on predicting the PTC power plants are based on analytical models, including steady-state and dynamic models, while machine learning models such as ANN models are rarely used.

For steady-state studies, Montes et al. [22] presented a model for the economic optimization of solar parabolic trough power plants with no hybridization or storage. They investigate thermal performances at maximum and part-load conditions for different solar field sizes. Rolim et al. [23] developed an analytic model for a solar power station with parabolic trough collectors combining models for the solar collector's field and power station. Conversion of solar radiation into heat considers the non-linear behavior of heat losses from the parabolic collectors. The power cycle is considered as endo-reversible because of the irreversibility arising from the limits of the energy source. The numerical results are compared with measurements obtained from the Solar VI power generation system installed in the Mojave Desert in California and showed a good agreement between modeling and experimentation. Abutayeh [24] presented a detailed model of a real solar thermal power plant developed from a steady state power plant simulation software. In this numerical model, the parabolic trough collectors track the sun movement on a single axis. Simulation results matched well with plant data, including data collected during warm-up and cool down transient operations. Patnode [25] developed a model for the solar field using the TRNSYS simulation tool. The steady-state power cycle performance was regressed in terms of heat transfer fluid mass flow rate,

the heat transfer fluid temperature, and condensing pressure. The model was validated with measured temperature and flow rate data from the Nine Electric Generation Systems VI plant (California, USA) from 1998 to 2005. Manzolini et al. [26] presented a steady-state model to predict performance and preliminary CSP plant sizing at normal nominal conditions for different plant layouts. The model was based on energy balance equations applied along the length of the HCE of the solar field and validated with experimental indoor tests from NREL.

For Dynamic model studies, García et al. [27] proposed a detailed performance model of a 50 MWe parabolic trough solar thermal power plant with two thermal storage molten salt tanks using Wolfram's Mathematica 7 software. The solar field is composed of 156 loops, of which each contains four solar collector assemblies (SCA) that consist of 12 solar collector elements (SCE). Empirical correlations obtained from the national renewable energy laboratory (NREL) for different commercial HCEs were implemented in the simulation program. The simulation results compared with measurements resulting from experiments for 42 days in summer at the Andasol2 power plant in Spain, showing good agreement for clear days. Schenk et al. [28] modeled parabolic trough concentrators in power plants using Dymola. Their study aimed to evaluate the transient behavior of concentrators, namely the start-up of power plants using thermal oil and parabolic trough concentrators. Due to the lack of data based on in situ measurements, the model is calibrated from another simulation model developed in the Ebsilon Professional environment. Tähtinen et al. [29] also developed a dynamic model of a power plant. Two solar field models are implemented using the Advanced Process Simulation Software (APROS), which is based on parabolic cylindrical and linear Fresnel reflector technologies. Both solar field models use water as a heat transfer fluid. Based on APROS, Wisam AbedKattea Al-Maliki [30] also developed a full-scale dynamic model of the power plant "Andasol II" located in Spain. The comparison between simulation results and validation data shows a good match between the model and actual operation. Rohani et al. [31] used the ColSimCSP tool developed at Fraunhofer ISE to assess performance parameters of solar field (thermal power and net electrical energy yield) associated with the commercial PTC power plant Andasol 3 (Spain) for ten consecutive days of three different months (July, September, and November). Special attention was given to storage strategy and start time operation. The simulation results showed that the lowest mean deviation of solar field thermal power and net electrical energy yield are 0.59% and 2.29%, respectively. A dynamic model was developed by Powell and Edgar [32] consisting of energy balances that are applied to the operating fluid, the absorber tube and the glass tube of

segments along the HCE of the trough collectors to simulate a 1 MWt CSP plant for controlling proposals; however, the paper does not show the experimental variables utilized to validate the model.

Gaps between physical and artificial intelligence models are not only present in the area of solar parabolic trough collectors but also in many solar energy systems (SES). To fill this gap, new modeling methods have been adopted by many researchers to predict system performance accurately. The ANN method has recently been successfully applied in the field of SES to handle different tasks like design and performance optimization, thanks to the advantages of self-adaption, self-learning, nonlinear mapping, and fault tolerance [33]. Elsheikh et al. [34] summarized ANN applications for modeling of different SES such as solar collectors, solar air and water heaters, solar-assisted heat pumps, and photovoltaic/thermal (PV/T) systems, solar dryers, solar stills, and solar cookers. In this bibliography analysis, different ANN types were discussed, like multilayer perceptron neural network, Elman neural network, the function of the radial basis, and neural networks using the wavelet. Also, different activation functions types used in different ANN, and different standard statistical performance evaluation criteria used in the evaluation of ANN performance were reported.

Few studies are devoted to the prediction of PTC performances based on Artificial Neural Networks. For small-scale PTC, Kalogirou et al. [35] applied ANN to investigate the thermal performance of a solar steam generator connected to a parabolic collector. Eight parameters were used as input of the ANN model (solar irradiance, ambient temperature, time, effective aperture-area, flash-vessel content, and flash-vessel dimensions of diameter, height, and thickness). The learning process was performed by using the back-propagation algorithm. ANN model gives better mapping capabilities than the analytical model. In a more recent study, Heng et al. [36] developed a fast and accurate method to predict the exit fluid temperature of a PTC tube. This method is a combination of an ANN model with the superposition principle. The input parameters of the ANN model are heat flux, fluid velocity, and time. In addition to the input and output layers, the ANN model's architecture consists of two hidden layers with 68 neurons in each one. The linear activation function was used in the input layer, while the logistic activation function was used for the hidden layers and the output layer. The developed method requires less than 1 min of computational time to predict the one-day exit fluid temperature. Prediction results show relatively small deviations from the finite element method. The overall mean absolute deviation is less than 2 K. For large-scale PTC, Boukelia et al. [37] applied the ANN method to determine the techno-economic

performances of a PTSTPP. Five inputs were chosen for the proposed model, such as design solar radiation, solar multiple, design ambient temperature, row spacing between parallel collectors, and the number of desired storage hours. The model outputs were selected to be the annual power generation and the levelized cost of electricity. To select the best ANN model, the feed-forward back-propagation learning algorithm was investigated with three different variants; Scaled Conjugate Gradient, Levenberg-Marquardt (LM), and Pola-Ribiere Conjugate Gradient. The obtained statistical parameters showed that the LM algorithm with 38 neurons in a single hidden layer looks like the best ANN model.

1.5   Conclusion

This chapter presents different CSP technologies and discusses the limitations of solar processes. Interest was given to the performance prediction of CSP plant as one of the most promising solution. Besides, explores a short literature review of different methods used for the estimation of parabolic trough solar power plant performances.

In summary, the performance prediction of CSP plants using PTCs has already been examined by numerous authors using mostly analytical models. However, PTC performances based on artificial intelligence modeling like Artificial Neural Networks are rarely used. One of the main objectives of this thesis is to explore the application of artificial intelligence modeling in predicting large scale PTCs power plant performance. Before that, an overview of the Integrated Solar Combined Cycle System (ISCC) of Ain Beni Mather in Morocco is presented in the next chapter.

Chapter 2: Integrated Solar Combined Cycle System of Ain Beni Mather in Morocco

Morocco initiated an ambitious renewable energies plan to produce electricity. Interest in solar energy comes at the top of the priorities of this plan. This optic shines with the start of the first Integrated solar combined cycle system (ISCCS) of Ain Beni Mathar (ABM) in the Eastern of Morocco. This ISCCS with parabolic trough technology is operational since 2011 and generates 470 MW of electricity. This chapter presents technical data and highlights the performances of ISCCS of ABM over the year 2015. Interest was given to the solar part to evaluate its impact on the power plant's overall performance. Also, a comparison was made between existing similar ISCCS with parabolic trough technology to class the current ABM power plant.

2.1   Introduction

In Morocco, the electricity demand is increasing rapidly, and about 91 % of energy needs are imported [38]. At the same time, Morocco is very rich in solar energy resources. The use of fossil energy sources is very costly, and electric networks' extension finds enormous problems. In this optic, Morocco is keenly interested in large-scale exploitation of its abundant solar resources, specifically using Concentrated Solar Power (CSP) technology.

Concentrating solar power (CSP) systems concentrate solar energy by focusing solar radiation onto a focal point or line. Multi-megawatt plants have been delivering the world's cheapest solar electricity for the last fifteen years. It is predicted that CSP will play a significant role in providing clean energy to meet the world's energy demands, increasing rapidly in response to the growing economy in both developed and developing countries [39]. Four technologies have been developed, including the parabolic trough, solar tower, solar dish, and linear Fresnel systems. Parabolic trough collector (PTC) power plants are the most proven system of CSP techniques.

The integrated solar combined cycle (ISCC) has been studied and demonstrated for more than three decades. The combined-cycle (CC) power plants consist of a gas cycle or Brayton cycle (topping cycle) and steam cycle or Rankine cycle (bottoming cycle). The two cycles are linked by a heat recovery steam generator (HRSG). Exhaust heat from the gas turbine is recovered in a HRSG to produce steam at suitable pressure and temperature. The produced steam is then used to produce further electricity in steam turbines [39]. There may be different

ISCC configurations according to the solar field technology: Linear Fresnel (LF), Power Tower (PT) and Parabolic Trough with Direct Steam Generation (PT-DSG) and Parabolic Trough with heat transfer fluid (PT-HTF) ([40], [41]), and also according to how the solar steam is injected in the CC (in HRSG or directly in steam turbine) [42].

Several ISCC power plants with parabolic trough technology have been commissioned recently all around the world. The configuration basically consists of a parabolic trough solar field coupled to the steam cycle of a CC power plant. Parabolic troughs are cooled by synthetic oil, so an intermediate oil to-water/steam heat exchanger is needed between the solar field and the power block. This particular configuration is called heat transfer fluid (HTF) technology, and it is the most used in parabolic trough thermal plants, where the power block is usually a steam cycle. Another scheme consists of a direct steam generation (DSG) parabolic trough plant coupled to the steam cycle of a CC power plant [43], [44].

In the MENA region, four power plants are already operating. Three of them are located in North Africa (Morocco, Algeria and Egypt) and the remaining one in Iran. Two ISCCS power plant are Scheduled in the Middle East, one of them is under construction in Saudi Arabia (Duba 1, 605 MW, with 43 MW from solar electricity) and the other is under development in Kuwait (Al-Abdaliya, 280 MW, with 60 MW from solar electricity). Tables 2.1 and 2.2 provide more details about the ISCCSs in the MENA region.

Project name	Company/ Owner	Country	Location	Capacity (MW)	Solar electrici-ty (MW)	Start year	Coordinates
Ain Beni Mathar	ONE	Morocco	Ain Beni-Mathar	470	20	2011	34°3'50.00"N 2°6'0.00"W
Hassi R'mel	Sonatrach	Algeria	Hassi R'mel	150	20	2011	33°7'27.00"N 3°21'25.00"E
Kuraymat	NREA	Egypt	Kuraymat	140	20	2011	29°16'43.00"N 31°14'56.00"E
Yazd	IEDO	Iran	Yazd	467	17	2010	31°57'48.24″N 54°3'53.64″E
Duba 1	Saudi Electricity Co.	Saudi Arabia	Duba	605	43	2017	-
Al-Abdaliya		Kuwait	Al-Abdaliya	280	60	-	-

Table 2.1: ISCCS power plants in the MENA region [45], [46].

Solar field	SCA manufacturer	Number of SCAs	Mirror manufacturer	Solar field aperature area	HCE	HTF
Ain Beni Mathar	Abengoa Solar (ASTRO)	224	Rioglass	183,120 m²	Schott (PTR 70)	Therminol VP-1
Hassi R'mel	Abengoa Solar (ASTRO)	224	Rioglass	183,860 m²	Schott (PTR 70)	Thermal oil
Kuraymat	Flagsol (SKAL-ET)	160	Flabeg (RP3)	130,800 m²	Schott (PTR 70)	Therminol VP-1
Duba 1	Flabeg (Ultimate Trough)	-	-	170,000 m²	Archimede Solar Energy	Thermal oil

Table 2.2: Solar field design data of ISCCS power plants in the MENA region [45], [46] .

The present chapter aims to detail the performance of the first ISCCS power plant in Morocco. This power plant uses natural gas as fuel from the Maghreb-Europe gas pipeline and solar energy from a solar field of parabolic trough collectors.

2.2 Potential and availability of solar energy in Morocco

2.2.1 Current situation of the energy in Morocco

The electricity demand in Morocco is increasing with economic development. Consequently, electricity demand is more than doubled from 16 TWh (TeraWatt-hour) in 2002 to 35 TWh in 2015, and is growing at an average rate of 6.2% per year since the year 2000 [47]. For this reason, the production of energy in Morocco increased by 6-7% per year between 2002 and 2012 to provide this demand grows [48]. In 2019, the total capacity installed in Morocco is 10 677 MW, with 34.6% of renewable energies with the following mix: Carbon (38.55%), natural gas (18.21%), hydropower (16.57%), fuel oil and diesel (8.58%), solar (6.66%) and wind power (11.43%) [49]. According to Ministry of Energy, Mines, Water and the Environment (MEMEE) of Morocco [50], future primary energy demand could reach 43 Mtoe (million tonnes of oil equivalent) in 2030. Also, Morocco imports electricity from the neighboring countries (Spain and Algeria).

To resolve its energy challenges, Morocco adopted since 2009 a national energy strategy to develop renewable energies and energy efficiency. This program was the first step to encourage and intensify the use of renewable energies. According to this strategy, Morocco

aims to supply 52% of its electrical power from renewable sources by 2030, which 4560 MW solar, 4200 MW wind, and 3100 MW hydropower [48].

2.2.2 Solar energy status and outlook

Thanks to its geographical location, Morocco is characterized by an intensive solar radiation with an average of 5.3 kWh/m^2 /day under annual sunshine durations varying from 2700 h in the north to approximately 3500 h in the south (see figure 2.1 [48]). To increase the capacity of the production, the kingdom of Morocco has a stated goal for solar energy terms of Concentrating Solar Power (CSP) and Photovoltaic (PV) of 14% (2000 MW) by 2020 and 20% (4560 MW) by 2030 of the country's production capacity [47].
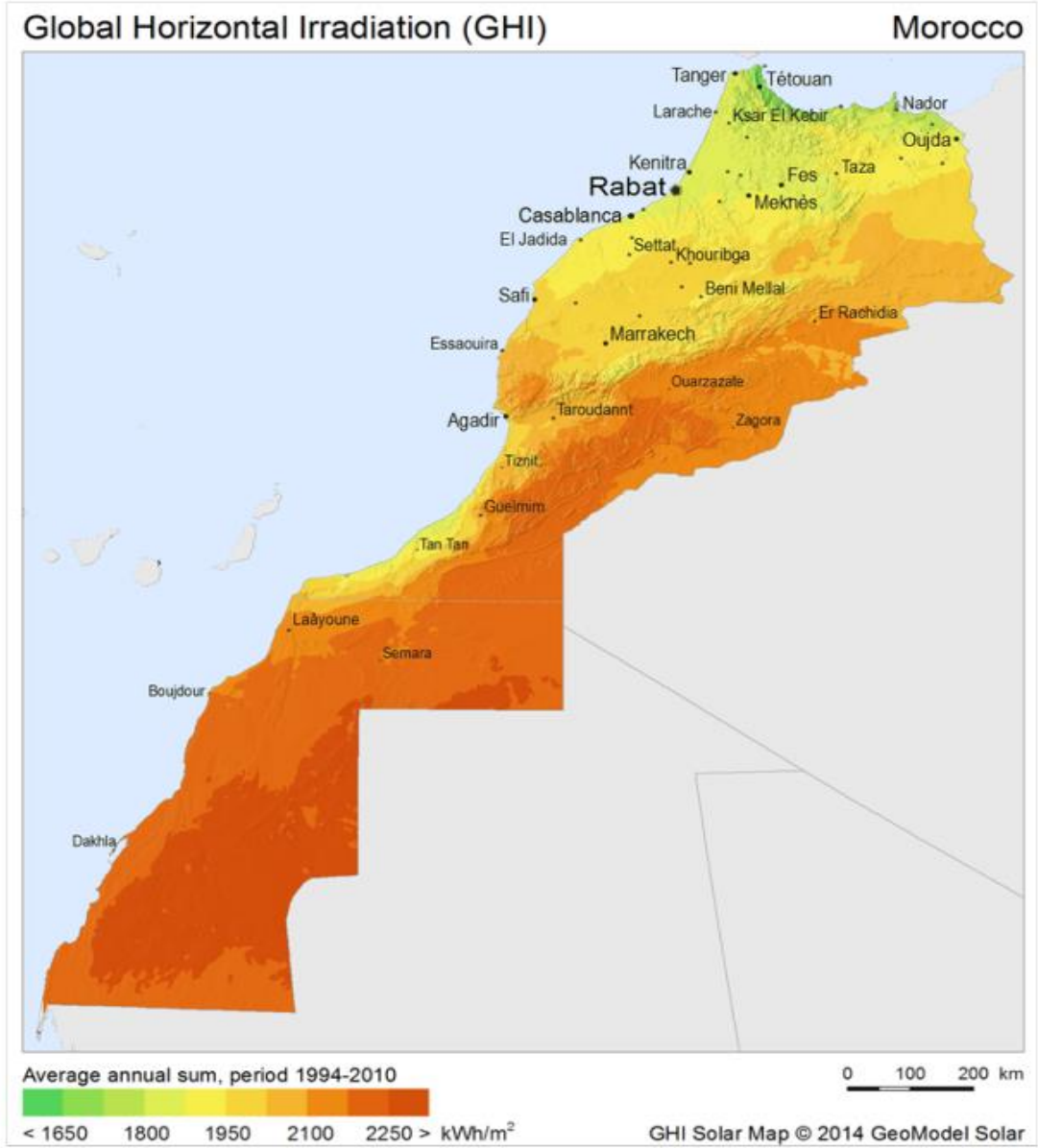
Figure 2.1: Moroccan solar potential [48].

Morocco's total installed solar power capacity constituted by CSP and PV technology at the end of 2019 [49] was 711 MW, including 580 MW Ouarzazate (Noor I, II, III and IV projects), 20 MW solar thermal CPS and gas - Ain Bni Mathar, 80 MW Laâyoune and 20 MW Boujdour. Moroccan Agency for Solar Energy (MASEN) is the responsible for many aspects of solar (CSP and PV) energy in the country and also ONEE is itself planning to create a number of medium-sized PV [51]. Table 2.3 shows the solar stations under service or are under development.

Site/power plant	Power in MW	Technology	Status
NOOR I Ouarzazate	160	CSP	Under service
NOOR II Ouarzazate	200	CSP	Under service
NOOR III Ouarzazate	150	CSP	Under service
NOOR IV Ouarzazate	70	PV	Under service
NOOR Midelt	300	CSP	Under development
	525	PV	Under development
Tata	400	CSP and PV	Under development
Ain Beni Mathar	20	CSP and gas	Under service
Noor Boujdour I	80 (20 installed)	PV	Under service
Noor Laâyoune I	80	PV	Under service
Noor Tafilalt (Zagora, Erfoud and Missour)	120 total (40 each site)	PV	Under development
Noor Atlas (Boudnib, Bouanane, Outat El Haj, Enjil, Ain Bni Mathar, Tata, Bouizakarne, and Tan Tan)	200 total (25- 40 per site)	PV	Under development
Noor Argana	100	PV	Under development
Tanger-Asilah	30	PV	Under development

Table 2.3: The solar stations under service or are under development in Morocco [48], [50], [51].

2.3   Main criteria for choosing the location of Ain Beni Mathar:

The technical choice of Ain Beni Mathar for the construction of the ISCCS power plant was therefore dictated by favorable conjunction of the following criteria:

- Proximity to the Maghreb-Europe gas pipeline,
- Sufficient solar irradiation,
- Availability of sufficient water flow,
- The proximity of the high voltage electricity grid for the evacuation of the produced energy and geographical balance of the productive park,
- Infrastructure
- Availability and cost of land,

- Wind speed

2.3.1 Proximity to the Maghreb-Europe gas pipeline

Morocco does not produce fossil energies, such as oil and gas. The ISCCS uses gas to run the gas turbines. So, the proximity to the Maghreb-Europe gas pipeline is mandatory to get the necessary gas to run the ISCCS power plant. It is well observed from figure 2.2 that the site of Ain Béni Mathar is near to Maghreb-Europe gas pipeline. A 13 km pipeline leading to a related depressurization station, a metering unit for gas, and a connection to the Maghreb-Europe gas pipeline.
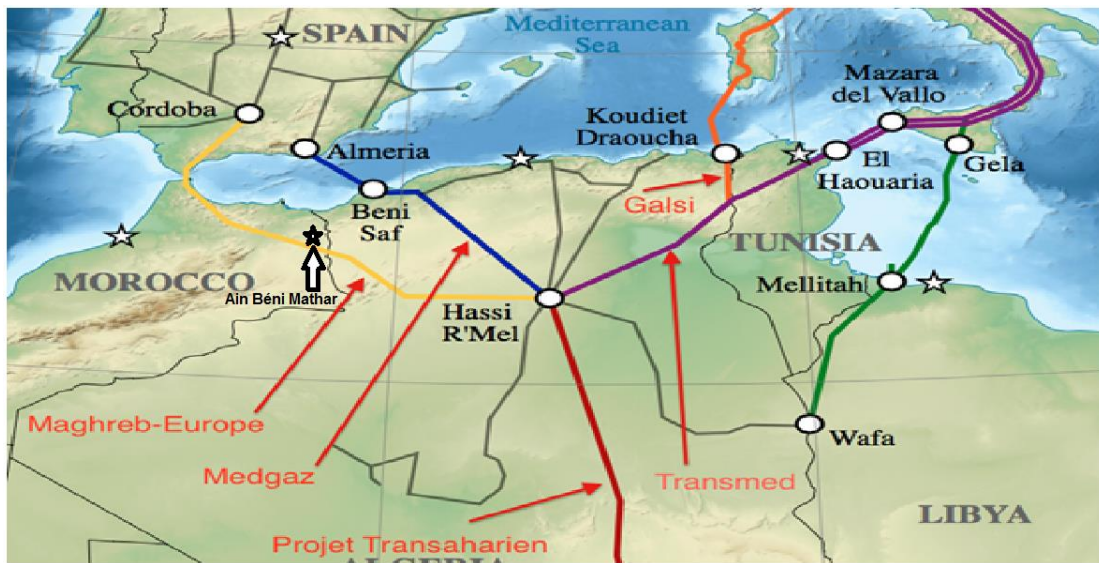
Figure 2.2 : Location of Maghreb–Europe Gas Pipeline [52].

2.3.2 Solar resource at the location of the ISCCS:

The climate in the plant's region is Csa Under the Köppen-Geiger climate classification with a mild to cold and rainy winter and hot summer. Knowing the fact that DNI is the main criterion for the CSP site assessment. figure 2.3 represents the average annual DNI of Morocco between 1994 and 2010. It is observed that the region of Ain Beni Mathar has valuable potential for implementing the solar field of the ISCCS power plants as it has a cumulative annual DNI superior to 2000 kWh/m^2 [53]. Because of economic considerations, the minimum annual DNI value required for a region to host CSP plants is 1800 kW h/m^2 [54], which means that the site is favorable for implementing the ISCCS power plant.
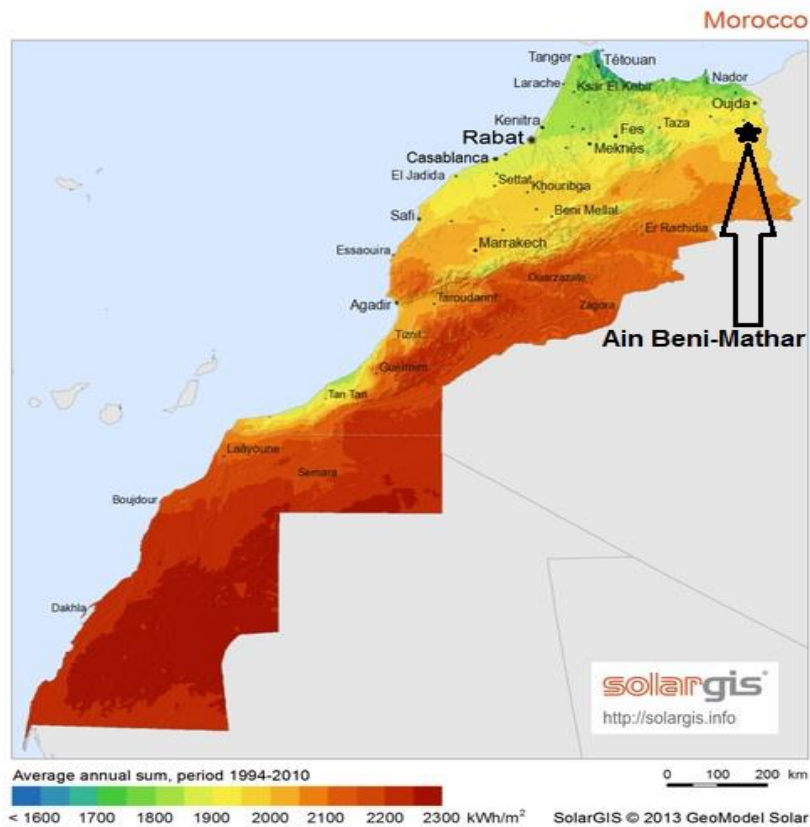
Figure 2.3: Average DNI of Morocco and the location of the ISCCS on the map of Morocco [48].

The cumulative annual DNI for the reference year is 2290 kWh/m²/year [55]. Figure 2.4 shows a comparison of this pattern for the year 2015 and the reference year. The 2015 annual value is about 2136 kWh/m² and is 6.7% lower than the reference year, spread relatively evenly throughout the year.
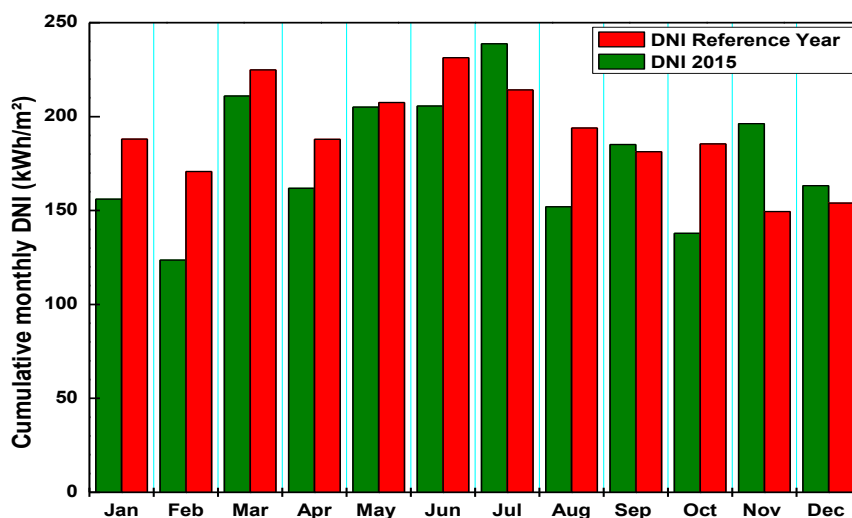
Figure 2.4: Direct Normal Irradiation: 2015 Actual vs. Reference Year.

2.3.3 Availability of sufficient water flow

For CSP technology, water availability is crucial, as water plays a major role in the operation of the solar power plant. Indeed, water is used to clean the solar mirrors, particularly in arid regions (like eastern Morocco where ABM situated), where dust presents a limiting efficiency factor for electricity production [56]–[58].

Cleaning is not the most water-consuming factor in a CSP plant if the wet cooling option is used. According to EASAC (European Academies' Science Advisory Council, https://easac.eu), 90% of the water is used for cooling and only 10% for cleaning. This issue becomes less important for the dry cooling option [59], [60]. In the ABM power plant, a dry cooling system is used instead of a wet cooling to decrease the water needs. An Aerocondenser provides dry cooling.

Figure 2.5 presents the hydrological network of Eastern Morocco. This network contains permanent waterways, dams, and underground water.
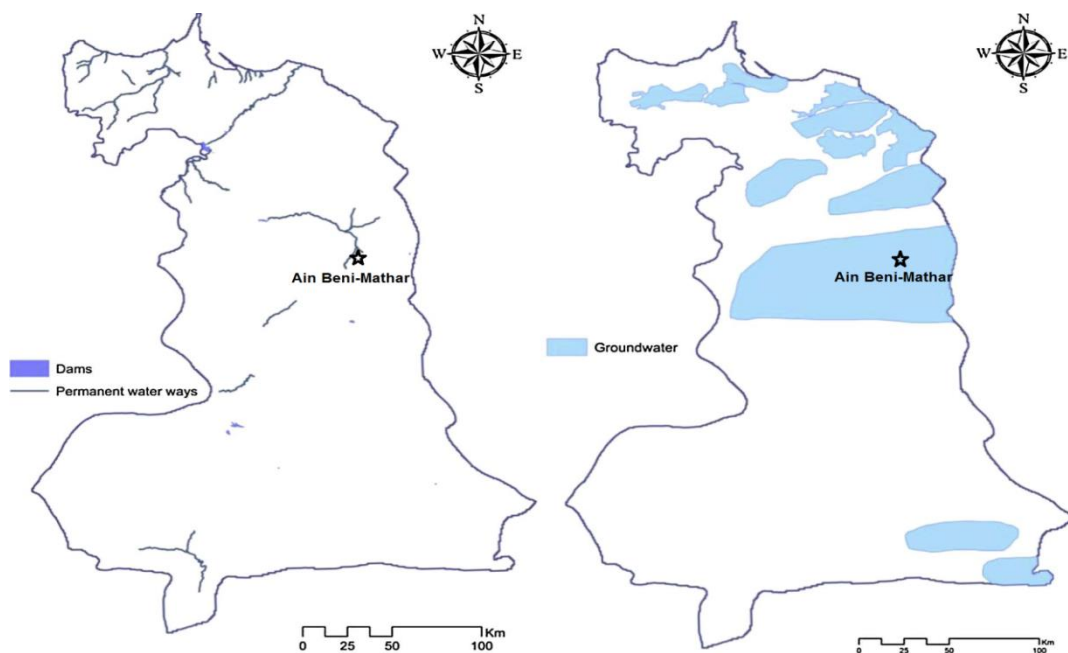
Figure 2.5: The hydrological network of Eastern Morocco. Left: waterways and dams, right: Groundwater [61].

The site of Ain Beni Mathar is located on one of the largest ground-water tables in North Africa [53]. The total water requirements of the power plant are about 1.5 million m^3 / year. These needs are drawn from the deep-water table of Ain Beni Mathar in the project area.

For this purpose, three boreholes were drilled by the agency called "Agence de Bassin de Moulouya". Water is pumped from the aquifer located below the site of Ain Beni Mathar.

Only two boreholes are used to pump quantities of water necessary for operation and maintenance of the power plant, particularly the cleaning of the solar collectors and operating of the steam cycle. Water reserves equivalent to one-day consumption are stored. The site wastewater is collected and treated in a two-hectare stabilization pond [53].

2.3.4 Infrastructure and proximity of the Power grid

Generally, an ISCCS power plant has to be accessible; it must be as close as possible to cities, roads, railways. Figure 2.6 shows the complete road network, the railway network, and Eastern Morocco cities.
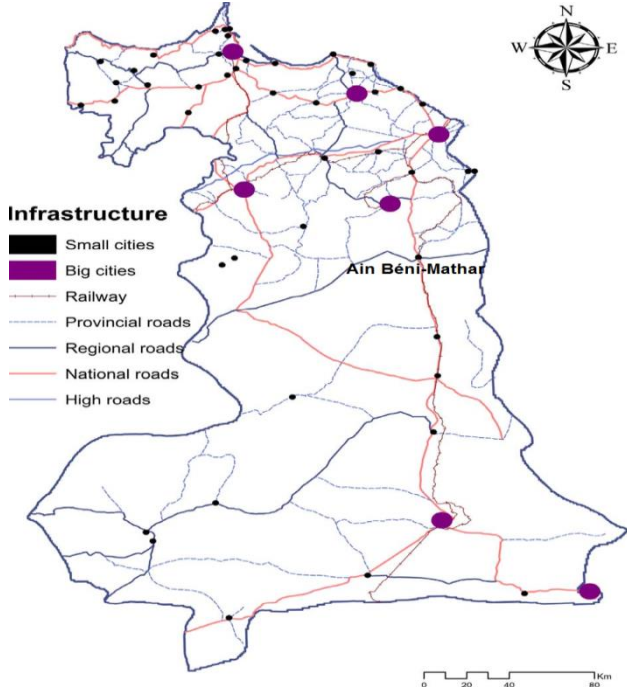
Figure 2.6 : The infrastructure map of Eastern Morocco, including the complete road network, the cities, and the railways [61].

Another key factor for selecting a site is accessibility to the power transmission line. The connection between the transmission line and the grid is financially expensive; hence the ISCCS plant must be close to the network. Morocco has an important alternating current network, covering not only the cities but also some unpopulated locations due to hydroelectric, gas turbines, and thermal power plants. The national grid is owned by the state and is schematically displayed in (figure 2.7 (a)). Morocco has approximately 23332 km of power lines [38]. As reported by the National Office of Electricity and Water (ONEE), there are 2765 km of transmission lines of 400 kV, 9680 km of transmission lines of 225 kV, 147

km of transmission lines of 150 kV, and about 12000 km of transmission lines of 60 kV. The complete power grid of Eastern Morocco is presented in (figure 2.7 (b)).
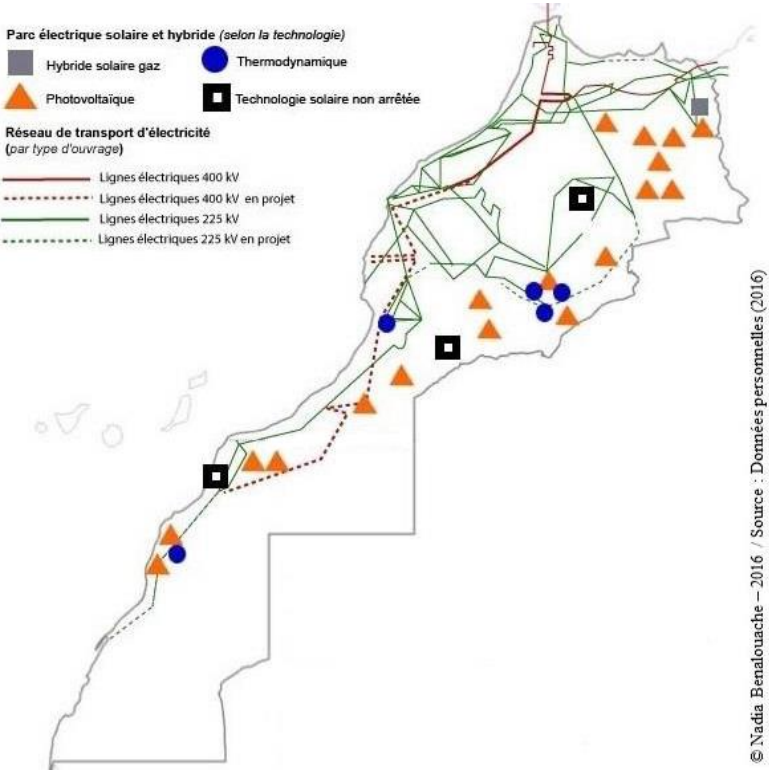
(a)
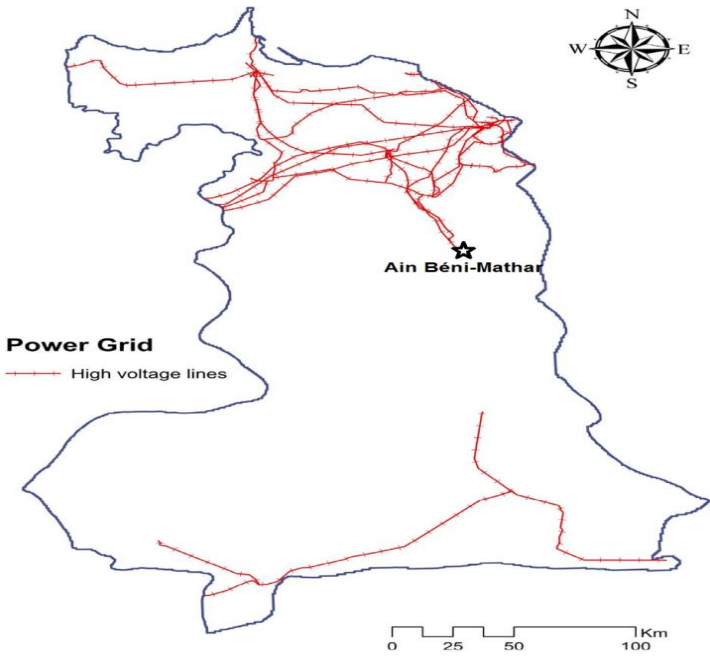
(b)

Figure 2.7 : (a) Moroccan electricity grid [62]; (b) The complete power grid of Eastern Morocco [61].

The power generated by the plant will be evacuated via two 225 Kilovolt (kV) transmission lines and one 60 kV back up transmission line. The first 225 kV transmission line was planned to carry power to the existing Oujda substation (110 km). The second 225 kV transmission line was to evacuate power to the Bourdim substation (70 km). The 60 kV line (10 km) was conceived to provide a backup power supply to the auxiliaries of the ISCC plant in case of emergency by connecting the existing 60/225 kV substation of Ain Beni Mathar city to the plant.

2.3.5 Availability and cost of land

The parabolic trough collectors' solar field is the mean component that takes most of the ISCCS power plant area. CSP power plants are highly affected by the land slope. It is considered a significant parameter for land assessment since it highly affects the feasibility and the cost of any solar project [63], [64]. Studies have shown that lands with a slope of less than 3% give the best LCOE [38]. The chosen sites require that their cost is reasonable. The location has to be free of agriculture activities or residences and has low biological habitat and seismic history [38]. The site of « Ain Beni Mathar » has these characteristics.

ONEE acquired 203 hectares of land for the construction and operation of the plant. 160 hectares are for the power plant (including 88 ha for the solar field), 6 hectares for the boreholes and water distribution, 31 hectares for the gas spur from the Maghreb-Europe pipeline to supply the power plant and the transmission lines, and 6 hectares for the access road [53].

2.3.6 Evaluation of wind

Wind assessment is mandatory at the design phase. The wind speed greatly influences the collector's design, representing 40% of the solar field cost [38]. Hence, the consideration of wind energy is essential to support the decision-making process.

In Ain Béni Mathar, a study of wind average speed over 4 years (2012-2015) shows that 76.46% of the values are less than 6 m/s (figure 2.8). The maximum velocity attained there was about 17 m/s, while normally, the CSP installation is designed to handle high wind speed (up to 30 m/s).
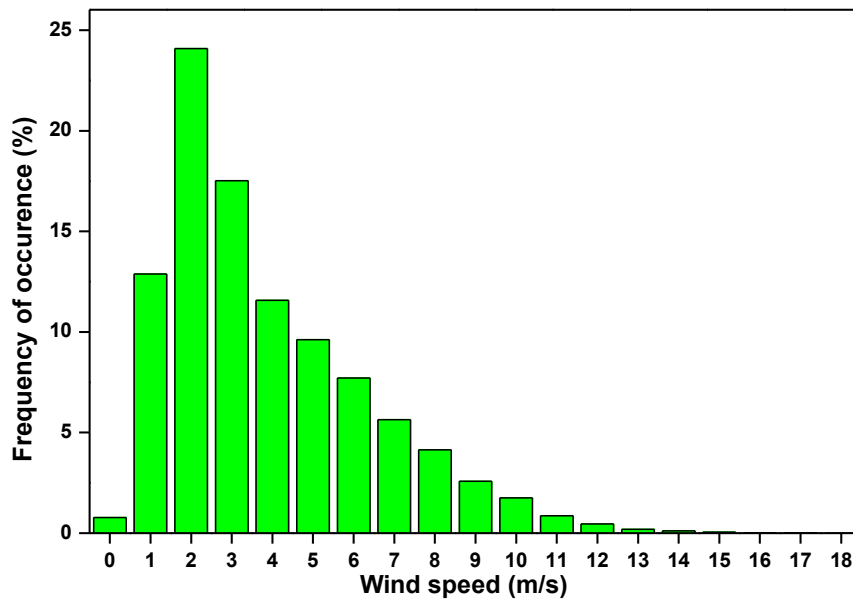
Figure 2.8: Frequency of occurrence of wind speed over 4 years (2012-2015).

2.4   Description of Aïn Beni-Mathar ISCC power plant

The main components of the ISCC are sketched in figure 2.9. It is installed in Aïn Beni-Mathar town (Morocco). It contains two Alstom gas turbines (Model GT13E) of 150.28 MWe brut capacity and a single Alstom steam turbine-generator (Model DKYZ2 1N41B COMAX) of 172 MWe capacity [53]. The solar section is equipped with a solar field of parabolic trough collectors (ET-150 type). It consists of 56 loops, and for each loop, 4 collectors are arranged in parallel rows. The collectors are single-axis tracking aligned in the north-south axis, thus tracking the sun from east to west. The PTR-70 2008 solar receiver tubes are located at the focal axis of the parabolic trough collectors. They contain Therminol VP-1 as a heat transfer fluid in which temperature can reach 393 °C [53].

Without solar integration, e.g., in the evening, the plant's design plant output is about 450 MWe. When solar steam is integrated into the heat recovery steam generator (HRSG) at design capacity, the design plant output increases to 472 MWe. Thus, the solar system adds approximately 20 MWe to the plant output (or 4.2%).
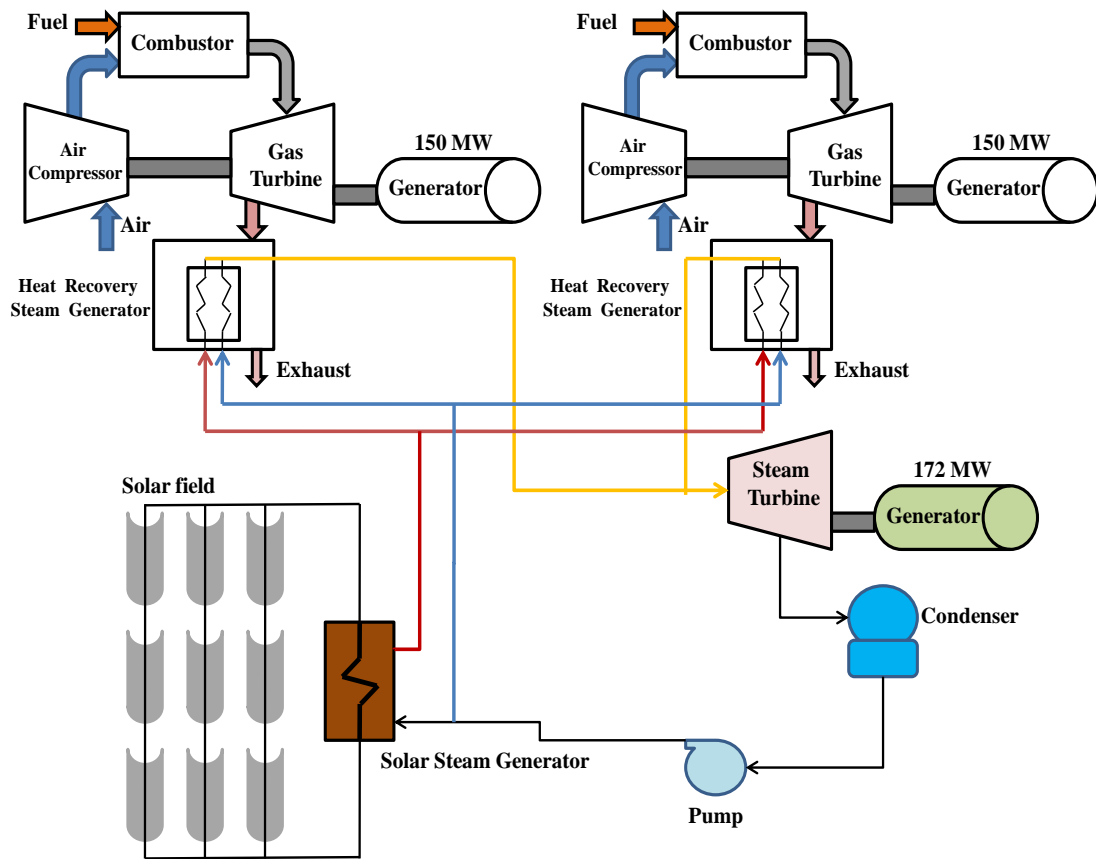
Figure 2.9: Components of the integrated solar combined cycle power plant [65].

The ISCC integrates solar steam into the Rankine steam "bottoming cycle" of a combined-cycle power plant. The gas turbine (GT) constitutes the "topping cycle." The exhaust gases with high temperatures from the gas turbine pass through the HRSG to generate superheated/saturated steam used to drive the steam turbine. The general concept in an ISCC is to oversize the ST to handle the increased steam capacity. At ABM, the solar energy collected by the solar field is used to generate an additional amount of steam through the solar steam generator (SSG) to supplement the steam being generated in the HRSG. The steam is generated in SSG and fed into the HRSG of the NGCC plant allowing for two different integration strategies modes: power boosting and fuel-saving mode. The former is considered when the additional solar steam increasing the NGCC power output while maintaining constant fuel input, the later when solar steam is used to reducing natural gas consumption while keeping power output constant [66]. Heat rejection from the turbines is accomplished with an air-cooled condenser, greatly reducing the plant's water usage.

2.5   Data generation

2.5.1   Annual performance

The monthly electrical net generation of the ISCCS power plant during the year 2015 is presented in figure 2.10. The annual net electricity was about 3293 GWh, and it varies between 207 GWh in February and 292 GWh in July. The average output of the electrical generation is about 274 GWh.

The Ain Beni Mathar ISSC plant is a baseload CC plant on the ONEE grid. The grid demand often calls for high production. However, it is sometimes constrained below full capacity, i.e., 100% capacity factor, due to reduced demand from the grid operator or operating issues at the plant itself. Figure 2.10 also illustrates that the Ain Beni Mathar plant operated at a high baseload level in 2015, with capacity factors up to 94%. Note that the lower limit of the scale in each plot is at a high level. The dip in February is due to the scheduled maintenance of one of the gas turbines.
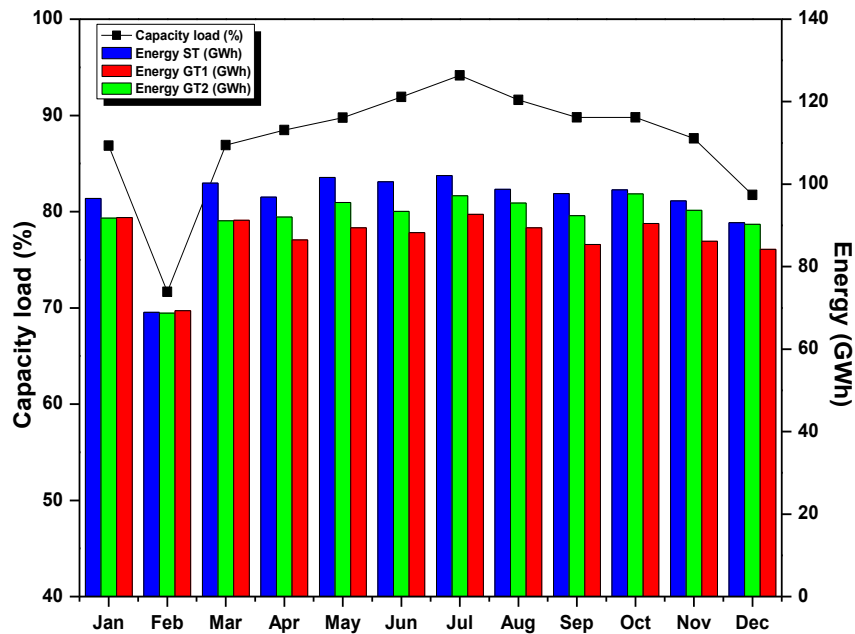
Figure 2.10: Monthly electrical net generation and the capacity factor of the ISCCS power plant ABM during 2015.
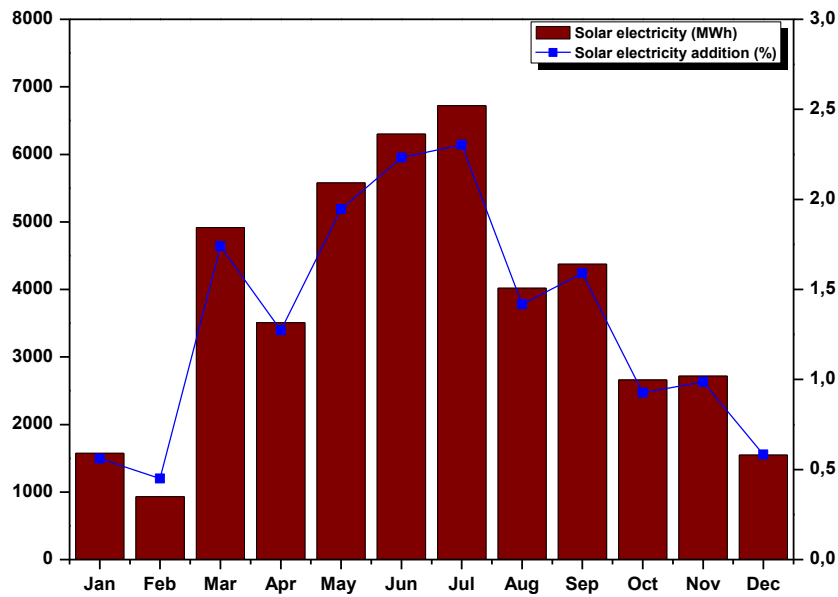
Figure 2.11: Monthly solar electricity net generation of the ISCCS power plant ABM during 2015.

For the solar part, figure 2.11 shows the solar electricity net generation during the year 2015. The yearly solar electricity was about 44.8 GWh. On a monthly scale, the highest solar electricity output was recorded in July (6722 MWh), while the lowest one was noticed in February (932 MWh). The monthly average solar electricity was found to be 3737 MWh.

Due to the solar system's size compared to the total ABM plant capacity, the average annual solar contribution is low, on the order of 1.36% annually, while reaching approximately 2% during peak months. Data on the monthly solar contribution over the year 2015 are shown in figure 2.11. The contribution is low in winter when solar production is lowest, and peaks in the March through September period.

2.5.2   Daily performance

To illustrate the solar field's performance and evaluate its effect on the ISCC power plant for the year 2015, four typical days that characterize each season were chosen. The procedure flowed to choose those days is based on the daily averages of DNI, ambient temperature, and energy production for each season. Consequently, January 04th, April 06th, July 20th, and October 05th have been selected as typical days.

Due to the variation of the amount of DNI received by the solar field over the seasons of the year, the solar contribution delivered to the steam turbine confronts some technical constraints. This means that the hours of solar electricity production vary from a season to

another. In fact, in winter (21st December – 20th March) and autumn (21st September – 20th December), the solar field of PTSTPP operates on average 8 hours/day by supplying hot HTF at 391°C to the power block. For spring (21st March – 20th June) and summer (21st June – 20th September), the power block produces electricity for an average of 10 and 11 hours/day, respectively.

The variation of solar energy absorbed by solar field and the thermal efficiency in four selected days, 04th January, 06th April, 20th July, and 05th October on an hourly basis, is shown in figure 2.12 & figure 2.13. We can conclude that the solar energy collected by the solar field might reach up to 110.36 MWh in summer. This value can be lower than 68 MWh in winter. This, due to the higher solar radiation, results in an increase in the thermal energy gain by the solar field in summer compared to lower solar radiation in winter. The solar energy gained can be reached to more than 87 MWh and 79 MWh respectively in spring and autumn. Also, it is obvious that the higher solar energy, the higher thermal efficiency where it might reach to 75.55% on 20th July and 44.47% on 04th January.
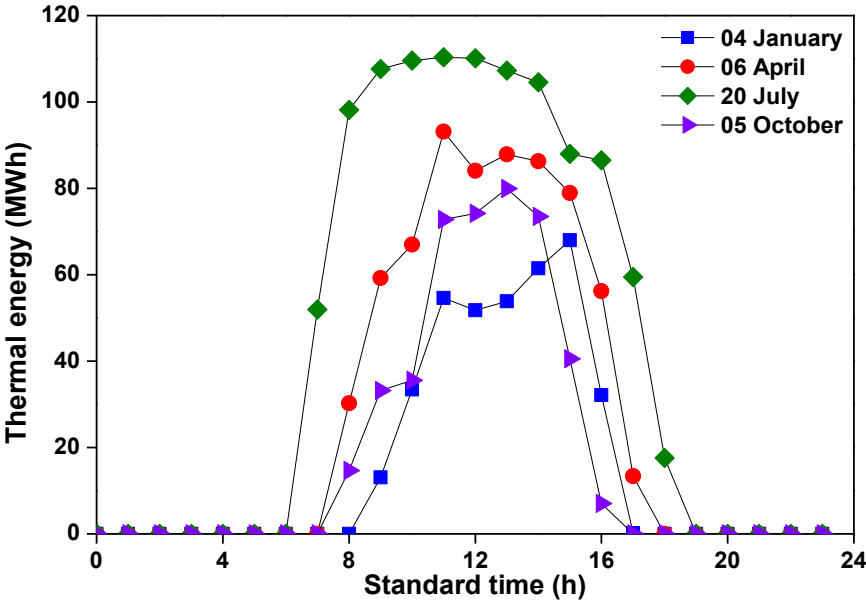
Figure 2.12: Solar field output for the four selected days.
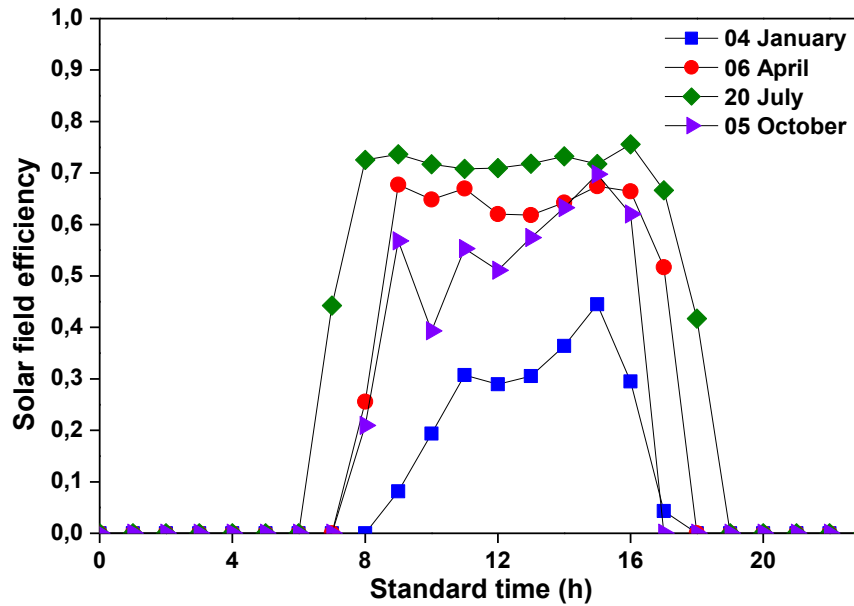
Figure 2.13: Solar Field Efficiency for the four selected days.

The ISCC power plant in ABM is working in power saving mode; this means the higher the solar energy input, the higher the power plant's electricity production. Solar electricity represents the energy produced by solar energy injected into the cycle and equal to the difference between the steam bottoming cycle's energy output in the case of NGCC and ISCC power plant. In fact, solar electricity is largely depending on the amount of solar thermal input. Figure 2.14 and figure 2.15 show the solar output produced and the net solar ratio at the four selected days. At thermal solar input equal to 0 MWh, the ISCC plant works as a conventional NGCC; thus, the solar electricity output is 0 MWh. The solar contribution peaks are noticed in midday, just when the gas turbine output is degraded due to high ambient air inlet temperatures. The high solar output reduces the level of gas use during this midday period, lowering plant greenhouse gas emissions. Solar electricity varies during a day with solar radiation intensity; it can reach a peak value of 28.69 MWh in summer and 17.68 MWh in winter. Similarly, the solar electricity ratio is about 7% in summer and 5% in winter.
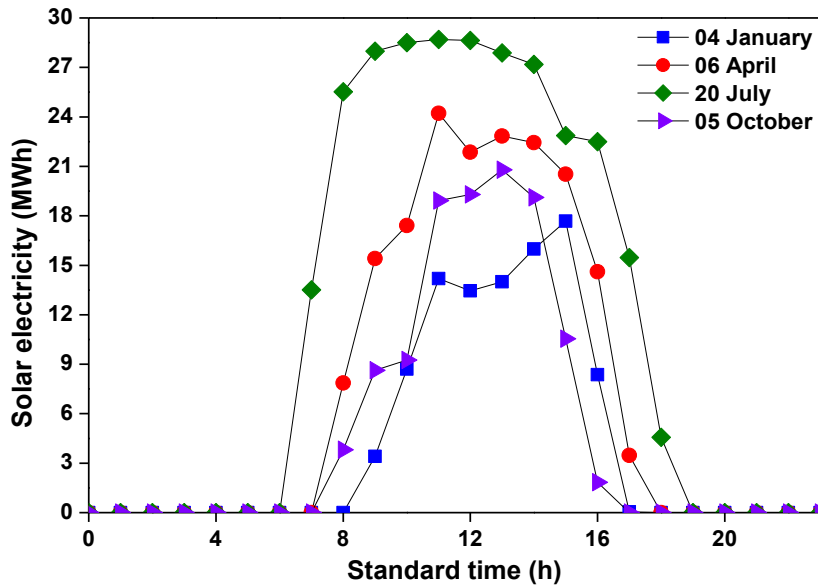
Figure 2.14: Solar Electricity for the four selected days.
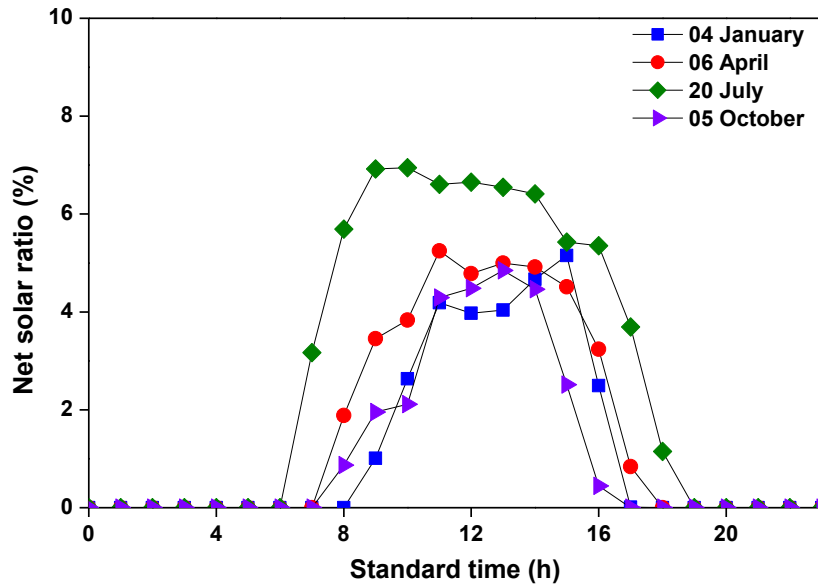
Figure 2.15: Net solar electricity ratio for the four selected days.

2.5.3 Comparison of ABM ISCCS power plant with other similar power plants.

Parabolic Trough collector technology represents one of the most promising options among available CSP systems for generating renewable electricity. Hence integrating this technology in an ISCCS power plant will definitively increase the power plant's overall efficiency. In this part of the work, an interest was given to the electricity coming from the solar field of parabolic trough collectors. Tables 2.4 and 2.5 show details of the selected ISCCSs with parabolic trough technology. It is well noted that the selected ISCC power plants with parabolic trough technology were chosen based on the availability of necessary data for comparison.

51

Project name	Company/ Owner	Country	Location	Capacity (MW)	Solar electricity (MW)	Start year	Coordina-tes
Agua Prieta II	Federal Electricity Commissi-on	Mexico	Agua Prieta	478	14	2014	31°19'33.00"N109°32'56.00"W
Archimede	ENEL	Italy	Priolo Gargallo	750	5	2010	37°8'3.12"N 15°13'0.15"E
City of Medicine Hat Demonst	City of Medicine Hat	Canada	Alberta	203	1.1	2014	50°2'24.00"N 110°43'12.00"W
Ain Beni Mathar	ONEE	Morocco	Ain Beni-Mathar	470	20	2011	34°3'50.00"N 2°6'0.00"W
Martin Next Generation Solar Energy Center	Florida Power & Light Co.	US	Indiantown, FL	3780	75	2010	27°3'13.00"N 80°33'46.00"W
Stillwater GeoSolar Hybrid Plant	Enel Green Power	US	Fallon, NV	61	2	March 2015	39°32'53.00"North118°33'20.00"West

Table 2.4: Selected ISCCS power plants [45], [46].

Solar field	SCA manufa-cturer	Number of SCAs	Mirror manufac turer	Solar field aperat-ure area	HCE	HTF
Agua Prieta II	Abengoa Solar (ASTRO)	104	Rioglass	85,000 m²	-	Thermal Oil
Archimede	COMES (ENEA)	54	Ronda Reflex	31,860 m²	Archimede Solar Energy	Molten salt
City of Medicine Hat	SkyFuel (SkyTrough®)	8	-	5,248 m²	-	Xceltherm®SST
Ain Beni Mathar	Abengoa Solar (ASTRO)	224	Rioglass	183,120 m²	Schott (PTR 70)	Thermi-nol VP-1
Martin Next Generation Solar Energy Center	Gossamer Space Frames (LAT 1)	1136	Rioglass	464,908 m²	Solel (UVAC 2008)	Dowther m A
Stillwater GeoSolar Hybrid Plant	SkyFuel (SkyTrough®)	44	SkyFuel (ReflecT ech®)	24,778 m²	-	Demine-ralised water

Table 2.5: Solar field design data of selected ISCCS power plants [45], [46].

Figure 2.16 presents a comparison between the average specific annual generation (the ratio between annual electricity generation and gross turbine capacity) of the solar part of the chosen ISCCSs. The highest average specific annual generation was noticed for Martin Next Generation Solar Energy Center (US) with about 2428 MWh/MW and the lowest value for the City of Medicine Hat (Canada) with about 1500 MWh/MW. The specific annual generation of ABM is about 2240 MWh/MW.
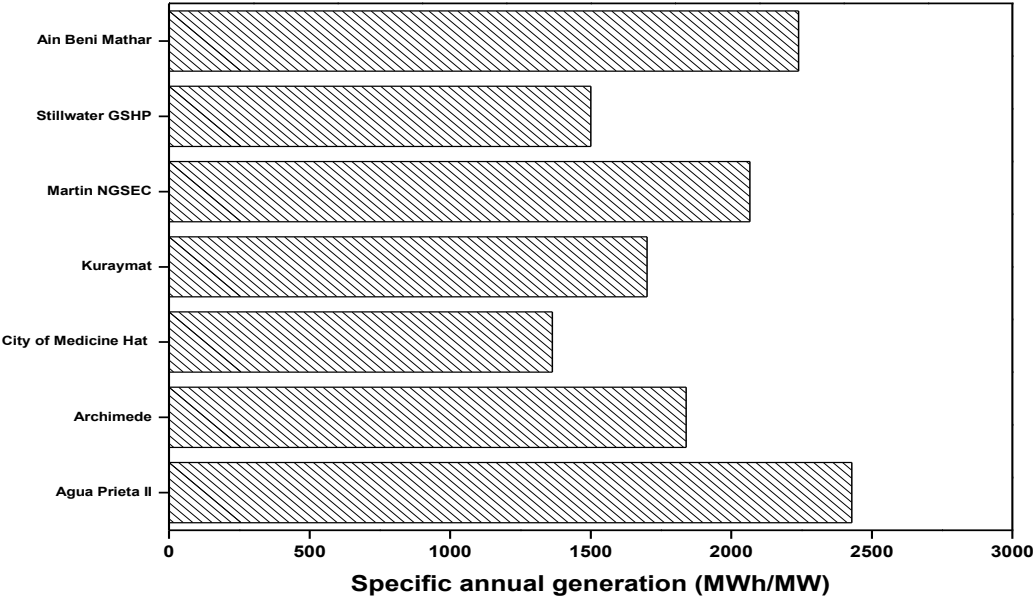
Figure 2.16: Average specific annual generation of the solar part of the chosen ISCCSs.

2.6 Conclusion

In this chapter, we technically outline the Ain Beni-Mathar ISCCS injecting electricity into the Moroccan grid. It comes to increase the contribution of renewable energy sources in Morocco's energy mix and add capacity to the power grid to help cope with the sustained growth in electricity demand.

At first, we present different parameters that have been taken into consideration for the selection of Ain Beni-Mathar as a suitable location for the implementation of the ISCCS power plant: Proximity to the Maghreb-Europe gas pipeline, sufficient solar potential, land suitability and availability, water availability, proximity to the infrastructure for the material transportation during the construction, as well as to the electrical grid to inject the produced electricity. This plant was operational since 2011 and produced 470 MW of electricity. The annual net electricity in 2015 was about 3293 GWh, including 44.8 GWh from solar electricity. A solar field performance comparison between the ABM power plant and other

ISCCSs worldwide was also reported. The specific annual generation of ABM is about 2240 MWh/MW.

Chapter 3: Thermal Performance simulation analysis of a solar field for parabolic trough collectors assigned for ambient conditions in Morocco

This chapter aims to assess the thermal performances of the solar field of the Integrated Solar Combined Cycle (ISCC) power plant at Aïn Beni Mather in Morocco for the year 2015. Thus, mathematical modeling of the Schott PTR-70 2008 solar receiver consists of energy balance equations that were solved using COMSOL Multiphysics software. Next, the model was validated with empirical data from the literature, so the comparison is satisfactory. Results analyze the plant's daily and annual thermal performances and compare simulated and actual plant operating results.

3.1 Introduction

Concentrating solar power (CSP) plants are one of the most promising technologies to produce electric power [67]. Four technologies have been developed, including the parabolic trough, solar tower, solar dish, and linear Fresnel systems. The parabolic trough collectors (PTCs) are actually the most commercialized and mature solar technology for solar harvesting [68], [69]. They are usually used for a solar steam generation due to their relatively high temperatures (up to 400°C). This technology can also be employed in other industrial applications at low temperatures, such as desalination and sterilization processes [70].

Reviews existing literature show that PTC performance models can be either steady-state models or dynamic models. S. A. Kalogirou [71] developed a detailed thermal model of solar parabolic trough collector that would have been installed in Cyprus University of Technology to determine its performances. In his analysis, the author took into account all modes of heat transfer between the modeled receiver elements. Equations have been solved using Engineering Equation Solver (EES), and then the proposed model was validated by experimental results conducted in Sandia National Laboratories (SNL). Accordingly, he concluded that the comparison was satisfactory. Under Moroccan meteorological conditions, Bouhal et al. [72] assessed a parabolic trough collector's thermal performance under six climatic regions in Morocco. A physical model is developed to determine flow parameters and heat transfer applied to PTC technology. They deduced that the installation location and weather conditions are determinant parameters in controlling the parabolic trough solar

collectors' global performance. The obtained results show also that the selection of thermal heat transfer fluid plays a crucial role in increasing CSP efficiency and cost-effectiveness.

For Algerian climate conditions, two references have been found in the literature: M. Ouagued et al. [73] and Y. Marif et al. [74], which examined thermal performances of a parabolic trough collector. In the reference [73], the study was simultaneously focused on the potential of direct solar irradiation of Algeria and the estimation of temperature, heat gain, and heat loss of a PTC in terms of various thermal oils. To reach this last objective, they undertook a heat transfer model subject to a solar tracking system. The solar absorber was divided into several segments. The energy conservation principle has been applied to each of them over a section of the heat collector element (solar receiver). Modified Euler Method allowed solving the obtained differential equations system. The results show that an increase in temperature of heat transfer fluid and absorber tube generates the augmentation of heat loss and the reduction of heat gain. As for the reference of Marif et al., [74], it dealt with numerical simulation of solar parabolic through collector. Their work was based on a one-dimensional energy balance approach solved using an implicit numerical finite difference scheme after meshing the absorber pipe, glass envelope, and the heat transfer fluid (HTF). Afterward, the established algebraic systems were simultaneously solved by Gauss-Seidel iterative method. Note that two fluids were used as HTF: TherminolVP-1™ synthetic oil and liquid water. Numerical simulation results were validated by experimental data obtained from SNL, and it was found that the thermal efficiency varies from 69.73 to 72.24%. Additionally, Yılmaz et al. [75] referred to the same subject when they developed thermo-mathematical modeling of a parabolic trough solar collector to simulate its thermal performance under different operating conditions. Indeed, as in previous several works, all modeled equations were solved using (EES) and compared to available SNL data. The comparison seems reasonable. Moreover, the proposed model was then applied to an existing parabolic trough solar collector module to highlight its thermal performances.

To predict the general performances of its pilot PTC during transient periods, the research team of PROMES laboratory [76] has benefited from the 1D thermal model. Furthermore, it describes the HTF's thermal behavior, the absorber tube, and the glass cover all the more, so uniform solar irradiation is considered. The model results have been firstly compared with those of two different experimental setups in steady-state conditions. Secondly, for comparison purposes during two periods of time with varying inlet conditions, experimental and numerical results were combined. As a result, it was found that the model is capable of

predicting the thermal behavior of the parabolic trough collector with changeable climate and environment conditions (DNI, mass flow, inlet temperature). In the worst case, the relative standard error value is 9.6%. García et al. [27] proposed a detailed performance model to predict the electricity output of a parabolic trough solar thermal power plant, including a thermal energy storage process. The simulation results were compared with measurements resulting from experiments for 42 days in summer at the Andasol2 power plant in Spain. More recently, Zaharil et al. [77] performs an energetic and exergetic study that aims to evaluate and compare performances of 6 different HTFs (Pressurized water, Therminol VP-1, Syltherm 800, Solar salt, Hitec XL, and liquid sodium) under various inlet temperature levels (300K-900K) and climatic conditions (based on Malaysian climatic condition). A 1D mathematical model has been developed and coded into MATLAB. It has been highlighted that the Liquid sodium at the temperature level of 700K showed the highest exergetic gain for any potential implementation of PTSC power plant in Malaysia.

In recent times, Conrado et al. [78] present an up-to-date review of thermal mathematical models applying to parabolic trough solar collectors. They concluded that a limited software number was used to analyze the thermodynamic performances of PTC collectors. The authors of reference [79], for their part, compared different models (1D) that have been developed in the past years. They are validated with the test data from SNL. It was found that the most accurate 1D model was precise enough compared with the three-dimensional (3D) model.

This chapter aims to assess the thermal performances of the solar field of the Integrated Solar Combined Cycle (ISCC) power plant at Aïn Beni Mather in Morocco for the year 2015. Thus, a mathematical model was conducted, and is mainly consists of three parts. The first part concerns the calculation of the incidence angle of solar radiation to determine the amount of solar energy received by the solar field. The second part consists of optical analysis. This part aims to calculate the optical efficiency of the PTCs, which is the ratio of the amount of energy arriving at the absorber tube to that which hits the reflector. The third part concerns the thermal analysis and aims to determine the energy absorbed by the HTF in the receiver tubes. Thus, the Schott PTR-70 2008 solar receiver's energy balance equations were solved using COMSOL Multiphysics software. Next, the model was validated with empirical data from the literature, so the comparison is satisfactory. Results analyze the plant's daily and annual thermal performances and a comparison between simulated and actual plant operating results.

3.2 Orientation angles and relative position to the sun

The solar radiation reaching the earth is partially reflected, absorbed, and scattered in the atmosphere. The remaining is referred to as beam radiation, which can be used as useful energy when a concentrated collector system manipulates it. To calculate accurately the amount of solar radiation received by the solar field, the determination of the incidence angle is mandatory due to the instant change of the sun position [80]. Hence, the need for geometric equations that make it possible to locate the sun's position during the day and the year for a given geographical location.

According to [81], for any location determined by its longitude (λ [°]) and its latitude (φ [°]), the following parameters can be evaluated: the equation of time (EQT [min]), the hour angle of the sun (ω [°]), the declination angle of the sun (δ [°]), the angle of the solar altitude (γ_S [°]) and the angle of solar azimuth (α_S [°]). These calculations have been considered for the parabolic trough solar field installed at Ain Beni-Mathar with the local geographical position (34°00'35"N, 2°01'29"W).

3.2.1 Hour angle (ω)

The hour angle can be known as the angle through which the earth has to revolve to get the meridian of any point straight under the sun [82]. The hour angle (in degrees) can be calculated from the following equation:

$$\omega = 15(12 - ST)(h) \tag{3.1}$$

Where ST is the solar local time, it is a time based on the sun's apparent angular motion across the sky with solar noon the time the sun crosses the meridian of the observer. The ST can be determined by [81]:

$$Solar\ time = Standard\ time + 4(L_{st} - L_{loc}) + EQT \tag{3.2}$$

where L_{st} stands for the standard meridian of the local time zone, L_{loc} represents the longitude of the location in question, and longitudes are in degrees west, that is, 0°< L < 360°. The parameter EQT called the equation of time (in minutes), and it can be determined by applying the following equation [81]:

$$EQT = 229.9(0.000075 + 0.001868 \cos B - 0.032077 \sin B - \tag{3.3}$$
$$0.014615 \cos 2B - 0.04089 \sin 2B)$$

where B measured in degrees can be calculated using the next equation [81]:

$$B = (n-1)\left(\frac{360}{365}\right) \tag{3.4}$$

where n represents the day of the year ($1 \leq n \leq 365$). The equation time is plotted and shown in figure 3.1.
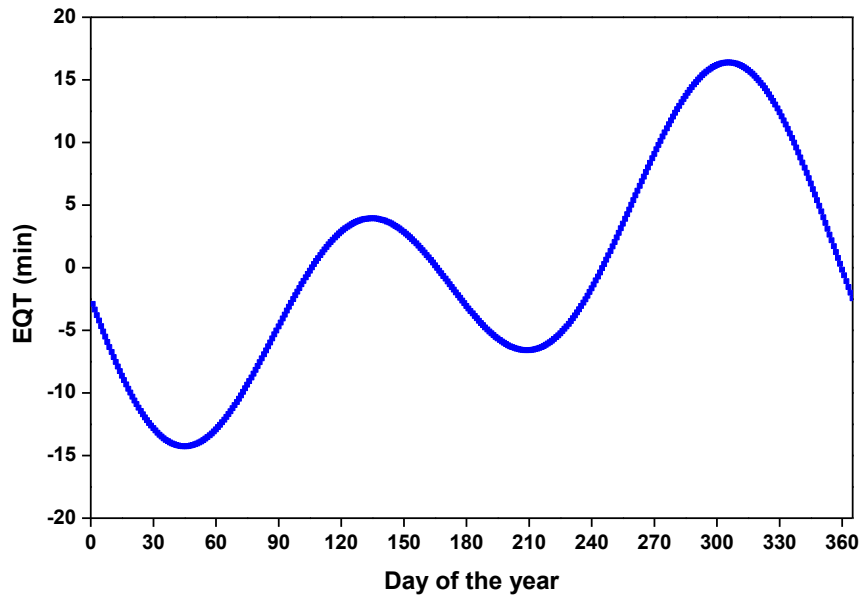
Figure 3.1: The equation of time E in minutes as a function of time of year.

3.2.2 Angle of solar declination (δ)

The earth rotates around itself; the rotation axis has an inclination of 23.45° concerning the earth-sun orbital plane. The angle between the earth-sun line (from their centers) and the equatorial plane is called solar declination. The solar declination varies throughout the year because the earth revolves around its axis. It varies between a value of -23.45° on December 21st and a value of + 23.45° on June 21st. Solar declination angle can be determined using Cooper's equation [83]:

$$\delta = 23.45 \sin\left(360\frac{284 + n}{365}\right) \tag{3.5}$$

3.2.3 Angle of solar altitude (γs)

The solar altitude angle is the angle between the horizontal and the line to the sun. It changes with the sun's movement. At sunrise or sunset, the solar altitude angle is near zero, while at noon, it becomes near to 90° (see figure 3.2). It is the complement of the zenith angle (the angle between the vertical and the line to the sun). The angle of solar altitude (sun height) γ_s can be determined using the following expression [84]:

$$\gamma_s = \arcsin\left(\cos\omega\cos\varphi\cos\delta + \sin\varphi\sin\delta\right) \qquad (3.6)$$

where φ is the latitude of the location.

3.2.4 Angle of solar azimuth (α_s):

There are several conventions for the solar azimuth. It is traditionally defined as the angle between a line due south and the shadow cast by a vertical rod on Earth. This convention states the angle is positive if the line is east of south and negative if it is west of the south. However, despite tradition, the most commonly accepted convention for analyzing solar irradiation, e.g., for solar energy applications, is clockwise from due north, so east is 90°, south is 180°, and west is 270°. This is the definition used by NREL in their solar position calculators [85]. The angle of solar azimuth αs become [84]:

$$\alpha_s = \begin{cases} 180° - \arccos\dfrac{\sin\gamma_s\sin\varphi - \sin\delta}{\cos\gamma_s\cos\varphi} & \text{if solar time } \leq 12\text{ h} \\[3mm] 180° + \arccos\dfrac{\sin\gamma_s\sin\varphi - \sin\delta}{\cos\gamma_s\cos\varphi} & \text{if solar time } > 12\,h \end{cases} \qquad (3.7)$$

3.2.5 Collector angles

Two angles define the orientation of the collectors: the tilt angle (γ_t [°]) for which 0° means that the surface is horizontal and 90° means that the surface is vertical; and also the orientation angle towards the azimuth (α_t [°]) for which 0° means that the surface is oriented towards the south, 90° means that the surface is oriented towards the west, 180° means that the surface is oriented towards the north, and 270° means that the surface is oriented towards east.

The next parameter that can be calculated is the solar angle of incidence on a tilted surface (θ [°]). The evaluation of this parameter is one of the most important problems that must be solved for the mathematical modelling of the parabolic through collectors (PTC).

Figure 3.2 (a), figure 3.2 (b), and figure 3.2 (c) present the PTC's characteristic angles, in an isometric view, in a lateral view, and a top view, respectively.
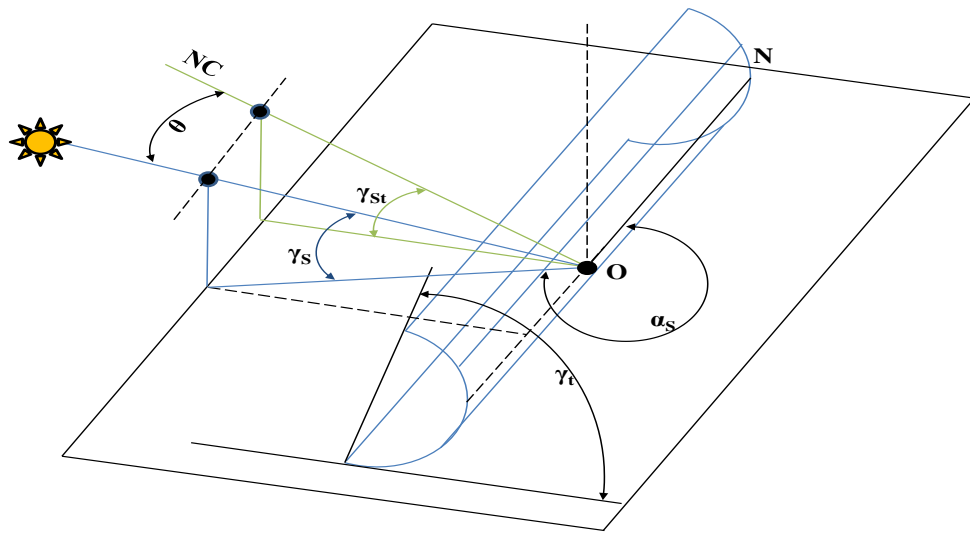
(a)
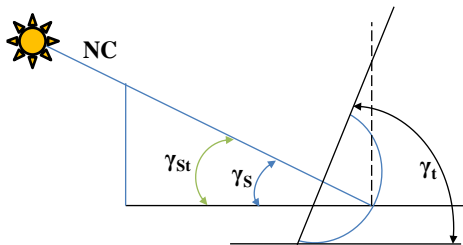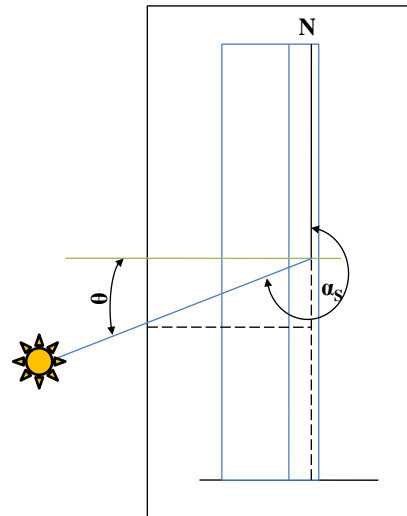
(b)   (c)

Figure 3.2: Characteristic angles of the parabolic concentrator collectors [65].

(a): Representation of characteristic angles for collectors with parabolic concentrators isometric view

(b): Representation of characteristic angles for collectors with parabolic concentrators lateral vision

(c): Representation of characteristic angles for collectors with parabolic concentrators top view

The North-South orientation of the PTC is more efficient than the East-West one, allowing the harvest of more solar energy during the whole year ([22], [71], [86], [87]).

For the North-South orientation of the PTC, a new algorithm for calculating the characteristic angles for the position and orientation of the PTC plane and the relative position between the PTC plane and the sun was proposed.

The projection of the angle of the solar altitude on the transversal plane of the collector was noted with γ_{st}. The collector must always be tilted so that $\gamma_{st} = \gamma_S$ because the projection of the solar beam on the transversal plane must always be normal to the plane of the collector. The tracking system controls this particular orientation. Under these circumstances, the tilt angle of the collector (γ_t) can be calculated as:

$$\gamma_t = 90° - \gamma_{st} \tag{3.8}$$

The projection of the solar altitude angle on the transversal plane of the collector (γ_{st}) can be calculated as a function of γ_S and α_S with the following relations:

$$\gamma_{st} = arctan \frac{\tan(\gamma_s)}{\cos(90° - \alpha_S)} \text{ for } \alpha_S < 180° \text{ and PTC orientation towards East} \tag{3.9}$$

$$\gamma_{st} = arctan \frac{\tan(\gamma_s)}{\cos(270° - \alpha_S)} \text{ for } \alpha_S \tag{3.10}$$
$$\geq 180° \text{ and PTC orientation towards West}$$

With the determined tilt angle of the collector (γ_t) and the orientation of the collector (α_t), the angle of incidence (θ) can be determined with the same relation used for the collectors without concentrators:

$$\theta = \arccos\left(- \cos(\gamma_s)\sin(\gamma_t)\cos(\alpha_S - \alpha_t) + \sin(\gamma_t)\cos(\gamma_t)\right) \tag{3.11}$$

The proposed incidence angle equation was validated against the relation tackled in [81]:

$$\theta = \arccos\left(\sqrt{\cos^2(\theta_z) + \cos^2(\delta)\sin^2(\omega)}\right) \tag{3.12}$$

where θ_z is the zenith angle and can be determined as follow:

$$\theta = 90° - \gamma_s \tag{3.13}$$

Figure 3.3 presents the flow chart for calculating the incidence angle with the proposed formula (Eq.4) and with the formula proposed in [81].
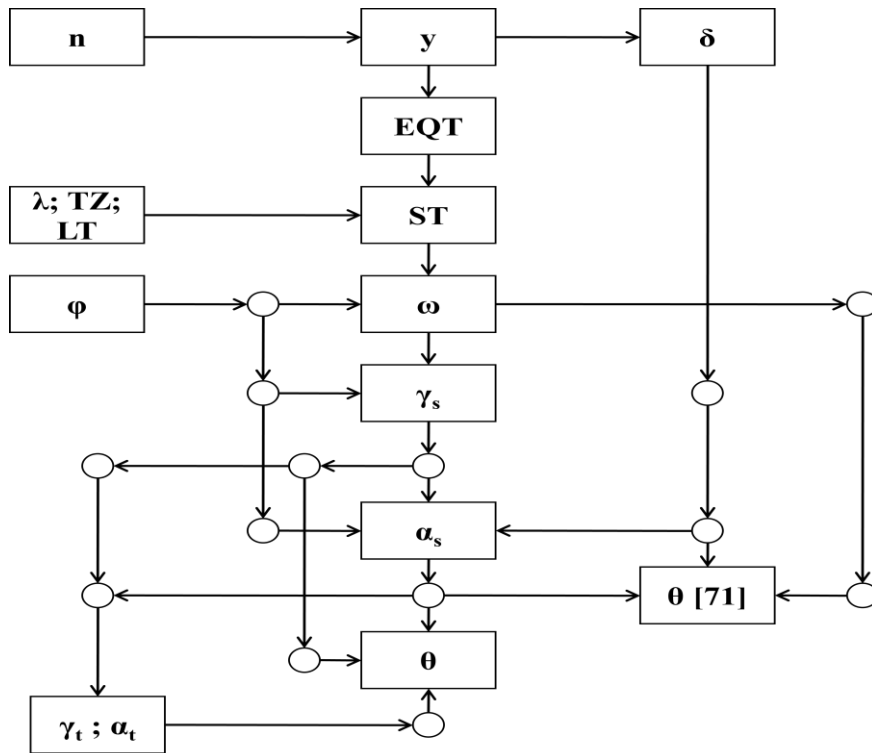
Figure 3.3: Flow chart for the step of the calculation of the incidence angle.

As a result, it was found that the two relations provide identical values for the angle of incidence during all days of the year (figure 3.4). The relative error doesn't exceed 4% in the worst case.
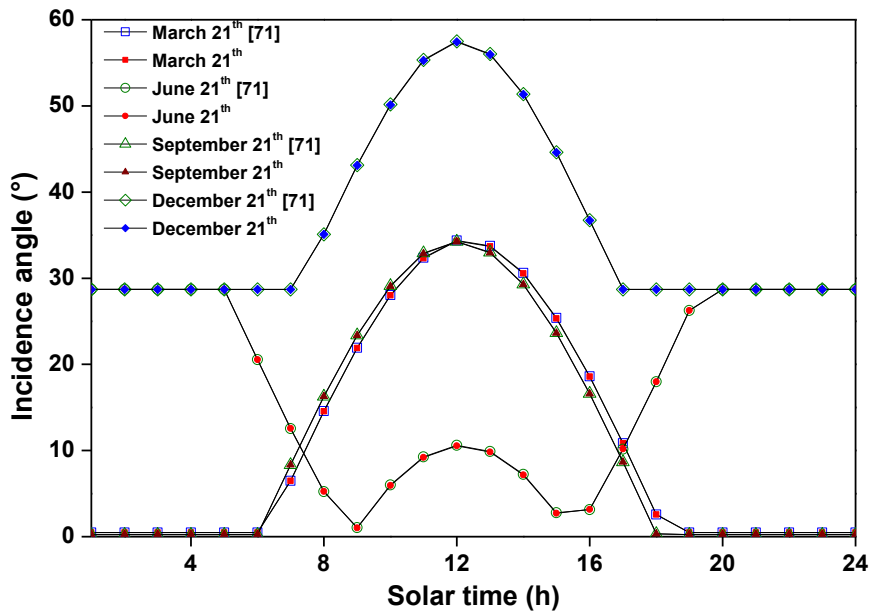
Figure 3.4: Comparison between the angle of incidence evaluated from [81] and the proposed equation at Ain Beni Mathar location

3.3 Optical Analysis of the Parabolic Trough Collector

In ideal conditions, 100% of the incident solar energy is reflected by the concentrator and absorbed by the receiver. However, in reality, the reflector does not reflect all solar radiation due to imperfections of the reflector, causing some optical losses. The optical efficiency relies on many factors, such as tracking error, geometrical error, and surface imperfections [88]. It can be presented by the following equation:

$$\eta_{opt}(\theta) = \eta_{opt,0}\, K(\theta) f_{RowShadow} f_{EndLoss} f_{Clean} f_{Dust} \eta_{track} f_1 \tag{3.14}$$

Where $\eta_{opt,0}$ is the peak optical efficiency (the optical efficiency at zero angle of incidence) and is expressed as follow [89]:

$$\eta_{opt,0} = \rho_{Cl} \tau_g \alpha_a \gamma\, \eta_{bellows} \tag{3.15}$$

ρ_{cl} is the reflectivity of the parabolic collector, τ_g is the transmissivity of the receiver's glass envelope, and α_a is the absorbance of the selective coating on the metallic pipe of the receiver's tube. γ is the interception factor related to the collector imperfections and misalignment resulting from manufacturing and assembly of mirrors, and $\eta_{bellows}$ is the active aperture area.

$K(\theta)$ is the incident angle modifier (IAM); $f_{RowShadow}$ is the row shading; $f_{EndLoss}$ is the end effect loss; f_{Clean} is the mirror cleanliness factor; $f_{DustEnv}$ is related to the light absorption of dust on the receiver glass cover; η_{track} is the tracking error and f_1 is an extra factor between 0 and 1 to account for any additional reduction in energy absorption by the Solar Field loops [27]. For the calculations in this work we used $f_{Clean}= 0.97$, $f_{DustEnv}= 0.98$, $\eta_{track}= 0.99$, $f_1=1$ [27].

3.3.1 Incident angle modifier K(θ)

The incident angle modifier $K(\theta)$ accounts for increasing or decreasing the incidence angle. The incident angle modifier is defined as the ratio of thermal efficiency at a given angle of incidence to the peak efficiency at normal incidence [90]. It is typically measured in experimental tests aimed to characterise a specific collector. Several expressions can be found in the literature for this factor. In the current study, $K(\theta)$ is taken from [22] for the Eurotrough ET150 module and the selected tracking strategy (N-S axis, tracking E-W):

$$K(\theta) = \cos(\theta) - 2.85962 * 10^{-5}\, \theta^2 - 5.25097 * 10^{-4}\, \theta \tag{3.16}$$

3.3.2 End loss $f_{EndLoss}$

At zero angle of incidence, the solar radiation reflected from the concentrator hit the entire heat collection element (HCE). However, when the angle of incidence starts to increase, some areas near the end of the receiver are not illuminated by solar radiation, as illustrated in figure 3.5. These losses are addressed with the term of end losses.
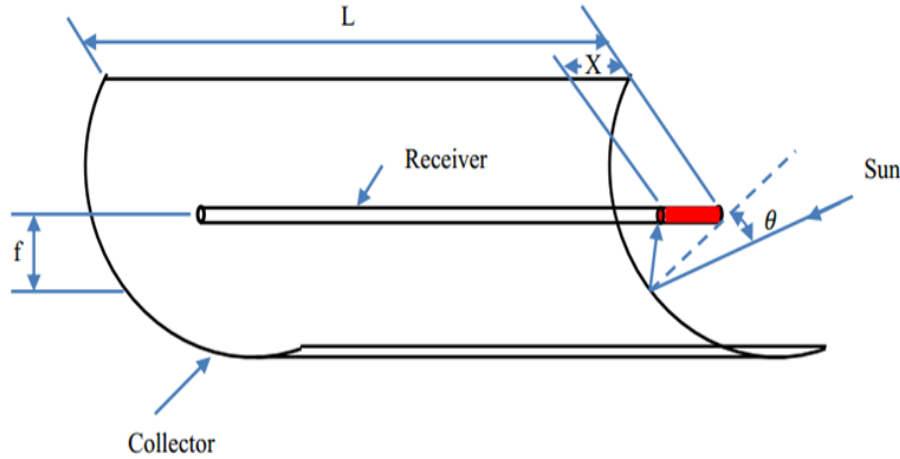
Figure 3.5: End losses [90].

The distance X corresponding to the length of the HCE that is not illuminated can be calculated as follows [90]:

$$X = f \tan (\theta) \tag{3.17}$$

The end loss is defined by [27]:

$$f_{EndLoss} = 1 - \frac{m_2 f}{L_{SCA}} \tan(\theta) + \left(\frac{(m_2 - 1)}{L_{SCA}}\right) max[0, f \tan(\theta) - d_2] \tag{3.18}$$

$$+ \left(\frac{(m_1 - 1)}{m_1 L_{SCA}}\right) max[0, f \tan(\theta) - d_2]$$

where L is the tube length, f the focal distance, d_1 is the spacing between consecutive SCAs in a row, d_2 is the spacing between consecutive SCEs in a SCA, m_1 is the number of SCAs in a row, and m_2 is the number of SCEs within a SCA. For the calculations in this work, we have used d_1= 1.5m, d_2= 0.25m, m_1= 2 and m_2=12m.

3.3.3 Row shading loss f RowShadow

At ABM power plant, the collectors are arranged in parallel rows, with about 17.2 m of spacing between each row. In the early morning, all of the collectors face due east. Due to

the sun's low solar altitude angle in the morning, the eastern-most row of collectors will receive full sun, but this row will shade all subsequent rows to the west [25]. As the sun rises and the collectors track the sun, this mutual row shading effect decreases until a critical zenith angle is reached, at which no row shading occurs. Collector rows remain un-shaded through the middle of the day, from late morning through early afternoon. Mutual row shading then re-appears in the late afternoon and evening, when the solar altitude angle is again very low [25]. Figure 3.6 depicts tracking of solar collectors from early to mid-morning and the consequent row shading that occurs over this period.
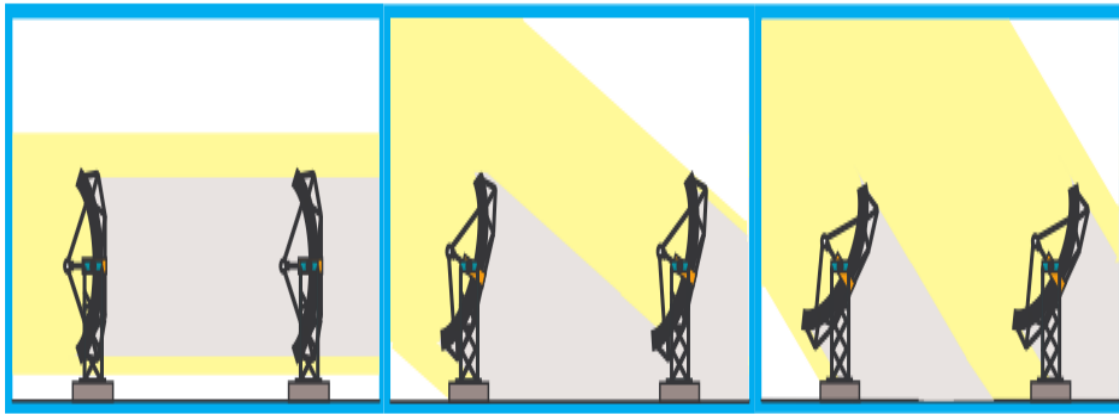
Figure 3.6: Collector tracking through the morning, showing digression of collector shading as the day progresses [25].

Parameter	value	Unit
A_c	3462	m^2
f	1.71	m
Height	0.61	m
L_{SCA}	142.8	m
L_{Space}	17.2	m
$W_{SCA,total}$	5.77	m
α_a	0.96	-
α_g	0.02	-
γ	0.94	-
ρ_{Cl}	0.94	-
τ_g	0.96	-
$\eta_{bellows}$	0.967	-
Geometric concentration	82	-
Rim angle	80	-

Table 3.1: Dimensions and optical parameters of PTC

Row shading decreases collector performance by decreasing the amount of radiation incident on the collectors. The width of the mirror aperture, which receives incident radiation (that is, the width of the aperture that is not shaded), is defined as the "effective mirror width". The row shadow factor is the ratio of the effective mirror width to the actual mirror width. This ratio can be derived from the geometry of the solar zenith angle, the incidence angle, and the layout of the collectors in a field [25]. $f_{RowShadow}$ is given by the following equation [30]:

$$f_{RowShadow} = \frac{L_{Space} \cos(\theta_z)}{W_{Sca,total} \cos(\theta)} \tag{3.19}$$

Where L_{Space} is the space between rows in the solar field and $W_{Sca,total}$ is the total aperture width of a single SCA.

Table 3.1 shows the dimensions and optical parameters of the collector and their corresponding values.

3.4 Thermal Analysis of the Parabolic Trough Collector

3.4.1 Description of the system

The considered system is among the most important part of a parabolic trough collector. It is a solar receiver (figure 3.7) or heat collection element (HCE) known as Schott PTR 70 type. Its specific characteristics are presented in table 3.2. Usually, it is installed at the focal axis of a PTC to receive the reflected direct solar irradiation coming from a parabolic reflector. The solar receiver comprises the stainless-steel surrounded by an evacuated glass envelope to decrease heat losses, an absorber tube, and heat transfer fluid (HTF). The role of the absorber is to transmit the heat energy to the HTF (Therminol VP-1), whose temperature can reach 391 °C. Note that the cylindrical coordinates (r, x) are adopted in this study.

The goal of the thermal model is to determine the energy that is absorbed by the heat transfer fluid (HTF) and describe all the heat losses from the receiver to the atmosphere due to heat transfer mechanisms: conduction, convection, and radiation. Then, the thermal efficiency, which is the ratio of the delivered energy to the energy arrived at the reflector, can be estimated.
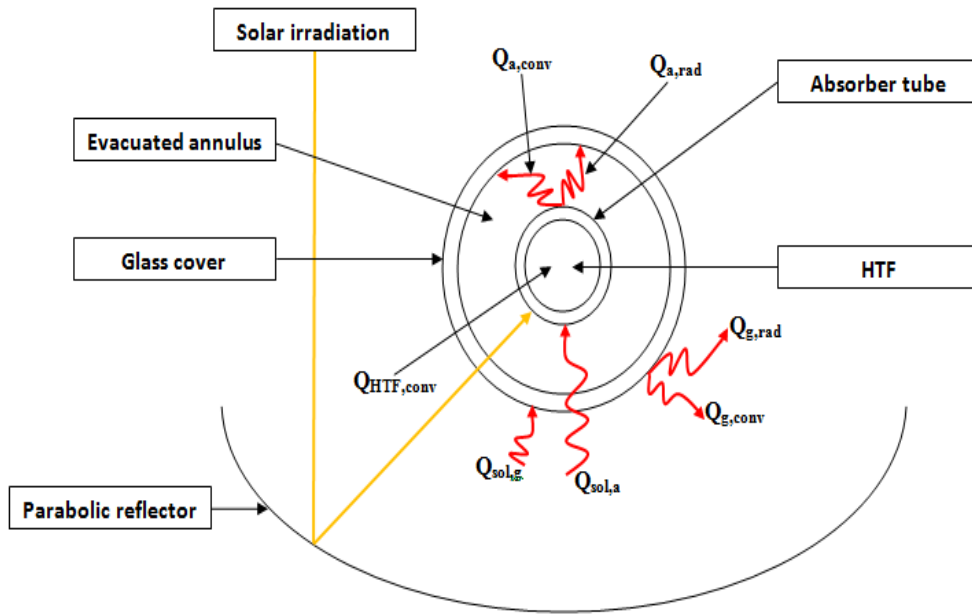
(a)
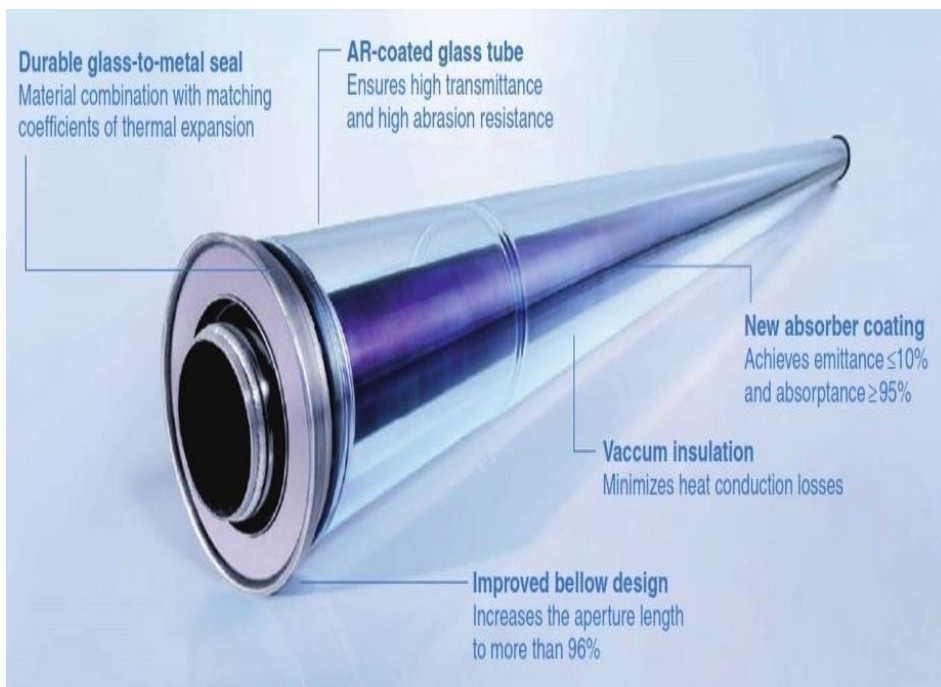
(b)

Figure 3.7: Schematic view of the solar receiver: (a) Schematic and heat transfer process of the receiver; (b) The solar receiver tube [91].

Designation	Characteristics
Receiver type	Schott PTR-70 2008
Absorber material type	304L
HTF type	Therminol VP-1
HTF density (kg/m^3)	$-0.90797*T(°C)+0.00078116*T^2(°C)-2.367*10^{-6}*T^3(°C)+1083.25$
HTF specific heat (kJ/kgK)	$0.002414*T(°C)+5.9591*10^6*T^2(°C)-2.9879*10^{-8}*T^3(°C)+1.498$
HTF thermal conductivity (W/mK)	$-8.19477*10^{-5}*T(°C)-1.92257*10^{-7}*T^2(°C)+2.5034*10^{-11}*T^3(°C)+0.137743$
HTF kinematic viscosity (mm^2/s)	$e^{([544.149/(T(°C)+114.43)]-2.59578)}$
Thermal conductivity of the absorber pipe (W/mK)	$0.013*T_a+15.2$
Density of the absorber pipe (kg/m^3)	8020
Specific heat of glass envelope (J/kgK)	1090
Density of glass envelope (kg/ m^3)	2230
Radiation emissivity of glass envelope (ε_g)	0.89
Radiation emissivity of absorber	$0.062+2*10^{-7}* T_a^2$
Absorber internal diameter (m)	0.066
Absorber external diameter (m)	0.07
Glass cover internal diameter (m)	0.114
Glass cover external diameter (m)	0.12

Table 3.2: Characteristics of the solar receiver [71], [92]–[94].

3.4.2 Hypotheses

The thermal model of the parabolic trough collector is based on energy balance inside the main elements of the solar receiver (glass envelope, absorber tube, and HTF), which are

coupled with appropriate boundary conditions. In order to simplify this mathematical model, the following assumptions are taken into account:

- 1D transient heat balance regime is considered,
- there is the vacuum in the annular between absorber and glass cover,
- there is no radial heat conduction within the glass envelope, the absorber tube, and the HTF,
- thermo-physical properties of the heat transfer fluid depend on the temperature,
- the HTF flow is turbulent, and its mass flow rate is assumed to be constant.

3.4.3 Mathematical formulation

Considering the previous hypotheses, the energy balance equation of each medium (element) is given below.

3.4.3.1 Governing equations for the HTF

The heat balance of the HTF could be expressed by the temperature differential equation [94]. For a segment ''i'' of length Δx along with the x position, the HTF partial equation is given:

$$m_{HTF} \frac{\partial (C_{p_{HTF}} T_{HTF})}{\partial t} = Q_x - Q_{(x+\Delta x)} + Q_{HTF,diff} + Q_{HTF,conv} \tag{3.20}$$

From the above equation, the heat balance per unit of segment length is as follows:

$$A_{HTF} \frac{\partial (\rho_{HTF} C_{p_{HTF}} T_{HTF})}{\partial t} = -\dot{m}_{HTF} \frac{\partial (C_{p_{HTF}} T_{HTF})}{\partial x} + A_{HTF} \frac{\partial}{\partial x} \left(k_{HTF} \frac{\partial T_{HTF}}{\partial x} \right) + \tag{3.21}$$
$$h_{HTF} \pi D_{ai} (T_a - T_{HTF})$$

with

$$A_{HTF} = \left(\frac{\pi D_{ai}{}^2}{4} \right) \tag{3.22}$$

3.4.3.2 Energy balance in the absorber tube

The heat balance associated with the absorber tube is expressed by [94]:

$$m_a C_{p_a} \frac{\partial T_a}{\partial t} = Q_{sol,a} + Q_{a,diff} - Q_{HTF,conv} - Q_{a,conv} - Q_{a,rad} \tag{3.23}$$

and then

$$\rho_a A_a C_{p_a} \frac{\partial T_a}{\partial t} = \frac{Q_{sol,a}}{L} + A_a k_a \frac{\partial^2 T_a}{\partial x^2} - h_{HTF} \pi D_{ai} (T_a - T_{HTF}) \tag{3.24}$$

$$- h_{an} \pi D_{ae} (T_a - T_g) - \frac{\sigma \pi D_{ae} \left(T_a{}^4 - T_g{}^4 \right)}{\frac{1}{\varepsilon_a} + \frac{(1-\varepsilon_g) D_{ae}}{\varepsilon_g D_{gi}}}$$

with

$$A_a = \frac{\pi \left(D_{ae}{}^2 - D_{ai}{}^2 \right)}{4} \text{ and } \varepsilon_a = 0.000327(T_a + 273.15) - 0.06597 \tag{3.25}$$

3.4.3.3 Energy balance in the glass envelope

For this main component, we get the following heat balance [94]:

$$m_g C_{p_g} \frac{\partial T_g}{\partial t} = Q_{sol,g} + Q_{g,diff} + Q_{a,conv} + Q_{a,rad} - Q_{g,conv} - Q_{g,rad} \tag{3.26}$$

Consequently,

$$\rho_g A_g C_{p_g} \frac{\partial T_g}{\partial t} = \frac{Q_{sol,g}}{L} + A_g k_g \frac{\partial^2 T_g}{\partial x^2} + h_{an} \pi D_{ae} (T_a - T_g) \tag{3.27}$$

$$+ \frac{\sigma \pi D_{ae} \left(T_a{}^4 - T_g{}^4 \right)}{\frac{1}{\varepsilon_a} + \frac{(1-\varepsilon_g) D_{ae}}{\varepsilon_g D_{gi}}} - h_{amb} \pi D_{ge} (T_g - T_{amb})$$

$$- \sigma \pi D_{ge} \left(T_g{}^4 - T_{sky}{}^4 \right)$$

with

$$A_g = \frac{\pi \left(D_{ge}{}^2 - D_{gi}{}^2 \right)}{4} \text{ and } \varepsilon_{sky} = 0.0553 \, T_{amb}{}^{1.5} \tag{3.28}$$

3.4.3.4 Estimation of convective heat transfer coefficients

This study requires knowledge of various convective heat transfer coefficients deduced from appropriate empirical correlations. These correlations are those of Nusselt numbers that depend on several main parameters, especially flow regime (laminar or turbulent) and convection type (free or forced).

> **Convective heat transfer coefficient between the HTF and the absorber tube:**

At typical operating conditions, the flow of HTF inside the absorber tube is considered to be turbulent and transitional, and the following correlation was chosen [95]:

$$Nu_{HTF} = \frac{\left(\frac{fr}{8}\right)(Re_{HTF} - 1000)Pr_{HTF}}{1 + 12.7\sqrt{\frac{fr}{8}}\left(Pr_{HTF}^{\frac{2}{3}} - 1\right)} \tag{3.29}$$

with

$$2300 \leq Re_{HTF} \leq 5 \times 10^6 \text{ and } 0.5 \leq Pr_{HTF} \leq 2000 \tag{3.30}$$

where

$$fr = (1.82\,log(Re_{HTF}) - 164)^{-2} \tag{3.31}$$

So, the convective heat transfer coefficient, h_{HTF}, between HTF the internal pipe wall is estimated by:

$$h_{HTF} = Nu_{HTF}\frac{k_{HTF}}{D_{ai}} \tag{3.32}$$

➢ **Convective heat transfer coefficient between the absorber tube and the glass envelope:**

We suppose that the HCE annulus is under vacuum to determine the convective heat transfer coefficient between the absorber and the glass envelope ($P_{an} \leq 100$ mmHg). The convective heat transfer between the absorber and the glass envelope is due to free-molecular convection [71]. Thus,

$$h_{an} = \frac{k_{std}}{\frac{D_{ae}}{2\,ln\left(\frac{D_{gi}}{D_{ae}}\right)} + b\lambda\left(\frac{D_{ae}}{D_{gi}} + 1\right)} \text{ for } Ra_{an} < \left(\frac{D_{gi}}{D_{gi} - D_{ae}}\right)^4 \tag{3.33}$$

This correlation includes the Rayleigh number (Ra_{an}) and other parameters defined below:

$$b = \frac{(2 - ac)(9\gamma - 5)}{2ac(\gamma + 1)}, \qquad \lambda = 2.33 \times 10^{-20}\frac{T_{av}}{P_{an}\delta^2} \tag{3.34}$$

$$\text{and } T_{av} = \frac{T_a + T_g}{2}$$

➢ **Convective heat transfer coefficient between the glass envelope and the ambient:**

In taking into account the presence of the wind (forced convection), the convective heat transfer coefficient, h_{amb}, between the external surface of the glass envelope and the ambient is deduced from the expression as follows [95]:

$$h_{amb} = Nu_{amb} \frac{k_{amb}}{D_{ge}}$$

(3.35)

with

$$Nu_{amb} = C \, Re_{D_{ge}}^{m} \, Pr_{amb}^{n} \left(\frac{Pr_{amb}}{Pr_{ge}}\right)^{1/4} \text{ for } 1.0 < Re_{D_{ge}} < 10^6$$

(3.36)

$$\text{and } 0.7 < Pr_{amb} < 500$$

The constant values of C and m are given in table 3.3 [95], and the exponent n was taken equal to 0.37 for $Pr_{ge} \leq 10$ and 0.36 in the case where $Pr_{ge} > 10$.

Re_{Dg}	C	m
1-40	0.75	0.4
40-1000	0.51	0.5
1000-200000	0.26	0.6
200000-10^6	0.076	0.7

Table 3.3: Constant values of C and m concerning Reynolds number range.

3.4.3.5 Estimation of the solar power absorption

➢ **Solar power absorbed by the absorber pipe:**

The portion of solar power absorbed by the absorber pipe is obtained by [31]:

$$Q_{sol,a} = DNI \, \eta_{opt}(\theta) A_c$$

(3.37)

where A_c is the mirror aperture area in a loop, DNI is the direct normal irradiation $\eta_{opt}(\theta)$ is the optical efficiency.

➢ **Solar power absorbed by the glass envelope:**

The portion of solar power absorbed by the glass envelope is discussed by [93] and evaluated here as:

$$Q_{sol,g} = DNI \, \eta_{opt}(\theta) A_c \, \frac{\alpha_g}{\tau_g \alpha_a}$$

(3.38)

3.4.3.6 Initial conditions

To solve the system of governing equations (3.21, 3.24, and 3.27), the HTF, the absorber pipe, and the glass cover are assumed to have a uniform initial temperature:

$$T_{HTF}(t = 0, x) = T_a(t = 0, x) = 293\ °C \qquad (3.39)$$

$$T_a(t = 0, x) = T_{amb} \qquad (3.40)$$

Regarding the boundary conditions, they are as follows:

- Among the operation conditions of the Aïn Beni-Mathar ISCC power plant, the inlet operating temperature (set-point HTF inlet temperature) at which the solar field operates is 293 °C. That is why we assumed that:

$$T_{HTF}(t = 0, x) = 293\ °C \qquad (3.41)$$

To justify this order of magnitude, the schematic diagram of an identical CSP plant, called Noor 1 (160 MW) and localized at Ouarzazate city (Morocco), is shown in figure 3.8 below. According to this figure, we can observe that the inlet operating temperature of HTF is $T_{HTF,in}$=289.75 °C, whereas its exit operating temperature (set-point HTF exit temperature) takes the value of 394.74 °C [70].

T$_{HTF, out}$ = 394.74 °C
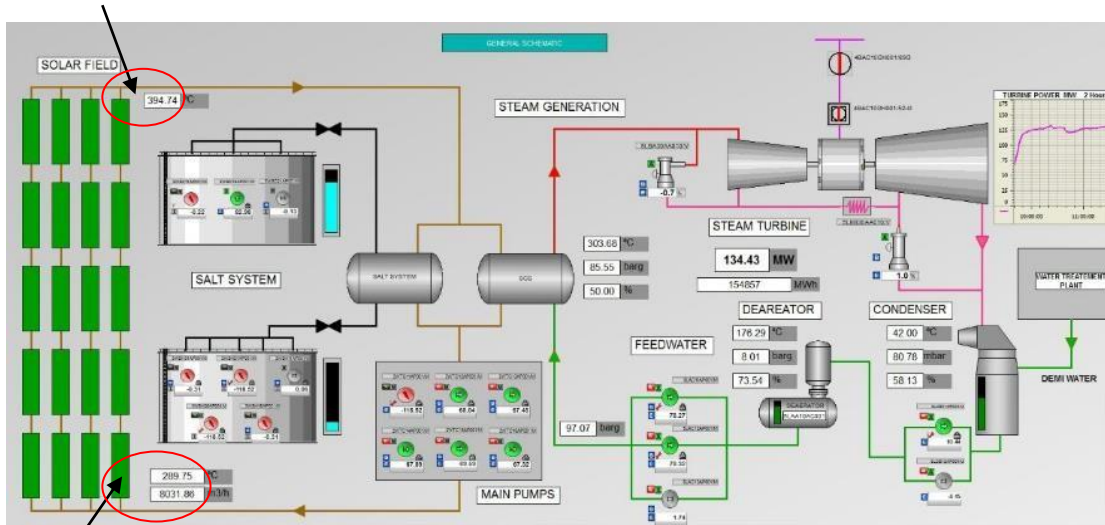
T$_{HTF, in}$ = 289.75 °C

Figure 3.8: Schematic diagram of a parabolic trough solar thermal power plant (Noor 1: 160 MW) localized at Ouarzazate (Morocco) [70].

- As for the boundary condition at x = L, it was considered that:

$$\left.\frac{\partial T_{HTF}}{\partial x}\right|_{x=L} = 0 \qquad (3.42)$$

- Thermal insulation at the absorber ends

$$\frac{\partial T_a}{\partial x}\bigg|_{x=0} = \frac{\partial T_a}{\partial x}\bigg|_{x=L} = 0 \tag{3.43}$$

- The heat flux at the inlet and outlet of the glass equal to 0 (Thermal insulation at the glass ends)

$$\frac{\partial T_g}{\partial x}\bigg|_{x=0} = \frac{\partial T_g}{\partial x}\bigg|_{x=L} = 0 \tag{3.44}$$

- The outer surface of the glass envelope was defined with a mixed boundary with convection and radiation.
- The absorber tube and the heat transfer fluid were defined as coupled fluid-solid interfaces in which the energy is conserved, and the temperature is the same ($T_{HTF} = T_a$).

3.5 Solar field characteristics

The studied solar field is a part of the ISCC power plant and is installed in Aïn Beni-Mathar town (Morocco) (See chapter II). It consists of 224 parabolic trough solar collectors classified in 56 parallel loops, consisting of 4 collectors and a total length of 600 meters (figure 3.9).
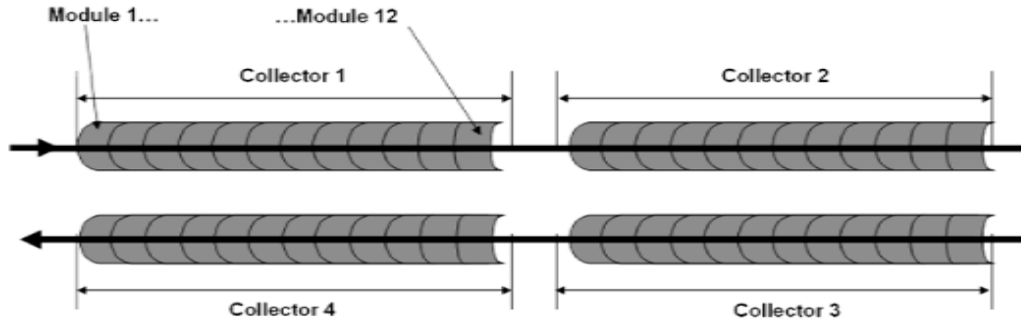
Figure 3.9: The receiver loop [22].

To calculate the useful thermal power supplied to the HTF, the heat losses of the receiver tubes $Q_{loss,HCE}$, and the of the pipes $Q_{loss,pipes}$ have to be determined and subtracted from the absorbed power. It can be calculated for a loop as [93]:

$$Q_u = Q_{sol,a} - \left(Q_{loss,HCE} + Q_{loss,pipes}\right) \tag{3.45}$$

To calculate the heat losses of the absorber tubes, an empirical correlation reported by NREL [93] was used since Schott's 2008 PTR70 receiver tubes are part of the solar field design. For

evacuated receiver tubes, the linear heat loss per HCE length (W/m) can be calculated by the following correlation:

$$HL_{PTR70-2008} = 4.05 + 0.247(T_{HTF} - T_{amb}) + 0.00146\, T_{HTF}^2$$
$$+ 5.65 \times 10^{-6}\, T_{HTF}^3$$
$$+ 7.62 \times 10^{-8} DNI \times K(\theta) \times T_{HTF}^2$$
$$+ \sqrt{V_w} \times [-1.70 + 0.0125(T_{HTF} - T_{amb})]$$

(3.46)

The final heat loss for HCE is given as follows:

$$Q_{loss,HCE} = HeatLossFactor\, \frac{HL_{PTR70-2008}}{W_{SCA,total}}\, A_c$$

(3.47)

where the heat loss factor value is 1.

Thermal losses from the piping leading to and from the loop in the solar field are accounted by the following empirical equation [25]:

$$Q_{loss,pipes} = \left[0.01693(T_{av,HTF} - T_{amb}) \right.$$
$$- 1.683 \times 10^{-4}(T_{av,HTF} - T_{amb})^2$$
$$\left. + 6.780 \times 10^{-7}(T_{av,HTF} - T_{amb})^3 \right] A_c$$

(3.48)

where $T_{av,HTF}$ is the HTF average temperature. More details about the model of the heat losses could be found in [25]. Also, the thermal efficiency, which is the net gain to the HTF on the amount of solar power that reaches the aperture area of the solar field is described by [96], and evaluated here as:

$$\eta_{th} = \frac{Q_u}{Q_{sol}} \quad \text{with} \quad Q_{sol} = DNI \times A_c$$

(3.49)

3.6   Mesh generation

Comsol Multiphysics is a commercial solver and simulation software used to solve the time-dependent one-dimensional partial differential equations (PDEs) system described above (Equations 3.21, 3.24, and 3.27) associated with appropriate boundary and initial conditions. It is based on the finite element method and has suitable criteria to generate the best-suited mesh, and it provides the discretization in the considered domain. The adequate mesh, ensuring the convergence of numerical solutions, was taken for this simulation study. Details of this software are given in reference [97].

3.7 Results and discussion

3.7.1 Weather conditions

The site of the Aïn Beni Mathar power plant is located in the Eastern part of Morocco (34°00'35" N, 2°01'29 "W) at about 560 km from the capital (Rabat). It is the first Moroccan solar thermal power plant. The climate in this region is classified as "Csa," according to Köppen-Geiger climate classification. The climatic data used in this study were taken from the weather station in situ. As a result, monthly averages of ambient temperature relative humidity of the air, wind speed, and Direct Normal Irradiation (DNI), will be presented here for 2015.

Indeed, the ambient temperature presents significant seasonal changes, as indicated in figure 3.10. The summer season is hotter than the other seasons. This important parameter influences the heat losses in the solar field of PTCs. The average monthly minimum value of the coldest month's temperature (February) is 6.5 °C, while the average of the hottest month's monthly maximum temperature (July) is about 30 °C. Besides, as expected, the relative humidity depends strongly on the ambient temperature since they vary oppositely, as shown in figure 3.10. Moreover, the ambient air is quite dry when it gets very hot during summer; the minimum average relative humidity recorded in July is 29.6 %. Conversely, the air is over-humidified in winter, with a maximum of 74.6 % recorded in February 2015 [70].
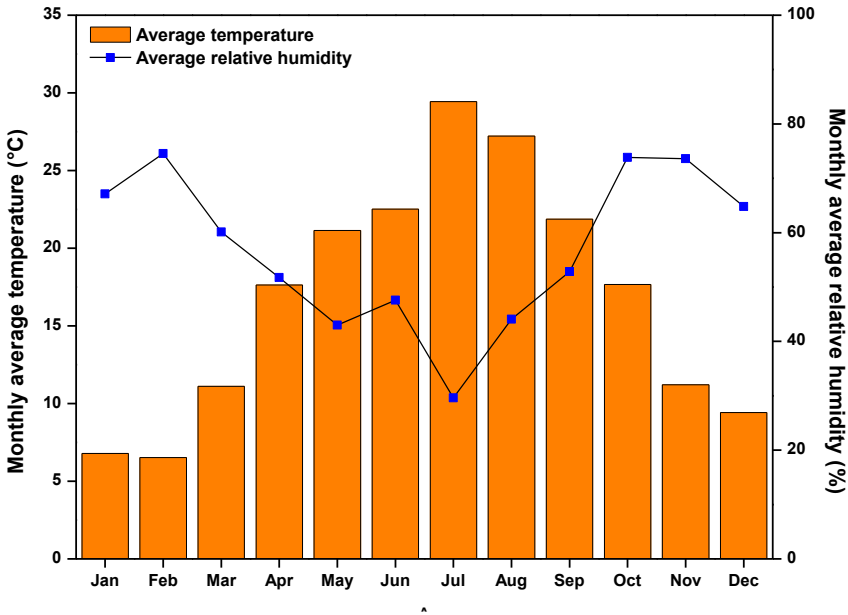
Figure 3.10: Monthly averages of the ambient temperature and relative humidity at the ISCC site (the year 2015).

Let us now examine the wind speed, which is manifestly one of the decisive parameters on the CSP plant efficiency. So, figure 3.11 depicts monthly averages of wind speed for the year 2015. It shows that average values are almost ranging from 1.74 m/s to 5.4 m/s. Note that the maximum average value (5.4 m/s) was recorded in February 2015. From an energy point of view, the power plant area is well exposed to sunlight with an average of daily direct normal irradiation (DNI) of 5.85 kWh/m^2, and the monthly averages are also presented in figure 3.11. The maximum and minimum values of DNI are 7.7 kWh/m^2 and 4.41 kWh/m^2, respectively, and they were recorded in July and February 2015. This parameter is considered as the most relevant factor influencing the energy production of a solar power plant.
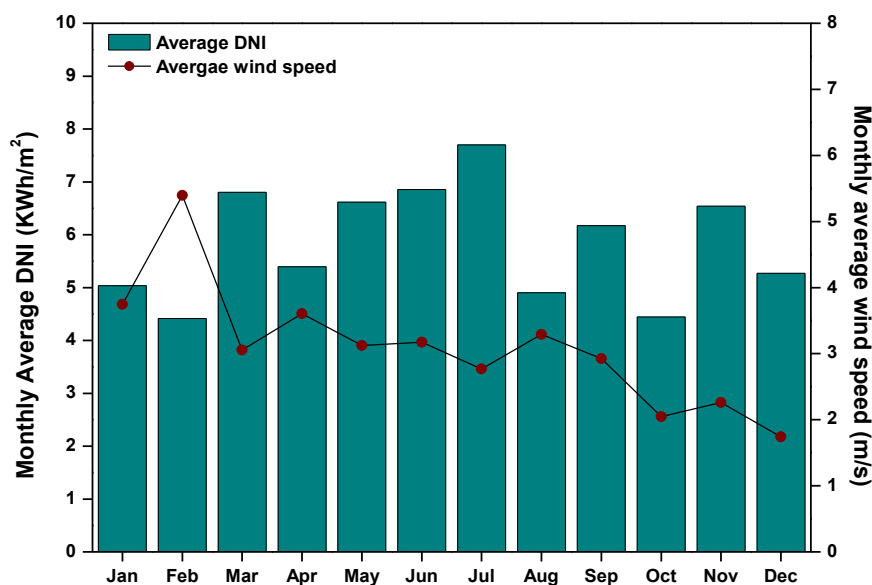
Figure 3.11: Monthly averages of DNI and wind speed at the ISCC site (the year 2015).

3.7.2 Model validation and temperature profiles

As usual in this type of study, model validation is quite often recommended. However, before starting this task, it is important to point out that databases of direct normal irradiation, ambient temperature, and wind speed were obtained from the Ain Beni Mathar ISCC power plant operators. The HTF system is designed for a HTF mass flow of Solutia's VP1 of 440 kg/s at 100% load (about 7.86 kg/s per loop). The inlet and the outlet HTF temperatures are about 293 °C and 391 °C, respectively, which are the operation conditions of the solar field.

The model validation will be conducted later in this section by comparing numerical results and correlations available in the literature [93]. Indeed, the PTR-70 2008 solar receiver's thermal performances have been estimated numerically and then compared with results of NREL [93]. The input parameters of the simulation are taken from [93] and presented in

Table 3.4. The simulation was done for an interval of 1h, and the results are presented at t=1h when the steady-state is maintain.

Total loop length (m)	588
Mass flow rate (kg/s)	9
I_b (W/m^2)	950
Incidence angle, θ (deg)	20
Wind speed (m/s)	2
Ambient temperature (°C)	30

Table 3.4: Input parameters [93].

Figure 3.12 depicts the linear heat loss against average HTF temperature and compares the results of the current study with the empirical correlation given above (Equ 3.46). It is obviously clear that the trends marked by the two curves are roughly the same. After that, we could conclude that the simulation results are in good agreement with those of the aforementioned correlation since the relative error does not exceed 2.5% in the worse case.

Additionally, for an increase in the HTF temperature from 293 °C to 391 °C, the liner heat losses increase from 92 W/m to 219 W/m for the empirical correlation and 94 W/m to 216 W/m for the numerical results. On average, every 10 °C increase in the HTF temperature generates an increase of about 12.7 W/m in the thermal loss. Furthermore, during the simulation process, it has been observed that the rate of increase in HTF temperature varies between 0.18°C and 0.16 °C/m at the inlet and the exit of the loop, respectively. It also noted that the net gain of energy decreases with the fluid flow inside the loop because of increased heat losses.
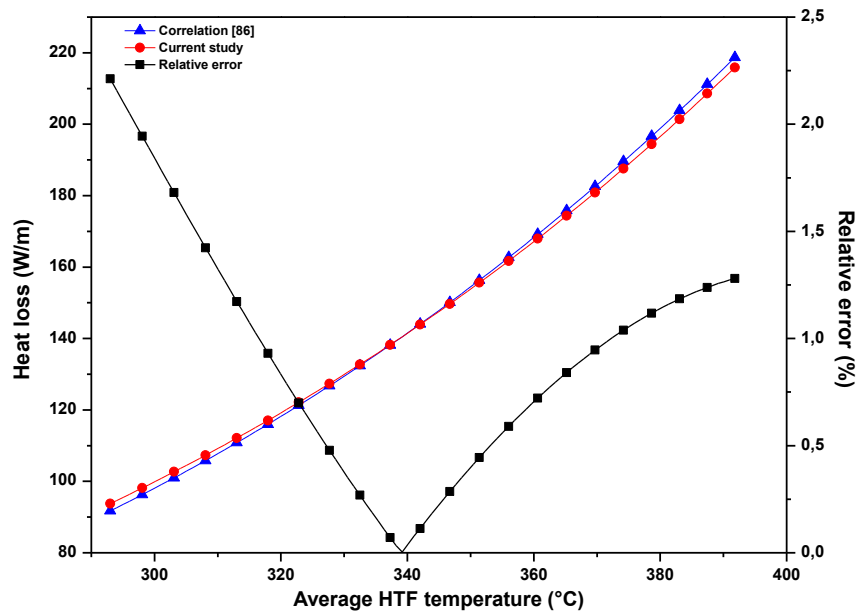
Figure 3.12: Comparison between numerical and empirical results [93] of the receiver linear thermal loss.

To confirm the model validation, HTF temperature profiles were compared in figure 3.13. Similar to the previous comparison (figure 3.12), it is evident that the two curves of HTF temperature, which appear to be linear, are nearly the same. Hence, the model validation is affirmed again since the relative error between these results is less than 0.15%.

Now we discuss the thermal behavior of the receiver's main components, namely, HTF, absorber pipe, and glass envelope, whose temperatures are exhibited in figure 3.14. These profiles are almost linear, and temperature values rise along the tube length. Due to these thermal properties, the absorber gets a significant amount of solar energy, so its temperature is higher than that of the two other elements (HTF and glass envelope) along the loop. The mean deviation from the HTF temperature is about 3.7 °C while it is about 292 °C from the glass envelope temperature. These differences could be explained by the disparity of thermal resistances of the three components of the solar receiver.
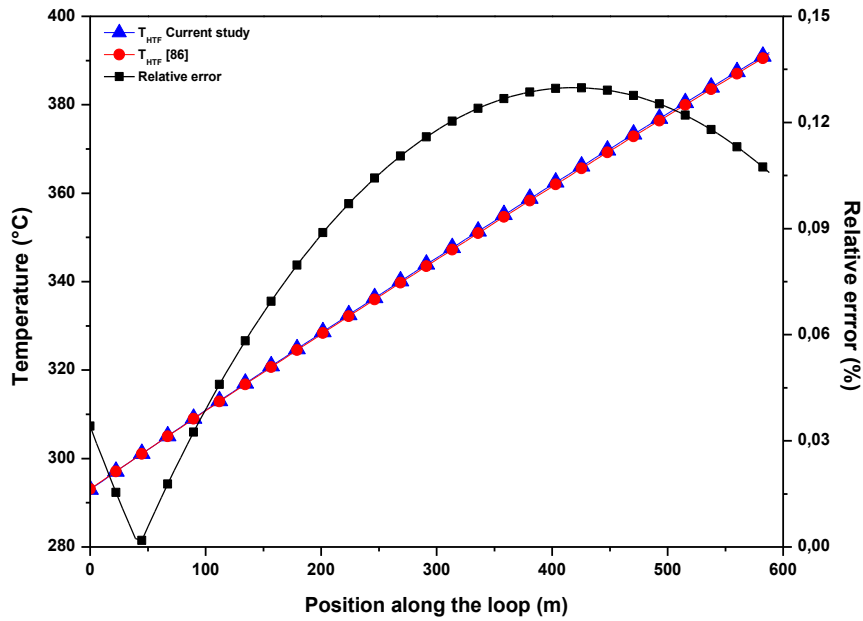
Figure 3.13: Comparison between numerical and empirical correlation results [93] corresponding to HTF temperatures along a single loop.
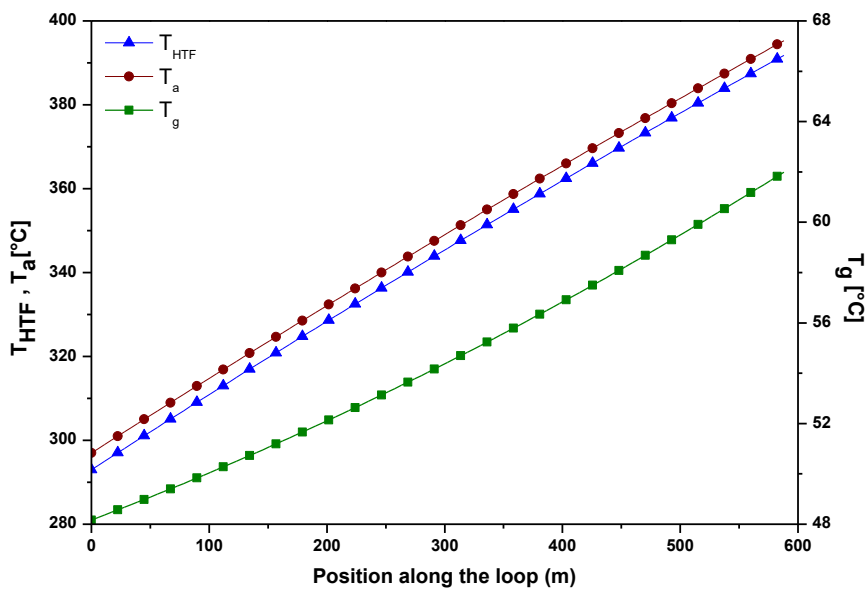
Figure 3.14: Variation of temperature along with position in one loop for the HTF, the absorber, and the glass envelope.

3.7.3 Thermal performances of Ain Beni Mathar ISCC power plant

In this part of work, daily and annual thermal performances of the solar field of Ain Beni Mathar ISCC power plant are discussed. For this purpose, daily data of the year 2015 were used to validate the capability of the model to estimate the thermal energy production and the

thermal efficiency of the solar field. The HTF system is designed for a HTF mass flow of Solutia's VP1 of 440 kg/s at 100% load (about 7.86 kg/s per loop).

3.7.3.1 Daily performance of the solar field of ABM - ISCC power plant (the year 2015)

To highlight the daily performance of the solar field of ABM power plant for the year 2015, the daily average of DNI, ambient temperature, and energy production for each season were carried out. This procedure aims to choose a typical day during each season. Consequently, January 4th, April 06th, August 16th, and October 5th, have been selected as typical days. The variation of DNI, ambient temperature, and wind speed are depicted in figure 3.15.
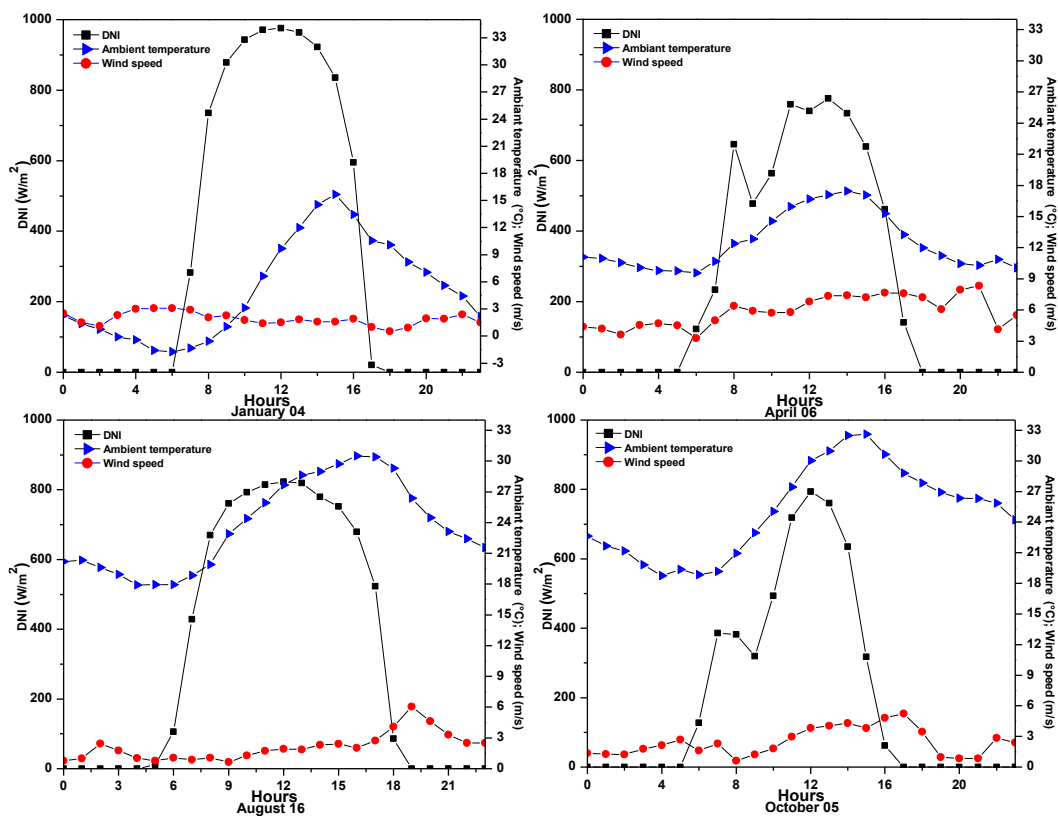
Figure 3.15: Hourly DNI, ambient temperature, and wind speed for the four different typical days.

For typical days (January 04th, April 06th, October 05th, and August 16th), figure 3.16 compares operating thermal energy and efficiency obtained from the ABM plant and those numerically simulated. Indeed, maximum operating thermal energy values, their associated efficiencies, and recording time are given in table 3.5.

As seen in the figure below (figure 3.16), it can be noticed that the trends and variations marked by the two curves are roughly the same. However, abrupt variations in energy production are difficult to model, whatever the type of model is considered. The only

situations where predictions are less accurate are those of low values of the produced thermal power that are normally associated with low values of DNI (especially the hours at the start and end of typical days). These overestimations can be explained by the fact that thermal inertia phenomena are not considered at the start-up period. As for the underestimations at the end of the day, they are mainly due to the low value of the shadow loss factor.
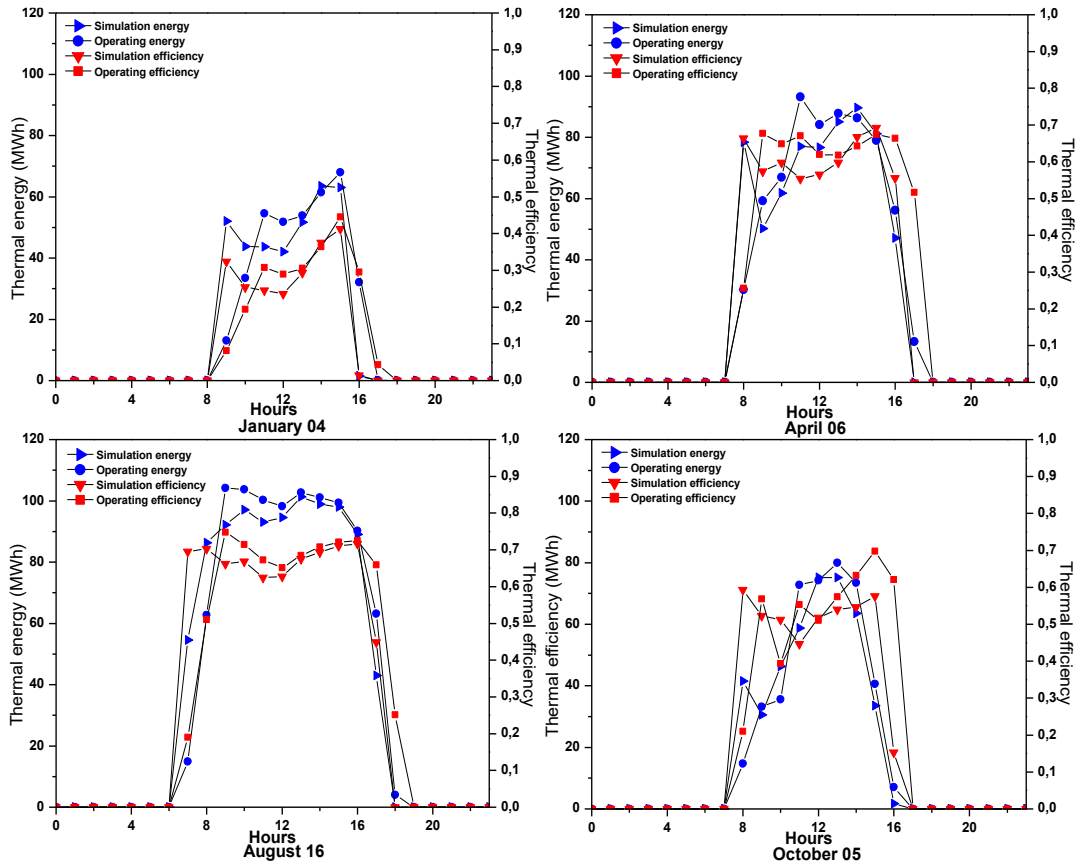
Figure 3.16: Hourly experimental and estimated thermal performances for the four different typical days.

Typical day	Peak operating thermal energy (MWh)	Efficiency (%)	Recording time
January 04th	68	44	15h
April 06th	93	67	11h
August 16th	104	74	9h
October 05th	80	57	13h

Table 3.5: Highest values of operating thermal energy as well as their associated efficiencies.

In figure 3.17, the model predictions of the outlet HTF temperature of one loop for the four studied typical days are presented. After the sunrise, the DNI increases during the daylight hours. As a result, the HTF temperature starts from 293 °C at the loop inlet to reach the selected temperature setpoint (391 °C) at the outlet, which is often used to calculate the heat losses from the HCEs and piping in the model.
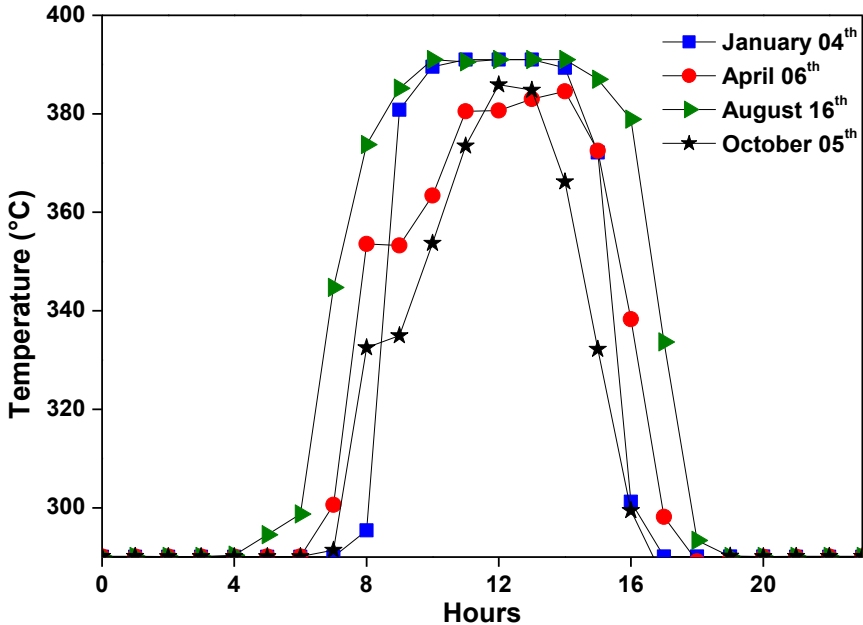
Figure 3.17: Variation of outlet HTF temperature of one loop

The estimates of thermal productions are more accurate in daily cumulative, as shown in figure 3.18. A comparison of daily net thermal energy production between the simulation results and operating data was made for ten days each season. The chosen ten days are: (1st -10th in January) for winter, (1st -10th in April) for spring, (1st -10th in July), and (3rd -12th in November) for autumn. In this graphical representation, red and blue dots are the amount of delivered thermal energy from the solar field to the power block at each specific day, whereas histograms present the daily cumulative DNI. It is obvious from these curves that the experimental thermal energy is very close to the simulated one for all considered days. Individual deviations in daily thermal energy production are less important, and obtained results are highly correlated with operating data.
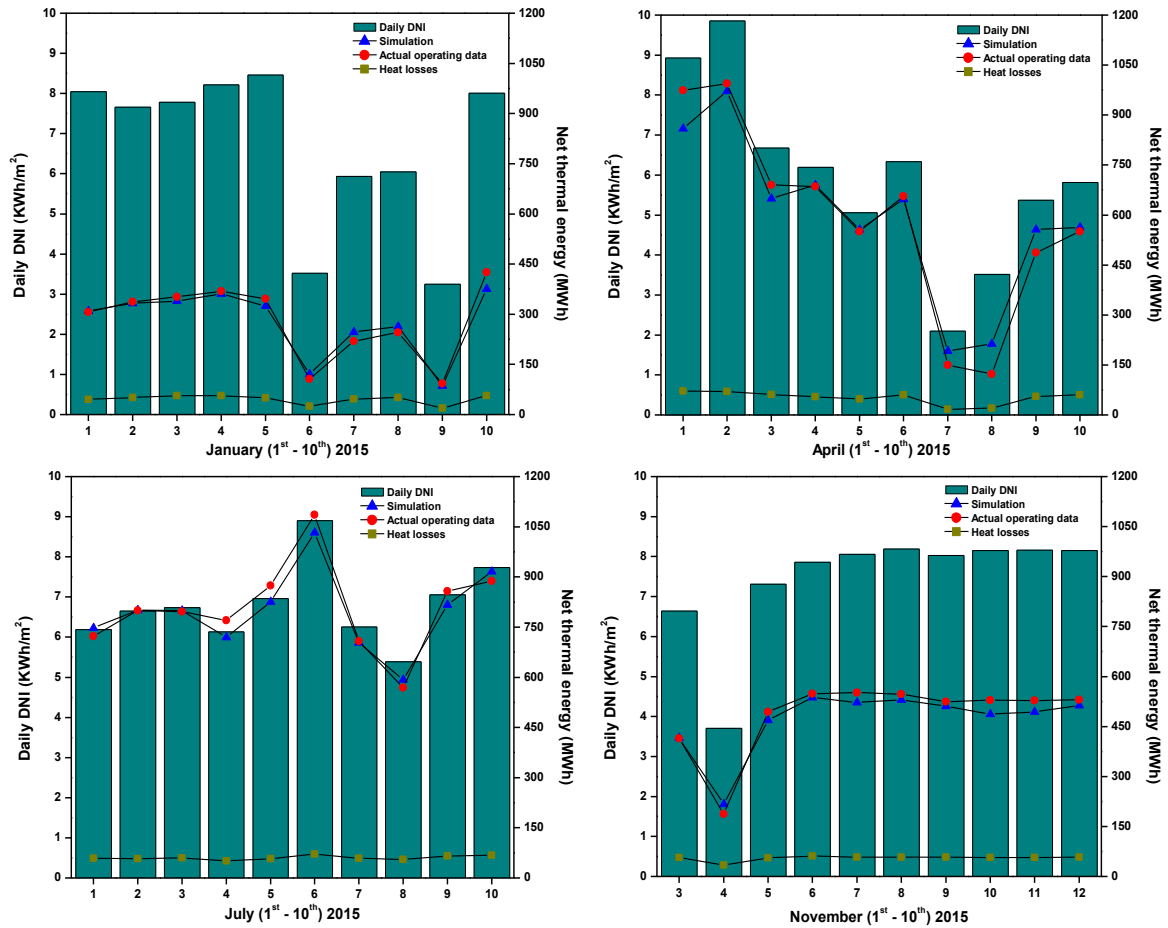
Figure 3.18: Daily net energy production for the ten days of each season: comparison of the experimental data and simulated results.

More details about thermal energy, heat losses, efficiency, and their corresponding deviations are presented in table 3.6, which presents the cumulative thermal energy, DNI, heat losses, and also overall thermal efficiency obtained for ten days of each season. Accordingly, the highest and lowest values of thermal energy production were respectively recorded in summer and winter. Thermal efficiency follows the same logic as thermal energy. Indeed, the operating cumulative thermal energy production is about 8.07 GWh for the first ten days of July, with a corresponding thermal efficiency of 64.79 %. The difference between this last result and that of the simulation is estimated at 1.47%. The lowest thermal efficiency (22.83%) is reached in January with about 2.8 GWh with a relative error of 1.46%. So, it can be concluded that the proposed model is more appropriate when the daily cumulative analysis is considered.

		DNI (kWh/m²-ten days)	Heat losses (MWh)	Thermal energy (MWh)	Efficiency (%)
January	**Operating**	66.96		2799.42	22.83
	Simulated	_	457.40	2758.44	22.50
	Relative error (%)	_		1.46	
April	**Operating**	59.87		5859.57	53.44
	Simulated	_	519.25	5897.44	53.79
	Relative error (%)	_		0.65	
July	**Operating**	68.03		8071.32	64.79
	Simulated	_	605.10	7952.44	63.83
	Relative error (%)	_		1.47	
November	**Operating**	74.29		4852.90	35.67
	Simulated	_	550.97	4694.31	34.51
	Relative error (%)	_		3.27	

Table 3.6: Cumulative thermal energy and efficiency of the solar field: comparison of operating and simulated results for the ten days of each season.

3.7.3.2 Annual performance of the solar field of ABM - ISCC power plant (the year 2015)

After dealing with daily performances of the solar field of ABM - ISCC power plant during 2015, we believe that it is useful to have a more accurate idea about its annual performances. Thus, table 7 and figure 3.19 offer a comparison of performances between the simulation and operating data.

Due to the variation of DNI during the year, the monthly average thermal production varies greatly. As expected, it is low in winter, unlike the summer season, where the peak production is around 25.86 GWh in July, for which the model underestimates the production with about 0.48 %. Additionally, the highest efficiency was recorded in June with about 64.38% and a

relative error of 2.98%. February has the lowest thermal energy production and the largest deviation (41.21%) between operating data and simulation results since the ABM plant was operating for only sixteen days (see figure 3.20).

Month	DNI (kWh/m²/month)	Solar field thermal output		Solar field thermal efficiency		Heat losses (GWh)	Relative error (%)
		Operating output (GWh)	Estimated output (GWh)	Operating efficiency (%)	Estimated efficiency (%)		
January	156.04	6.05	6.25	21.17	21.89	0.95	3.40
February	123.65	3.58	5.06	15.82	22.34	0.67	41.21
March	210.90	18.91	17.63	48.96	45.65	1.69	6.77
April	161.83	13.49	13.81	45.53	46.60	1.31	2.36
May	205.07	21.45	22.68	57.13	60.39	1.72	5.70
June	205.61	24.24	23.52	64.38	62.46	1.85	2.98
July	238.71	25.86	25.73	59.15	58.86	1.88	0.48
August	152.00	15.46	16.55	55.55	59.45	1.47	7.02
September	185.09	16.83	18.51	49.66	54.61	1.56	9.96
October	137.81	10.23	10.21	40.52	40.48	1.18	0.11
November	196.21	10.45	10.34	29.10	28.78	1.30	1.10
December	163.29	5.95	5.99	19.89	20.05	1.03	0.80
Annual	2136.21	172.51	176.29	44.10	45.07	16.61	2.19

Table 3.7: Performances of the ABM solar field during 2015.

According to figure 3.20, associated with February, it is evident that the model better estimates thermal energy production under normal operating conditions. However, some days whose production appears to have overestimated because of various causes, especially maintenance days or high wind speed values (see figure 3.11). For illustration, if the particular days of 3rd, 15th, 24th, and 27th February, for which the thermal energy is overestimated, are

not considered, the relative error will be reduced from 41.21 % to only 18.5%. After all, it is always interesting and helpful to have more information on a different operation such as maintenance or others to simulate ABM plant performances better.

The annual operating thermal production is about 172.5 GWh versus 176.3 GWh estimated from the simulation, which represents an overestimation of only 2.2%. The annual heat losses were about 16.6 GWh. Before concluding this work, it is important to emphasize that the performances of the ABM plant could be improved if a heat storage system were used [98]–[101].
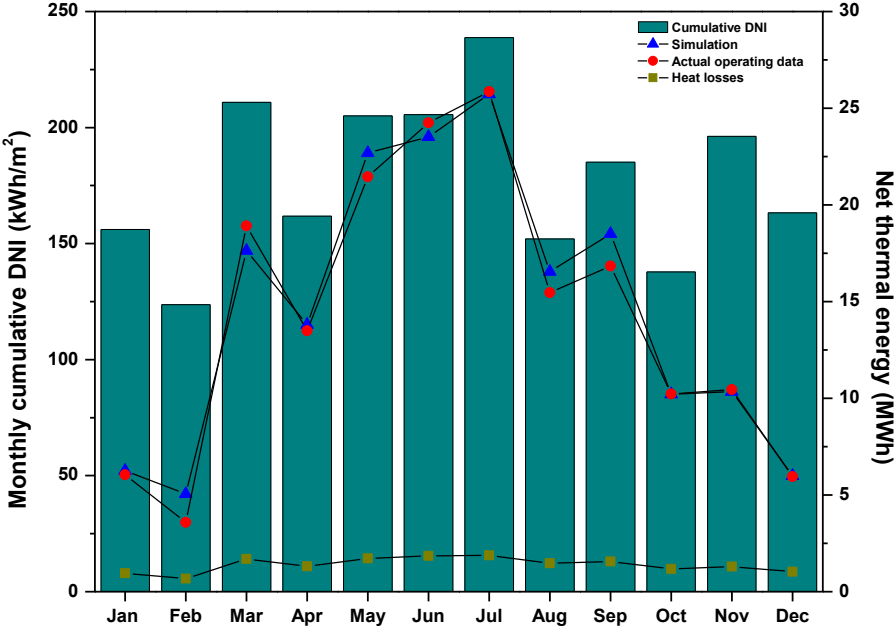
Figure 3.19: Monthly net thermal energy production for 2015: comparison of the experimental data and simulated results
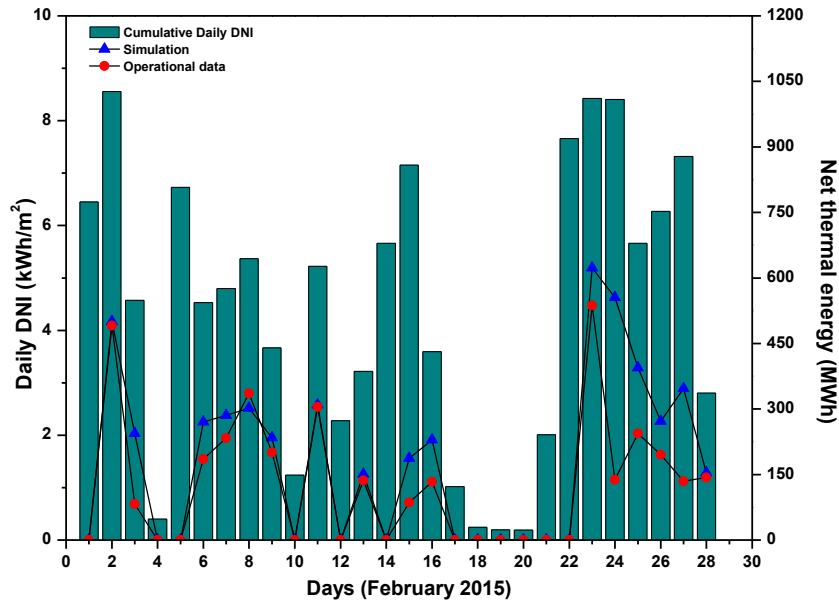
Figure 3.20: Daily net energy production for February: comparison of the experimental data and simulated results.

3.8   Conclusion

In this chapter, thermal performances of the solar field of Aïn Beni Mathar ISCC power plant were analyzed for the year 2015. Firstly, the solar receiver Schott PTR-70 2008 was modeled and simulated using Comsol Multiphysics software. Next, the model was validated with empirical data from NREL, so the comparison is satisfactory. It should be noted that the main results have been focused on daily and annual thermal performances, as well as a comparison between simulated results and actual plant operating ones.

For selected typical days, it was concluded that the model's predictions seem to be adequate except at the beginning and end of each day. On the other hand, the estimates of cumulative thermal productions for selected ten days of each season were also carried out. As a result, the actual operating thermal energy is very close to the simulated one for all chosen days. As an illustration, actual energy output and its corresponding thermal efficiency for the first ten days of July are respectively 8.07 GWh and 64.79 %, with a relative error of 1.47% compared to the simulation result. Conversely, with a relative error of 1.46%, the month of January recorded the lowest production (about 2.8 GWh) with a thermal efficiency of 22.83%. So, it can be concluded that the proposed model is more appropriate when the daily cumulative analysis is considered.

As expected, the monthly average thermal production is low in winter, unlike the summer season. The peak production is around 25.86 GWh in July, for which the model

underestimates the production by about 0.48 %. Additionally, the highest efficiency was recorded in June with about 64.38% and a relative error of 2.98%. February has the lowest thermal energy production and the largest deviation (41.21%) between operating data and simulation results since the ABM plant was operating for only sixteen days.

Chapter 4: Estimation of the energy production of a parabolic trough solar thermal power plant using analytical and artificial neural networks models

In this chapter, three models were conducted to estimate the hourly electric production of a parabolic trough solar thermal power plant (PTSTPP) located at Ain Beni-Mathar in Eastern Morocco. First, two analytical models are considered. Those models include the absorbed solar energy collected on the parabolic trough field, the useful energy gained by heat transfer fluid (HTF) circling inside the receiver, and the electric energy produced at the output of the steam turbine. The first analytical model (AM I) is based on calculating the heat losses of parabolic trough collectors (PTCs), while the second analytical model (AM II) is based on the thermal efficiency of PTCs. The third model is an artificial neural network (ANN) model derived from artificial intelligence techniques. This black box model is based on hourly energy production and meteorological data. A large amount of data is used to train and validate a three layers feed-forward ANN (Multi-Layers Perceptron (MLP)). Several architectures have been tested to select the best ANN model by varying the set of input variables and the number of neurons in the hidden layer. All models are validated using one year of real operating data.

4.1 Introduction

Energy is a vital resource for the economic and social development of a country. The economic level of a country is highly related to its energy consumption since countries that consume much energy produce a lot of products or services. Traditionally, the most widely used energy sources were natural ones such as oil, coal, and natural gas. These sources are not inexhaustible, and their use has adverse environmental effects such as global warming, climate change, emissions of greenhouse gas, and depletion of the ozone layer [37]. These fossil fuels are nonrenewable (exhaustible) and can, therefore, gradually tend towards extinction [102]. So, it is necessary to consider replacing these sources with new and clean sources, such as renewable energies. However, those energies are still competing with conventional fossil fuel plants that run predominantly on coal, natural gas, and to a lesser extent, oil [103].

Concentrating solar power (CSP) energy system has been growing strongly in recent years. It aims at transforming the energy radiated by the sun into heat at high temperatures and then into mechanical and electrical energy through a thermodynamic cycle machine [104]. The accurate estimation of the solar power plant production is an important issue because of the fluctuations in meteorological parameters like solar radiation, ambient temperature, wind speed, and humidity. These natural fluctuations cause production fluctuations and power delivery problems on the electricity grid [105].

As discussed in chapter 1, the literature review shows that most studies on the optimization of parabolic trough power plants are based on analytical models, including steady-state and dynamic models, while machine learning models such as ANN models are rarely used.

This chapter compares the accuracy in predicting the hourly based energy production of a PTSTPP using analytical and ANN methods. First, two analytical models are considered. Those models include the absorbed solar energy collected on the parabolic trough field, the useful energy gained by heat transfer fluid (HTF) circling inside the receiver, and the electric energy produced at the output of the steam turbine. Both models comprise a steady-state approach. The first analytical model (AM I) is a well-known model and is based on calculating the heat losses of PTC, whereas the second analytical model (AM II) is based on a formula to calculate the global thermal efficiency of PTCs. The third model is an artificial neural network (ANN) model derived from artificial intelligence techniques. This black box model is based on hourly energy production and meteorological data. A large amount of data is used to train and validate a three layers feed-forward ANN (Multi-Layers Perceptron (MLP)). To select the best ANN model, several architectures have been tested by varying the set of input variables and the number of neurons in the hidden layer. In addition to the frequency distributions of the differences between operating and predicted model results, different statistical parameters were used for verifying the accuracy of the analytical and ANN models. To this end, simulations were conducted using MATLAB software.

4.2   Data characteristics

4.2.1   Climate data at the power plant location

The study refers to a PTSTPP integrated into a combined cycle using two gas turbines and located at Ain Beni-Mathar (ABM) in the Eastern part of Morocco. The climatic data used in this study were taken from the meteorological station available at the power plant site. Hourly

data were taken during 1522 days from the first of November 2011 to the 31st of December 2015[65].

The ambient temperature in the region of the plant presents significant seasonal variability as indicated in (figure 4.1 (a)). The summer seasons are hot and winters are cold. This parameter highly affects thermal losses in the solar collectors. The minimum value of the monthly average temperature of the coldest month (February 2012) is 5.2 °C while the maximum of the average temperature of the hottest month (August 2012) is 30 °C. Besides, as expected, the relative humidity depends strongly on the ambient temperature since they vary in an opposite way as shown in (figure 4.1 (b)). The ambient air is quite dry in summer when it gets very hot during summers; the minimum average relative humidity is 21.8% and was recorded in August 2012. Conversely, the ambient air is rather humid on winters, with a maximum of 77% recorded in December 2014 [65].

The wind speed has also considerable impact on the CSP efficiency. (figure 4.1 (c)) depicts monthly averages of wind speed. The average values are almost ranging from 2 m/s to 5 m/s. Note that the maximum average value (5.4 m/s) was recorded in February 2015. In an energy point of view, the area of the power plant is well exposed to sunlight with an average of Daily Direct Normal Irradiation (DNI_d) of 5.2 kWh/m^2. The monthly averages DNI_d are presented in (figure 4.1 (d)). The maximum DNI_d value of 8.86 kWh/m^2 was recorded in June 2013 and the minimum value of 3.08 kWh/m^2 was recorded in November 2012. As this parameter determines the level of the energy resource used by the plant, DNI_d largely determines the energy output of a PTSTPP [65].
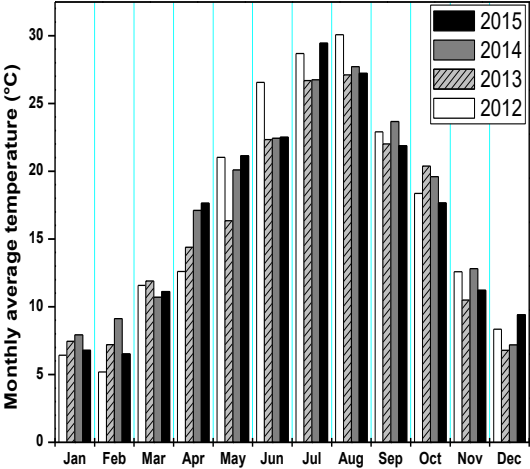
(a) Monthly averages of ambient temperature

(b) Monthly averages of relative humidity
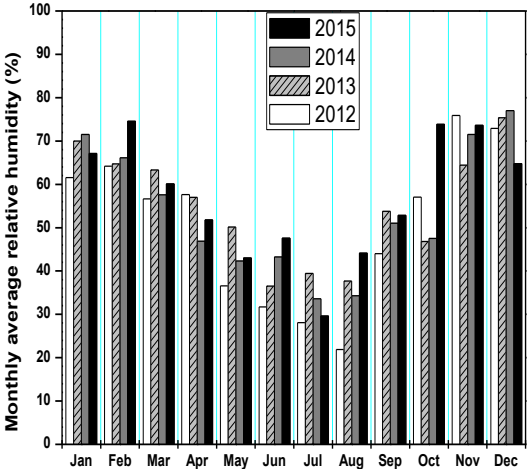
(c) Monthly averages of wind speed   (d) Monthly averages of DNI_d
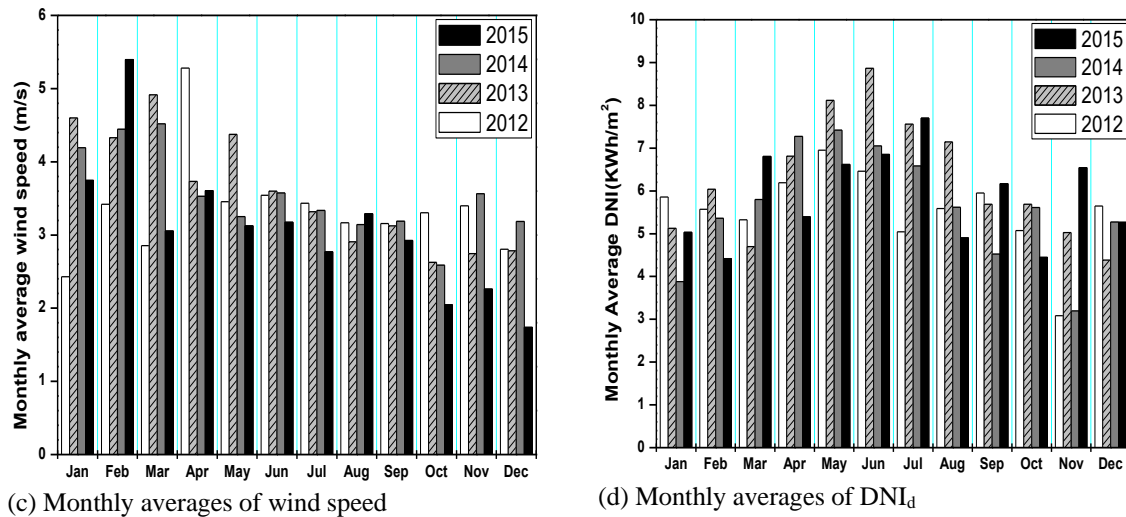
Figure 4.1: Climatic data at study site location for 4 years

4.2.2 Solar electricity production

Our study focuses only on the solar part of the power plant, where the solar energy collected by the parabolic trough collectors generates the steam that feeds the HRSGs. A metal pipe absorbs the solar energy concentrated by the collectors inside a vacuum glass tube. The heat transfer fluid (HTF) circulating inside the pipe is heated to a temperature near 400 °C. This fluid is then pumped through a conventional heat exchanger to produce steam at high temperatures and pressures. The steam is used in a Rankine cycle to produce electrical energy via the steam turbine generator.
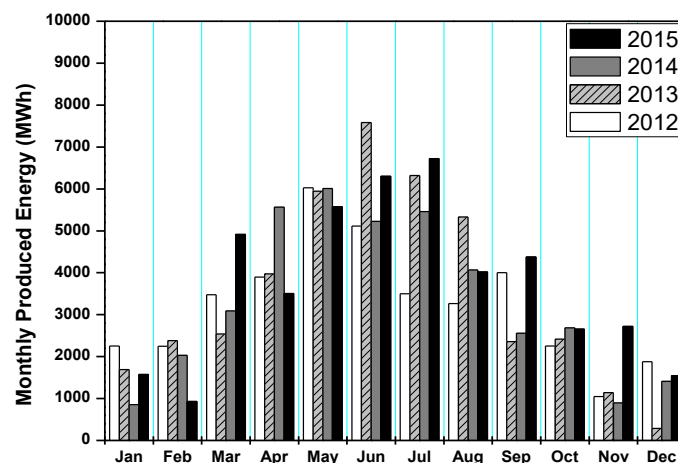
Figure 4.2: Monthly production of electrical energy by the plant for 4 years

Figure 4.2 shows the electrical energy production of the power plant over 4 years (2012-2015). The produced energy is about 39 GWh in 2012, 42 GWh in 2013, 40 GWh in 2014, and 44.8 GWh in 2015. Energy production varies according to the seasons. Obviously, hot

seasons (Spring and Summer) correspond to the highest production levels, while cold seasons (Autumn and Winter) correspond to the lowest production levels. The highest energy production was recorded in June 2013 (7.6 GWh), while the lowest was recorded in December 2013 (0.3 GWh).

4.3 Methods

In this part, the analytical and ANN models are used to estimate the energy production of the ABM solar power plant. Two mathematical models based on analytical relations were considered. The first one, Analytical Model I (AM I), is based on explicit calculations of heat losses in the solar field of PTCs, while the second, Analytical Model II (AM II), is based on a global evaluation of the thermal efficiency of the PTCs. Both analytical models comprise a steady-state approach to evaluate the thermal losses and thermal efficiency of the PTCs. The third model is an artificial neural network (ANN) model. This black box model is based on hourly energy production and meteorological data. The main characteristics and governing equations of each model are presented and discussed in detail. All models are validated using experimental data derived from the ABM power plant during the year 2015.

4.3.1 Analytical model I (AM I)

In this part, the analytical model of heat losses of PTCs is presented. This model mainly consists of four parts. The first part concerns the calculation of the incidence angle of solar radiation to determine the amount of solar energy received by the solar field (see chapter 3, section 3.2). The second part is devoted to optical analysis. The goal of this part is to calculate the optical efficiency of the PTCs, which is the ratio of the amount of energy arriving at the absorber tube, and that hits the reflector (see chapter 3, section 3.3). The third part concerns the thermal analysis and aims to determine the energy absorbed by the HTF in the receiver tubes. For this purpose, solar field heat losses from the Heat Collection Element (HCE) and piping were determined using empirical correlation. The last part deals with thermo-electric analysis, and it concerns the estimation of the electrical energy at the output of the alternator. This energy was calculated based on the provided efficiency of the power block. Figure 4.3 shows a simplified schematic with the general structure of the AM I information flow.
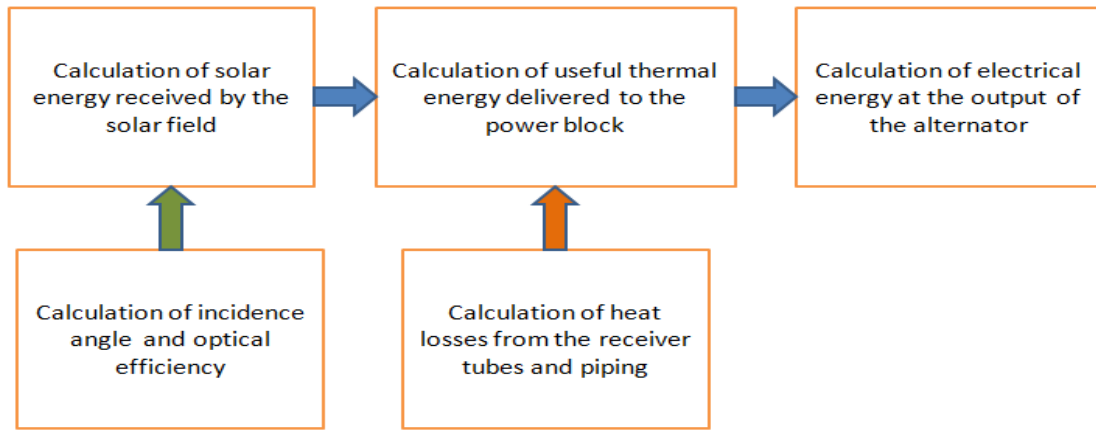
Figure 4.3: Schematic with the general structure of the information flow within the AM I.

4.3.1.1 Thermal analysis

Thermal analysis of the receiver system is significant in determining how much of the solar radiation is converted into useful gain. In this stage, the heat losses of the receiver tubes $Q_{loss,HCE}$, and the total heat losses of the pipes $Q_{loss,pipes}$ have to be calculated and subtracted from the absorbed power. The useful thermal power supplied to the HTF can be calculated using equations form (3.45) to (3.48). Note here that the useful thermal power is estimated for the total area of the solar field A_p. Also, it is worth mentioning that among the operation conditions of the solar field, the HTF inlet, and outlet temperatures [70]. These temperatures are significant for the operation of the solar field to generate steam at the desired temperature and pressure. In this study, the inlet and outlet HTF temperatures are 293 °C and 391 °C, respectively, which means that $T_{av,HTF}$= 342 °C. More details about the model could be found in (chapter 3 section 3.5).

The useful heat stored in the heat transfer fluid corresponding to any period of time (τ [h]) can be calculated as:

$$Q_u(AM\ I) = Q_u\ \tau \tag{4.1}$$

4.3.1.2 Thermo-electric analysis

The ratio of the electrical power produced Q_{el} to the total thermal power is the global efficiency of the power plant:

$$\eta_g = \frac{Q_{el}}{Q_u} \tag{4.2}$$

This value is fixed in our model of the ABM power plant at $\eta_g = 26\%$, according to the operators of the power plant. A value of 26% may be considered relatively low, but it seems

realistic as the thermal power plant is a hybrid plant. The temperature and pressure of the steam produced by the hot source are relatively low.

4.3.2 Analytical model for thermal efficiency of parabolic trough collectors (AM II)

4.3.2.1 Model description

In this part, the analytical model is based on the global thermal efficiency of the PTC. The model uses the same correlation as in the AM I to calculate the incidence angle and electric energy that comes from the heat exchanger. However, it differs in optical and thermal analyses, which are reduced to the calculation of the global thermal efficiency of the PTC (η [-]) using the following formula:

$$\eta = K_T \, K_L \, \eta_{opt,0} - K_1 \frac{\Delta t}{DNI} - K_2 \frac{\Delta t^2}{DNI} \tag{4.3}$$

where:

- k_T is the correction coefficient, due to the transversal angle of incidence (α_T); ($k_T = 1$)
- k_L is the correction coefficient, due to the longitudinal angle of incidence (α_L); it is also known as IAM.
- k_1 [W/m^{2}K] is a correction coefficient that takes into account thermal losses;
- k_2 [W/m^{2}K^2] is a correction coefficient that takes into account thermal losses;
- Δt [K] is the temperature difference between the mean temperature of the heat transfer fluid of the collector (342 °C) and the temperature of the exterior environment (T_{amb});

The optical efficiency is usually available for many types of PTC, but the correction coefficients k_1 and k_2 are not available in the literature and in the technical sheets of the PTC. In this study, these coefficients were evaluated using the curve fitting method of thermal efficiency with HTF temperature for the PTC used in ABM and some PTCs. Curve fitting is based on the least-squares method. The aim is to compare the performances of these PTCs with the one used in the ABM power plant and compare the accuracy in predicting the hourly based energy production of a PTSTPP with the other models.

The useful heat stored in the heat transfer fluid per unit plane surface area of PTC (Q_{HTF} [Wh/m^2]), corresponding to any period of time (τ [h]) can be calculated as:

$$Q_{HTF} = \eta \, DNI \, \tau \tag{4.4}$$

The total useful heat generated by the solar field becomes:

$$Q_u(AM\ II) = Q_{HTF}A_p \qquad\qquad (4.5)$$

Figure 4.4 shows a simplified schematic with the general structure of the AM II information flow.
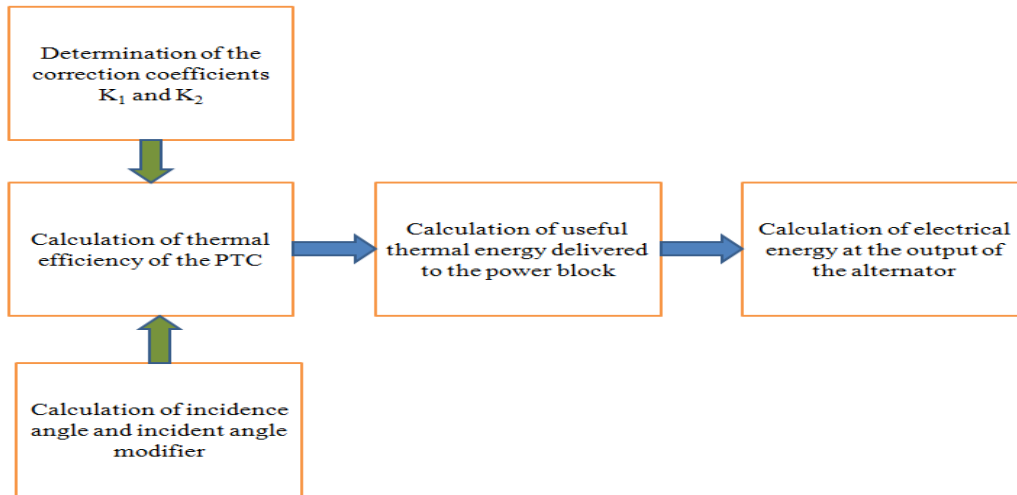
Figure 4.4: Schematic representation of the information flow within the AM II.

4.3.2.2 Estimation of correction coefficients k_1 and k_2 for the studied PTCs

The aim of this part is the determination of the correction coefficients of different PTCs. The nature of the HTF and the operating temperature for several commercial PTC are presented in table 4.1. table 4.2 deals with the recommended equations for the calculation of the IAM for different PTC.

Reference	Type of collector	HTF	Temperature [°C]
[106]	SEGS LS-2	Syltherm 800	400
[107]	EuroTrough (ET100; ET150)	NA	400
[22]	EuroTrough ET150	Therminol VP-1	400 (370)
[108]	EuroTrough II	Steam	280-411
[41]	EuroTrough ET100	Therminol VP-1	400
[30]	FLAGSOL	Therminol VP-1	295-393
[109]	UrssaTrough	NA	293-393
[110]	INDITEP	Steam	NA
[111]	NEP PT1800	NA	100-300
[112]	SKAL-ET	Solar salt	450 (500)
[113]	SOLTIGUA PTMx-36	NA	250

Table 4.1: The thermal agent and the operating temperature for some PTCs

Reference	Equations	Obs.
[106]	$K_L = \cos(\theta) - 0.0003512\,\theta - 0.0003137\,\theta^2$	From measurements
[30], [31], [41], [87], [108], [114], [115]	$K_L = \cos(\theta) - 0.000525097\,\theta - 0.0002859621\,\theta^2$	
[116]	$K_L = \cos(\theta) - 0.00044\,\theta - 0.0003\,\theta^2$	Steam in collectors
[112]	$K_L = 1 - 0.0004\,\theta - 0.00017\,\theta^2$	From experiment
[109]	$K_L = \cos(\theta) - 0.0007\,\theta - 0.00036\,\theta^2$	Est-West orientation
[113]	$K_L = 1 - 0.0018\,\theta - 0.00013\,\theta^2$	From technical data

Table 4.2: Equations recommended for the calculation of the IAM

The solar field of the ABM power plant is equipped with ET150 PTCs and Scott PTR 70 (2008) receivers. The correction coefficients k_1 and k_2 were determined based on the variation curve of the thermal efficiency at DNI = 800 W/m^2 and for Δt in the range of (100…500) °C, available in [117]. Note that in reference [117], the thermal efficiency variation with HTF temperature was determined by establishing a one-dimensional and steady-state model. The estimated coefficients are k_1= 0.0949 and k_2= 2.29 10^{-4}. The maximum difference between the reference and the calculated efficiencies is 4.5% (figure 4.5).
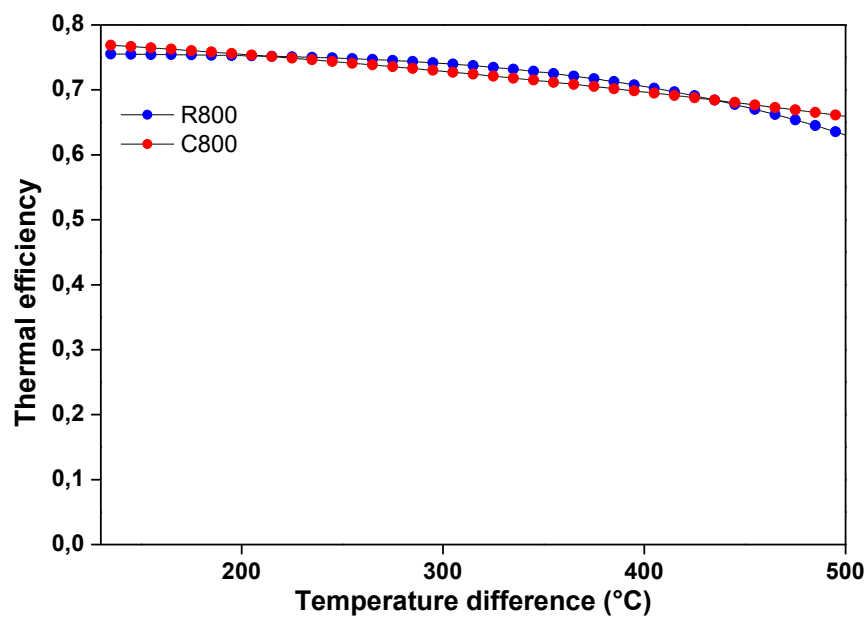
Figure 4.5: Thermal efficiency variation for ET150-PTR70 (2008). Codes significance: R800 = based on reference [117] at DNI = 800 W/m^2; C800 = calculated with proposed coefficients at DNI = 800 W/m^2.

The study [106] proposes a slightly different equation to evaluate the thermal efficiency (η [-]) of the SEGS LS-2 type of PTC:

$$\eta = K_L\left(\eta_{opt,0} - a_0\,\Delta t\right) - a_1\,\frac{\Delta t}{DNI} - a_2\,\frac{\Delta t^2}{DNI} \qquad (4.\,6)$$

Table 4.3 presents the optical efficiency and the correction coefficients: a_0, a_1, and a_2 for the LS-2 PTC.

PTC Type	$\eta_{opt,0}$	a_0	a_1	a_2
LS-2 Cermet with vacuum annulus (LS2-CV)	0.733	0.00007276	0.00496	0.000691
LS-2 Cermet with air in annulus (LS2-CA)	0.734	0.00008030	0.09680	0.000669
LS-2 Black chrome with vacuum annulus (LS2-BV)	0.736	0.00004206	-0.07440	0.000958
LS-2 Black chrome with air in annulus (LS2-BA)	0.738	0.00006460	0.12160	0.000641

Table 4.3: The optical efficiency and the correction coefficients: a_0, a_1 and a_2

Based on this equation, the correction coefficients k_1 and k_2 were determined for the LS-2 PTC. The maximum differences between the thermal efficiencies calculated with the proposed equations and those available in the literature [106], for DNI in the range of (200…1000) W/m^2 and Δt in the range of (0…500) °C, are 7.6 %, 7.5 %, 5.0 % and 14.1 % for LS2-CV, LS2-CA, LS2-BV, and LS2-BA, respectively. (figure 4.6 (a)) and (figure .6 (b)) present the thermal efficiency variation for LS2-CV and LS2-BV respectively for DNI in the range of (200…1000) W/m^2 and Δt in the range of (0…500) °C.
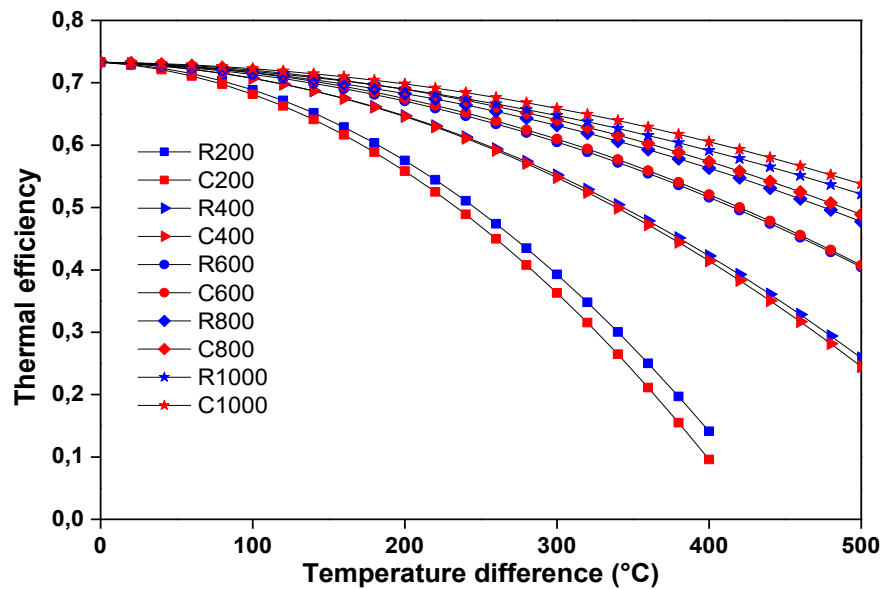
(a) LS2-CV;
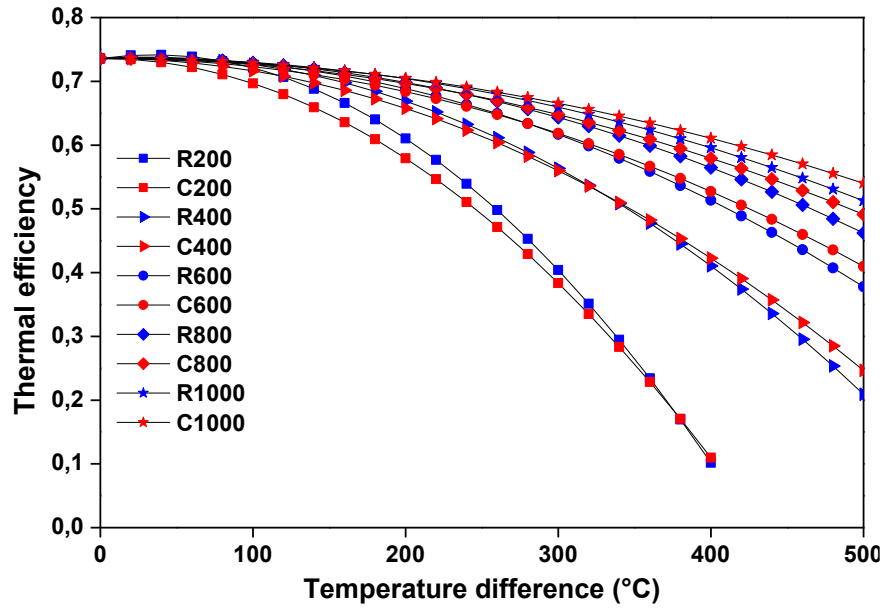
(b) LS2-BV

Figure 4.6: Thermal efficiency variation. Codes significance: R number: R = based on reference [106]; number = DNI [W/m^2]; C number: C = calculated with proposed coefficients; number = DNI [W/m^2]

For the UrssaTrough (UT) PTC equipped with PTR 70 receiver, the correction coefficients k_1 and k_2 were determined based on the variation curve of the thermal efficiency at DNI = 864 W/m2 and for Δt in the range of (0…350) °C, available in [109]. Figure 4.7 presents the thermal efficiency variation for UT-PTR70. The maximum difference between the measured and the calculated efficiencies is 1.5 %.
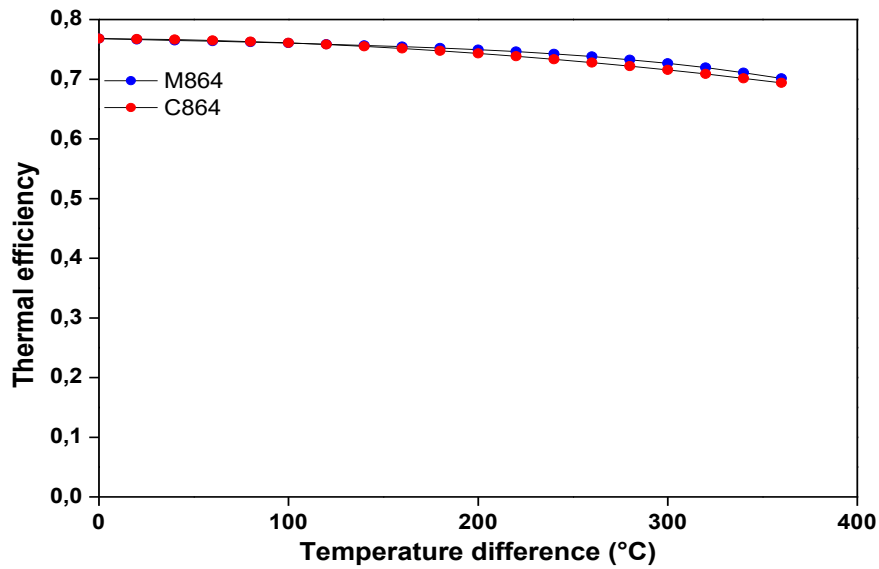
Figure 4.7: Thermal efficiency variation for UT-PTR70. Codes significance: M864 = measured at DNI = 864 W/m^2; C864 = calculated with proposed coefficients at DNI = 864 W/m^2

For the EuroTrough ET150 PTC with Solel (now Siemens) receiver, the correction coefficients k_1 and k_2 were determined based on the variation curves of the thermal efficiency at DNI in the range of (200…1000) W/m² and for Δt in the range of (0…500) °C, available in [86]. For Δt = 500 °C, the maximum differences between the measured and the calculated efficiencies are of 10 %, 1.2 %, 2.4 %, 1.2 % and 2.2 % for DNI = 200, 400, 600, 800 and 1000 W/m², respectively. The difference of 10 % corresponds to Δt = 500 °C and DNI = 200 W/m². Under these conditions, the measured efficiency is η= 10 %, and the calculated efficiency is η = 9 %. For the values of $\Delta t \leq$ 400 °C, even for DNI = 200, the maximum difference between the measured and the calculated efficiencies drops to 4.7 %. Figure 4.8 presents the thermal efficiency variation for ET150-Solel for DNI in the range of (200…1000) W/m² and Δt in the range of (0…500) °C.

Figure 4.8: Thermal efficiency variation for ET150. Codes significance: M number: M = measured in [86]; number = DNI [W/m²]; C number: C = calculated with proposed coefficients; number = DNI [W/m²]

Table 4.4 summarizes for different PTCs types the optical efficiency and the new proposed correction coefficients k_1 and k_2. The maximum difference between the thermal efficiency from reference and calculated by the proposed formula (%) is also presented.

Collector	η_0	k_1	k_2	Max difference (%)
LS-2 Cermet with vacuum annulus (LS2-CV)	0.733	0.0306	0.000720	7.6
LS-2 Cermet with air in annulus (LS2-CA)	0.734	0.0810	0.000819	7.5
LS-2 Black chrome with vacuum annulus (LS2-BV)	0.736	0.0	0.000783	5
LS-2 Black chrome with air in annulus (LS2-BA)	0.738	0.1800	0.000567	14.1
UrssaTrough (UT) with PTR 70	0.768	0.018	0.0004441	1.5
EuroTrough ET150 (ET150) with Solel	0.760	0.018	0.0005	10
Soltigua PTMx	0.747	0.64	0.0	-
ET150 with PTR70 (2008)	0.79	0.0949	0.000229	4.5

Table 4.4: The proposed optical efficiency and the correction coefficients k_1 and k_2 [65].

In the rest of the study, only the evacuated PTCs were considered: LS2-CV, LS2-BV, ET150-Solel, UT- PTR70, and ET150- PTR70.

4.3.3 ANN model

ANNs are data-processing systems and machine learning techniques inspired from biological neural systems. ANNs are used to solve many different engineering and science problems, especially in certain areas where conventional modeling methods fail [118]. ANN prediction is usually much faster than conventional simulation models since iterative calculations are not necessary to solve differential equations. However, the topology definition and parameters computation of the neural network is time-consuming [119].

The structure of ANN is a significant factor that influences the learning performances of networks. The multilayer perceptron (MLP), known as the feed-forward neural network (FFNN), is effective for modeling energy conversion systems, thanks to its capability of arbitrary input-output mapping. MLP, as the most successful and the most popular ANN model from many ANNs models, is adopted in the present study [120]. Generally, MLP comprises three layers: an input layer, an output layer, and a hidden layer/s. The network function is specified largely by the connections between the nodes (a node is a place where computation happens) of different layers. Each node receives an input signal, which is the total 'information' from other nodes or external stimuli, processes it locally through a transfer or activation function, and produces a transformed output signal to other nodes or external outputs [121].

Figure 4.9 illustrates the structure of a MLP model used in this study. The input layer takes the data from the network. The hidden layer processes the raw information received from the input layer. The obtained value is then sent to the output layer, which will also process the information from the hidden layer and produce the output [122].
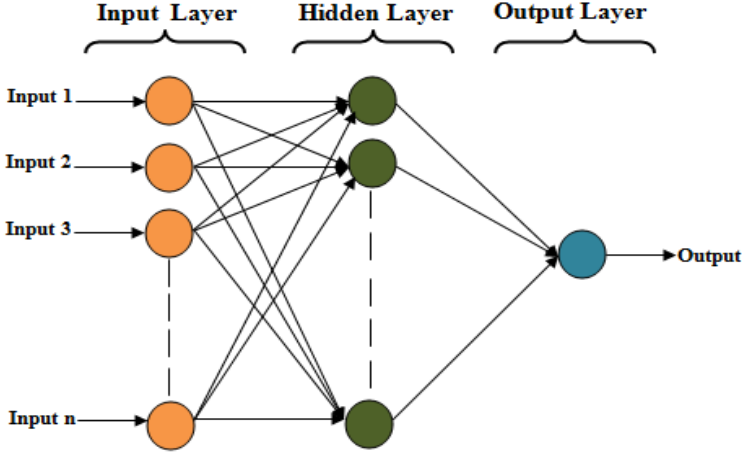
Figure 4.9: Structure of a MLP (FFNN)

The backpropagation is a supervised learning method for the MLP neural networks. It is used to obtain the relationships between inputs and outputs and is considered one of the most extensively used and popular ones [123]. This algorithm has been developed in various variants, including gradient descent and momentum gradient descent, which are considered as two important methods. However, these algorithms are slow because of the low speed of iterative learning. The Levenberg–Marquardt (LM) is a faster algorithm because it is based on performant optimization techniques ([124], [125]). Hence, the LM algorithm was selected in this study. More details about back-propagation and LM algorithms are presented in the Appendix.

To translate signals between different layers of the MLP, several transfer functions are available. The logistic sigmoid, tangent sigmoid, and the linear transfer functions are classically used. Those functions were examined and compared in terms of the accuracy of the resulting ANN function [119].

The following equation defines the logistic sigmoid function:

$$f(net_j) = O_j = \frac{1}{1 + exp(-net_j)} \tag{4.7}$$

The tangent sigmoid function is given by:

$$f(net_j) = O_j = \frac{2}{1 + exp(-2net_j)} - 1 \qquad (4.8)$$

where O_j is the output of the j_{th} neuron and net_j is the weighted sum of the inputs obtained by:

$$net_j = \sum_{i=1} W_{ij} O_i \qquad (4.9)$$

W_{ij} is the weight of the connection from neuron i in the previous layer to neuron j in the current layer, and O_i is the output of the ith neuron in the previous layer.

In this study, several combinations of input variables have been tested to estimate the hourly energy production (E_h). The input variables taken into account are the hourly direct normal irradiation (DNI_h), the hour of the year ($\tau_{h,y}$), the hour of the day ($\tau_{h,d}$), ambient temperature (t_h), relative humidity (φ_h), and wind speed (w_h). For each hour h, the previous hourly energy productions (E_{h-1}) are also used as an input variable. Data covering a period of 4 years of the studied power plant (with the inputs supposed and output) are selected. Then, 75% of these data (about 3 years: from 01 November 2011 to 31 December 2014) were used for training while the remained were used for validation (One year: 2015). In the training process, the ANN model was provided with the data of the inputs and output that the network will compute, and then the errors between actual results (operational data) and those predicted (determined by ANN) are calculated. This process aims to reduce these errors to a minimum. To improve the ANN model's reliability linking solar electric energy production and meteorological data, we only take into account the hours of solar energy production. The other data were considered as being irrelevant. During these hours, there is no solar energy production due to the: maintenance of the solar components, dangerous wind speed, and nights.

The MLP model has been developed using MATLAB© software. To select the most relevant input variables of the model, we adopt an incremental method by adding progressively new variables and observing their influence on the model accuracy. Several variable combinations were investigated to evaluate the performances of the incremental method. In all cases, we used an ANN model with 5 nodes in the hidden layer [126]. Finally, the model was improved by testing different numbers of hidden neurons. In this study, a single hidden layer ANN model is considered to simplify the computation. The desired parameters of the ANN model are listed in table 4.5.

Parameters	Value
Number of hidden layers	1
Number of epochs	1000
Train function	trainlm (Levenberg-Marguardt)
Function of performance	MSE
Hidden layer function	logsig
Output layer function	tansig

Table 4.5: Final parameters setting of the ANN model.

It's worth mentioning that there is no rule for selecting the neuron numbers or the middle layer numbers in the network. The correct way is built on trial and error. Therefore, there are some of the diverse neuron numbers and internal layers are tried and assessed. The execution of each model is checked, and the structure with the minimum number of neurons and internal layers is usually selected as illustrated in figure 4.10.
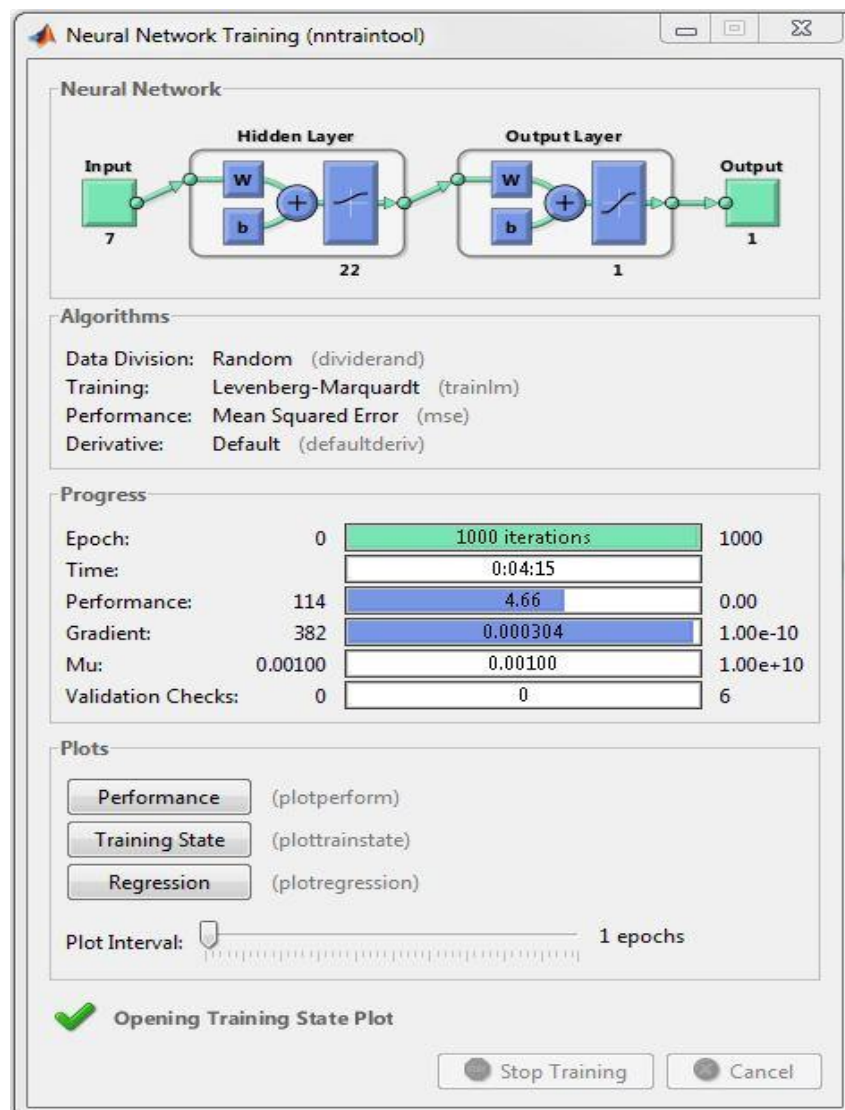
Figure 4.10: Training window of ANN

In the following, the ANN model accuracy is evaluated by the coefficient of determination (R), root mean square error (RMSE), relative root mean square error (RRMSE), relative mean bias error (RMBE), and mean absolute error (MAE) [126]. Those accuracy parameters are defined as:

$$R = \frac{\sum_{k=1}(y_k - \bar{y})(t_k - \bar{t})}{\sqrt{\sum_{k=1}(y_k - \bar{y})^2 \sum_{k=1}(t_k - \bar{t})^2}} \qquad (4.\,10)$$

$$RMSE = \sqrt{\frac{1}{N}\sum_{k=1}(t_k - \bar{t})^2} \qquad (4.\,11)$$

$$RRMSE = \frac{100}{\bar{t}}\sqrt{\frac{1}{N}\sum_{k=1}(t_k - \bar{t})^2} \qquad (4.\,12)$$

$$RMBE = 100\,\frac{\sum_{k=1}(t_k - y_k)}{\sum_{k=1}(y_k)} \qquad (4.\,13)$$

$$MAE = \frac{1}{N}\sum_{k=1}|(t_k - y_k)| \qquad (4.\,14)$$

where y_k and t_k denote respectively, the measured and the predicted output values for the kth data while $\bar{y}$ and $\bar{t}$ are respectively the measured and the predicted mean values.

When an ANNs model may peculiarly provide the maximum standards of R, and minimum standards of RMSE, RRMSE, RMBE and MAE, it can be definitely approved to be the right and superior ANN model.

Figure 4.11 shows a simplified schematic flowchart of the proposed ANN model.
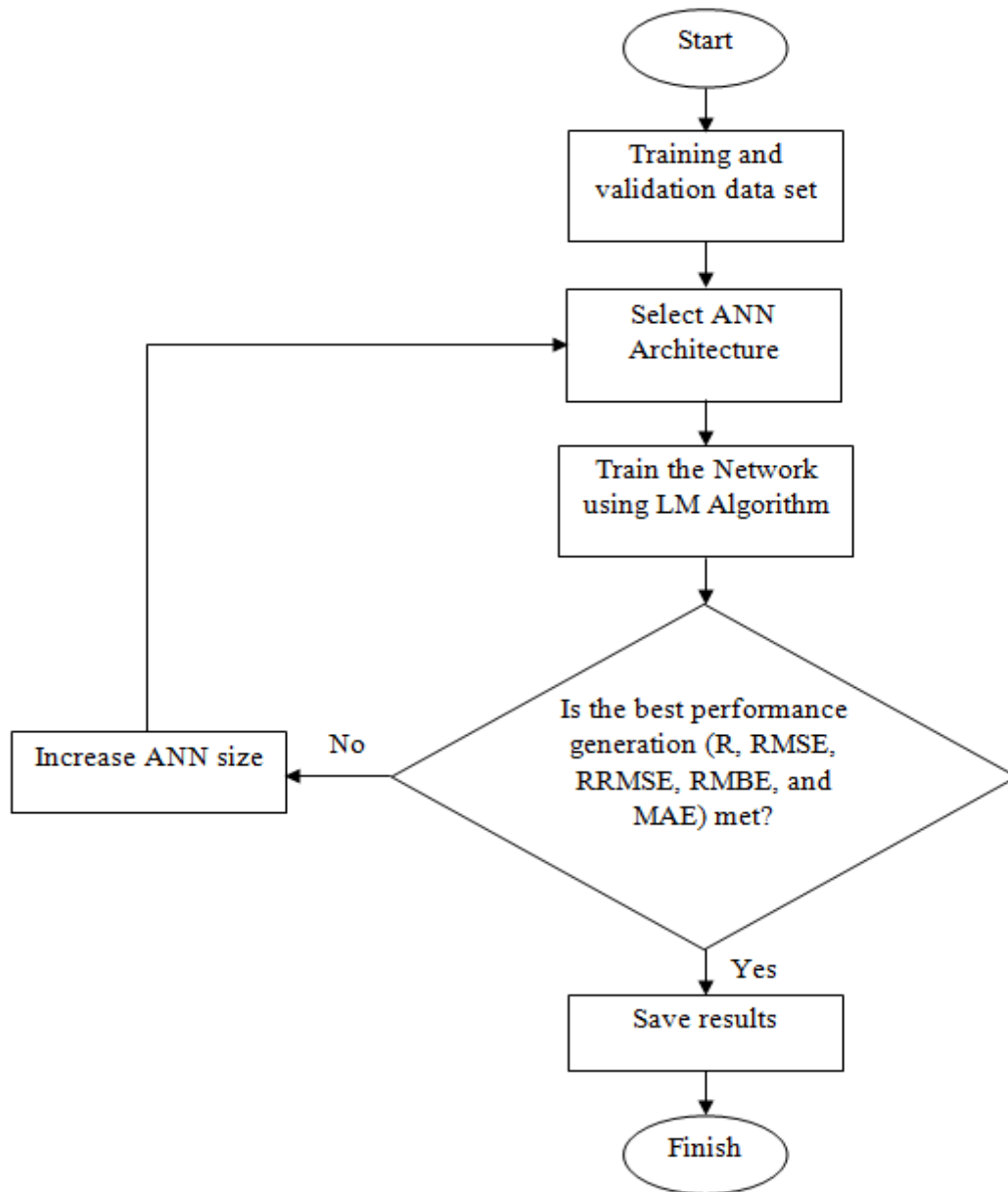
Figure 4.11: Flowchart of the proposed ANN model

4.4 Results and discussion

In the following, the analytical models AMI and AM II are compared to the experimental results. Next, we deal with the ANN model: we investigate several input combinations and the number of hidden neurons to optimize the ANN architecture. Finally, we compare the performances of the three models.

4.4.1 Results of the Analytical models

The AM I and AM II were used to obtain electric energy during 2015 and compared with operating data. For this purpose, the hourly measurements of the DNI, the ambient

temperature, and the wind speed during the year 2015 at the location of the PTSTPP situated in Ain Beni-Mathar, were used as input data.

The performance indicators of the AM I and AM II are presented in table 4.6. The results show that the regression coefficient R, the RRMSE, and the MAE values are 0.8388, 32.45 %, and 3.5 MWh for AM I. These values are 0.8636, 32.15 %, and 3.09 MWh for AM II.

	R	*RMSE(MWh)*	*RRMSE (%)*	*MAE (MWh)*	*RMBE (%)*
AM I	0.8388	5.0349	32.4591	3.4931	-1.88
AM II	0.8636	4.9880	32.1567	3.0865	12.1
ANN model	0.9692	2.3725	15.2949	1.6272	-4.73

Table 4.6: Comparison of validation performance of the analytical models with the ANN model.

The comparison between operating and analytical model results for all the months of the year is presented in figure 4.12. The total operating electric production is 44.7 GWh/year, while the predicted ones are 43.84 GWh/year and 50.08 GWh/year for AM I and AM II. The underestimation of the AM I is about 1.88%. This underestimation is noticed in the RMBE value, which equals -1.88%. AM II overestimates the energy production of about 12.1%. This overestimation can be explained by the fact that the heat losses from piping from and to the solar field were not included by the reference [117].
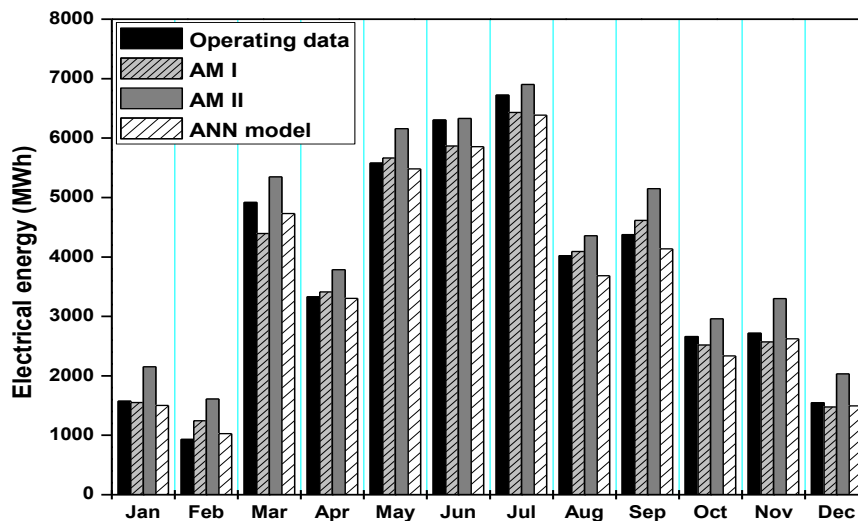
Figure 4.12: Comparison between operating energy production with the predicted by analytical models and ANN model

Let us now discuss the performances of different PTCs mentioned in AM II. This part evaluates the energy produced by different PTCs and compares it with the one used in the ABM power plant. So, we used the same solar field aperture area for all considered PTCs.

According to figure 4.13, it was found that the annual electric energy production is about 41.49 GWh/year, 42.13 GWh/year, 47.41 GWh/year, 47.07 GWh/year, and 50.08 GWh/year, respectively for LS2-CV, LS2-BV, UT-PTR 70, ET150- Solel and ET150-PTR70 (2008). Hence, we can conclude that the PTC of ET150-PTR70 (2008) used in the ABM power plant gives the highest energy production, which can be explained by the fact that its high thermal efficiency characterizes it compared to the other PTCs. The lowest production was provided by the solar field composed of the LS2-CV collectors.
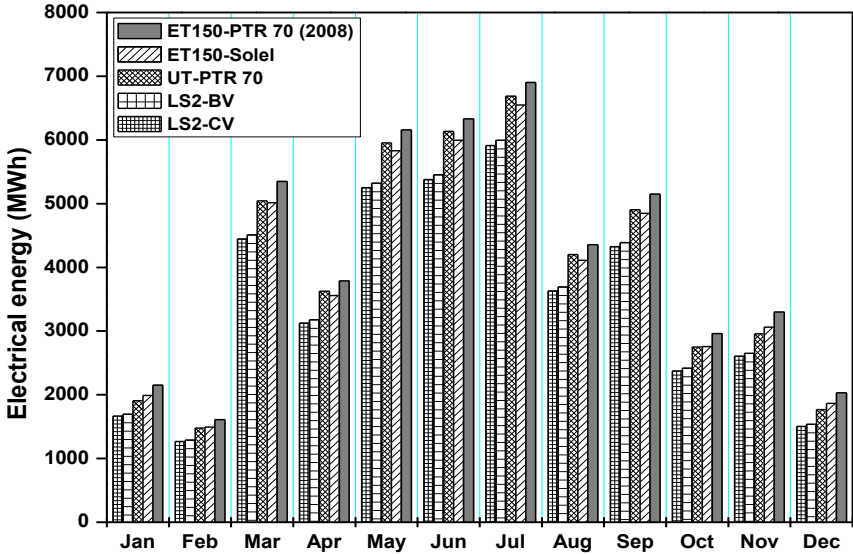
Figure 4.13: Comparison of monthly energy production of different PTCs (AM II)

4.4.2   Results of the ANN model

The first step in developing ANN models consists of selecting its input parameters, namely the decision variables. For this purpose, the ANN model's average performance is calculated by running the ANN simulation model 10 times. These simulations are performed by varying the structure of the set of input variables. The set of input variables is gradually increased by adding new items or changing the selection of items.

As mentioned before, 4 years of in situ measurements are used for the training and the validation of the ANN model. These data are separated into two sets: the training set formed by data from 01 November 2011 to 31 December 2014 and the validation set formed by data of the year 2015. The training set is classically used to compute the parameters and define the structure of the ANN. The validation data set is used to estimate the ANN's ability to interpolate values beyond the scope of its learning phase.

Table 4.7 summarizes the average performance obtained over the set of hourly validation data. From the values of R resulting from the sensitivity analysis, we observe that the first

parameter DNI_h is the most relevant decision variable. We also observe that the values of R, RMSE, RRMSE, RMBE, and MAE are minimized by using the combination of DNI_h, $\tau_{h.y}$, $\tau_{h.d}$, t_h, φ_h, w_h, and E_{h-1}, namely all the decision variables of the problem.

The R-value of 0.9609 is quite high, especially when compared to the R-values obtained by the analytical models, which reach values of 0.84 and 0.86. This value corresponds to an average quadratic error (RMSE) of 2.69 MWh, which can be regarded as very low compared to the 40970 MWh produced during one year by the power plant. Some other combinations of decision variables using fewer decision variables than the best still perform significantly better. These simpler combinations can also be used and remain effective, as they can be calculated more quickly while remaining reasonably accurate.

The choice of the number of hidden neurons is a parameter of great importance in determining the performance of an ANN. Therefore, several numerical experiments were carried out by gradually varying the number of neurons in the hidden layer from 1 to 30 to determine the most performant structure of ANN. The decision variables DNI_h, $\tau_{h.y}$, $\tau_{h.d}$, t_h, φ_h, w_h, and E_{h-1} are inputs in all runs. The number of hidden neurons varies from 1 to 30 by adding a neuron to each new test. For all architectures tested, the average performance of the model in terms of R, RMSE, RRMSE, RMBE, and MAE values are presented in table 4.8 for the training and validation datasets.

Input variables							Performance indicators				
DNI_h	$\tau_{h.y}$	$\tau_{h.d}$	t_h	φ_h	W_h	E_{h-1}	R	RMSE	RRMSE	RMBE	MAE
x							0.715	6.137	41.420	-0.846	5.027
x	x						0.879	4.648	29.966	-9.915	3.710
x	x	x					0.933	3.642	23.482	-9.383	2.841
x	x	x	x				0.934	3.588	23.130	-9.167	2.788
x	x	x	x	x			0.937	3.524	22.720	-9.064	2.766
x	x	x	x	x	x		0.940	3.461	22.312	-8.919	2.698
x	x	x	x	x	x	x	0.961	2.693	17.362	-5.671	1.954
x	x	x				x	0.957	2.845	18.339	-6.112	2.089
x	x	x	x			x	0.958	2.805	18.083	-5.975	2.033
x	x	x	x	x		x	0.958	2.780	17.920	-5.727	1.985
x	x	x		x		x	0.958	2.800	18.048	-5.944	2.021
x	x	x			x	x	0.959	2.776	17.896	-6.094	2.065

Table 4.7: Average performances of ANN model for different combinations of decision variables.

Number of hidden neurons	R	RMSE	RRMSE	RMBE	MAE	Number of hidden neurons	R	RMSE	RRMSE	RMBE	MAE
1	0.913	3.825	24.657	-5.227	2.862	16	0.968	2.422	15.611	-5.086	1.701
2	0.930	3.515	22.661	-6.170	2.630	17	0.969	2.414	15.562	-5.251	1.704
3	0.950	3.042	19.610	-6.137	2.322	18	0.969	2.389	15.399	-4.791	1.670
4	0.959	2.759	17.788	-5.317	2.054	19	0.969	2.387	15.388	-4.769	1.636
5	0.961	2.693	17.362	-5.671	1.954	20	0.969	2.415	15.569	-5.292	1.700
6	0.963	2.598	16.751	-5.300	1.839	21	0.968	2.407	15.519	-4.815	1.707
7	0.965	2.565	16.538	-5.804	1.860	22	0.969	2.373	15.295	-4.735	1.627
8	0.966	2.511	16.186	-5.067	1.762	23	0.968	2.417	15.584	-4.980	1.718
9	0.966	2.512	16.198	-5.331	1.777	24	0.968	2.417	15.582	-4.837	1.675
10	0.967	2.462	15.875	-5.219	1.728	25	0.969	2.402	15.483	-4.884	1.683
11	0.967	2.463	15.878	-5.017	1.731	26	0.968	2.443	15.748	-5.108	1.727
12	0.968	2.440	15.730	-5.339	1.726	27	0.968	2.415	15.569	-4.868	1.699
13	0.968	2.421	15.607	-5.059	1.700	28	0.968	2.411	15.545	-4.789	1.672
14	0.969	2.409	15.528	-5.148	1.695	29	0.968	2.433	15.684	-4.979	1.743
15	0.969	2.387	15.387	-4.744	1.659	30	0.968	2.429	15.661	-4.867	1.700

Table 4.8: Average performances of ANN models for different number of hidden neurons for the validation dataset.

We can notice that the best R, RMSE, RRMSE, RMBE, and MAE values are obtained for 22 hidden neurons. The combination of DNI_h, $\tau_{h.y}$, $\tau_{h.d}$, t_h, φ_h, w_h, and E_{h-1} with 22 hidden neurons is regarded as the best ANN model for estimating the energy production of a PTSTPP on an hourly scale. Table 4.9 presents the statistical parameters obtained from the training and validation data sets by considering the best ANN model obtained with the complete set of decision variables and 22 hidden neurons. The accuracy for the training dataset is higher than for the validation dataset since the ANN model has been parameterized from the first dataset.

	R	RMSE	RRMSE	MAE
Training dataset (ANN)	0.9703	2.1593	14.6308	1.3645
Validation dataset (ANN)	0.9692	2.3725	15.2949	1.6272

Table 4.9: Training and validation performances of the ANN model

Figure 4.14 shows the comparison between the energy production obtained from in situ measurements and ANN predictions for training and validation datasets.
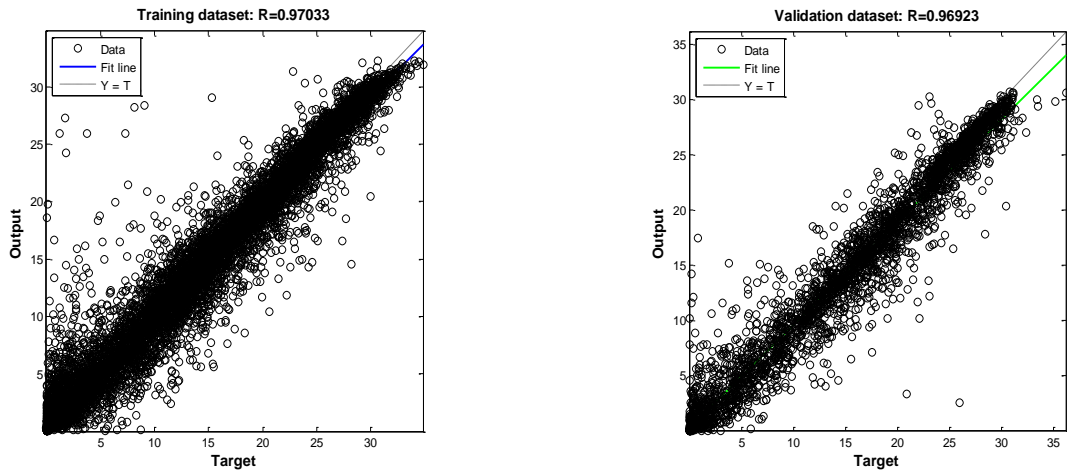
Figure 4.14: In situ measurements and ANN predictions for training and validation datasets.

The monthly distribution of operating and ANN predicted energy production is shown in figure 4.12. The electrical energy production is 44.7 GWh/year, while that predicted by the ANN model is 42.6 GWh/year. Therefore, the ANN underestimates energy production by a factor of 5%, which corresponds to the RMBE value.

4.4.3 Comparison between analytical models and ANN model

In this part, a comparison between analytical models and ANN model is presented. This comparison allows for evaluating the performance and capability of each model. Table 4.6 presents the performances obtained for validation datasets for ANN and analytical models. The values of the comparison tools prove that the ANN model is more performant and constitute a good model for estimating the electric energy production of a PTSTPP. The value of regression was about 0.97 for the ANN model, while for the AM I and AM II, the values were respectively 0.8388 and 0.8636.

Figure 4.15 shows the frequency distributions of the difference between operating and predicted values of PTSTPP energy production for the ANN and analytical models for the validation year. This frequency distribution shows that approximately 86.77% of the power generation deviations are less than 3 MWh for the ANN model. This value is 61.84 % for the AM I and 74.96 % for the AM II.
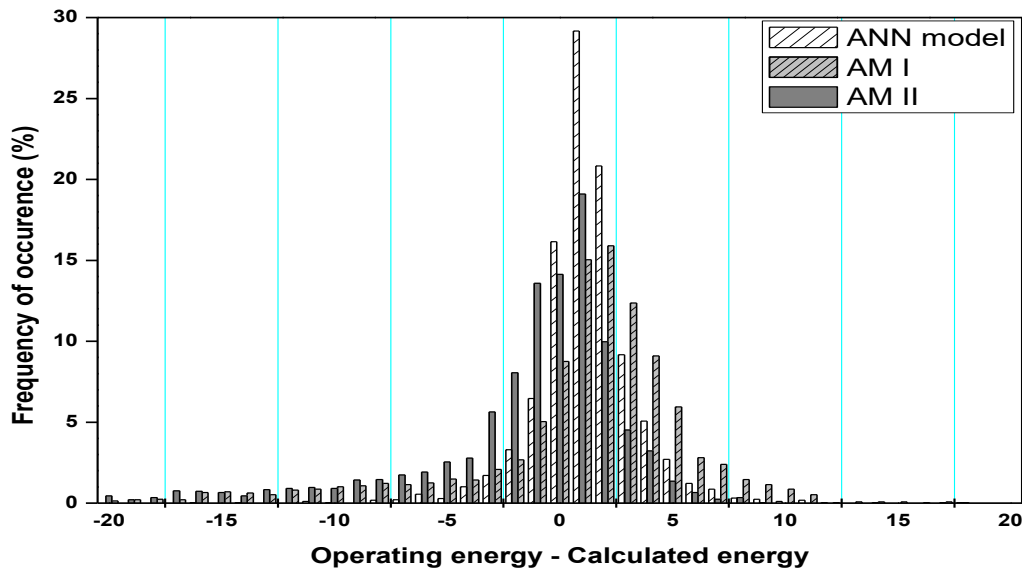
Figure 4.15: Frequency distributions of the differences between measured and predicted energy production for the validation dataset

Figure 4.12 illustrates the energy production obtained by the ANN model and the analytical ones and their comparison with the operating energy for different months of the year. It was found that the ANN model underestimates the annual energy production by 4.73% while AM I by 1.88%. The AM II overestimates the energy production by 12.1 %.

To obtain a more detailed comparison between the ANN and Analytical models and observe the performance variation of the power plant, the daily performance of the PTSTPP was highlighted. Four typical days of the year that characterize each season were chosen to compare the performance of the ANN and analytical models in predicting the energy production of the PTSTPP. The selected typical days are: January 04th, April 06th, August 16th, and October 05th.

The results obtained in figure 4.16 & table 4.10 present the energy obtained for typical days by using ANN and analytical models and their corresponding performances. The AM I and ANN model underestimate the energy production for every typical day considered in the figure. Whereas the AM II overestimates the energy production for all typical days. The trends and variations of the operating energy productions are very close to those predicted by the ANN model. Analytical models present lower precision in the estimations than the ANN model, but it can provide a good prognosis of electric energy production. The only situations in which the predictions with the analytical methods are less accurate correspond to the low values of the produced electric energy that are normally associated with low values of DNI (especially in the morning). However, abrupt variations in energy production are difficult to

114

model, whatever the type of model is considered. Nevertheless, the ANN model is more efficient on this point than the analytical model, especially at the beginning of each start-up period.
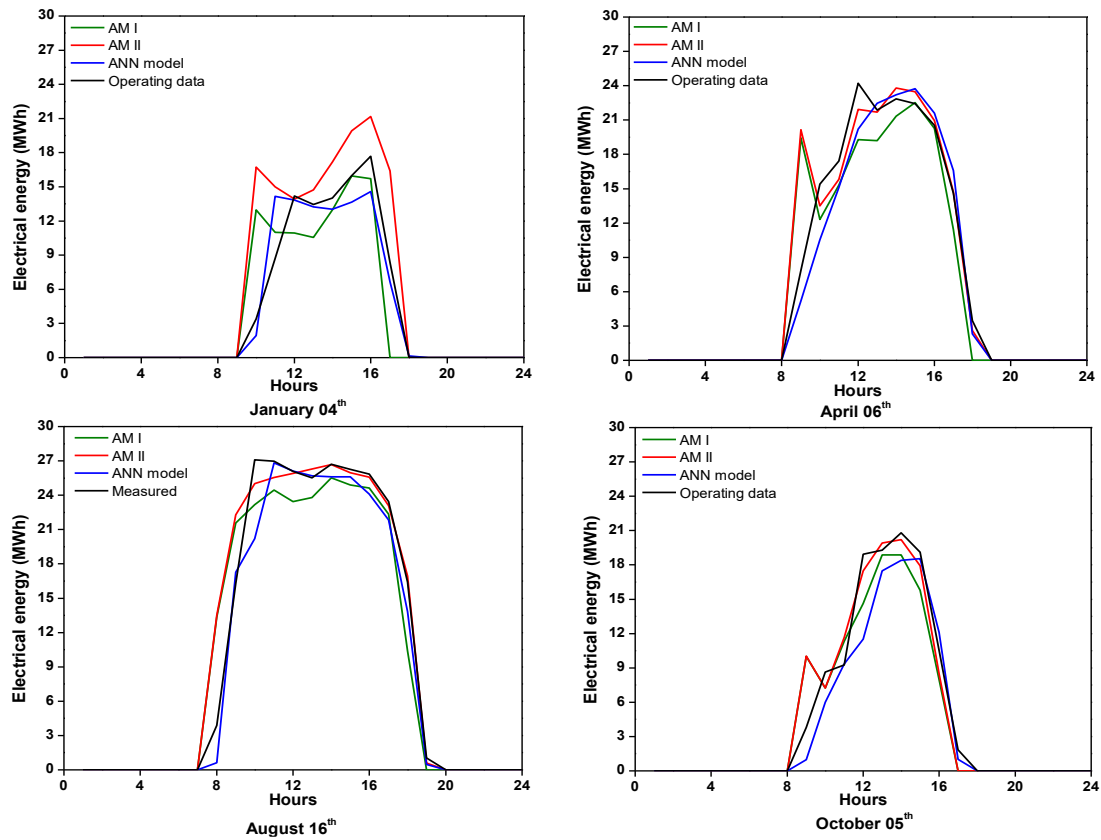
Figure 4.16: Hourly experimental and predicted energy (validation dataset) for the four different typical days.

Typical day \ Performances	January 4th			April 6th			August 16th			October 5th		
	AM I	AM II	ANN model	AM I	AM II	ANN model	AM I	AM II	ANN model	AM I	AM II	ANN model
R	0,67	0,74	0,91	0,77	0,80	0,95	0,90	0,94	0,98	0,90	0,93	0,94
RMSE (MWh)	4,60	5,98	0,76	4,52	4,06	2,47	4,01	3,37	1,25	3,12	2,54	3,03
RRMSE (%)	43,23	56,13	22,36	26,47	23,82	14,46	19,59	16,48	12,07	25,03	20,40	24,27
MAE (MWh)	3,27	4,43	1,74	3,29	2,16	2,03	3,12	1,83	1,64	2,67	1,97	2,24
RMBE (%)	-5,93	40,97	-4,78	-5,60	4,68	-5,65	-3,24	4,85	-7,05	-6,64	0,68	-14,98
Total energy (MWh)	90,14	135,9	91,24	161,0	178,6	160,9	237,5	257,4	228,2	104,7	112,9	95,40

Table 4.10: Performances obtained for typical days by using ANN and analytical models.

4.5 Conclusion

Analytical and ANN models are knowledge and data-based models that have different advantages and disadvantages. Analytical models are slow but explanatory, while ANN models are quickly computable but only predictive. Analytical models are well suited to design since they can anticipate structural changes in the simulated system. An ANN model cannot anticipate phenomena that are beyond the scope of the data that contributed to its development. On the other hand, ANN models are well suited for controlling physical systems that require fast reactions to changing situations.

In this chapter, both types of models have been investigated in the particular context of a parabolic trough solar thermal power plant. The models aim to predict the electric energy production at the output of the electric generator and, more especially, the hourly energy production of the power plant. Several ANN models are presented that vary the number and types of input variables and the number of neurons in the hidden layer; the best ANN model obtained is very accurate in evaluating energy production since it leads to an R-value (coefficient of determination) of 96%. Since Morocco is planning to implement further solar power plants with parabolic trough technology. The suggested ANN model could be used to estimate energy production of similar PTSTPP design as in ABM for other locations in Morocco.

The analytical models proposed in this paper lead to similar but lower accuracy levels than the ANN model. Compared to the experimental data, their characteristic R-value (coefficient of determination) is about 84% for AM I and 86% for AM II. From the observation of the power plant's energy production and its dynamic behavior, it can be seen that the analytical models do not correspond to most of the sudden changes in energy production. This lack of precision can be explained by the fact that our analytical models are mainly based on the modeling of steady-state phenomena. An important perspective of this work is developing a dynamic model that considers the thermal inertia phenomena that influence the dynamic behavior of thermal power plants.

Chapter 5: Estimation of Daily Energy Production of a Solar Power Plant Using Artificial Intelligence Techniques

This chapter presents a comparative study between artificial neural networks (ANNs) and an adaptive neuro-fuzzy inference system (ANFIS) to estimate the daily electric energy production of a parabolic trough solar thermal power plant (PTSTPP) in Eastern Morocco. For this purpose, data from 1 November 2011 until 31 December 2015 were used to train and validate the ANN and ANFIS models. The inputs of the models are daily direct normal irradiation (DNI), day of the month, daily average ambient temperature, daily average wind velocity, daily average relative humidity, and previous daily electric production. To select the best architecture, several models were developed. For the ANN model, the number of hidden neurons was varied, while the number of radius was varied for the ANFIS model.

5.1 Introduction

The concentrated solar power (CSP) plant has gained large importance due to its good environmental aspect. However, the exploitation of solar energy raises some technical challenges. Like wind energy, it is intermittent and random energy: its availability varies greatly without the possibility of control. The integration of such sources on the electricity grid generates problems for maintaining the balance between consumption and production [127].

Two main avenues are used to overcome this limitation. The first one is storage: the storage of energy would stabilize electricity production by storing thermal power during periods of high production to restore it during production falls [128]. However, storing large amounts of energy remains a challenge at the moment, especially in terms of cost and technology. The second tool is forecasting: forecasting the production of intermittent energies would make it possible to anticipate the availability of generation sources and thus facilitate the management of the grid. In the last two decades, artificial intelligence had been used widely to forecast energy production. Many studies with artificial neural networks and fuzzy logic, genetic algorithm, or the combination of two techniques show their powerful ability to predict energy production with suitable accuracy.

In [129], the authors use a MLP neural network with two inputs, temperature, and irradiance, to predict the power produced by a PV installation. An ANFIS with an echo state network (ESN) for short term PV power prediction was developed and compared in [130]. The artificial intelligence techniques capability such as feed-forward and Elman neural network for forecasting the energy production of a photovoltaic resource was explored in [131]. For solar thermal energy systems (STES), W. Yaïci and E. Entchev [123], [132] predict the performance parameters of a STES under different weather conditions in Canada by applying ANN and ANFIS models. Many other works using ANN and ANFIS models to predict the energy generation from different nature like solar, wind, hydraulic system can be found in [126], [133], [134].

The present chapter focuses on predicting a solar power plant's daily electric production in Ain Beni-Mathar by using ANN and ANFIS models. Data from 1 November 2011 until 31 December 2015 were used to train and validate the models. The data are presented as a time series, and forecasting time series data is an integral component for management, planning, and decision-making. Comparisons were made between the two techniques in order to define their prediction accuracy.

5.2   Data normalization

In this study, direct normal irradiation, ambient temperature, relative humidity, and wind speed values, collected at Ain Beni-Mathar station located in Eastern Morocco, were used to predict electric energy using ANN and ANFIS models. To enhance the network prediction processing, the data were normalized between 0 and 1 according to the following equation [134] .

$$X_i = \frac{X_{ki} - \min(X_k)}{\max(X_k) - \min(X_k)} \tag{5.1}$$

where X_i is the ith normalized value, and X_{ki} is the ith input of the vector $X_k = (X_{k1}, \ldots, X_{kn})$ that we will normalize.

5.3   Application of Artificial Neural Networks and Adaptive Neuro-Fuzzy Inference system

5.3.1   Artificial neural networks:

(See chapter 4, section 4.3.3).

5.3.2 Adaptative neuro-fuzzy inference system

Adaptive neuro-fuzzy inference system (ANFIS) is a combination of artificial intelligence methods that allows the application of ANN and fuzzy logic together [135]. The advantage of this method is that it uses the benefit of both methods. It is capable of solving nonlinear and complex problems. ANFIS architecture is an adaptive network that uses supervised learning, which has a function similar to the model of Takagi–Sugeno fuzzy inference system and has a five-layered architecture (figure 5.1).

Analyzing the mapping relation between the input and output data, ANFIS can establish the optimal distribution of membership functions using either a back propagation gradient descent algorithm alone or in combination with a least-squares method.
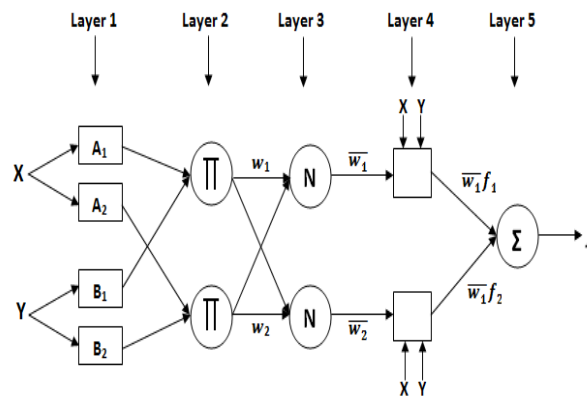
Figure 5.1: Adaptive neuro-fuzzy inference system structure.

5.3.3 Selection of the best model

To compare and test the constructed models and select the best one, the models performance were evaluated using regular comparison tools in modeling involving the coefficient of determination (R), root mean square error (RMSE), and mean absolute error (MAE). (See chapter 4).

5.4 Results and discussion

Our study aims to use and compare ANN and ANFIS models to predict the daily electric energy generation of a PTSTPP. The input variables are daily direct normal irradiation (DNI), day of the month (D_m), daily average ambient temperature (T_a), daily average relative humidity (H_r), daily average wind speed (W_s) and daily previous production (E_{t-1}), while the daily electric energy production is the output variable. To train and validate the models, the MATLAB platform was used.

The data set used in this study covers a period of more than 4 years between 01 November 2011 and 31 December 2015. The data between 01 November 2011 and 31 December 2014 were used for the training phase, and the data of the year 2015 were used for the validation procedure.

For the ANN model, the network was trained and validated using a Levenberg-Marquardt back propagation algorithm (table 5.1). We choose this algorithm because it was performed the best in the predicting procedure. The number of neurons in the hidden layer was varied from 1 to 10.

For the ANFIS model, to find the smallest architecture representing the relationship between the inputs and the output, we select the Subtractive Clustering as the FIS generation method. Various numbers of radius between 0.5 and 1 have been tested in the current study to see who performed the best in terms of R, RMSE, and MAE. Of course, the variables [DNI D_m T_a H_r W_s E_{t-1}] have been taken as inputs in all runs. More information and details about the ANFIS model are given in table 5.2.

ANN info	Parameters
Number of hidden layers	1
Number of epochs	1000
Training algorithm of network	Back propagation
Type of activation functions	Logsig, Tansig

Table 5.1: Parameters of the ANN model

ANFIS info	Characteristics
Fuzzy structure	Sugeno-type
Initial FIS for training	Genfis2
Epoch	50
Output membership function	Linear
Training algorithm	Hybrid

Table 5.2: Parameters of the AFIS model

Table 5.3 shows for each tested architecture, the average performances in term of R, RMSE, and MAE for 10 runs. It is found that the architecture that yielded the best generalization results is the architecture with 4 hidden neurons. Table 5.4 shows for each tested ANFIS architecture, the average performances in terms of R, RMSE, and MAE for different numbers of the radius. It is noticed that the best architecture for the validation phase is obtained with

radius = 0.9. According to the obtained result, it is clear that both ANN and ANFIS models give the same accuracy for the training and validation phase, with a negligible difference. For both models, the value of regression is around 0.94, RMSE and MAE are about 0.09 and 0.066 respectively.

Number of hidden neurons	Training phase			Validation phase		
	R	RMSE	MAE	R	RMSE	MAE
1	0,9224	0,0868	0,0634	0,9203	0,0972	0,0716
2	0,9330	0,0809	0,0600	0,9304	0,0943	0,0697
3	0,9396	0,0769	0,0570	0,9386	0,0925	0,0701
4	**0,9451**	**0,0735**	**0,0539**	**0,9408**	**0,0899**	**0,0662**
5	0,9465	0,0725	0,0531	0,9362	0,0906	0,0684
6	0,9494	0,0706	0,0509	0,9389	0,0896	0,0654
7	0,9503	0,0699	0,0508	0,9369	0,0907	0,0661
8	0,9516	0,0691	0,0501	0,9335	0,0912	0,0658
9	0,9536	0,0676	0,0490	0,9380	0,0901	0,066
10	0,9554	0,0663	0,0484	0,9330	0,0925	0,0685

Table 5.3: Average performances obtained for different numbers of hidden neurons.

Number of Radius	Training phase			Validation phase		
	R	RMSE	MAE	R	RMSE	MAE
0,50	0,9672	0,0571	0,0415	0,9099	0,1028	0,0759
0,55	0,9650	0,0590	0,0431	0,9139	0,0975	0,0717
0,60	0,9619	0,0615	0,0443	0,9218	0,0974	0,0721
0,65	0,9553	0,0664	0,0480	0,9213	0,0984	0,0741
0,70	0,9534	0,0678	0,0484	0,9355	0,0912	0,0686
0,75	0,9531	0,0680	0,0488	0,9361	0,0916	0,0685
0,80	0,9519	0,0688	0,0497	0,9299	0,0963	0,0703
0,85	0,9483	0,0713	0,0513	0,9375	0,0895	0,0668
0,90	**0,9481**	**0,0714**	**0,0514**	**0,9377**	**0,0893**	**0,0664**
0,95	0,9427	0,0749	0,0551	0,9373	0,0903	0,0670
1.00	0,9426	0,0750	0,0553	0,9368	0,0907	0,0677

Table 5.4: Average performances obtained for different numbers of radius

In this part, the results obtained from PTSTPP electric energy production using ANN and ANFIS models will be compared. Figure 5.2 and figure 5.3 show a comparison of the energy production between the measured ANN and ANFIS models, respectively, for the training and validation phases. It is observed from both figures that the energy production curves follow the same trends with a minor difference, which means that both ANN and ANFIS models can predict the energy production.
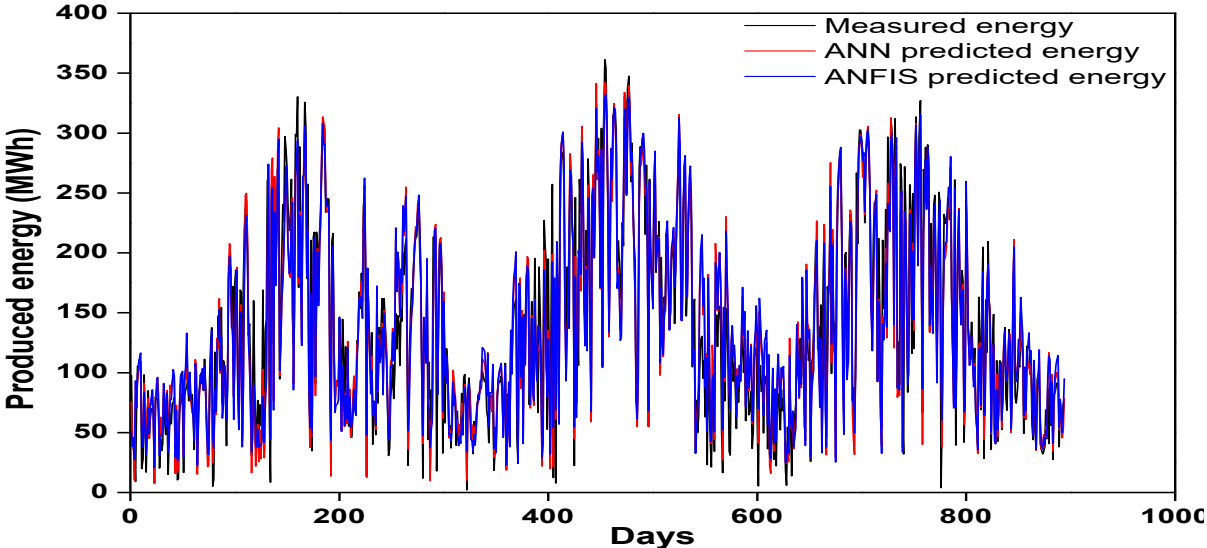
Figure 5.2: Comparison between measured, ANN, and ANFIS predicted energy production for the training set.
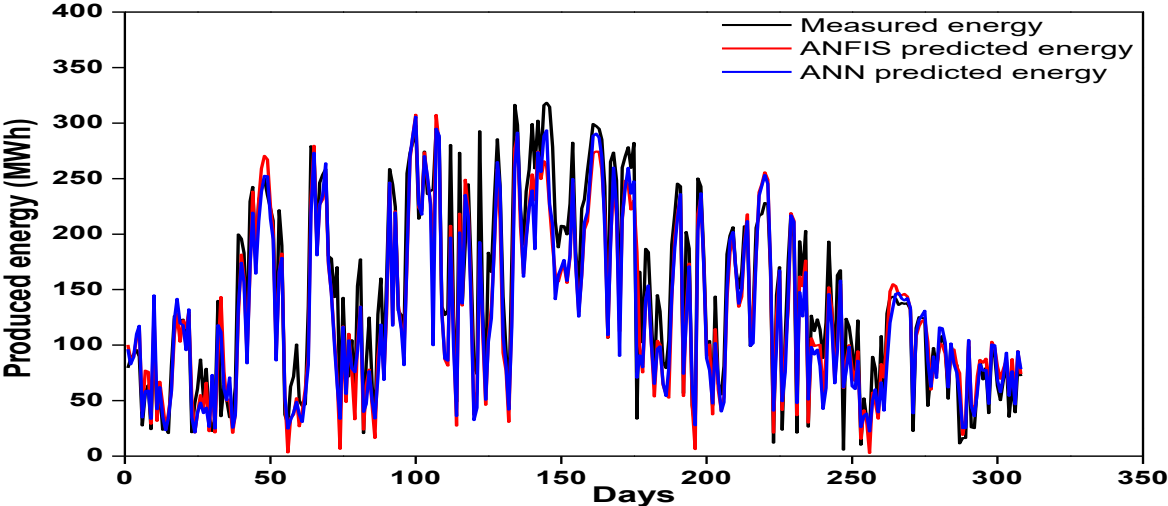
Figure 5.3: Comparison between measured, ANN, and ANFIS predicted energy production for the validation set

To have a good observation of the energy production curves, a zoom on figures 2 and 3 was applied. A continuous 10 days were considered from different years of the study. For the

122

training phase, the years are: 2012 (figure 5.4 (a)), 2013 (figure 5.4 (b)), and 2014 (figure 5.4 (c)). The year 2015 (figure 5.4 (d)) was considered for the validation phase. We associated the absolute values of prediction errors for training and validation days. It is well noticed that both ANN and ANFIS models provide curves that perfectly follow the shape of real ones, despite amplitude default in some points, thus, demonstrate the capability of the proposed models to predict the electric energy production of PTSTPP.

(a): 2012

(b): 2013

(c): 2014

(d): 2015
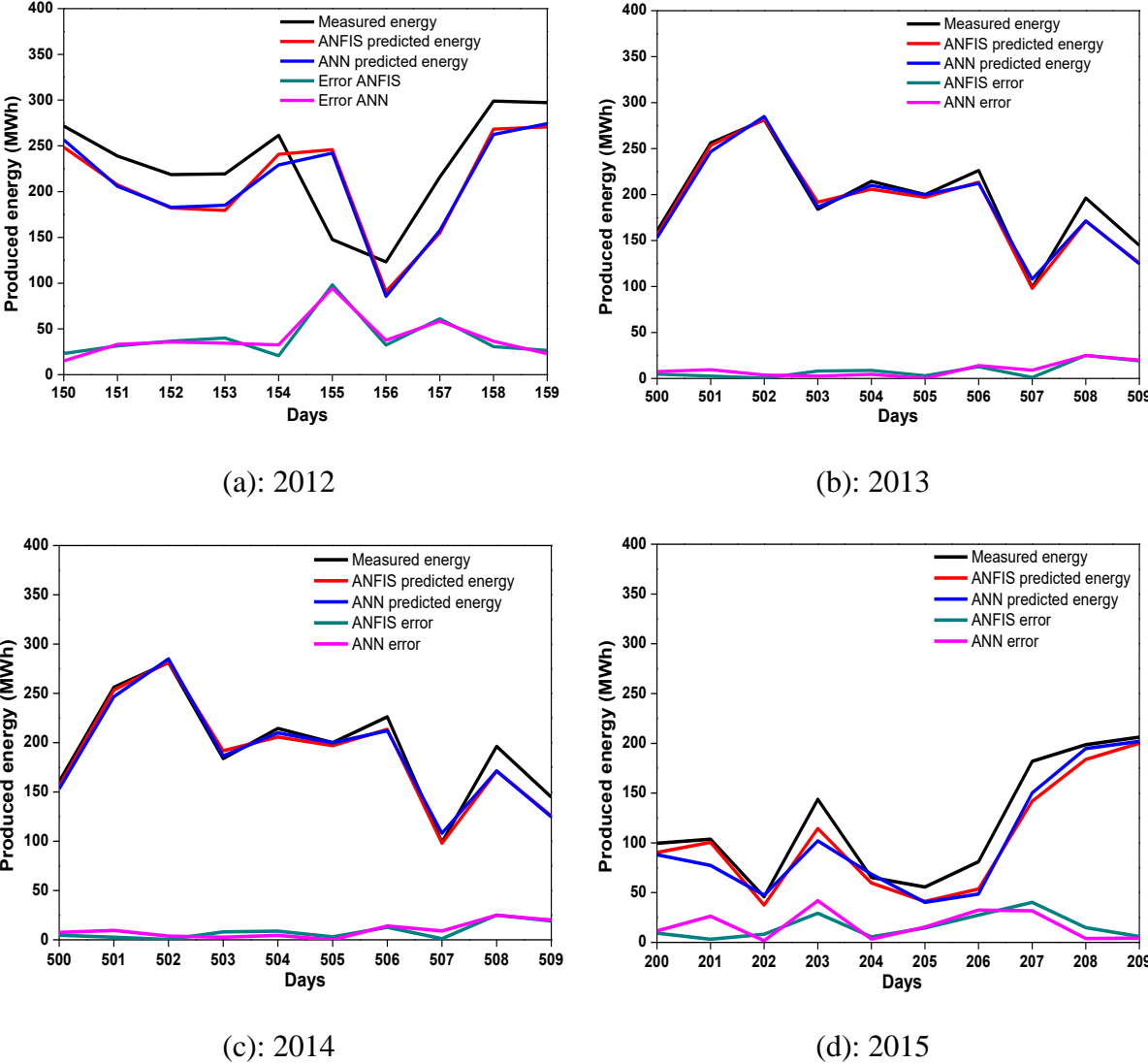
Figure 5.4: Zoom on measured and predicted energy

A comparison between monthly ANN, ANFIS predicted, and measured electric energy production for the solar plant is presented in figure 5.5. The total yearly ANN and ANFIS predicted energy productions are, respectively, 39341 MWh/year and 39907 MWh/year for the validation year (2015). The operating production is about 44138 MWh/year. The

predicted energy production underestimated with approximately 10.86% by the ANN model and about 9.58% by the ANFIS model.

The monthly errors between ANN, ANFIS predicted, and measured values of the solar power plant's electric energy are presented in figure 5.6. For the ANN model, the highest absolute error value of about 21.3% was noticed in October, and the lowest value of about 1.2% was noticed in November. For the ANFIS model, the highest absolute error value of about 22% was noticed in April, and the lowest value of about 1.7% was noticed in February.
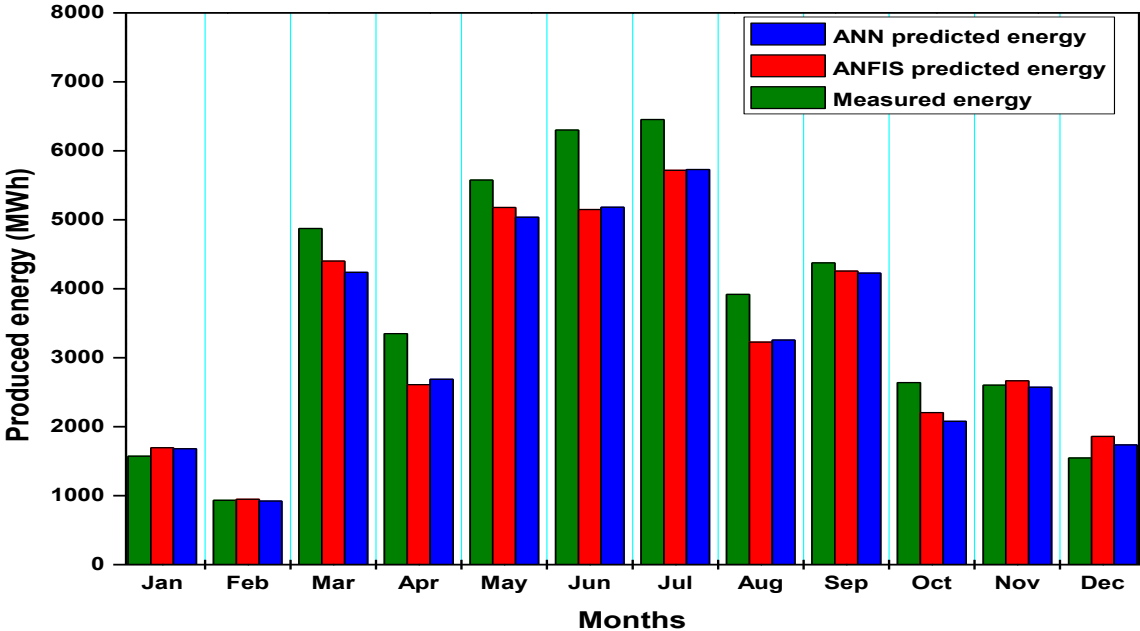
Figure 5.5: Comparison between ANN, ANFIS predicted, and measured energy production for the validation year.
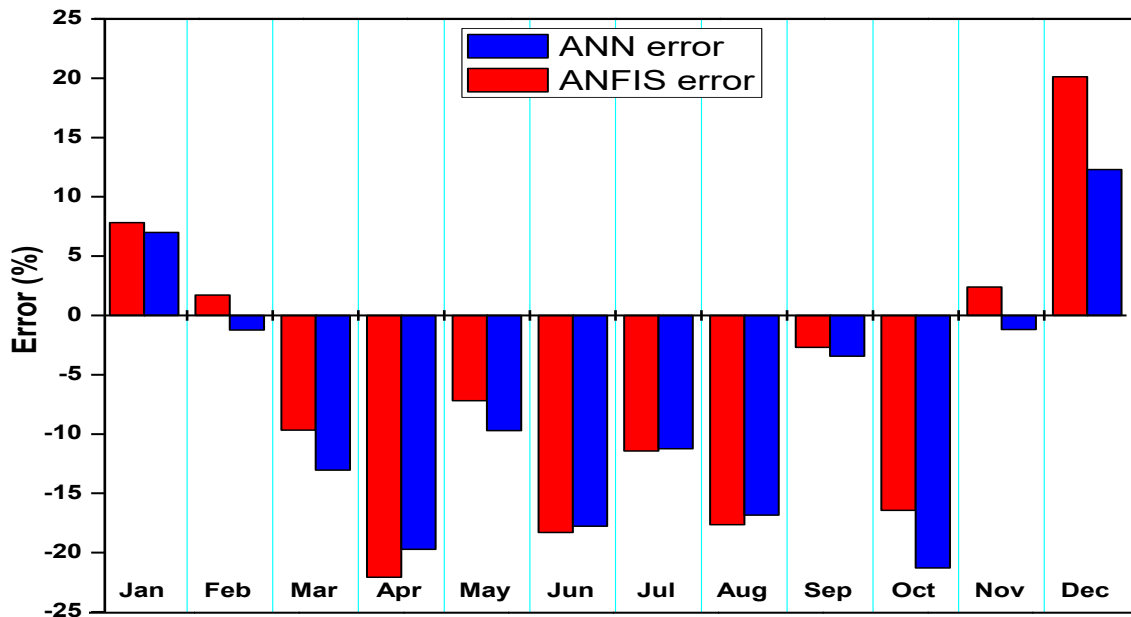
Figure 5.6: Monthly error for the validation year.

5.5 Conclusion

In this chapter, the daily electric energy production of a PTSTPP has been estimated using ANN and ANFIS methods. The ANN and ANFIS models were developed considering six input variables (daily DNI, daily average ambient temperature, time in the day of the month, daily average relative humidity, daily average wind speed, and daily previous energy production) and one output data. The ANN and ANFIS models' estimated values were found to be close to the real ones, with values of regression about R = 0.94 for the validation phase. ANFIS underestimated the yearly energy production by 9.58%, with monthly absolute errors in the range of 1.7% to 22%. ANN underestimated the yearly energy production by 10.86%, with monthly absolute errors ranging from 1.2 to 21.3%. Based on the obtained results, it can be concluded that ANN and ANFIS models can successfully estimate daily PTSTPP energy production.

Conclusions and outlooks

The concentrated solar power plant with parabolic trough concentrators is an attractive technology for generating electricity from solar thermal energy. Therefore, the main objective of this thesis is to simulate the performance of a parabolic trough solar concentrator integrated into a solar thermal power plant under Moroccan ambient conditions. At first, an overview of the integrated solar combined cycle (ISCC) power plant of Ain Béni Mathar (ABM) was presented. Interest was given to the solar part to evaluate its impact on the power plant's overall performance. Indeed, existing similar worldwide power plants with parabolic trough technology are reviewed and compared. The power plant's annual production was about 3293 GWh, with 44.8 GWh from the solar part.

The second part aims to assess the thermal performances of the ISCC power plant's solar field at ABM. Thus, mathematical modeling of the Schott PTR-70 2008 solar receiver consists of energy balance equations that were solved using COMSOL Multiphysics software. Next, the model was validated with empirical data from the literature, so the comparison is satisfactory. Results analyze the plant's daily and annual thermal performances and compare simulated and actual plant operating results. The third part presents a comparison between analytical and artificial neural networks (ANN) models. The models aim to predict the electric energy production of a parabolic trough solar power plant at the electric generator's output and, more especially, the hourly energy production of the power plant. Several ANN models are presented that vary the number and types of input variables and the number of neurons in the hidden layer. The best ANN model obtained is very accurate in evaluating energy production since it leads to an R-value (coefficient of determination) of 96%. Two analytical models are proposed and investigated. Both lead to similar but lower levels of accuracy than the ANN model. Compared to the experimental data, their characteristic R-value is about 84% for AM I and 86% for AM II.

In the last part, two artificial intelligence models are investigated artificial neural networks (ANN) and adaptive neuro-fuzzy inference system (ANFIS) to estimate the daily electric energy generation of a solar power plant in Ain Beni-Mathar. Six input variables (daily direct normal irradiation, day of the month, daily average ambient temperature, daily average wind velocity, daily average relative humidity, and previous daily electric production) served as the inputs of the ANN and ANFIS models. The results showed that both the ANN and ANFIS models performed similarly in terms of prediction accuracy.

This work concludes that analytical and artificial intelligence models are knowledge and data-based models with different advantages and disadvantages. Analytical models are slow but explanatory, while artificial intelligence models are quickly computable but only predictive. Analytical models are well suited to design since they can anticipate structural changes in the simulated system. An artificial intelligence model cannot anticipate phenomena beyond the scope of the data that contributed to its development. On the other hand, artificial intelligence models are well suited for controlling physical systems that require fast reactions to changing situations.

The following outlooks should be considered for further research in this area:

- To conduct a 4E (Energy-Exergy-Environmental-Economic) study of the integrated solar combined cycle power plant of Ain Béni Mathar.
- To investigate thermal energy storage integration into ISCC power plant.
- Future research should address model hybridization to predict performances of the solar power plant, i.e., models combining machine learning and physical modeling. Dynamic analytical models are generally difficult to develop and solve, whereas modeling and simulation of dynamic phenomena with artificial neural networks is much easier and more efficient.
- Data of solar radiation could be used to validate models that predict global and diffuse solar radiation for Ain Béni Mathar. It is also recommended to compare and generate these data with modern methods such as artificial neural networks.

References

[1]   K. M. Powell, K. Rashid, K. Ellingwood, J. Tuttle, and B. D. Iverson, "Hybrid concentrated solar thermal power systems: A review," *Renewable and Sustainable Energy Reviews*, vol. 80. pp. 215–237, 2017, doi: 10.1016/j.rser.2017.05.067.

[2]   F. Zaversky, R. Medina, J. García-Barberena, M. Sánchez, and D. Astrain, "Object-oriented modeling for the transient performance simulation of parabolic trough collectors using molten salt as heat transfer fluid," *Sol. Energy*, vol. 95, pp. 192–215, 2013, doi: 10.1016/j.solener.2013.05.015.

[3]   F. Cavallaro, "Fuzzy TOPSIS approach for assessing thermal-energy storage in concentrated solar power (CSP) systems," *Appl. Energy*, vol. 87, no. 2, pp. 496–503, 2010, doi: 10.1016/j.apenergy.2009.07.009.

[4]   N. Belyakov, *Sustainable power generation: Current status, future challenges, and perspectives*. 2019.

[5]   K. Lovegrove and W. S. Csiro, "Introduction to concentrating solar power (CSP) technology," in *Concentrating Solar Power Technology*, 2012, pp. 3–15.

[6]   C. S. Turchi, J. Stekli, and P. C. Bueno, "Concentrating solar power," in *Fundamentals and Applications of Supercritical Carbon Dioxide (SCO2) Based Power Cycles*, 2017, pp. 269–292.

[7]   R. Pitz-Paal, "Concentrating solar power," in *Future Energy: Improved, Sustainable and Clean Options for Our Planet*, 2020, pp. 413–430.

[8]   G. Zhu, T. Wendelin, M. J. Wagner, and C. Kutscher, "History, current state, and future of linear Fresnel concentrating solar collectors," *Sol. Energy*, vol. 103, pp. 639–652, 2014, doi: 10.1016/j.solener.2013.05.021.

[9]   J. I. Ortega, J. I. Burgaleta, and F. M. Tellez, "Central receiver system solar power plant using molten salt as heat transfer fluid," *J. Sol. Energy Eng. Trans. ASME*, vol. 130, no. 2, pp. 0245011–0245016, 2008, doi: 10.1115/1.2807210.

[10]   A. Poullikkas, G. Kourtis, and I. Hadjipaschalis, "Parametric analysis for the installation of solar dish technologies in Mediterranean regions," *Renewable and Sustainable Energy Reviews*, vol. 14, no. 9. 2010, doi: 10.1016/j.rser.2010.07.021.

[11]   J. I. Burgaleta, S. Arias, and D. Ramirez, "Gemasolar, the first tower thermosolar commercial plant with molten salt storage," *Solarpaces*, pp. 1–8, 2011.

[12]   U. Srivastva, R. K. Malhotra, and S. C. Kaushik, "Review of heat transport properties of solar heat transfer fluids," *Journal of Thermal Analysis and Calorimetry*, vol. 130, no. 2. pp. 605–621, 2017, doi: 10.1007/s10973-017-6441-y.

[13]   K. Vignarooban, X. Xu, A. Arvay, K. Hsu, and A. M. Kannan, "Heat transfer fluids for concentrating solar power systems - A review," *Applied Energy*, vol. 146. pp. 383–396, 2015, doi: 10.1016/j.apenergy.2015.01.125.

[14] G. Flamant *et al.*, "Dense suspension of solid particles as a new heat transfer fluid for concentrated solar thermal plants: On-sun proof of concept," *Chem. Eng. Sci.*, vol. 102, pp. 567–576, 2013, doi: 10.1016/j.ces.2013.08.051.

[15] A. E. Bergles, "ExHFT for fourth generation heat transfer technology," *Exp. Therm. Fluid Sci.*, vol. 26, no. 2–4, pp. 335–344, 2002, doi: 10.1016/S0894-1777(02)00145-0.

[16] O. Behar, A. Khellaf, and K. Mohammedi, "A review of studies on central receiver solar thermal power plants," *Renewable and Sustainable Energy Reviews*, vol. 23. pp. 12–39, 2013, doi: 10.1016/j.rser.2013.02.017.

[17] M. Thirugnanasambandam, S. Iniyan, and R. Goic, "A review of solar thermal technologies," *Renewable and Sustainable Energy Reviews*, vol. 14, no. 1. pp. 312–322, 2010, doi: 10.1016/j.rser.2009.07.014.

[18] A. Evans, V. Strezov, and T. J. Evans, "Assessment of utility energy storage options for increased renewable energy penetration," *Renewable and Sustainable Energy Reviews*, vol. 16, no. 6. pp. 4141–4147, 2012, doi: 10.1016/j.rser.2012.03.048.

[19] "Solar Irradiance data | Solargis." https://solargis.com/ (accessed Mar. 30, 2021).

[20] NREL, "Borges Termosolar | Concentrating Solar Power Projects," *SOLARPACES*, 2013. https://solarpaces.nrel.gov/borges-termosolar.

[21] J. H. M. Neto, M. A. Pessoa, E. B. Borges, and F. R. S. Lima, "Experimental test of the parabolic trough solar collectors of the first demonstration testing facility of Brazil using the QDT model," *Appl. Therm. Eng.*, vol. 163, 2019, doi: 10.1016/j.applthermaleng.2019.114405.

[22] M. J. Montes, A. Abánades, J. M. Martínez-Val, and M. Valdés, "Solar multiple optimization for a solar-only thermal power plant, using oil as heat transfer fluid in the parabolic trough collectors," *Sol. Energy*, vol. 83, no. 12, pp. 2165–2176, 2009, doi: 10.1016/j.solener.2009.08.010.

[23] M. M. Rolim, N. Fraidenraich, and C. Tiba, "Analytic modeling of a solar power plant with parabolic linear collectors," *Sol. Energy*, vol. 83, no. 1, pp. 126–133, 2009, doi: 10.1016/j.solener.2008.07.018.

[24] M. Abutayeh, Y. D. Goswami, and E. K. Stefanakos, "Solar Thermal Power Plant Simulation," vol. 32, no. 2, pp. 417–424, 2013, doi: 10.1002/ep.

[25] A. M. Patnode, "Simulation and Performance Evaluation of Parabolic Trough Solar Power Plants," University of Wisconsin Madison, 2006.

[26] G. Manzolini, A. Giostri, C. Saccilotto, P. Silva, and E. Macchi, "Development of an innovative code for the design of thermodynamic solar power plants part A: Code description and test case," *Renew. Energy*, vol. 36, no. 7, pp. 1993–2003, 2011, doi: 10.1016/j.renene.2010.12.027.

[27] I. Llorente García, J. L. Álvarez, and D. Blanco, "Performance model for parabolic trough solar thermal power plants with thermal storage: Comparison to operating plant data," *Sol. Energy*, vol. 85, no. 10, pp. 2443–2460, 2011, doi:

10.1016/j.solener.2011.07.002.

[28] H. Schenk, J. Dersch, T. Hirsch, and T. Polklas, "Transient Simulation of the Power Block in a Parabolic Trough Power Plant," in *Proceedings of the 11th International Modelica Conference, Versailles, France, September 21-23, 2015*, 2015, vol. 118, pp. 605–614, doi: 10.3384/ecp15118605.

[29] M. Jegoroff, M. Tähtinen, H. Mikkonen, and T. Leino, "Dynamic Modelling Platform for Integrated Power Plants," *4th Sol. Integr. Work.*, no. November, 2014.

[30] W. A. K. Al-Maliki, F. Alobaid, V. Kez, and B. Epple, "Modelling and dynamic simulation of a parabolic trough power plant," *J. Process Control*, vol. 39, pp. 123–138, 2016, doi: 10.1016/j.jprocont.2016.01.002.

[31] S. Rohani, T. P. Fluri, F. Dinter, and P. Nitz, "Modelling and simulation of parabolic trough plants based on real operating data," *Sol. Energy*, vol. 158, pp. 845–860, 2017, doi: 10.1016/j.solener.2017.10.023.

[32] K. M. Powell and T. F. Edgar, "Modeling and control of a solar thermal power plant with thermal energy storage," *Chem. Eng. Sci.*, vol. 71, pp. 138–145, 2012, doi: 10.1016/j.ces.2011.12.009.

[33] F. Yang, H. Cho, H. Zhang, J. Zhang, and Y. Wu, "Artificial neural network (ANN) based prediction and optimization of an organic Rankine cycle (ORC) for diesel engine waste heat recovery," *Energy Convers. Manag.*, vol. 164, pp. 15–26, 2018, doi: 10.1016/j.enconman.2018.02.062.

[34] A. H. Elsheikh, S. W. Sharshir, M. Abd Elaziz, A. E. Kabeel, W. Guilan, and Z. Haiou, "Modeling of solar energy systems using artificial neural network: A comprehensive review," *Solar Energy*, vol. 180. pp. 622–639, 2019, doi: 10.1016/j.solener.2019.01.037.

[35] S. A. Kalogirou, C. C. Neocleous, and C. N. Schizas, "Artificial neural networks for modelling the starting-up of a solar steam-generator," *Appl. Energy*, vol. 60, no. 2, pp. 89–100, 1998, doi: 10.1016/S0306-2619(98)00019-1.

[36] S. Y. Heng, Y. Asako, T. Suwa, and K. Nagasaka, "Transient thermal prediction methodology for parabolic trough solar collector tube using artificial neural network," *Renew. Energy*, vol. 131, pp. 168–179, 2019, doi: 10.1016/j.renene.2018.07.037.

[37] T. E. Boukelia, O. Arslan, and M. S. Mecibah, "ANN-based optimization of a parabolic trough solar thermal power plant," *Appl. Therm. Eng.*, vol. 107, pp. 1210–1218, 2016, doi: 10.1016/j.applthermaleng.2016.07.084.

[38] Z. Aqachmar, A. Allouhi, A. Jamil, B. Gagouch, and T. Kousksou, "Parabolic trough solar thermal power plant Noor I in Morocco," *Energy*, 2019, doi: 10.1016/j.energy.2019.04.160.

[39] Y. Aldali and K. Morad, "Numerical simulation of the integrated solar/North Benghazi combined power plant," *Appl. Therm. Eng.*, vol. 108, pp. 785–792, 2016, doi: 10.1016/j.applthermaleng.2016.07.178.

[40] P. Palenzuela, G. Zaragoza, D. C. Alarcón-Padilla, E. Guillén, M. Ibarra, and J. Blanco, "Assessment of different configurations for combined parabolic-trough (PT) solar power and desalination plants in arid regions," *Energy*, vol. 36, no. 8, pp. 4950–4958, 2011, doi: 10.1016/j.energy.2011.05.039.

[41] A. Giostri, M. Binotti, M. Astolfi, P. Silva, and E. Macchi, "Comparison of different solar plants based on parabolic trough technology," *Sol. Energy*, vol. 86, no. 5, pp. 1208–1221, 2012, doi: 10.1016/j.solener.2012.01.014.

[42] F. Antoñanzas-Torres Enrique Sodupe-Ortega Andrés Sanz-García Roberto Fernández-Martínez Francisco Javier Martínez-de-Pisón-Ascacíbar and U. de La Rioja España, "Technical feasibility assessment of integrated solar combined cycle power plants in Ciudad Real (Spain) and Las Vegas (USA)." Accessed: Feb. 07, 2021. [Online]. Available: http://www.mineriadatos.com.

[43] M. Eck, E. Zarza, M. Eickhoff, J. Rheinländer, and L. Valenzuela, "Applied research concerning the direct steam generation in parabolic troughs," *Sol. Energy*, vol. 74, no. 4, pp. 341–351, 2003, doi: 10.1016/S0038-092X(03)00111-7.

[44] E. Zarza *et al.*, "Direct steam generation in parabolic troughs: Final results and conclusions of the DISS project," *Energy*, vol. 29, no. 5–6, pp. 635–644, 2004, doi: 10.1016/S0360-5442(03)00172-5.

[45] NREL, "Concentrating Solar Power Projects | Concentrating Solar Power Projects." https://solarpaces.nrel.gov/ (accessed Feb. 07, 2021).

[46] O. Behar, A. Khellaf, K. Mohammedi, and S. Ait-kaci, "A review of integrated solar combined cycle system (ISCCS) with a parabolic trough technology," *Renew. Sustain. Energy Rev.*, vol. 39, pp. 223–250, 2014, doi: 10.1016/j.rser.2014.07.066.

[47] "Site web officiel de l'ONEE - Branche Electricité," *Brochure Institutionnelle ONEE - COP22 (Novembre 2016)*. http://www.one.org.ma/FR/pages/index.asp (accessed Feb. 07, 2021).

[48] M. Azeroual, A. El Makrini, H. El Moussaoui, and H. El Markhi, "Renewable energy potential and available capacity for wind and solar power in Morocco towards 2030," *J. Eng. Sci. Technol. Rev.*, vol. 11, no. 1, pp. 189–198, 2018, doi: 10.25103/jestr.111.23.

[49] "Site web officiel de l'ONEE - Branche Electricité," *Rapport d'activités 2019*. http://www.one.org.ma/FR/pages/index.asp (accessed Feb. 07, 2021).

[50] "Ministry of Energy, Mines, Water and the Environment (MEMEE) of Morocco." https://www.mem.gov.ma/Pages/index.aspx (accessed Feb. 07, 2021).

[51] "Masen | L'Agence Marocaine pour l'Energie Durable." https://www.masen.ma/ (accessed Feb. 07, 2021).

[52] "Maghreb–Europe Gas Pipeline - Wikipedia." https://en.wikipedia.org/wiki/Maghreb–Europe_Gas_Pipeline (accessed Mar. 30, 2021).

[53] The World Bank, "Implementation Completion and Results Report (TF-58314) on a Grant in the Amount of US\$ 43.2 Million from the Global Environment Facility Trust

Fund to the Office National De L'Electricite et de L'Eau Potable (Onee) of the Kingdom of Morocco for an Integr," 2013.

[54]   C. Breyer and G. Knies, "Global Energy Supply Potential of Concentrating," *SolarPACES 2009*, pp. 15–18, 2009.

[55]   R. No *et al.*, "Document of The World Bank, Report No: ICR2693, Implementation completion and results (TF-58314) on a grant in the amount of US$ 43.2 Million from the global environment facility trust fund to the office national de l'électricité et de l'eau potable (ONEE," 2013.

[56]   S. Ghazi, A. Sayigh, and K. Ip, "Dust effect on flat surfaces - A review paper," *Renewable and Sustainable Energy Reviews*, vol. 33. pp. 742–751, 2014, doi: 10.1016/j.rser.2014.02.016.

[57]   E. Urrejola *et al.*, "Effect of soiling and sunlight exposure on the performance ratio of photovoltaic technologies in Santiago, Chile," *Energy Convers. Manag.*, vol. 114, pp. 338–347, 2016, doi: 10.1016/j.enconman.2016.02.016.

[58]   A. A. Merrouni, A. Mezrhab, A. Ghennioui, and Z. Naimi, "Measurement, comparison and monitoring of solar mirror's specular reflectivity using two different Reflectometers," in *Energy Procedia*, 2017, vol. 119, pp. 433–445, doi: 10.1016/j.egypro.2017.07.045.

[59]   L. Qoaider and A. Liqreina, "Optimization of dry cooled parabolic trough (CSP) plants for the desert regions of the Middle East and North Africa (MENA)," *Sol. Energy*, vol. 122, pp. 976–985, 2015, doi: 10.1016/j.solener.2015.10.021.

[60]   A. Liqreina and L. Qoaider, "Dry cooling of concentrating solar power (CSP) plants, an economic competitive option for the desert regions of the MENA region," *Sol. Energy*, vol. 103, pp. 417–424, 2014, doi: 10.1016/j.solener.2014.02.039.

[61]   A. Alami Merrouni, F. Elwali Elalaoui, A. Ghennioui, A. Mezrhab, and A. Mezrhab, "A GIS-AHP combination for the sites assessment of large-scale CSP plants with dry and wet cooling systems. Case study: Eastern Morocco," *Sol. Energy*, vol. 166, pp. 2–12, 2018, doi: 10.1016/j.solener.2018.03.038.

[62]   N. Benalouache, "L'énergie solaire pour la production d'électricité au Maghreb: transition énergétique et jeux d'échelles," 2017.

[63]   J. Domínguez Bravo, X. García Casals, and I. Pinedo Pascua, "GIS approach to the definition of capacity and generation ceilings of renewable energy technologies," *Energy Policy*, vol. 35, no. 10, pp. 4879–4892, 2007, doi: 10.1016/j.enpol.2007.04.025.

[64]   A. Gastli, Y. Charabi, and S. Zekri, "GIS-based assessment of combined CSP electric power and seawater desalination plant for Duqum-Oman," *Renewable and Sustainable Energy Reviews*, vol. 14, no. 2. pp. 821–827, 2010, doi: 10.1016/j.rser.2009.08.020.

[65]   A. Zaaoumi *et al.*, "Estimation of the energy production of a parabolic trough solar thermal power plant using analytical and artificial neural networks models," *Renew. Energy*, vol. 170, pp. 620–638, Jun. 2021, doi: 10.1016/j.renene.2021.01.129.

[66] B. J. Alqahtani and D. Patiño-Echeverri, "Integrated Solar Combined Cycle Power Plants: Paving the way for thermal solar," in *Applied Energy*, 2016, vol. 169, pp. 927–936, doi: 10.1016/j.apenergy.2016.02.083.

[67] S. A. Kalogirou, "Solar thermoelectric power generation in Cyprus : Selection of the best system," *Renew. Energy*, vol. 49, pp. 278–281, 2013, doi: 10.1016/j.renene.2012.01.014.

[68] A. Mwesigye, İ. H. Yılmaz, and J. P. Meyer, "Numerical analysis of the thermal and thermodynamic performance of a parabolic trough solar collector using SWCNTs-Therminol®VP-1 nanofluid," *Renew. Energy*, vol. 119, pp. 844–862, 2018, doi: 10.1016/j.renene.2017.10.047.

[69] S. Marrakchi, Z. Leemrani, H. Asselman, A. Aoukili, and H. Asselman, "ScienceDirect ScienceDirect ScienceDirect ScienceDirect Temperature distribution analysis of parabolic trough solar collector Temperature distribution analysis parabolic trough solar using of CFD 2017 , collector using CFD Costing for capacity optimizatio," *Procedia Manuf.*, vol. 22, pp. 773–779, 2018, doi: 10.1016/j.promfg.2018.03.110.

[70] A. Zaaoumi, M. Asbik, H. Hafs, A. Bah, and M. Alaoui, "Thermal performance simulation analysis of solar field for parabolic trough collectors assigned for ambient conditions in Morocco," *Renew. Energy*, vol. 163, pp. 1479–1494, 2021, doi: 10.1016/j.renene.2020.08.151.

[71] S. A. Kalogirou, "A detailed thermal model of a parabolic trough collector receiver," *Energy*, vol. 48, no. 1, pp. 298–306, 2012, doi: 10.1016/j.energy.2012.06.023.

[72] T. Bouhal *et al.*, "Technical feasibility of a sustainable Concentrated Solar Power in Morocco through an energy analysis," in *Renewable and Sustainable Energy Reviews*, 2018, vol. 81, no. August 2017, pp. 1087–1095, doi: 10.1016/j.rser.2017.08.056.

[73] M. Ouagued, A. Khellaf, and L. Loukarfi, "Estimation of the temperature , heat gain and heat loss by solar parabolic trough collector under Algerian climate using different thermal oils," *Energy Convers. Manag.*, vol. 75, pp. 191–201, 2013, doi: 10.1016/j.enconman.2013.06.011.

[74] Y. Marif, H. Benmoussa, H. Bouguettaia, M. M. Belhadj, and M. Zerrouki, "Numerical simulation of solar parabolic trough collector performance in the Algeria Saharan region," *Energy Convers. Manag.*, vol. 85, pp. 521–529, 2014, doi: 10.1016/j.enconman.2014.06.002.

[75] I. H. Yilmaz and M. S. Söylemez, "Thermo-mathematical modeling of parabolic trough collector," *Energy Convers. Manag.*, vol. 88, pp. 768–784, 2014, doi: 10.1016/j.enconman.2014.09.031.

[76] T. Fasquelle, Q. Falcoz, P. Neveu, F. Lecat, and G. Flamant, "A thermal model to predict the dynamic performances of parabolic trough lines," *Energy*, vol. 141, pp. 1187–1203, 2017, doi: 10.1016/j.energy.2017.09.063.

[77] H. A. Zaharil and M. Hasanuzzaman, "Modelling and performance analysis of parabolic trough solar concentrator for different heat transfer fluids under Malaysian condition," *Renew. Energy*, vol. 149, pp. 22–41, 2020, doi:

10.1016/j.renene.2019.12.032.

[78] L. Salgado Conrado, A. Rodriguez-Pulido, and G. Calderón, "Thermal performance of parabolic trough solar collectors," *Renewable and Sustainable Energy Reviews*, vol. 67. pp. 1345–1359, 2017, doi: 10.1016/j.rser.2016.09.071.

[79] H. Liang, S. You, and H. Zhang, "Comparison of different heat transfer models for parabolic trough solar collectors," *Appl. Energy*, vol. 148, pp. 105–114, 2015, doi: 10.1016/j.apenergy.2015.03.059.

[80] İ. H. Yılmaz, M. S. Söylemez, H. Hayta, and R. Yumrutaş, "Model-based performance analysis of a concentrating parabolic trough collector array," in *Progress in Exergy, Energy, and the Environment*, 2014, pp. 815–828.

[81] J. Duffie and W. Beckman, *Solar Engineering of Thermal Processes. 2nd ed. John Wiley and Sons. New York: USA*. 1991.

[82] S. Kalogirou, *Kalogirou, Soteris. Solar energy engineering : processes and systems / Soteris Kalogirou.—1st ed.* 2009.

[83] S. P. P. Sukhatme, J. K. Nayak, and J. K. Naik, *Solar Energy Principles of Thermal Collection and Storage*. 2014.

[84] V. Quaschning, *Understanding renewable energy systems*, vol. 9781315800. 2014.

[85] "Solar azimuth angle - Wikipedia." https://en.wikipedia.org/wiki/Solar_azimuth_angle (accessed Feb. 07, 2021).

[86] M. Günther, M. Joemann, and S. Csambor, "Chapter 5 Parabolic Trough Technology," *Adv. CSP Teach. Mater.*, p. 106, 2011.

[87] F. De Luca, V. Ferraro, and V. Marinelli, "On the performance of CSP oil-cooled plants, with and without heat storage in tanks of molten salts," *Energy*, vol. 83, pp. 230–239, 2015, doi: 10.1016/j.energy.2015.02.017.

[88] M. Marefati, M. Mehrpooya, and M. B. Shafii, "Optical and thermal analysis of a parabolic trough solar collector for production of thermal energy in different climates in Iran with comparison between the conventional nanofluids," *J. Clean. Prod.*, vol. 175, pp. 294–313, 2018, doi: 10.1016/j.jclepro.2017.12.080.

[89] P. H. Wagner, "Thermodynamic simulation of solar thermal power stations with liquid salt as heat transfer fluid," Technical University of Munich, 2012.

[90] M. A. A. Alfellag, "Modeling and Experimental Investigation of Parabolic Trough Modeling and Experimental Investigation of Parabolic Trough Solar Collector Solar Collector," Embry-Riddle Aeronautical University, 2014.

[91] B. Hoffschmidt, S. Alexopoulos, J. Göttsche, M. Sauerborn, and O. Kaufhold, "High concentration solar collectors," in *Comprehensive Renewable Energy*, vol. 3, 2012, pp. 165–209.

[92] Solutia, "Therminol VP-1," in *Solutia*, 2014, pp. 1–5, [Online]. Available:

http://twt.mpei.ac.ru/TTHB/HEDH/HTF-VP1.PDF%0Ahttp://twt.mpei.ac.ru/tthb/hedh/htf-vp1.pdf.

[93] F. Burkholder and C. F. Kutscher, "Heat loss testing of Schott's 2008 PTR70 parabolic trough receiver," *NREL Tech. Rep.*, no. May, p. 58, 2009, [Online]. Available: http://www.nrel.gov/docs/fy09osti/45633.pdf.

[94] A. Benidir, F. Khaldi, A. H. Benmachiche, and F. Bouras, "Numerical thermal analysis of schott 2008 PTR70 solar receiver under hassi R'Mel power plant operation conditions," *J. Eng. Sci. Technol.*, vol. 13, no. 1, pp. 122–140, 2018.

[95] F. P. Incropera, D. P. DeWitt, T. L. Bergman, and A. S. Lavine, *Fundamentals of Heat and Mass Transfer in Fabrics*, vol. 6th. 2007.

[96] T. A. Yassen, N. D. Mokhlif, and M. A. Eleiwi, "Performance investigation of an integrated solar water heater with corrugated absorber surface for domestic use," *Renew. Energy*, vol. 138, pp. 852–860, 2019, doi: 10.1016/j.renene.2019.01.114.

[97] COMSOL Inc., "COMSOL Multiphysics Reference Manual (version 5.3a)," *Comsol*, 2018.

[98] K. El Alami, M. Asbik, H. Agalit, N. Zari, and S. Rachidi, "A literature review of igneous Moroccan rocks for thermal energy storage in CSP plants," in *AIP Conference Proceedings*, 2019, vol. 2126, doi: 10.1063/1.5117730.

[99] K. El Alami, M. Asbik, N. Zari, and S. Rachidi, "Thermocline Thermal Storage Using a Packed bed of Moroccan Rocks," in *IOP Conference Series: Earth and Environmental Science*, 2018, vol. 161, no. 1, doi: 10.1088/1755-1315/161/1/012016.

[100] K. El Alami, M. Asbik, and H. Agalit, "Identification of natural rocks as storage materials in thermal energy storage (TES) system of concentrated solar power (CSP) plants – A review," *Sol. Energy Mater. Sol. Cells*, vol. 217, 2020, doi: 10.1016/j.solmat.2020.110599.

[101] Y. Jemmal, N. Zari, M. Asbik, and M. Maaroufi, "Experimental characterization and thermal performance comparison of six Moroccan rocks used as filler materials in a packed bed storage system," *J. Energy Storage*, vol. 30, 2020, doi: 10.1016/j.est.2020.101513.

[102] R. A. Barreto, "Fossil fuels, alternative energy and economic growth," *Econ. Model.*, vol. 75, pp. 196–220, 2018, doi: 10.1016/j.econmod.2018.06.019.

[103] E. Foster, M. Contestabile, J. Blazquez, B. Manzano, M. Workman, and N. Shah, "The unstudied barriers to widespread renewable energy deployment: Fossil fuel price responses," *Energy Policy*, vol. 103, pp. 258–264, 2017, doi: 10.1016/j.enpol.2016.12.050.

[104] H. L. Zhang, J. Baeyens, J. Degrève, and G. Cacères, "Concentrated solar power plants: Review and design methodology," *Renewable and Sustainable Energy Reviews*, vol. 22. pp. 466–481, 2013, doi: 10.1016/j.rser.2013.01.032.

[105] J. J. Vidal-Amaro, P. A. Østergaard, and C. Sheinbaum-Pardo, "Optimal energy mix

for transitioning from fossil fuels to renewable energy sources - The case of the Mexican electricity system," *Appl. Energy*, vol. 150, pp. 80–96, 2015, doi: 10.1016/j.apenergy.2015.03.133.

[106] Vernon E. Dudley *et al.*, "SEGS LS2 solar collector-test results," *Unknown*. 1994, [Online].   Available: http://www.nrel.gov/csp/troughnet/pdfs/segs_ls2_solar_collector.pdf%5Cnhttp://adsabs.harvard.edu/abs/1994STIN...9611437D.

[107] M. Geyer, E. Lüpfert, R. Osuna, P. Nava, J. Langenkamp, and E. Mandelberg, "EUROTROUGH - Parabolic Trough Collector Developed for Cost Efficient Solar Power Generation," *11th SolarPACES Int. Symp. Conc. Sol. Power Chem. Energy Technol.*, no. October 2015, p. 7, 2002, [Online]. Available: http://sbp.de/es/html/contact/download/EuroTrough_Paper2002.pdf.

[108] G. Morin, J. Dersch, W. Platzer, M. Eck, and A. Häberle, "Comparison of Linear Fresnel and Parabolic Trough Collector power plants," *Sol. Energy*, vol. 86, no. 1, pp. 1–12, 2012, doi: 10.1016/j.solener.2011.06.020.

[109] L. Valenzuela, R. López-Martín, and E. Zarza, "Optical and thermal performance of large-size parabolic-trough solar collectors from outdoor experiments: A test method and a case study," *Energy*, vol. 70, pp. 456–464, 2014, doi: 10.1016/j.energy.2014.04.016.

[110] N. Fraidenraich, C. Oliveira, A. F. Vieira da Cunha, J. M. Gordon, and O. C. Vilela, "Analytical modeling of direct steam generation solar power plants," *Sol. Energy*, vol. 98, no. PC, pp. 511–522, 2013, doi: 10.1016/j.solener.2013.09.037.

[111] M. Larcher, M. Rommel, A. Bohren, E. Frank, and S. Minder, "Characterization of a parabolic trough collector for process heat applications," in *Energy Procedia*, 2014, vol. 57, pp. 2804–2811, doi: 10.1016/j.egypro.2014.10.313.

[112] H. Schenk, T. Hirsch, J. F. Feldhoff, and M. Wittmann, "Energetic comparison of linear Fresnel and parabolic trough collector systems," *J. Sol. Energy Eng. Trans. ASME*, vol. 136, no. 4, 2014, doi: 10.1115/1.4027766.

[113] "SOLTIGUA : experience in FP7 projects," 2013.

[114] M. J. Montes, "Análisis Y Propuestas De Sistemas Solares De Alta Exergía Que Emplean Agua Como Fluido Calorífero," *Dep. Ing. Energética y Fluidomecánica Esc. Técnica Super. Ing. Ind.*, p. 323, 2008.

[115] A. Giostri, M. Binotti, P. Silva, E. Macchi, and G. Manzolini, "Comparison of two linear collectors in solar thermal plants: Parabolic trough vs fresnel," in *ASME 2011 5th International Conference on Energy Sustainability, ES 2011*, 2011, no. PARTS A, B, AND C, pp. 621–630, doi: 10.1115/ES2011-54312.

[116] N. Fraidenraich, C. Oliveira, A. F. Vieira, J. M. Gordon, and O. C. Vilela, "ScienceDirect Analytical modeling of direct steam generation solar power plants," *Sol. Energy*, vol. 98, pp. 511–522, 2013, doi: 10.1016/j.solener.2013.09.037.

[117] H. Yang, Q. Wang, X. Huang, J. Li, and G. Pei, "Performance study and comparative

analysis of traditional and double-selective-coated parabolic trough receivers," *Energy*, vol. 145, pp. 206–216, 2018, doi: 10.1016/j.energy.2017.12.126.

[118] G. Najafi, B. Ghobadian, T. Tavakoli, D. R. Buttsworth, T. F. Yusaf, and M. Faizollahnejad, "Performance and exhaust emissions of a gasoline engine with ethanol blended gasoline fuels using artificial neural network," *Appl. Energy*, vol. 86, no. 5, pp. 630–639, 2009, doi: 10.1016/j.apenergy.2008.09.017.

[119] B. Khoshnevisan, S. Rafiee, M. Omid, and H. Mousazadeh, "Development of an intelligent system based on ANFIS for predicting wheat grain yield on the basis of energy inputs," *Inf. Process. Agric.*, vol. 1, no. 1, pp. 14–22, 2014, doi: 10.1016/j.inpa.2014.04.001.

[120] M. Karamirad, M. Omid, R. Alimardani, H. Mousazadeh, and S. N. Heidari, "ANN based simulation and experimental verification of analytical four- and five-parameters models of PV modules," *Simul. Model. Pract. Theory*, vol. 34, pp. 86–98, 2013, doi: 10.1016/j.simpat.2013.02.001.

[121] Ö. Altan Dombayci and M. Gölcü, "Daily means ambient temperature prediction using artificial neural network method: A case study of Turkey," *Renew. Energy*, vol. 34, no. 4, pp. 1158–1161, 2009, doi: 10.1016/j.renene.2008.07.007.

[122] M. Imran and S. A. Alsuhaibani, "A neuro-fuzzy inference model for diabetic retinopathy classification," in *Intelligent Data Analysis for Biomedical Applications: Challenges and Solutions*, 2019, pp. 147–172.

[123] W. Yaïci and E. Entchev, "Performance prediction of a solar thermal energy system using artificial neural networks," in *Applied Thermal Engineering*, 2014, vol. 73, no. 1, pp. 1348–1359, doi: 10.1016/j.applthermaleng.2014.07.040.

[124] S. A. Kalogirou, "Artificial neural networks in renewable energy systems applications: A review," *Renewable and Sustainable Energy Reviews*, vol. 5, no. 4. pp. 373–401, 2000, doi: 10.1016/S1364-0321(01)00006-5.

[125] Haykin S, "Neural networks and learning machines. 3rd ed. Englewood Cliffs (NJ, USA): Prentice-Hall; 2008," *arXiv Prepr.*, pp. 1–10, 2014, [Online]. Available: https://arxiv.org/pdf/1312.6199v4.pdf.

[126] B. Ihya, A. Mechaqrane, R. Tadili, and M. N. Bargach, "Prediction of hourly and daily diffuse solar fraction in the city of Fez (Morocco)," *Theor. Appl. Climatol.*, vol. 120, no. 3–4, pp. 737–749, 2015, doi: 10.1007/s00704-014-1207-y.

[127] A. Zaaoumi, A. Bah, and M. Alaoui, "Application of artificial neural networks and adaptive neuro-fuzzy inference system to estimate the energy generation of a solar power plant in Ain Beni-Mathar (Morocco)," *2018 10th Int. Conf. Electron. Comput. Artif. Intell.*, pp. 1–6, 2018.

[128] M. S. Guney, "Solar power and application methods," *Renewable and Sustainable Energy Reviews*, vol. 57. pp. 776–785, 2016, doi: 10.1016/j.rser.2015.12.055.

[129] F. Almonacid, C. Rus, P. J. Pérez, and L. Hontoria, "Estimation of the energy of a PV generator using artificial neural network," *Renew. Energy*, vol. 34, no. 12, pp. 2743–

2750, 2009, doi: 10.1016/j.renene.2009.05.020.

[130] I. Jayawardene and G. K. Venayagamoorthy, "Comparison of adaptive neuro-fuzzy inference systems and echo state networks for PV power prediction," in *Procedia Computer Science*, 2015, vol. 53, no. 1, pp. 92–102, doi: 10.1016/j.procs.2015.07.283.

[131] C.-D. Dumitru, A. Gligor, and C. Enachescu, "Solar Photovoltaic Energy Production Forecast Using Neural Networks," *Procedia Technol.*, vol. 22, pp. 808–815, 2016, doi: 10.1016/j.protcy.2016.01.053.

[132] W. Yaici and E. Entchev, "Prediction of the performance of a solar thermal energy system using adaptive neuro-fuzzy inference system," in *3rd International Conference on Renewable Energy Research and Applications, ICRERA 2014*, 2014, pp. 601–604, doi: 10.1109/ICRERA.2014.7016455.

[133] C. D. Dumitru and A. Gligor, "Daily Average Wind Energy Forecasting Using Artificial Neural Networks," in *Procedia Engineering*, 2017, vol. 181, pp. 829–836, doi: 10.1016/j.proeng.2017.02.474.

[134] A. T. Hammid, M. H. Bin Sulaiman, and A. N. Abdalla, "Prediction of small hydropower plant power production in Himreen Lake dam (HLD) using artificial neural network," *Alexandria Eng. J.*, vol. 57, no. 1, pp. 211–221, 2018, doi: 10.1016/j.aej.2016.12.011.

[135] J. S. R. Jang, "ANFIS : Adap tive-Ne twork-Based Fuzzy Inference System. IEEE Transactions on Systems," *Man Cybern.*, vol. 23, no. 3, pp. 665–685, 1993.

[136] D. . Rumelhart, G. . Hinton, and R. . Williams, "Learning Internal Representations By Error Propagation (original)," *Explorations in the Micro-Structure of Cognition Vol. 1 : Foundations*, no. V. pp. 318–362, 1986.

[137] A. Varjani, "Neural network application in power systems load forecasting," *Univ. Wollongong Thesis Collect. 1954-2016*, Jan. 1994, Accessed: Apr. 06, 2021. [Online]. Available: https://ro.uow.edu.au/theses/2462.

[138] F. Sherwani, B. S. K. K. Ibrahim, and M. M. Asad, "Hybridized classification algorithms for data classification applications: A review," *Egyptian Informatics Journal*. 2020, doi: 10.1016/j.eij.2020.07.004.

[139] G. Wang, L. Guo, and H. Duan, "Wavelet neural network using multiple wavelet functions in target threat assessment," *Sci. World J.*, vol. 2013, 2013, doi: 10.1155/2013/632437.

[140] N. M. Nawi, M. Z. Rehman, and M. I. Ghazali, "Noise-induced hearing loss prediction in malaysian industrial workers using gradient descent with adaptive momentum Algorithm," *Int. Rev. Comput. Softw.*, vol. 6, no. 5, pp. 740–748, 2011.

[141] Z. Qadir, E. Ever, and C. Batunlu, "Use of Neural Network Based Prediction Algorithms for Powering Up Smart Portable Accessories," *Neural Process. Lett.*, vol. 53, no. 1, pp. 721–756, 2021, doi: 10.1007/s11063-020-10397-3.

[142] M. A. Costa, A. de P. Braga, and B. R. de Menezes, "Improving generalization of

MLPs with sliding mode control and the Levenberg-Marquardt algorithm," in *Neurocomputing*, 2007, vol. 70, no. 7–9, pp. 1342–1347, doi: 10.1016/j.neucom.2006.09.003.

[143] F. Declercq and R. De Keyser, "Using Levenberg-Marquardt Minimization in Neural Model Based Predictive Control," *IFAC Proc. Vol.*, vol. 29, no. 7, pp. 289–293, 1996, doi: 10.1016/s1474-6670(17)43733-5.

[144] J. Iqbal, A. Iqbal, and M. Arif, "Levenberg-Marquardt method for solving systems of absolute value equations," *J. Comput. Appl. Math.*, vol. 282, pp. 134–138, 2015, doi: 10.1016/j.cam.2014.11.062.

[145] D. W. Marquardt, "An Algorithm for Least-Squares Estimation of Nonlinear Parameters," *J. Soc. Ind. Appl. Math.*, vol. 11, no. 2, pp. 431–441, 1963, doi: 10.1137/0111030.

[146] M. T. Hagan and M. B. Menhaj, "Training Feedforward Networks with the Marquardt Algorithm," *IEEE Trans. Neural Networks*, vol. 5, no. 6, pp. 989–993, 1994, doi: 10.1109/72.329697.

[147] D. S. Pandey, S. Das, I. Pan, J. J. Leahy, and W. Kwapinski, "Artificial neural network based modelling approach for municipal solid waste gasification in a fluidized bed reactor," *Waste Manag.*, vol. 58, pp. 202–213, 2016, doi: 10.1016/j.wasman.2016.08.023.

Appendix

➤ **The Back-propagation (BP) neural networks algorithm**

To enable a NN successfully operation an initial training (learning) process would be required. The back propagation learning algorithm (BP) is the most popular algorithm for training a neural network. This algorithm is developed to overcome the limitation of the original perception [136], [137]. Simple linearly separable problems can be classified by perception, and more complex, non-linear problems can be solved by Multi-Layer Perceptions (MLP), shown in figure A.l. In a MLP network adjusting the weights between nodes in layers is needed to minimize the outputs errors. Back-propagation learning algorithm is used for this purpose. It solves this problem by assuming that ail processing elements (PEs) and connections are somewhat to responsible for an erroneous output. Therefore, the output error backwards through the connections to the previous layers. This process is repeated until the input layer is reached [137].
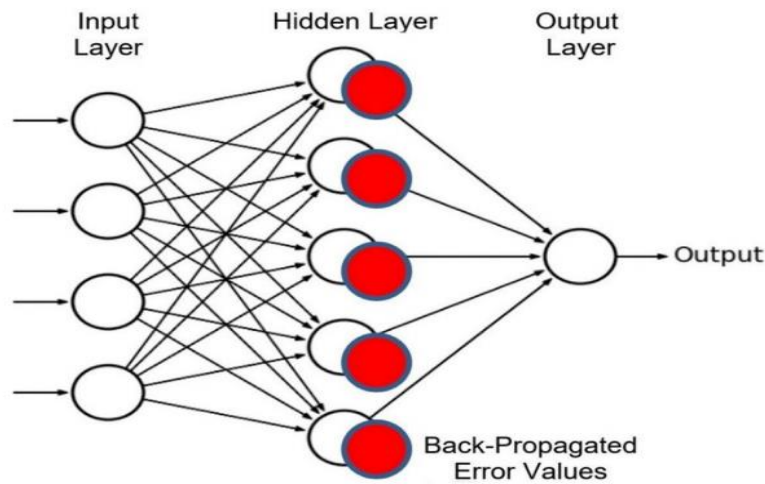
Figure A.1: Basic structure of back-propagation neural networks [138].

In BP Algorithm, the main purpose of the process of learning is to reduce the difference between the predicted output O_k and the actual output t_k through the optimization of the weights w* in the network [138]. The Error function is defined as [138]–[140].

$$E = \sum_{k=1}^{n}(t_k - O_k)^2$$

(A. 1)

Figure A.2 shows the 3D visualization of the error function in weight space. The point (a) at which the error function is the highest is called as the global maxima, point (c) at which the

error function is the smallest is known as the global minima, whereas, every other minima is referred to as local minima.
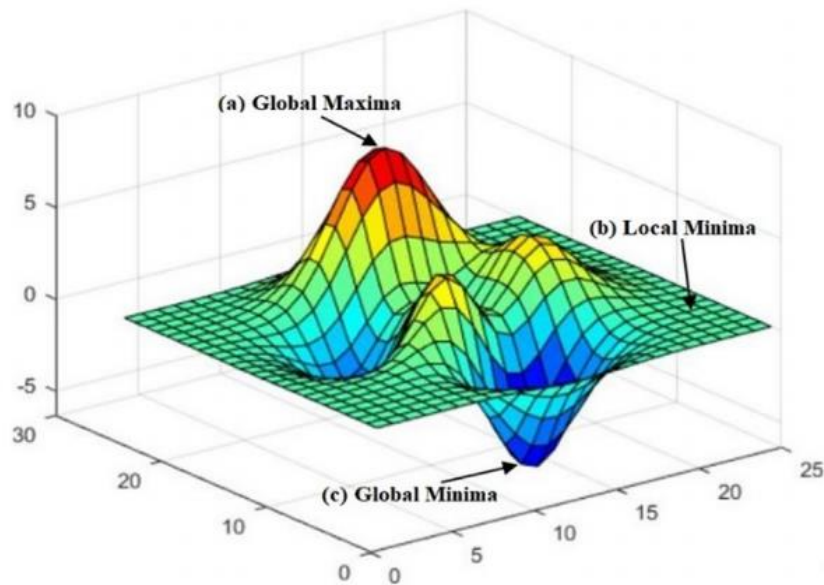
Figure A.2: 3D visualization of error function [138].

The error function can be defined as a non-linear function of weights in networks within excess of one layer and it may possess numerous local minima [138]. The gradient of total error function E relative to weights can be denoted by using the following equation:

$$\nabla E(\omega) = 0 \tag{A. 2}$$

Eq. (A.2) can be used to evaluate the network error by equating the difference of actual output of network against the anticipated output. The error is propagated back through the network as a reference, after it is computed, to perform the weight adjustment. This process continues until the maximum epoch or the target error is achieved by the network. Although, BP neural networks algorithm employ local learning gradient descent technique, nonetheless it is prone to problems like slow learning or even network stagnancy [138].

Hence, initial parameters such as weights and biases, network topology, activation function, learning rate and momentum coefficient are very crucial to decide and should be calculated accordingly. These parameters can cause the network convergence to slow down and can also create network stagnancy if they are not selected appropriately [138].

➢ The Levenberg-Marquardt (LM) neural networks algorithm

BP algorithm is commonly known as the steepest descent method but it also suffers from slow convergence problems. Therefore Levenberg-Marquardt (LM) algorithm is introduced which is known of its capability to converge even in highly complex optimization problems. The commonly used name for these algorithms are damped least square (DLS) and are used to confront non-linear least square problems quite efficiently [141], [142]. However, these algorithms are mainly used for curve fitting problems providing a local minimum [141]. Two minimization methods are used for generalizing the LM algorithms [143].

The first one updates the parameters in order to reduce the least square function, as parameters are far from optimal value is known as Gradient descent method [144], whereas, the second one assumes the least square function to be quadratic and computes the minimum of quadratic known as Gauss-Newton method. The reduction is in turn achieved as the parameters are close to their optimal values [145]. In the LM, the Jacobian (J) is calculated using the back-propagation technique described in [146] followed by Hessian (H=J^{T}J) and gradient (g=J^{T}e) calculation, e being the network error. The network weight and bias terms (x) are then updated as (A.3):

$$x_{k+1} = x_k - [J^T J + \mu I]^{-1} J^T e \qquad \text{(A. 3)}$$

Where I is the identity matrix, and μ is a scalar (called combination coefficient), whose zero or large values make the training algorithm similar to Newton's method, using approximate Hessian or gradient descent with small step size respectively. After each successful step the value of μ is decreased or alternatively increased if the cost function is not decreased in a step [147]. Based on the above reason, the LM algorithm is used for minimizing the mean squared error (MSE) between the network output and target output.
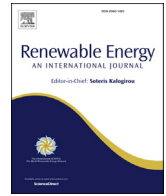
Estimation of the energy production of a parabolic trough solar thermal power plant using analytical and artificial neural networks models

Anass Zaaoumi [a, *], Abdellah Bah [a], Mihaela Ciocan [b], Patrick Sebastian [c], Mugur C. Balan [d], Abdellah Mechaqrane [e], Mohammed Alaoui [a]

[a] Center of Energy, ERTE, École Nationale Supérieure des Arts et Métiers, Mohammed V University in Rabat, BP 6207, Rabat, 10100, Morocco
[b] University Politehnica of Bucharest, Romania
[c] University of Bordeaux, I2M UMR CNRS 5295, Talence, France
[d] Technical University of Cluj-Napoca, Bd. Muncii 103-105, 400641, Cluj-Napoca, Romania
[e] Laboratory of Renewable Energies and Smart Systems, FST, Sidi Mohamed Ben Abdellah University, B.P. 2202, Fez, Morocco

ARTICLE INFO

ABSTRACT

The accurate estimation of a concentrated solar power plant production is an important issue because of the fluctuations in meteorological parameters like solar radiation, ambient temperature, wind speed, and humidity. In this work, three models were conducted in order to estimate the hourly electric production of a parabolic trough solar thermal power plant (PTSTPP) located at Ain Beni-Mathar in Eastern Morocco. First, two analytical models are considered. The first analytical model (AM I) is based on calculating the heat losses of parabolic trough collectors (PTCs), while the second analytical model (AM II) is based on the thermal efficiency of PTCs. The third model is an artificial neural networks (ANN) model derived from artificial intelligence techniques. All models are validated using one year of real operating data. The simulation results indicate that the ANN model performs much better than the analytical models. Accordingly, the ANN model results show that the estimated annual electrical energy is about 42.6 GW h/ year, while the operating energy is approximately 44.7 GWh/year. The frequency of occurrence shows that 86.77% of hourly values were estimated with a deviation of less than 3 MW h. The developed ANN model is readily useable to estimate energy production for PTSTPP.

© 2021 Elsevier Ltd. All rights reserved.

1. Introduction

Energy is a vital resource for the economic and social development of a country. The economic level of a country is highly related to its energy consumption since countries that consume much energy produce a lot of products or services. Traditionally, the most widely used energy sources were natural such as oil, coal, and natural gas. These sources are not inexhaustible, and their use has adverse environmental effects such as global warming, climate change, emissions of greenhouse gas, and depletion of the ozone layer [1]. These fossil fuels are nonrenewable (exhaustible) and can, therefore, gradually tend towards extinction [2]. So, it is necessary to consider replacing these sources with new and clean sources,

such as renewable energies. Renewable energy sources such as solar [3], wind [4], biomass [5–7], geothermal [8], and hydropower [9] are utilized to reproduce energy and are therefore extensively useful to combat energy crises. Solar energy is the most abundant and cleanest renewable energy source available. Various solar technologies already exist to convert this energy for multiple uses, including generating electricity, heating, cooling, commercial or industrial use.

Concentrating solar power (CSP) energy system has been growing strongly in recent years. It is a solar technology that aims at transforming the energy radiated by the sun into heat at high temperatures and then into mechanical and electrical energy through a thermodynamic cycle machine [10]. The accurate estimation of the solar power plant production is an important issue because of the fluctuations in meteorological parameters like solar radiation, ambient temperature, wind speed, and humidity. These natural fluctuations cause production fluctuations and power

Nomenclature

a_0	Correction coefficient (1/K)
a_1	Correction coefficient (W/m²K)
a_2	Correction coefficient (W/m²K²)
A_p	Solar field aperture area (m²)
DNI_d	Daily direct normal irradiation (W/m²)
DNI_h	Hourly direct normal irradiation (W/m²)
E_h	Hourly electrical production (MWh)
E_{h-1}	Previous hourly electrical production (MWh)
f	Focal distance of the collector (m)
f_1	Factor between 0 and 1 to account for any additional reduction in energy absorption by the solar field loops
f_{clean}	Mirror cleanliness factor
$f_{dustEnv}$	Factor related to the light absorption of dust on the receiver glass cover
$f_{EndLoss}$	End effect loss
$f_{RowShad}$	Row shading
k_1	Correction coefficient that takes into account thermal losses (W/m²K)
k_2	Correction coefficient that takes into account thermal losses (W/m² K²)
k_L	The correction coefficient, due to the longitudinal angle of incidence (α_L)
k_T	The correction coefficient, due to the transversal angle of incidence (α_T)
L	Absorber tube length (m)
l_{Space}	The space between rows in the solar field (m)
n	Number of the day
N_L	Loops number
net_j	Network
O_j	Output
Q_{loss}	The heat loss from the heat collector element (W/m)
Q_u	The useful thermal power supplied to the HTF (W)
Q_{ele}	The electrical power produced (W)
$Q_u(AM\ I)$	The useful heat stored in the HTF calculated using AM I (Wh)
$Q_u(AM\ II)$	The useful heat stored in the HTF calculated using AM II (Wh)
Q_{HTF}	The useful heat stored in the heat transfer fluid per unit plane surface area of PTC (Wh/m²)
R	Coefficient of correlation
t_h	Ambient temperature (°C)
t_k	Predicted output
$\bar{t}$	Predicted mean output
w_h	Wind speed (m/s)
W_{ij}	Weight
$w_{Sca,\ total}$	The total aperture width of a single SCA (m)
y	Day angle (°)
y_k	Measured output
$\bar{y}$	Measured mean output

Abbreviations

ABM	Ain Beni-Mathar
AM	Analytical model
ANN	Artificial neural networks
EQT	Equation of time (min)

HCE	Heat Collection Element
HTF	Heat transfer fluid
IAM	Incident angle modifier
MAE	Mean absolute error
MLP	Multi-layers perceptron
MLT	Mean local time (min)
PTC	Parabolic trough collector
PTSTPP	Parabolic trough solar thermal power plant
RMBE	Relative mean bias error
RRMSE	Relative root mean square error
RMSE	Root mean square error
SCA	Solar Collector Assemblies
SNL	Sandia National Laboratories

Greek letters

α_{abs}	Absorbance of the selective coating on the metallic pipe of the absorber tube
α_{gl}	Absorbance of the glass envelope
α_L	Longitudinal angle of incidence (°)
α_S	Angle of solar azimuth (°)
α_T	Transversal angle of incidence (°)
α_t	Azimuth angle of the collector (°)
γ	Interception factor
γ_S	Angle of the solar altitude (°)
γ_{st}	The projection of the γ_S on the transversal plane of the collector (°)
γ_t	Tilt angle of the collector (°)
δ	Declination angle of the sun (°)
ε_{gl}	Glass envelope emissivity
η	Global thermal efficiency of the PTC
η_0	The optical efficiency of the PTC
η_g	Global efficiency (thermal-electrical)
$\eta_{opt}(\theta)$	Optical efficiency
$\eta_{opt,0}$	Peak optical efficiency
η_{track}	Tracking error
λ	Longitude (°)
ρ_{cl}	Reflectivity of the parabolic collector
ϕ	Latitude (°)
ϕ_h	Air relative humidity (%)
ω	Hour angle of the sun (°)
θ	Incidence angle (°)
θ_z	Zenith angle (°)
τ	Time (hour)
τ_{env}	Transmissivity of the receiver's glass envelope
$\tau_{h,d}$	Time (hour of the day)
$\tau_{h,y}$	Time (hour of the year)
$K(\theta)$	Incident angle modifier
Δt	Temperature difference between the mean temperature of the heat transfer fluid of the collector (342 °C) and the temperature of the exterior environment (K)

Subscripts

amb	Ambient
HTF	Heat transfer fluid
h	Time step (hour)
h-1	Previous time step (hour)
d	Time step (day)

delivery problems on the electricity grid [11].

In the last decades, solar thermal power plants based on parabolic trough concentrators have been widely deployed in the electricity production sector. Indeed, they are considered the most mature solar technologies around the world. A recent literature review shows that most studies on the optimization of parabolic trough power plants are based on physical or analytical models, including steady-state and dynamic models, while machine learning models such as artificial neural networks (ANN) models are rarely used.

For steady-state studies, Montes et al. [12] presented a model for the economic optimization of solar parabolic trough power plants with no hybridization or storage. They investigate thermal performances at maximum and part-load conditions for different solar field sizes. Rolim et al. [13] developed an analytic model for a solar power station with parabolic trough collectors combining models for the solar collectors field and power station. Conversion of solar radiation into heat considers the non-linear behavior of heat losses from the parabolic collectors. The power cycle is considered endo-reversible because of the irreversibility arising from the energy source's limits. The numerical results are compared with measurements obtained from the Solar VI power generation system installed in the Mojave Desert in California and showed a good agreement between modeling and experimentation. Abutayeh [14] presented a detailed model of a real solar thermal power plant developed from steady-state power plant simulation software. In this numerical model, the parabolic trough collectors track the sun movement on a single axis. Simulation results matched well with plant data, including data collected during warm-up and cool down transient operations. Patnode [15] developed a model for the solar field using the TRNSYS simulation tool. The steady-state power cycle performance was regressed in terms of heat transfer fluid mass flow rate, the heat transfer fluid temperature, and condensing pressure. The model was validated with measured temperature and flow rate data from the Nine Electric Generation Systems VI plant (California, USA) from 1998 to 2005. Manzolini et al. [16] presented a steady-state model to predict performance and preliminary CSP plant sizing at normal nominal conditions for different plant layouts. The model was based on energy balance equations applied along the length of the heat collection element of the solar field and validated with experimental indoor tests from NREL.

For Dynamic model studies, García et al. [17] propose a detailed performance model to facilitate the prediction of a parabolic trough solar thermal power plant's electricity output, including a thermal energy storage process. The simulation results were compared with measurements resulting from experiments during 42 days in summer at the Andasol2 power plant in Spain. Schenk et al. [18] modeled parabolic trough concentrators in power plants using Dymola. Their study aimed to evaluate the transient behavior of concentrators, namely the start-up of power plants using thermal oil and parabolic trough concentrators. Due to the lack of data based on in situ measurements, the model is calibrated from another simulation model developed in the Ebsilon Professional environment. Tähtinen et al. [19] also developed a dynamic model of a power plant. Two solar field models are implemented using the Advanced Process Simulation Software (APROS), which is based on parabolic cylindrical and linear Fresnel reflector technologies. Both solar field models use water as a heat transfer fluid. Based on APROS, Wisam AbedKattea Al-Maliki [20] also developed a full-scale dynamic model of the power plant "Andasol II" located in Spain. The comparison between simulation results and validation data shows a good match between the model and actual operation. Rohani et al. [21] used the ColSimCSP tool developed at Fraunhofer ISE to assess performance parameters of solar field (thermal power and net electrical energy yield) associated with the commercial PTC

power plant Andasol 3 (Spain) for ten consecutive days of three different months (July, September, and November). Special attention was given to storage strategy and start time operation. The simulation results showed that the lowest mean deviation of solar field thermal power and net electrical energy yield are 0.59% and 2.29%, respectively.

Gaps between physical and artificial intelligence models are not only present in the area of solar parabolic trough collectors but also in many solar energy systems (SES). To fill this gap, new modeling methods have been adopted by many researchers to predict system performance accurately. The ANN method has recently been successfully applied in the field of SES to handle different tasks like design and performance optimization, thanks to the advantages of self-adaption, self-learning, nonlinear mapping, and fault tolerance [22]. Elsheikh et al. [23] summarized ANN applications for modeling of different SES such as solar collectors, solar air and water heaters, solar-assisted heat pumps, and photovoltaic/thermal (PV/T) systems, solar dryers, solar stills, and solar cookers. In this bibliography analysis, different ANN types were discussed, like multilayer perceptron neural network, Elman neural network, the function of the radial basis, and neural networks using the wavelet. Also, different activation functions types used in different ANN, and different standard statistical performance evaluation criteria used in the evaluation of ANN performance were reported.

Few studies are devoted to the prediction of PTC performances based on Artificial Neural Networks. For small-scale PTC, Kalogirou et al. [24] applied ANN to investigate the thermal performance of a solar steam generator connected to a parabolic collector. Eight parameters were used as input of the ANN model (solar irradiance, ambient temperature, time, effective aperture-area, flash-vessel content, and flash-vessel dimensions of diameter, height, and thickness). The learning process was performed by using the back-propagation algorithm. ANN model gives better mapping capabilities than the analytical model. In a more recent study, Heng et al. [25] developed a fast and accurate method to predict the exit fluid temperature of a PTC tube. This method is a combination of an ANN model with the superposition principle. The input parameters of the ANN model are heat flux, fluid velocity, and time. In addition to the input and output layers, the ANN model's architecture consists of two hidden layers with 68 neurons in each one. The linear activation function was used in the input layer, while the logistic activation function was used for the hidden layers and the output layer. The developed method requires less than 1 min of computational time to predict the one-day exit fluid temperature. Prediction results show relatively small deviations from the finite element method. The overall mean absolute deviation is less than 2 K. For large-scale PTC, Boukelia et al. [1] applied the ANN method to determine the techno-economic performances of a PTSTPP. Five inputs were chosen for the proposed model, such as design solar radiation, solar multiple, design ambient temperature, row spacing between parallel collectors, and the number of desired storage hours. The model outputs were selected to be the annual power generation and the levelized cost of electricity. To select the best ANN model, the feed-forward back-propagation learning algorithm was investigated with three different variants; Scaled Conjugate Gradient, Levenberg-Marquardt (LM), and Pola-Ribiere Conjugate Gradient. The obtained statistical parameters showed that the LM algorithm with 38 neurons in a single hidden layer looks like the best ANN model.

This paper compares the accuracy in predicting the hourly based energy production of a PTSTPP using analytical and ANN methods. First, two analytical models are considered. Those models include the absorbed solar energy collected on the parabolic trough field, the useful energy gained by heat transfer fluid (HTF) circling inside the receiver, and the electric energy produced at the output of the

steam turbine. Both models comprise a steady-state approach. The first analytical model (AM I) is a well-known model and is based on calculating the heat losses of PTC, whereas the second analytical model (AM II) is based on a formula to calculate the global thermal efficiency of PTCs. The third model is an artificial neural network (ANN) model derived from artificial intelligence techniques. This black box model is based on hourly energy production and meteorological data. A large amount of data is used to train and validate a three layers feed-forward ANN (Multi-Layers Perceptron (MLP)). To select the best ANN model, several architectures have been tested by varying the set of input variables and the number of neurons in the hidden layer. In addition to the frequency distributions of the differences between operating and predicted model results, different statistical parameters were used for verifying the accuracy of the analytical and ANN models. To this end, simulations were conducted using MATLAB software.

2. Material

2.1. Location of the power plant and climate data

The study refers to a PTSTPP integrated into a combined cycle using two gas turbines and located at Ain Beni-Mathar (ABM) (34°00′35″N, 2°01′29″W) in the Eastern part of Morocco at about 560 km from the Capital (Rabat). It is the first Moroccan solar thermal plant [26]. The climate in the region of the plant is considered as Csa (Under Köppen-Geiger climate classification). The climatic data used in this study were taken from the meteorological station available at the power plant site. Hourly data were taken during 1522 days from the first of November 2011 to the December 31, 2015.

The ambient temperature in the plant region presents significant seasonal variability, as indicated in Fig. 1a. The summer seasons are hot, and winters are cold. This parameter highly affects thermal losses in solar collectors. The minimum value of the monthly average temperature of the coldest month (February 2012) is 5.2 °C while the maximum of the average temperature of the hottest month (August 2012) is 30 °C. Besides, as expected, the relative humidity depends strongly on the ambient temperature since they vary oppositely, as shown in Fig. 1b. The ambient air is quite dry in summer when it gets hot during summers; the minimum average relative humidity is 21.8% and was recorded in August 2012. Conversely, the ambient air is rather humid in winters, with a maximum of 77% recorded in December 2014.

The wind speed also has a considerable impact on the CSP efficiency. Fig. 1c depicts monthly averages of wind speed. The average values are almost ranging from 2 m/s to 5 m/s. Note that the maximum average value (5.4 m/s) was recorded in February 2015. From an energy point of view, the power plant area is well exposed to sunlight with an average of Daily Direct Normal Irradiation (DNI_d) of 5.2 kWh/m^2. The monthly averages DNI_d are presented in Fig. 1d. The maximum DNI_d value of 8.86 kWh/m^2 was recorded in June 2013, and the minimum value of 3.08 kW h/m^2 was recorded in November 2012. As this parameter determines the level of the plant's energy resource, DNI_d largely determines the energy output of a PTSTPP.

2.2. Description of the plant

Integrated solar combined cycle power plants are composed of a PTSTPP and a natural gas-fired combined cycle power plant [27]. Combined gas cycles are solutions that meet both production and environmental requirements. Besides, it is possible to increase these environmental and technical performances by hybridizing these combined cycle plants with renewable energy sources and/or

storage techniques.

The principal scheme of the considered power plant (Ain Beni-Mathar (ABM)) is presented in Fig. 2. It is composed of two natural gas turbines (150 MW each), a steam turbine (172 MW), two heat recovery steam generators (HRSG), a solar field of parabolic trough collectors, and a heat exchanger (solar-steam generator). Table 1 illustrates the most significant technical characteristics of the solar field of the power plant.

Our study focuses only on the solar part of the power plant, where the solar energy collected by the parabolic trough collectors generates the steam that feeds the HRSGs. A metal pipe absorbs the solar energy concentrated by the collectors inside a vacuum glass tube. The heat transfer fluid (HTF) circulating inside the pipe is heated to a temperature near 400 °C. This fluid is then pumped through a conventional heat exchanger to produce steam at high temperatures and pressures. The steam is used in a Rankine cycle to produce electrical energy via the steam turbine generator.

Fig. 3 shows the electrical energy production of the power plant over 4 years (2012−2015). The produced energy is about 39 GWh in 2012, 42 GWh in 2013, 40 GWh in 2014, and 44.8 GWh in 2015. Energy production varies according to the seasons. Obviously, hot seasons (Spring and Summer) correspond to the highest production levels, while cold seasons (Autumn and Winter) correspond to the lowest production levels. The highest energy production was recorded in June 2013 (7.6 GWh), while the lowest was recorded in December 2013 (0.3 GWh).

3. Methods

In this part, the analytical and ANN models are used to estimate the energy production of the ABM solar power plant. Two mathematical models based on analytical relations were considered. The first one, Analytical Model I (AM I), is based on explicit calculations of heat losses in the solar field of PTCs, while the second, Analytical Model II (AM II), is based on a global evaluation of the thermal efficiency of the PTCs. Both analytical models comprise a steady-state approach to evaluate the thermal losses and thermal efficiency of the PTCs. The third model is an artificial neural network (ANN) model. This black box model is based on hourly energy production and meteorological data. The main characteristics and governing equations of each model are presented and discussed in detail. All models are validated using experimental data derived from the ABM power plant during the year 2015.

3.1. Analytical model I (AM I)

In the following, the analytical model of heat losses of PTCs is presented. This model mainly consists of four parts. The first part concerns the calculation of the incidence angle of solar radiation in order to determine the amount of solar energy received by the solar field. The second part is devoted to optical analysis. The goal of this part is to calculate the optical efficiency of the PTCs, which is the ratio of the amount of energy arriving at the absorber tube, and that hits the reflector. The third part concerns the thermal analysis and aims to determine the energy absorbed by the HTF in the receiver tubes. For this purpose, solar field heat losses from the Heat Collection Element (HCE) and piping were determined using empirical correlation. The last part deals with thermo-electric analysis, and it concerns the estimation of the electrical energy at the output of the alternator. This energy was calculated based on the provided efficiency of the power block.

3.1.1. Orientation angles and relative position to the sun

For all types of applications, the calculation of instantaneous available solar energy supposes that the relative position between
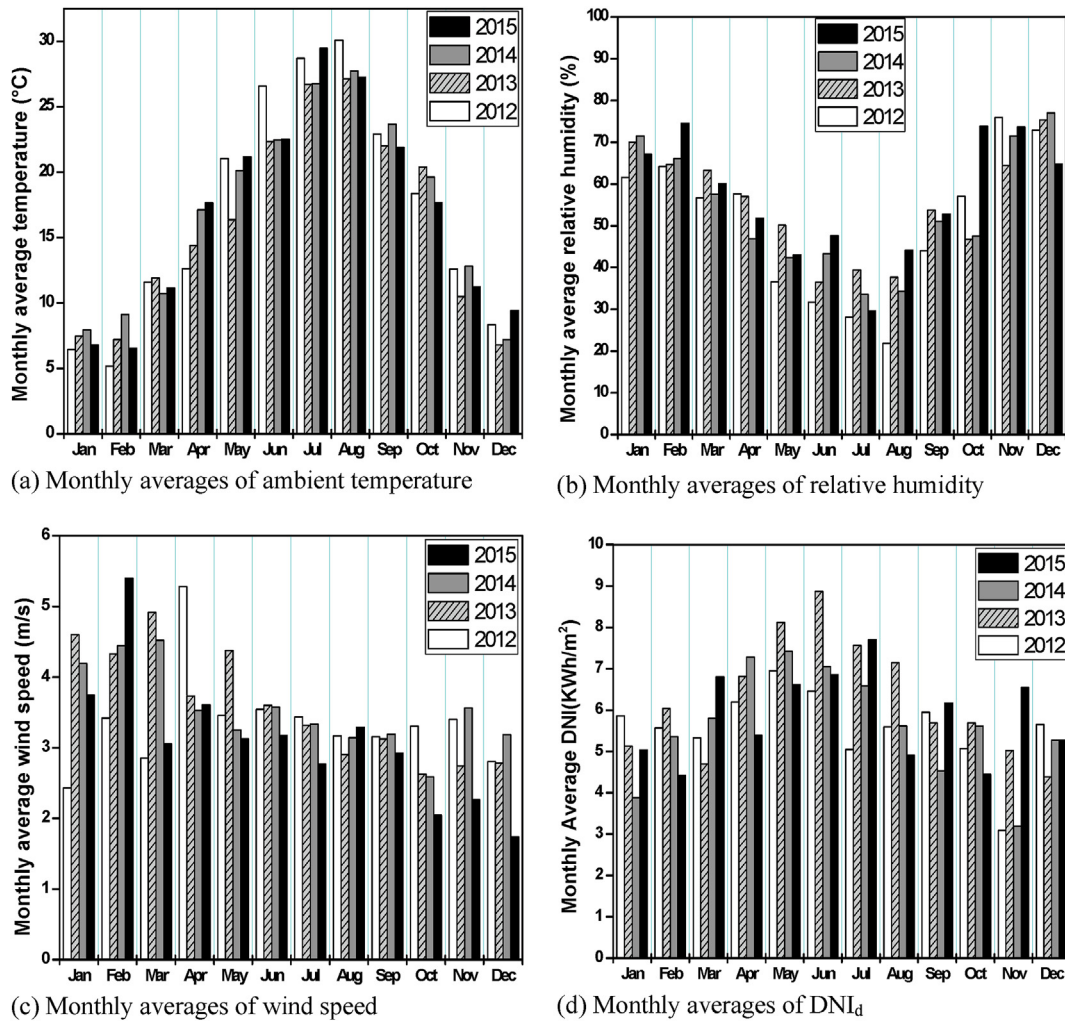
Fig. 1. Climatic data at study site location for 4 years. (a) Monthly averages of ambient temperature. (b) Monthly averages of relative humidity. (c) Monthly averages of wind speed. (d) Monthly averages of DNI$_d$.

the sun and the collectors is known.

According to Ref. [28], for any location determined by its longitude (λ [°]) and its latitude (ϕ [°]), the following parameters can be evaluated: the day angle (y [°]), the declination angle of the sun (δ [°]), the equation of time (EQT [min]), the mean local time (MLT [min]), the hour angle of the sun (ω [°]), the angle of the solar altitude (γ_S [°]) and the angle of solar azimuth (α_S [°]).

Two angles define the orientation of the collectors: the tilt angle (γ_t [°]) for which 0° means that the surface is horizontal and 90° means that the surface is vertical and also the orientation angle towards the azimuth (α_t [°]) for which 0° means that the surface is oriented towards the south, 90° means that the surface is oriented towards the west, 180° means that the surface is oriented towards the north, and 270° means that the surface is oriented towards east.

The next parameter that can be calculated is the solar angle of incidence on a tilted surface (θ [°]). The evaluation of this parameter is one of the most important problems that must be solved for the mathematical modeling of the parabolic through collectors (PTC).

Fig. 4a, Fig. 4b and 4c present the characteristic angles of the PTC, in an isometric view, in a lateral view, and a top view, respectively.

The North-South orientation of the PTC is more efficient than the East-West one, allowing the harvest of more solar energy during the whole year ([12,29−32]).

For the North-South orientation of the PTC, a new algorithm for calculating the characteristic angles for the position and orientation of the PTC plane and the relative position between the PTC plane and the sun was proposed.

The projection of the solar altitude angle on the transversal plane of the collector was noted with γ_{st}. The collector must always be tilted so that $\gamma_{st} = \gamma_s$ because the projection of the solar beam on the transversal plane must always be normal to the plane of the collector. The tracking system controls this particular orientation. Under these circumstances, the tilt angle of the collector (γ_t) can be calculated as:

$$\gamma_t = 90° - \gamma_{st} \tag{1}$$

The projection of the solar altitude angle on the transversal plane of the collector (γ_{st}) can be calculated as a function of γ_S and α_S with the following relations:

$$\gamma_{st} = \arctan \frac{\tan(\gamma_s)}{\cos(90° - \alpha_S)} \quad \text{for } \alpha_S < 180° \text{ and} \tag{2}$$

PTC orientation towards East
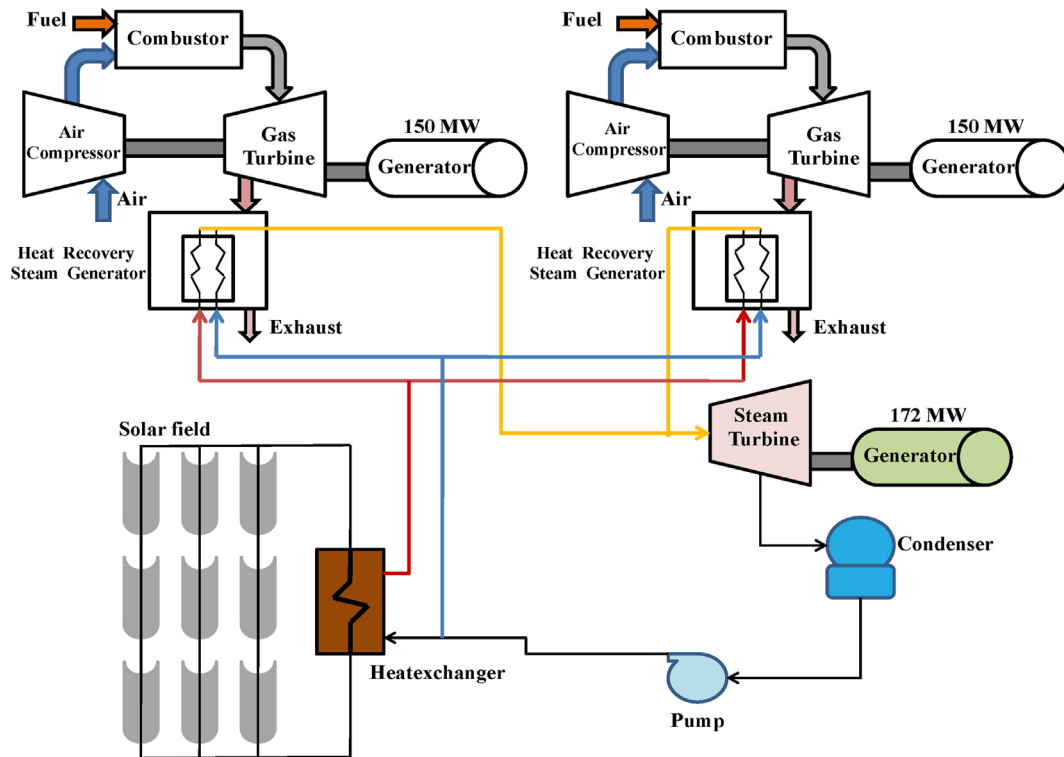
Fig. 2. Components of the integrated solar combined cycle power plant.

Table 1
Technical characteristics of the ABM solar field.

Characteristics	Value	U.M.
Parabolic Trough Collectors (type)	ET-150	–
Number of Loops (NL)	56	–
Number of Solar Collectors Assembly (SCA) per Loop	4	–
Number of SCA	224	–
SCA Length	150	m
Solar-Field Aperture Area	183,120	m^2
Solar-Field Outlet Temp	391	°C
Heat Collector Elements Manufacturer (Model)	Schott (PTR70)	–
Number of Heat Collector Elements	8064	–
Heat-Transfer Fluid Type	Therminol VP-1	–

$$\gamma_{st} = \arctan \frac{\tan(\gamma_s)}{\cos(270° - \alpha_S)} \quad \text{for } \alpha_S$$

$$\geq 180° \text{ and PTC orientation towards West} \tag{3}$$

With the determined tilt angle of the collector (γ_t) and the orientation of the collector (α_t), the angle of incidence (θ) can be determined with the same relation used for the collectors without concentrators:

$$\theta = \arccos(-\cos(\gamma_s) \cdot \sin(\gamma_t) \cdot \cos(\alpha_S - \alpha_t) + \sin(\gamma_S) \cdot \cos(\gamma_t)) \tag{4}$$

The proposed incidence angle formula was validated against the formula tackled in Ref. [28]:

$$\theta = \arccos\left(\sqrt{\cos^2\theta_z + \cos^2\delta \cdot \sin^2\omega}\right) \tag{5}$$

where θ_z is the zenith angle and can be determined as follow:

$$\theta_z = 90° - \gamma_s \tag{6}$$

Fig. 5 presents the flow chart for calculating the incidence angle with the proposed formula (Eq. (4)) and with the formula proposed in Ref. [28].

As a result, it was found that the two relations provide identical values for the angle of incidence during all days of the year (Fig. 6). The relative error doesn't exceed 4% in the worst case.

3.1.2. Optical analysis

In ideal conditions, 100% of the incident solar energy is reflected by the concentrator and absorbed by the receiver. However, in reality, the reflector does not reflect all solar radiation due to imperfections of the reflector, causing some optical losses. The optical efficiency relies on many factors, such as tracking error, geometrical error, and surface imperfections [33].

The power absorbed by the parabolic trough receiver tubes can be written as [21]:

$$Q_{sol,abs} = DNI \, \eta_{opt}(\theta)A_p \tag{7}$$

where A_p is the solar field aperture area, DNI is the direct normal irradiation, and $\eta_{opt}(\theta)$ is the optical efficiency given by the following equation:

$$\eta_{opt}(\theta) = \eta_{opt,0}K(\theta)f_{RowShadow}f_{EndLoss}f_{Clean}f_{DustEnv}\eta_{track}f_1 \tag{8}$$

Where $\eta_{opt,0}$ is the peak optical efficiency (the optical efficiency at zero angle of incidence) and is expressed as follow [34]:

$$\eta_{opt,0} = \rho_{Cl}\tau_{env}\alpha_{abs}\gamma \, \eta_{bellows} \tag{9}$$

ρ_{cl} is the reflectivity of the parabolic collector, τ_{env} is the transmissivity of the receiver's glass envelope, and α_{abs} is the
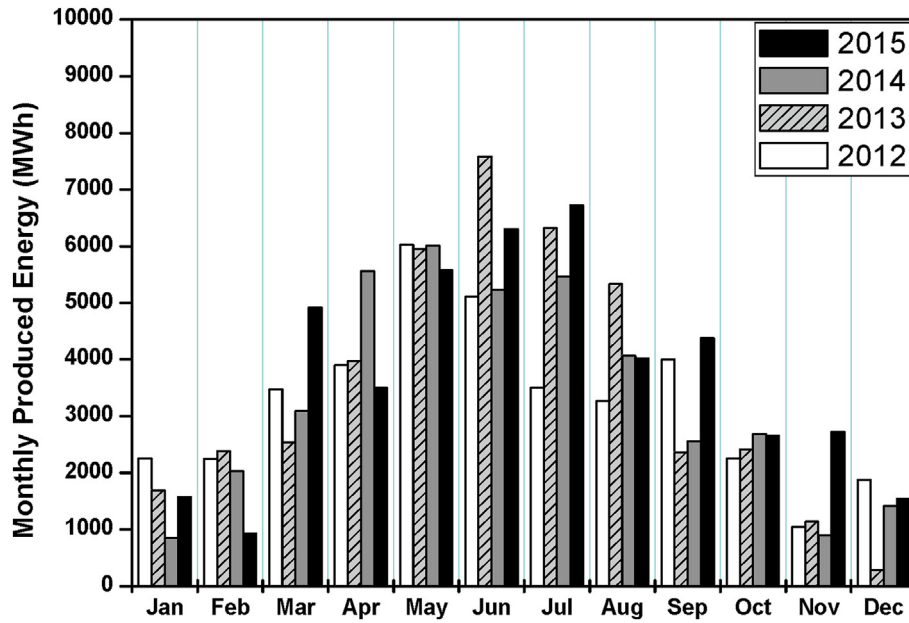
Fig. 3. Monthly production of electrical energy by the plant for 4 years.

absorbance of the selective coating on the metallic pipe of the receiver's tube. γ is the interception factor related to the collector imperfections and misalignment resulting from manufacturing and assembly of mirrors, and $\eta_{bellows}$ is the active aperture area.

$K(\theta)$ is the incident angle modifier (IAM); $f_{RowShadow}$ is the row shading; $f_{EndLoss}$ is the end effect loss; f_{Clean} is the mirror cleanliness factor; $f_{DustEnv}$ is related to the light absorption of dust on the receiver glass cover; η_{track} is the tracking error and f_1 is an extra factor between 0 and 1 to account for any additional reduction in energy absorption by the Solar Field loops [17]. For the calculations in this paper we used $f_{Clean} = 0.97$, $f_{DustEnv} = 0.98$, $\eta_{track} = 0.99$, $f_1 = 1$ [17].

The incident angle modifier $K(\theta)$ is taken from the literature [12] for the Eurotrough ET150 module and the tracking strategy (N–S axis, tracking E-W):

$$K(\theta) = \cos(\theta) - 2.859621 \cdot 10^{-5}\theta^2 - 5.25097 \cdot 10^{-4}\theta \quad (10)$$

The end effect loss factor $f_{EndLoss}$ is defined by Ref. [17]:

$$f_{endloss} = 1 - \frac{m_2 f}{L} tan(\theta) + \left(\frac{(m_2 - 1)}{L}\right) max[0, f\, tan(\theta) - d_2]$$
$$+ \left(\frac{(m_1 - 1)}{m_1 L}\right) max[0, f\, tan(\theta) - d_1] \quad (11)$$

where L is the tube length, f the focal distance, d_1 is the spacing between consecutive SCAs in a row, d_2 is the spacing between consecutive SCEs in a SCA, m_1 is the number of SCAs in a row, and m_2 is the number of SCEs within a SCA. For the calculations in this paper we have used $d_1 = 1.5$ m, $d_2 = 0.25$ m, $m_1 = 2$ and $m_2 = 12$ m.

$f_{RowShadow}$ is the row shadowing factor due to the shadows of collectors on one another. This factor is given by the following equation [20]:

$$f_{RowShadow} = \frac{l_{Space}}{w_{Sca,total}} \cdot \frac{\cos(\theta_z)}{\cos(\theta)} \quad (12)$$

where l_{Space} is the space between rows in the solar field and

$w_{Sca,total}$ is the total aperture width of a single SCA. Table 2 shows the dimensions and optical parameters of the collector and their corresponding values.

3.1.3. Thermal analysis

Thermal analysis of the receiver system is significant in determining how much of the solar radiation is converted into useful gain. In this stage, the heat losses of the receiver tubes $Q_{loss,HCE}$, and the total heat losses of the pipes $Q_{loss, pipes}$ have to be calculated and subtracted from the absorbed power. The useful thermal power supplied to the HTF can be calculated as [35]:

$$Q_u = Q_{sol,abs} - \left(Q_{loss,HCE} + Q_{loss,pipes}\right) \quad (13)$$

To calculate the heat loss of the receiver tubes, an empirical correlation reported by NREL [36] has been widely used in similar studies where Schott's 2008 PTR70 receiver tubes are part of the solar field design. For evacuated receiver tubes, the average amount of heat per HCE length (W/m) that is lost in the solar field is given by Ref. [36]:

$$HL_{PTR70} = \frac{HL_1 + HL_2 + HL_3 + HL_4}{(T_{out} - T_{in})} \quad (14)$$

$$HL_1 = \left(4.05 - 1.7 \cdot \sqrt{V_{wind}}\right)(T_{out} - T_{in}) \quad (15)$$

$$HL_2 = \left(0.247 + 0.0125 \cdot \sqrt{V_{wind}}\right)\left(\frac{T_{out}^2 - T_{in}^2}{2} - T_{amb}(T_{out} - T_{in})\right) \quad (16)$$

$$HL_3 = \frac{(-0.00146 + 0.0000000762 \cdot k(\theta) \cdot DNI)}{3}\left(T_{out}^3 - T_{in}^3\right) \quad (17)$$

$$HL_4 = \frac{0.00000565}{4}\left(T_{out}^4 - T_{in}^4\right) \quad (18)$$
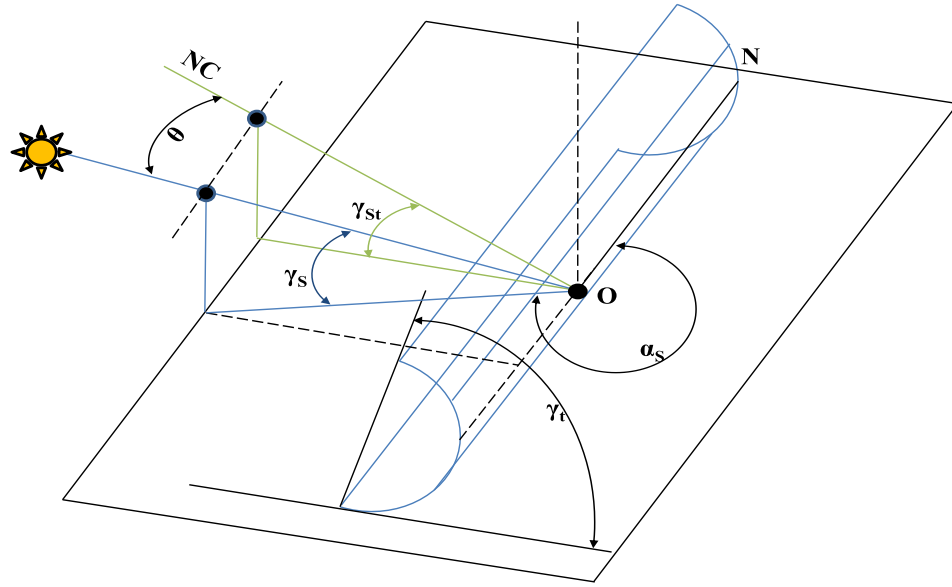
(a)
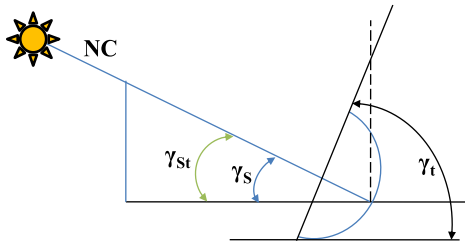
(b)
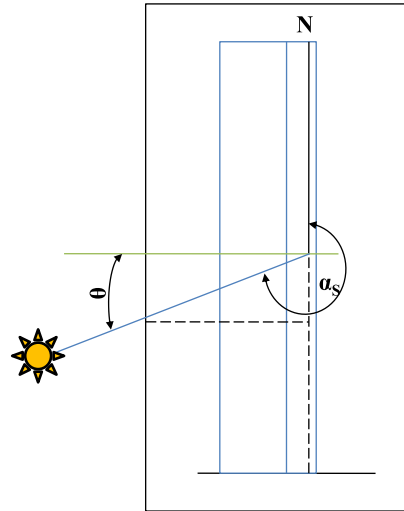
(c)

Fig. 4. Characteristic angles of the parabolic concentrator collectors. (a): Representation of characteristic angles for collectors with parabolic concentrators (isometric view). (b): Representation of characteristic angles for collectors with parabolic concentrators (lateral vision). (c): Representation of characteristic angles for collectors with parabolic concentrators (top view).

T_{in} and T_{out} are the temperatures of HTF at the inlet and outlet of the receiver tube. T_{amb} is the ambient temperature, and V_{wind} the wind speed. The final heat loss is given as follows:

$$Q_{loss,HCE} = HeatLossFactor \frac{HL_{PTR70}}{w_{Sca,total}} A_p \qquad (19)$$

Heat losses from the piping to and from the solar field are calculated by the following empirical equation [15]:

$$Q_{loss,pipes} = \left(0.01693\left(T_{av,HTF} - T_{amb}\right)\right.$$
$$- 1.683 \cdot 10^{-4}\left(T_{av,HTF} - T_{amb}\right)^2 \qquad (20)$$
$$\left. + 6.780 \cdot 10^{-7}\left(T_{av,HTF} - T_{amb}\right)^3\right)A_p$$

Where $T_{av,HTF}$ is the HTF average temperature. It is worth mentioning that among the operation conditions of the solar field,
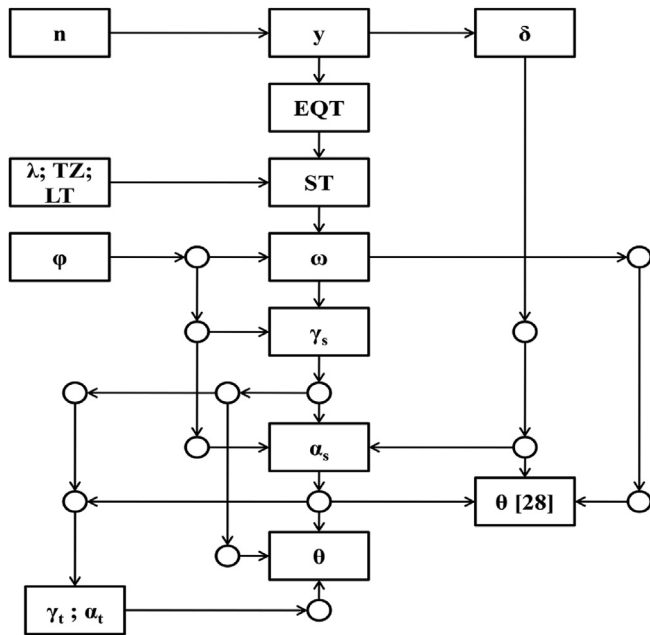
Fig. 5. Flow chart for the step of the calculation of the incidence angle.
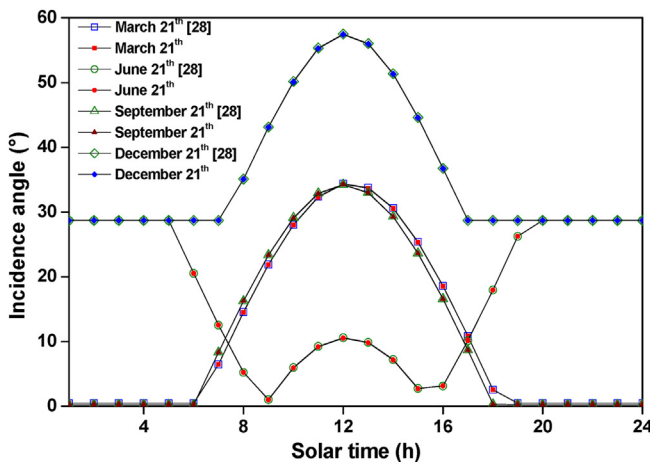
Fig. 6. Comparison between the angle of incidence evaluated from Ref. [28] and the proposed formula at Ain Beni Mathar location.

Table 2
Dimensions and optical parameters of PTC.

Parameter	value	Unit
ρ_{cl}	0.94	–
τ_{env}	0.96	–
α_{abs}	0.96	–
γ	0.94	–
$\eta_{bellows}$	0.967	–
ε_{gl}	0.89	–
L	148.5	m
f	1.71	m
l_{Space}	18	m
$w_{Sca, total}$	5.77	m

the HTF inlet, and outlet temperatures [35]. These temperatures are significant for the operation of the solar field to generate steam at the desired temperature and pressure. In this study, the inlet and outlet HTF temperatures are 293 °C and 391 °C, respectively, which

means that $T_{av,HTF} = 342$ °C. More details about the model could be found in ([36,37]).

The useful heat stored in the heat transfer fluid corresponding to any period of time (τ [h]) can be calculated as:

$$Q_u(AM\ I) = Q_u . \tau \tag{21}$$

3.1.4. Thermo-electric analysis

The ratio of the electrical power produced Q_{el} to the total thermal power is the global efficiency of the power plant:

$$\eta_g = \frac{Q_{el}}{Q_u} \tag{22}$$

This value is fixed in our model of the ABM power plant at $\eta_g = 26\%$, according to the operators of the power plant. A value of 26% may be considered relatively low, but it seems realistic as the thermal power plant is a hybrid plant. The temperature and pressure of the steam produced by the hot source are relatively low.

3.2. Analytical model for thermal efficiency of parabolic trough collectors (AM II)

3.2.1. Model description

In this part, the analytical model is based on the global thermal efficiency of the PTC. The model uses the same correlations as in the AM I to calculate the incidence angle and electric energy that comes from the heat exchanger. However, it differs in optical and thermal analyses, which are reduced to the calculation of the global thermal efficiency of the PTC (η [−]) using the following formula:

$$\eta = k_T \cdot k_L \cdot \eta_{opt,0} - k_1 \frac{\Delta t}{DNI} - k_2 \frac{\Delta t^2}{DNI} \tag{23}$$

where:

k_T is the correction coefficient, due to the transversal angle of incidence (α_T); ($k_T = 1$).

k_L is the correction coefficient, due to the longitudinal angle of incidence (α_L); it is also known as IAM.

k_1 [W/m²K] is a correction coefficient that takes into account thermal losses;

k_2 [W/m²K²] is a correction coefficient that takes into account thermal losses;

Δt [K] is the temperature difference between the mean temperature of the heat transfer fluid of the collector (342 °C) and the temperature of the exterior environment (T_{amb});

The optical efficiency is usually available for many types of PTC, but the correction coefficients k_1 and k_2 are not available in the literature and in the technical sheets of the PTC. In this study, these coefficients were evaluated using the curve fitting method of thermal efficiency with HTF temperature for the PTC used in ABM and some PTCs. Curve fitting is based on the least-squares method. The objective is to compare the performances of these PTCs with the one used in the ABM power plant and compare the accuracy in predicting the hourly based energy production of a PTSTPP with the other models.

The useful heat stored in the heat transfer fluid per unit plane surface area of PTC (Q_{HTF} [Wh/m²]), corresponding to any period of time (τ [h]) can be calculated as:

$$Q_{HTF} = \eta \cdot DNI \cdot \tau \tag{24}$$

The total useful heat generated by the solar field becomes:

$$Q_u(AM\ II) = Q_{HTF} \cdot A_p \qquad (25)$$

3.2.2. Estimation of correction coefficients k_1 and k_2 for the studied PTCs

The aim of this part is the determination of the correction coefficients of different PTCs. The nature of the HTF and the operating temperature for several commercial PTC are presented in Table 3. Table 4 deals with the recommended equations for the calculation of the IAM for different PTC.

The solar field of the ABM power plant is equipped with ET150 PTCs and Scott PTR 70 (2008) receivers. The correction coefficients k_1 and k_2 were determined based on the variation curve of the thermal efficiency at DNI = 800 W/m² and for Δt in the range of (100 … 500) °C, available in Ref. [49]. Note that in Ref. [49], the thermal efficiency variation with HTF temperature was determined by establishing a one-dimensional and steady-state model. The estimated coefficients are $k_1 = 0.0949$ and $k_2 = 2.29\ 10^{-4}$. The maximum difference between the reference and the calculated efficiencies is 4.5% (Fig. 7).

The study [38] proposes a slightly different equation to evaluate the thermal efficiency (η [−]) of the SEGS LS-2 type of PTC:

$$\eta = k_L \cdot (\eta_0 - a_0 \cdot \Delta t) - a_1 \frac{\Delta t}{DNI} - a_2 \frac{\Delta t^2}{DNI} \qquad (26)$$

Table 5 presents the optical efficiency and the correction coefficients: a_0, a_1, and a_2 for the LS-2 PTC.

Based on this equation, the correction coefficients k_1 and k_2 were determined for the LS-2 PTC. The maximum differences between the thermal efficiencies calculated with the proposed equation and those available in the literature [38], for DNI in the range of (200 … 1000) W/m² and Δt in the range of (0 … 500) °C, are 7.6%, 7.5%, 5.0% and 14.1% for LS2-CV, LS2-CA, LS2-BV, and LS2-BA, respectively. Fig. 8a and Fig. 8b present the thermal efficiency variation for LS2-CV and LS2-BV respectively for DNI in the range of (200 … 1000) W/m² and Δt in the range of (0 … 500) °C.

For the UrssaTrough (UT) PTC equipped with PTR 70 receiver, the correction coefficients k_1 and k_2 were determined based on the variation curve of the thermal efficiency at DNI = 864 W/m² and for Δt in the range of (0 … 350) °C, available in Ref. [42]. Fig. 9 presents the thermal efficiency variation for UT-PTR70. The maximum difference between the measured and the calculated efficiencies is 1.5%.

For the EuroTrough ET150 PTC with Solel (now Siemens) receiver, the correction coefficients k_1 and k_2 were determined based on the variation curves of the thermal efficiency at DNI in the range of (200 … 1000) W/m² and for Δt in the range of (0 … 500) °C, available in Ref. [29]. For $\Delta t = 500$ °C, the maximum differences

between the measured and the calculated efficiencies are of 10%, 1.2%, 2.4%, 1.2% and 2.2% for DNI = 200, 400, 600, 800 and 1000 W/m², respectively. The difference of 10% corresponds to $\Delta t = 500$ °C and DNI = 200 W/m². Under these conditions, the measured efficiency is $\eta = 10\%$, and the calculated efficiency is $\eta = 9\%$. For the values of $\Delta t \leq 400$ °C, even for DNI = 200, the maximum difference between the measured and the calculated efficiencies drops to 4.7%. Fig. 10 presents the thermal efficiency variation for ET150-Solel for DNI in the range of (200 … 1000) W/m² and Δt in the range of (0 … 500) °C.

Table 6 summarizes for different PTCs types the optical efficiency and the new proposed correction coefficients k_1 and k_2. The maximum difference between the thermal efficiency from reference and calculated by the proposed formula (%) is also presented.

In the rest of the study, only the evacuated PTCs were considered: LS2-CV, LS2-BV, ET150- Solel, UT- PTR70, and ET150- PTR70.

3.3. ANN model

ANNs are data-processing systems and machine learning techniques inspired from biological neural systems. ANNs are used to solve many different engineering and science problems, especially in certain areas where conventional modeling methods fail [50]. ANN prediction is usually much faster than conventional simulation models since iterative calculations are not necessary to solve differential equations. However, the topology definition and parameters computation of the neural network is time-consuming [51].

The structure of ANN is a significant factor that influences the learning performances of networks. The multilayer perceptron (MLP), known as the feed-forward neural network (FFNN), is effective for modeling energy conversion systems, thanks to its capability of arbitrary input-output mapping. MLP, as the most successful and the most popular ANN model from many ANNs models, is adopted in the present study [52]. Generally, MLP comprises three layers: an input layer, an output layer, and a hidden layer/s. The network function is specified largely by the connections between the nodes (a node is a place where computation happens) of different layers. Each node receives an input signal, which is the total 'information' from other nodes or external stimuli, processes it locally through a transfer or activation function, and produces a transformed output signal to other nodes or external outputs [53].

Fig. 11 illustrates the structure of a MLP model used in this study. The input layer takes the data from the network. The hidden layer processes the raw information received from the input layer. The obtained value is then sent to the output layer, which will also process the information from the hidden layer and produce the output [54].

The backpropagation is a supervised learning method for the MLP neural networks. It is used to obtain the relationships between inputs and outputs and is considered one of the most extensively used and popular ones [55]. This algorithm has been developed in various variants, including gradient descent and momentum gradient descent, which are considered as two important methods. However, these algorithms are slow because of the low speed of iterative learning. The Levenberg–Marquardt (LM) is a faster algorithm because it is based on performant optimization techniques ([56–58]). Hence, the LM algorithm was selected in this study.

To translate signals between different layers of the MLP, several transfer functions are available. The logistic sigmoid, tangent sigmoid, and the linear transfer functions are classically used. Those functions were examined and compared in terms of the accuracy of the resulting ANN function [51].

The following equation defines the logistic sigmoid function:

Table 3
The thermal agent and the operating temperature for some PTCs.

Reference	Type of collector	HTF	Temperature [°C]
[38]	SEGS LS-2	Syltherm 800	400
[39]	EuroTrough (ET100; ET150)	NA	400
[12]	EuroTrough ET150	Therminol VP-1	400 (370)
[40]	EuroTrough II	Steam	280−411
[41]	EuroTrough ET100	Therminol VP-1	400
[20]	FLAGSOL	Therminol VP-1	295−393
[42]	UrssaTrough	NA	293−393
[43]	INDITEP	Steam	NA
[44]	NEP PT1800	NA	100−300
[45]	SKAL-ET	Solar salt	450 (500)
[46]	SOLTIGUA PTMx-36	NA	250

Table 4
Equations recommended for the calculation of the IAM.

Reference	Equations	Obs.
[38]	$k_L = \cos(\theta) - 0.0003512 \cdot \theta - 0.00003137 \cdot \theta^2$	From measurements
[20,21,31,39–41,47,48]	$k_L = \cos(\theta) - 0.000525097 \cdot \theta - 0.00002859621 \cdot \theta^2$	
[43]	$k_L = \cos(\theta) - 0.00044 \cdot \theta - 0.00003 \cdot \theta^2$	Steam in collectors
[45]	$k_L = 1 - 0.0004 \cdot \theta - 0.00017 \cdot \theta^2$	From experiment
[42]	$k_L = \cos(\theta) - 0.0007 \cdot \theta - 0.000036 \cdot \theta^2$	Est-West orientation
[46]	$k_L = 1 - 0.0018 \cdot \theta - 0.00013 \cdot \theta^2$	From technical data
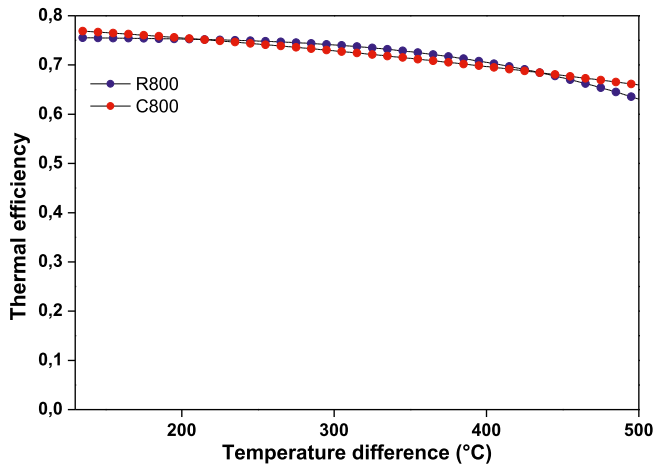
Fig. 7. Thermal efficiency variation for ET150-PTR70 (2008). Codes significance: R800 = based on reference [49] at DNI = 800 W/m^2 C800 = calculated with proposed coefficients at DNI = 800 W/m^2.

$$f(net_j) = O_j = \frac{1}{1 + \exp(-net_j)} \tag{27}$$

The tangent sigmoid function is given by:

$$f(net_j) = O_j = \frac{2}{1 + \exp(-2net_j)} - 1 \tag{28}$$

where O_j is the output of the jth neuron and net_j is the weighted sum of the inputs obtained by:

$$net_j = \sum_{i=1} W_{ij} O_i \tag{29}$$

W_{ij} is the weight of the connection from neuron i in the previous layer to neuron j in the current layer, and O_i is the output of the ith neuron in the previous layer.

In this study, several combinations of input variables have been tested to estimate the hourly energy production (E_h). The input variables taken into account are the hourly direct normal irradiation (DNI_h), the hour of the year ($\tau_{h,y}$), the hour of the day ($\tau_{h,d}$), ambient temperature (t_h), relative humidity (ϕ_h), and wind speed (w_h). For each hour h, the previous hourly energy productions (E_{h-1}) are also used as an input variable. Data covering a period of 4 years

of the studied power plant (with the inputs supposed and output) are selected. Then, 75% of these data (about 3 years: from November 01, 2011 to December 31, 2014) were used for training while the remained were used for validation (One year: 2015). In the training process, the ANN model was provided with the data of the inputs and output that the network will compute, and then the errors between actual results (operational data) and those predicted (determined by ANN) are calculated. This process aims to reduce these errors to a minimum. To improve the ANN model's reliability linking solar electric energy production and meteorological data, we only take into account the hours of solar energy production. The other data were considered as being irrelevant. During these hours, there is no solar energy production due to the: maintenance of the solar components, dangerous wind speed, and nights.

The MLP model has been developed using MATLAB© software. To select the most relevant input variables of the model, we adopt an incremental method by adding progressively new variables and observing their influence on the model accuracy. Several variable combinations were investigated to evaluate the performances of the incremental method. In all cases, we used an ANN model with 5 nodes in the hidden layer [59]. Finally, the model was improved by testing different numbers of hidden neurons. In this study, a single hidden layer ANN model is considered to simplify the computation. The desired parameters of the ANN model are listed in Table 7.

In the following, the ANN model accuracy is evaluated by the coefficient of determination (R), root mean square error (RMSE), relative root mean square error (RRMSE), relative mean bias error (RMBE), and mean absolute error (MAE) [59]. Those accuracy parameters are defined as:

$$R = \sum_{k=1} \left(\right) \frac{}{\sqrt{\sum_{k=1}(y_k - \bar{y})^2 \cdot \sum_{k=1}(t_k - \bar{t})^2}} \tag{30}$$

$$RMSE = \sqrt{\frac{1}{N} \cdot \sum_{k=1}(t_k - \bar{t})^2} \tag{31}$$

$$RRMSE = 100 \frac{1}{\bar{t}} \sqrt{\frac{1}{N} \cdot \sum_{k=1}(t_k - y_k)^2} \tag{32}$$

Table 5
The optical efficiency and the correction coefficients: a_0, a_1 and a_2.

PTC Type	η_0	a_0	a_1	a_2
LS-2 Cermet with vacuum annulus (LS2-CV)	0.733	0.00007276	0.00496	0.000691
LS-2 Cermet with air in annulus (LS2-CA)	0.734	0.00008030	0.09680	0.000669
LS-2 Black chrome with vacuum annulus (LS2-BV)	0.736	0.00004206	−0.07440	0.000958
LS-2 Black chrome with air in annulus (LS2-BA)	0.738	0.00006460	0.12160	0.000641

(a) LS2-CV;
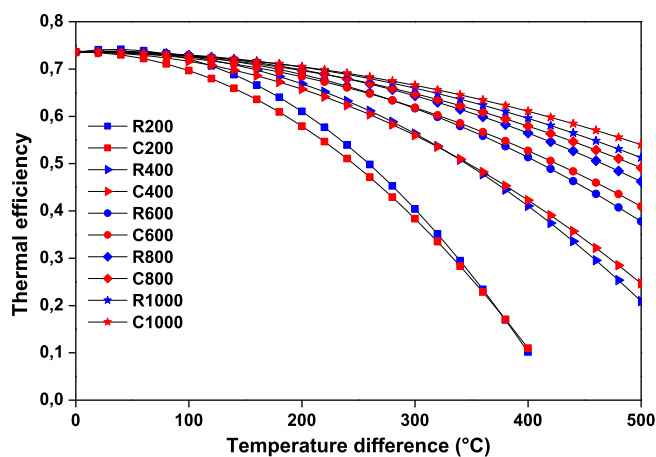
(b) LS2-BV

Fig. 8. Thermal efficiency variation Codes significance: R_{number}: R = based on reference [38]; number = DNI [W/m^2]. C_{number}: C = calculated with proposed coefficients; number = DNI [W/m^2].
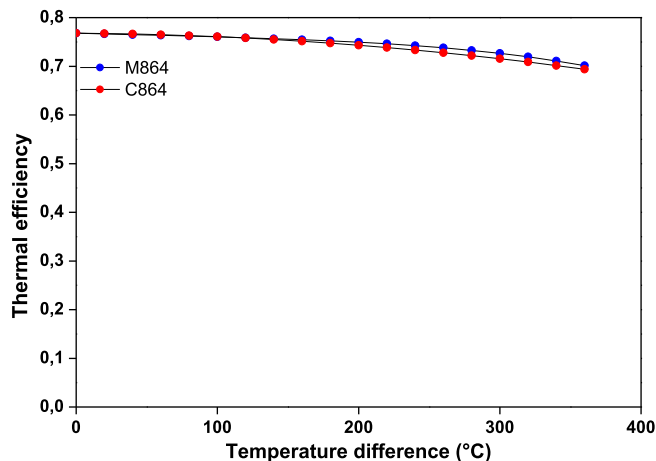
Fig. 9. Thermal efficiency variation for UT-PTR70. Codes significance: M864 = measured at DNI = 864 W/m^2. C864 = calculated with proposed coefficients at DNI = 864 W/m^2.
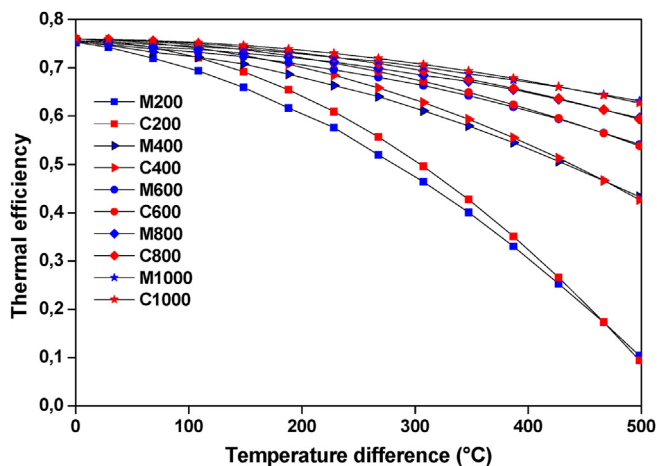
Fig. 10. Thermal efficiency variation for ET150. Codes significance: M number: M = measured in Ref. [29]; number = DNI [W/m^2]; C number: C = calculated with proposed coefficients; number = DNI [W/m^2].

$$RMBE = 100 \cdot \frac{\sum_{k=1}(t_k - y_k)}{\sum_{k=1}(y_k)} \qquad (33)$$

$$MAE = \frac{1}{N} \cdot \sum_{k=1} |(t_k - y_k)| \qquad (34)$$

where y_k and t_k denote respectively, the measured and the predicted output values for the k_{th} data while $\bar{y}$ and $\bar{t}$ are respectively the measured and the predicted mean values.

4. Results and discussion

In the following, the analytical models AM I and AM II are compared to the experimental results. Next, we deal with the ANN model: we investigate several input combinations and the number of hidden neurons to optimize the ANN architecture. Finally, we compare the performances of the three models.

4.1. Results of the analytical models

The AM I and AM II were used to obtain electric energy during 2015 and compared with operating data. For this purpose, the hourly measurements of the DNI, the ambient temperature, and the wind speed during the year 2015 at the location of the PTSTPP situated in Ain Beni-Mathar, were used as input data.

The performance indicators of the AM I and AM II are presented in Table 8. The results show that the regression coefficient R, the RRMSE, and the MAE values are 0.8388, 32.45%, and 3.5 MW h for AM I. These values are 0.8636, 32.15%, and 3.09 MWh for AM II.

The comparison between operating and analytical model results for all the months of the year is presented in Fig. 12. The total operating electric production is 44.7 GWh/year, while the predicted ones are 43.84 GWh/year and 50.08 GWh/year for AM I and AM II. The underestimation of the AM I is about 1.88%. This underestimation is noticed in the RMBE value, which equals −1.88%. AM II overestimates the energy production of about 12.1%. This overestimation can be explained by the fact that the heat losses from piping from and to the solar field were not included by reference [49].

Table 6
The proposed optical efficiency and the correction coefficients k_1 and k_2.

Collector	η_0	k_1	k_2	Max difference (%)
LS-2 Cermet with vacuum annulus (LS2-CV)	0.733	0.0306	0.000720	7.6
LS-2 Cermet with air in annulus (LS2-CA)	0.734	0.0810	0.000819	7.5
LS-2 Black chrome with vacuum annulus (LS2-BV)	0.736	0.0	0.000783	5
LS-2 Black chrome with air in annulus (LS2-BA)	0.738	0.1800	0.000567	14.1
UrssaTrough (UT) with PTR 70	0.768	0.018	0.0004441	1.5
EuroTrough ET150 (ET150) with Solel	0.760	0.018	0.0005	10
Soltigua PTMx	0.747	0.64	0.0	–
ET150 with PTR70 (2008)	0.79	0.0949	0.000229	4.5

Fig. 11. Structure of a MLP (FFNN).

Table 7
Final parameters setting of the ANN model.

Parameters	Value
Number of hidden layers	1
Number of epochs	1000
Train function	trainlm (Levenberg-Marguardt)
Hidden layer function	logsig
Output layer function	tansig

Table 8
Comparison of validation performance of the analytical models with the ANN model.

	R	RMSE (MWh)	RRMSE (%)	MAE (MWh)	RMBE (%)
AM I	0.8388	5.0349	32.4591	3.4931	−1.88
AM II	0.8636	4.9880	32.1567	3.0865	12.1
ANN model	0.9692	2.3725	15.2949	1.6272	−4.73

Fig. 12. Comparison between operating energy production with the predicted by analytical models and ANN model.

Let us now discuss the performances of different PTCs mentioned in AM II. This part evaluates the energy produced by different PTCs and compares it with the one used in the ABM power plant. So, we used the same solar field aperture area for all considered PTCs. According to Fig. 13, it was found that the annual electric energy production is about 41.49 GWh/year, 42.13 GWh/year, 47.41 GWh/year, 47.07 GWh/year, and 50.08 GWh/year, respectively for LS2-CV, LS2-BV, UT-PTR 70, ET150- Solel and ET150-PTR70 (2008). Hence, we can conclude that the PTC of ET150-PTR70 (2008) used in the ABM power plant gives the highest energy production, which can be explained by the fact that its high
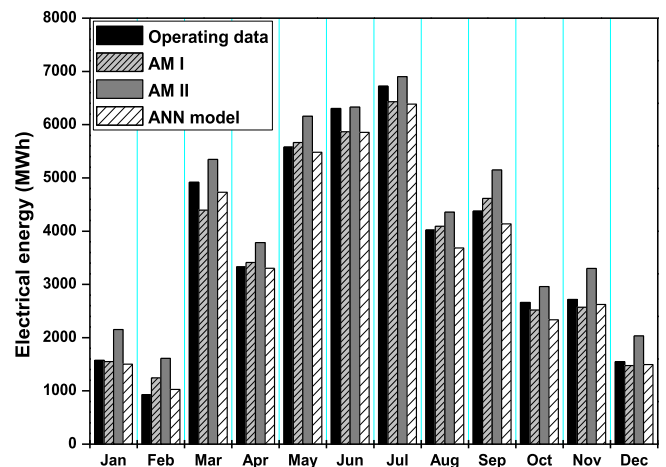
thermal efficiency characterizes it compared to the other PTCs. The lowest production was provided by the solar field composed of the LS2-CV collectors.

4.2. Results of the ANN model

The first step in developing ANN models consists of selecting its input parameters, namely the decision variables. For this purpose,
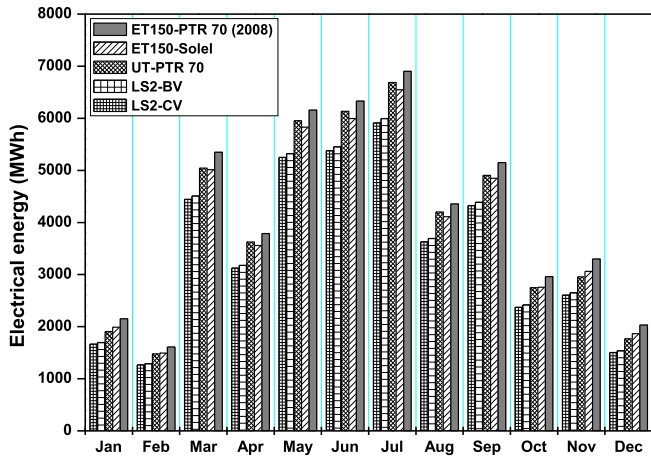
Fig. 13. Comparison of monthly energy production of different PTCs (AM II).

the ANN model's average performance is calculated by running the ANN simulation model 10 times. These simulations are performed by varying the structure of the set of input variables. The set of input variables is gradually increased by adding new items or changing the selection of items.

As mentioned before, 4 years of in situ measurements are used for the training and the validation of the ANN model. These data are separated into two sets: the training set formed by data from November 01, 2011 to December 31, 2014 and the validation set formed by data of the year 2015. The training set is classically used to compute the parameters and define the structure of the ANN. The validation data set is used to estimate the ANN's ability to interpolate values beyond the scope of its learning phase.

Table 9 summarizes the average performance obtained over the set of hourly validation data. From the values of R resulting from the sensitivity analysis, we observe that the first parameter DNI_h is the most relevant decision variable. We also observe that the values of R, RMSE, RRMSE, RMBE, and MAE are minimized by using the combination of DNI_h, $\tau_{h.y}$, $\tau_{h.d}$, t_h, ϕ_h, w_h, and E_{h-1}, namely all the decision variables of the problem.

The R-value of 0.9609 is quite high, especially when compared to the R-values obtained by the analytical models, which reach values of 0.84 and 0.86. This value corresponds to an average quadratic error (RMSE) of 2.69 MWh, which can be regarded as very low compared to the 44.7 GWh produced during one year by the power plant. Some other combinations of decision variables using fewer decision variables than the best still perform significantly better. These simpler combinations can also be used and remain

effective, as they can be calculated more quickly while remaining reasonably accurate.

The choice of the number of hidden neurons is a parameter of great importance in determining the performance of an ANN. Therefore, several numerical experiments were carried out by gradually varying the number of neurons in the hidden layer from 1 to 30 to determine the most performant structure of ANN. The decision variables DNI_h, $\tau_{h.y}$, $\tau_{h.d}$, t_h, ϕ_h,w_h, and E_{h-1} are inputs in all runs. The number of hidden neurons varies from 1 to 30 by adding a neuron to each new test. For all architectures tested, the average performance of the model in terms of R, RMSE, RRMSE, RMBE, and MAE values are presented in Table 10 for the training and validation datasets.

We can notice that the best R, RMSE, RRMSE, RMBE, and MAE values are obtained for 22 hidden neurons. The combination of DNI_h, $\tau_{h.y}$, $\tau_{h.d}$, t_h, ϕ_h, w_h, E_{h-1} with 22 hidden neurons is regarded as the best ANN model for estimating the energy production of a PTSTPP on an hourly scale.

Table 11 presents the statistical parameters obtained from the training and validation data sets by considering the best ANN model obtained with the complete set of decision variables and 22 hidden neurons. The accuracy for the training dataset is higher than for the validation dataset since the ANN model has been parameterized from the first dataset.

Fig. 14 shows the comparison between the energy production obtained from in situ measurements and ANN predictions for training and validation datasets.

The monthly distribution of operating and ANN predicted energy production is shown in Fig. 12. The electrical energy production is 44.7 GWh/year, while that predicted by the ANN model is 42.6 GWh/year. Therefore, the ANN underestimates energy production by a factor of 5%, which corresponds to the RMBE value.

4.3. Comparison between analytical models and ANN model

In this part, a comparison between analytical models and ANN model is presented. This comparison allows for evaluating the performance and capability of each model. Table 8 presents the performances obtained for validation datasets for ANN and analytical models. The values of the comparison tools prove that the ANN model is more performant and constitute a good model for estimating the electric energy production of a PTSTPP. The value of regression was about 0.97 for the ANN model, while for the AM I and AM II, the values were respectively 0.8388 and 0.8636.

Fig. 15 shows the frequency distributions of the difference between operating and predicted values of PTSTPP energy production for the ANN and analytical models for the validation year. This frequency distribution shows that approximately 86.77% of the

Table 9
Average performances of ANN model for different combinations of decision variables.

Input variables							Performances indicators				
DNI_h	$\tau_{h.y}$	$\tau_{h.d}$	t_h	ϕ_h	w_h	E_{h-1}	R	RMSE	RRMSE	RMBE	MAE
x							0.715	6.137	41.420	−0.846	5.027
x	x						0.879	4.648	29.966	−9.915	3.710
x	x	x					0.933	3.642	23.482	−9.383	2.841
x	x	x	x				0.934	3.588	23.130	−9.167	2.788
x	x	x	x	x			0.937	3.524	22.720	−9.064	2.766
x	x	x	x	x	x		0.940	3.461	22.312	−8.919	2.698
x	x	x	x	x	x	x	0.961	2.693	17.362	−5.671	1.954
x	x	x				x	0.957	2.845	18.339	−6.112	2.089
x	x	x	x			x	0.958	2.805	18.083	−5.975	2.033
x	x	x	x	x		x	0.958	2.780	17.920	−5.727	1.985
x	x	x		x		x	0.958	2.800	18.048	−5.944	2.021
x	x	x			x	x	0.959	2.776	17.896	−6.094	2.065

Table 10
Average performances of ANN models for different number of hidden neurons for the validation dataset.

Number of hidden neurons	R	RMSE	RRMSE	RMBE	MAE	Number of hidden neurons	R	RMSE	RRMSE	RMBE	MAE
1	0.913	3.825	24.657	−5.227	2.862	**16**	0.968	2.422	15.611	−5.086	1.701
2	0.930	3.515	22.661	−6.170	2.630	**17**	0.969	2.414	15.562	−5.251	1.704
3	0.950	3.042	19.610	−6.137	2.322	**18**	0.969	2.389	15.399	−4.791	1.670
4	0.959	2.759	17.788	−5.317	2.054	**19**	0.969	2.387	15.388	−4.769	1.636
5	0.961	2.693	17.362	−5.671	1.954	**20**	0.969	2.415	15.569	−5.292	1.700
6	0.963	2.598	16.751	−5.300	1.839	**21**	0.968	2.407	15.519	−4.815	1.707
7	0.965	2.565	16.538	−5.804	1.860	**22**	0.969	2.373	15.295	−4.735	1.627
8	0.966	2.511	16.186	−5.067	1.762	**23**	0.968	2.417	15.584	−4.980	1.718
9	0.966	2.512	16.198	−5.331	1.777	**24**	0.968	2.417	15.582	−4.837	1.675
10	0.967	2.462	15.875	−5.219	1.728	**25**	0.969	2.402	15.483	−4.884	1.683
11	0.967	2.463	15.878	−5.017	1.731	**26**	0.968	2.443	15.748	−5.108	1.727
12	0.968	2.440	15.730	−5.339	1.726	**27**	0.968	2.415	15.569	−4.868	1.699
13	0.968	2.421	15.607	−5.059	1.700	**28**	0.968	2.411	15.545	−4.789	1.672
14	0.969	2.409	15.528	−5.148	1.695	**29**	0.968	2.433	15.684	−4.979	1.743
15	0.969	2.387	15.387	−4.744	1.659	**30**	0.968	2.429	15.661	−4.867	1.700

Table 11
Training and validation performances of the ANN model.

	R	RMSE	RRMSE	MAE
Training dataset (ANN)	0.9703	2.1593	14.6308	1.3645
Validation dataset (ANN)	0.9692	2.3725	15.2949	1.6272

power generation deviations are less than 3 MW h for the ANN model. This value is 61.84% for the AM I and 74.96% for the AM II.

Fig. 12 illustrates the energy production obtained by the ANN model and the analytical ones and their comparison with the operating energy for different months of the year. It was found that the ANN model underestimates the annual energy production by 4.73% while AM I by 1.88%. The AM II overestimates the energy production by 12.1%.

To obtain a more detailed comparison between the ANN and Analytical models and observe the performance variation of the power plant, the daily performance of the PTSTPP was highlighted. Four typical days of the year that characterize each season were chosen to compare the performance of the ANN and analytical models in predicting the energy production of the PTSTPP. The procedure flowed to choose the typical days is based on the daily averages of DNI, ambient temperature, and energy production for each season. Consequently, January 04th, April 06th, August 16th, and October 05th have been selected as typical days. The variation of DNI, ambient temperature and wind speed are depicted in Fig. 16.

Due to the variation of the amount of DNI received by the solar field of the PTSTPP over the seasons of the year, the operation of the power plant confronts some technical constraints. This means that the hours of electricity production vary from a season to another. In fact, in winter (21st December − 20th March) and autumn (21st September − 20th December), the solar field of PTSTPP operates on average 8 h/day by supplying hot HTF at 391 °C to the power block. For spring (21st March − 20th June) and summer (21st June − 20th September), the power block produces electricity for an average of 10 and 11 h/day, respectively.

The results obtained in Fig. 17 & Table 12 present the energy obtained for typical days by using ANN and analytical models and their corresponding performances. The AM I and ANN model underestimate the energy production for every typical day considered in the figure. Whereas the AM II overestimates the energy production for all typical days. The trends and variations of the operating energy productions are very close to those predicted by the ANN model. Analytical models present lower precision in the estimations than the ANN model, but it can provide a good prognosis of electric energy production. The only situations in which the predictions with the analytical methods are less accurate correspond to the low values of the produced electric energy that are normally associated with low values of DNI (especially in the morning). However, abrupt variations in energy production are difficult to model, whatever the type of model is considered. Nevertheless, the ANN model is more efficient on this point than

Fig. 14. In situ measurements and ANN predictions for training and validation datasets.
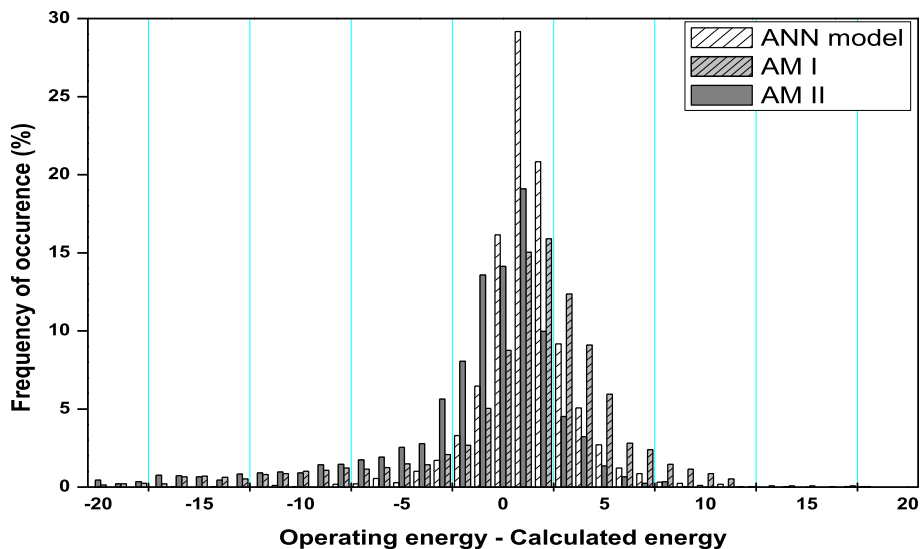
Fig. 15. Frequency distributions of the differences between measured and predicted energy production for the validation dataset.
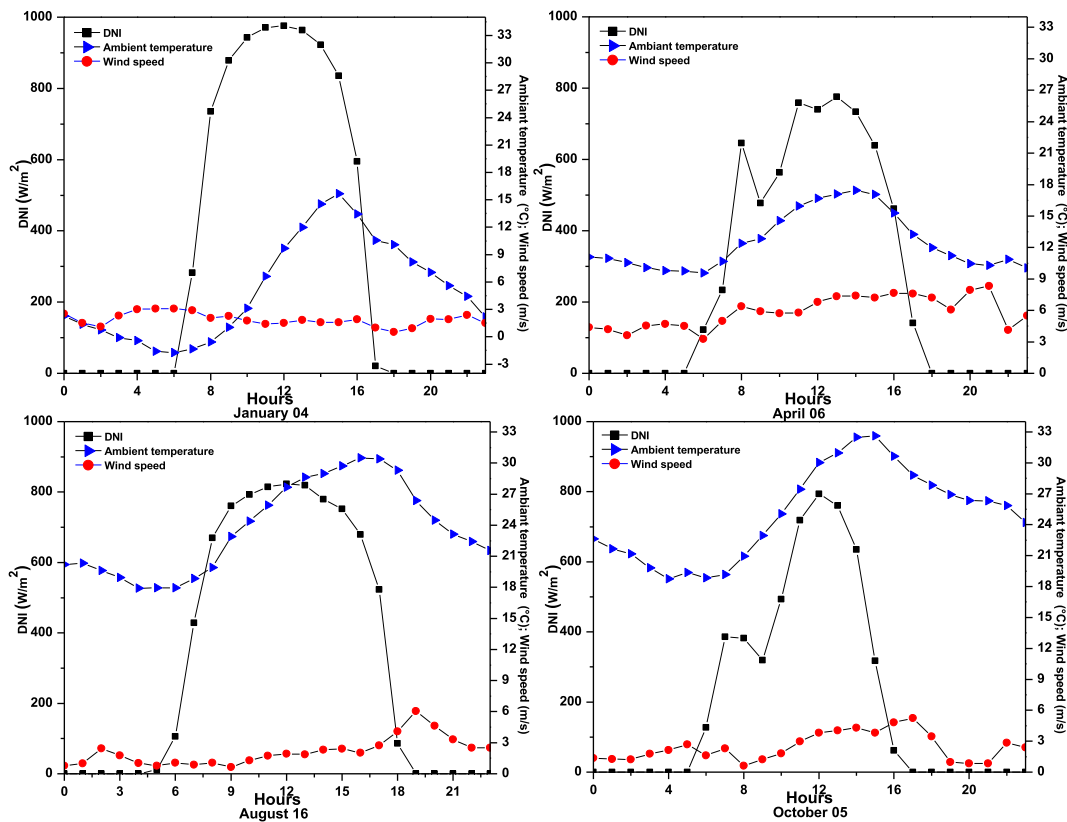
Fig. 16. Hourly DNI, ambient temperature, and wind speed for the four different typical days.

the analytical model, especially at the beginning of each start-up period.

5. Conclusions

Analytical and ANN models are knowledge and data-based models that have different advantages and disadvantages. Analytical models are slow but explanatory, while ANN models are quickly computable but only predictive. Analytical models are well suited to design since they can anticipate structural changes in the simulated system. An ANN model cannot anticipate phenomena that are beyond the scope of the data that contributed to its development. On the other hand, ANN models are well suited for controlling physical systems that require fast reactions to changing situations.

In this paper, both types of models have been investigated in the particular context of a parabolic trough solar thermal power plant. The models aim to predict the electric energy production at the
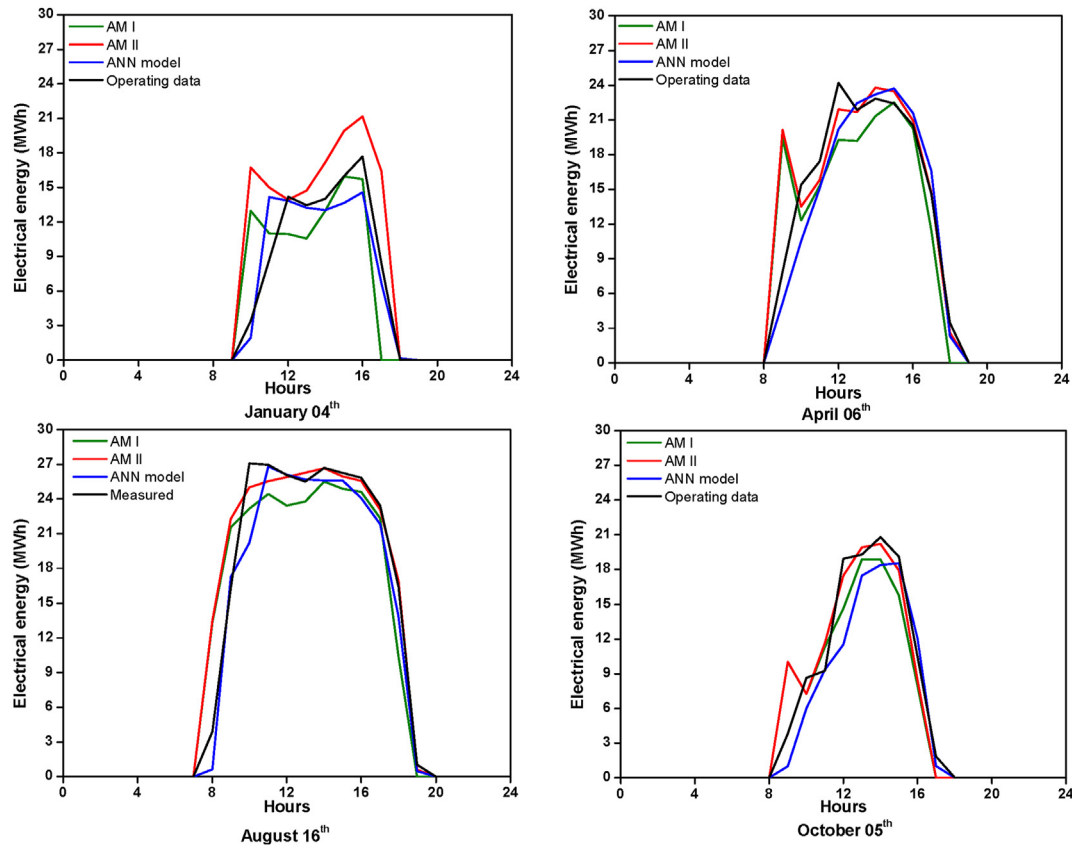
Fig. 17. Hourly experimental and predicted energy (validation dataset) for the four different typical days.

Table 12
Performances obtained for typical days by using ANN and analytical models.

Typical day												
Performances	January 4th			April 6th			August 16th			October 5th		
	AM I	AM II	ANN model	AM I	AM II	ANN model	AM I	AM II	ANN model	AM I	AM II	ANN model
R	0,67	0,74	0,91	0,77	0,80	0,95	0,90	0,94	0,98	0,90	0,93	0,94
RMSE (MWh)	4,60	5,98	0,76	4,52	4,06	2,47	4,01	3,37	1,25	3,12	2,54	3,03
RRMSE (%)	43,23	56,13	22,36	26,47	23,82	14,46	19,59	16,48	12,07	25,03	20,40	24,27
MAE (MWh)	3,27	4,43	1,74	3,29	2,16	2,03	3,12	1,83	1,64	2,67	1,97	2,24
RMBE (%)	−5,93	40,97	−4,78	−5,60	4,68	−5,65	−3,24	4,85	−7,05	−6,64	0,68	−14,98
Total energy (MWh)	90,14	135,09	91,24	161,07	178,61	160,98	237,56	257,43	228,20	104,75	112,96	95,40

output of the electric generator and, more especially, the hourly energy production of the power plant. Several ANN models are presented that vary the number and types of input variables and the number of neurons in the hidden layer; the best ANN model obtained is very accurate in evaluating energy production since it leads to an R-value (coefficient of determination) of 96%. Since Morocco is planning to implement further solar power plants with parabolic trough technology. The suggested ANN model could be used to estimate energy production of similar PTSTPP design as in ABM for other locations in Morocco.

The analytical models proposed in this paper lead to similar but lower accuracy levels than the ANN model. Compared to the experimental data, their characteristic R-value (coefficient of determination) is about 84% for AM I and 86% for AM II. From the observation of the power plant's energy production and its dynamic behavior, it can be seen that the analytical models do not correspond to most of the sudden changes in energy production. This lack of precision can be explained by the fact that our analytical

models are mainly based on the modeling of steady-state phenomena. An important perspective of this work is developing a dynamic physical model that considers the thermal inertia phenomena that influence the dynamic behavior of thermal power plants.

From a more general scientific perspective, our work and its future developments focus on model hybridization, i.e., models combining machine learning and physical modeling. Dynamic analytical models are generally difficult to develop and solve, whereas modeling and simulation of dynamic phenomena with ANNs is much easier and more efficient. Given the practical modalities of observation and measurement of thermal behavior and given their high thermal inertia, it seems important and feasible to first develop models of the dynamic behavior of solar collectors.

CRediT authorship contribution statement

Anass Zaaoumi: Conceptualization, Methodology, Numerical

Simulation, Formal analysis, Results interpretation, Formal analysis, Writing - original draftWriting — original draft, Writing - review & editingWriting — review & editing. **Abdellah Bah:** Methodology, Supervision, Project administration. **Mihaela Ciocan:** Methodology, Numerical Simulation, Formal analysis, Results interpretation, Formal analysis, Writing - original draftWriting — original draft. **Patrick Sebastian:** Supervision, Methodology, Formal analysis, Results interpretation, Formal analysis, Writing - original draftWriting — original draft, Writing - review & editingWriting — review & editing. **Mugur C. Balan:** Supervision, Methodology, Numerical Simulation, Formal analysis, Results interpretation, Formal analysis, Writing - original draftWriting — original draft. **Abdellah Mechaqrane:** Supervision. **Mohammed Alaoui:** Supervision.

Declaration of competing interest

The authors declare that they have no known competing financial interests or personal relationships that could have appeared to influence the work reported in this paper.

Acknowledgment

References

[1] T.E. Boukelia, O. Arslan, M.S. Mecibah, ANN-based optimization of a parabolic trough solar thermal power plant, Appl. Therm. Eng. 107 (2016) 1210—1218, https://doi.org/10.1016/j.applthermaleng.2016.07.084.
[2] R.A. Barreto, Fossil fuels , alternative energy and economic growth, Econ. Modell. 75 (2018) 196—220, https://doi.org/10.1016/j.econmod.2018.06.019.
[3] S.A. Kalogirou, Solar Energy Engineering: Processes and Systems, Academic Press, 2013.
[4] I. Janajreh, L. Su, F. Alan, Wind energy assessment: masdar City case study, Renew. Energy 52 (2013) 8—15, https://doi.org/10.1016/j.renene.2012.09.025.
[5] Z. Al-Hamamre, A. Al-Mater, F. Sweis, K. Rawajfeh, Assessment of the status and outlook of biomass energy in Jordan, Energy Convers. Manag. 77 (2014) 183—192, https://doi.org/10.1016/j.enconman.2013.09.041.
[6] A. Sepehri, M.H. Sarrafzadeh, Effect of nitrifiers community on fouling mitigation and nitrification efficiency in a membrane bioreactor, Chemical Engineering and Processing-Process Intensification 128 (2018) 10—18, https://doi.org/10.1016/j.cep.2018.04.006.
[7] A. Sepehri, M.H. Sarrafzadeh, Activity enhancement of ammonia-oxidizing bacteria and nitrite-oxidizing bacteria in activated sludge process: metabolite reduction and CO2 mitigation intensification process, Applied Water Science 9 (5) (2019) 131, https://doi.org/10.1007/s13201-019-1017-6.
[8] E. Barbier, Geothermal energy technology and current status: an overview, Renew. Sustain. Energy Rev. 6 (1—2) (2002) 3—65, https://doi.org/10.1016/S1364-0321(02)00002-3.
[9] B.C. Kusre, D.C. Baruah, P.K. Bordoloi, S.C. Patra, Assessment of hydropower potential using GIS and hydrological modeling technique in Kopili River basin in Assam (India), Appl. Energy 87 (1) (2010) 298—309, https://doi.org/10.1016/j.apenergy.2009.07.019.
[10] H.L. Zhang, J. Baeyens, J. Degrève, G. Cacères, Concentrated solar power plants : review and design methodology, Renew. Sustain. Energy Rev. 22 (2013) 466—481, https://doi.org/10.1016/j.rser.2013.01.032.
[11] J.J. Vidal-amaro, P. Alberg, C. Sheinbaum-pardo, Optimal energy mix for transitioning from fossil fuels to renewable energy sources — the case of the Mexican electricity system, Appl. Energy 150 (2015) 80—96, https://doi.org/10.1016/j.apenergy.2015.03.133.
[12] M.J. Montes, A. Abánades, J.M. Martínez-Val, M. Valdés, Solar multiple optimization for a solar-only thermal power plant. using oil as heat transfer fluid in the parabolic trough collectors, Sol. Energy 83 (2009) 2165—2176, https://doi.org/10.1016/j.solener.2009.08.010.
[13] M.M. Rolim, N. Fraidenraich, C. Tiba, Analytic modeling of a solar power plant with parabolic linear collectors, Sol. Energy 83 (2009) 126—133, https://doi.org/10.1016/j.solener.2008.07.018.
[14] M. Abutayeh, Y.D. Goswami, E.K. Stefanakos, Solar thermal power plant simulation, Environ. Prog. Sustain. Energy 32 (2013) 417—424, https://doi.org/10.1002/ep.11636.
[15] A.M. Patnode, Simulation and Performance Evaluation of Parabolic Trough Solar Power Plants, Ph.D. thesis, University of WisconsinMadison. Department of Mechanical Engineering, 2006.
[16] G. Manzolini, A. Giostri, C. Saccilotto, P. Silva, E. Macchi, Development of an innovative code for the design of thermodynamic solar power plants part A: code description and test case, Renew. Energy 36 (2011) 1993—2003, https://doi.org/10.1016/j.renene.2010.12.027.
[17] I.L. García, D. Blanco, A. Luis, Performance model for parabolic trough solar thermal power plants with thermal storage: comparison to operating plant data, Sol. Energy 85 (2011) 2443—2460, https://doi.org/10.1016/j.solener.2011.07.002.
[18] H. Schenk, J. Dersch, T. Hirsch, T. Polklas, Transient simulation of the power block in a parabolic trough power plant, in: 11th International Modelica Conference.Versailles.France, 2015, https://doi.org/10.3384/ecp15118605.
[19] M. Tahtinen, L. Kannari, R. Weiss, H. Mikkonen, Dynamic modelling of concentrated solar power and power plant integration, in: 4th Solar Integration Workshop. Berlin.Germany, 2014.
[20] W.A.K. Al-maliki, F. Alobaid, V. Kez, B. Epple, Modelling and dynamic simulation of a parabolic trough power plant, J. Process Contr. 39 (2016) 123—138, https://doi.org/10.1016/j.jprocont.2016.01.002.
[21] S. Rohani, T.P. Fluri, F. Dinter, P. Nitz, Modelling and simulation of parabolic trough plants based on real operating data, Sol. Energy 158 (2017) 845—860, https://doi.org/10.1016/j.solener.2017.10.023.
[22] F. Yang, H. Cho, H. Zhang, J. Zhang, Y. Wu, Artificial neural network (ANN) based prediction and optimization of an organic Rankine cycle (ORC) for diesel engine waste heat recovery, Energy Convers. Manag. 164 (2018) 15—26, https://doi.org/10.1016/j.enconman.2018.02.062.
[23] A.H. Elsheikh, S.W. Sharshir, M. Abd Elaziz, A.E. Kabeel, W. Guilan, Z. Haiou, Modeling of solar energy systems using artificial neural network: a comprehensive review, Sol. Energy 180 (2019) 622—639, https://doi.org/10.1016/j.solener.2019.01.037.
[24] S.A. Kalogirou, C.C. Neocleous, C.N. Schizas, Artificial neural networks for modelling the starting-up of a solar steam-generator, Appl. Energy 60 (2) (1998) 89—100, https://doi.org/10.1016/S0306-2619(98)00019-1.
[25] S.Y. Heng, Y. Asako, T. Suwa, K. Nagasaka, Transient thermal prediction methodology for parabolic trough solar collector tube using artificial neural network, Renew. Energy 131 (2019) 168—179, https://doi.org/10.1016/j.renene.2018.07.037.
[26] H. Othieno, J. Awange, Energy Resources in Africa, Distribution, Opportunities and Challenges, Springer, 2016.
[27] B.J. Alqahtani, D. Patiño-Echeverri, Integrated solar combined cycle power plants: paving the way for thermal solar, Appl. Energy 169 (2016) 927—936, https://doi.org/10.1016/j.apenergy.2016.02.083.
[28] J. Duffie, W.A. Beckman, Solar Engineering of Thermal Processes, second ed., John Wiley & Sons, Singapore, 1991.
[29] M. Günther, M. Joemann, S. Csambor, Advanced CSP Teaching Materials. Chapter 5. Parabolic Trough Technology, ENERMENA, 2011.
[30] S.A. Kalogirou, A detailed thermal model of a parabolic trough collector receiver, Energy 48 (1) (2012) 298—306, https://doi.org/10.1016/j.energy.2012.06.023.
[31] F. De Luca, V. Ferraro, V. Marinelli, On the performance of CSP oil-cooled plants, with and without heat storage in tanks of molten salts, Energy 83 (2015) 230—239, https://doi.org/10.1016/j.energy.2015.02.017.
[32] T. Crescenzi, M. Falchetta, A. Fontanella, E. Metelli, A. Miliozzi, F. Spinelli, L. Sipion, Opportunità di applicazione delle tecnologie solari termodinamiche in Italia, Agenzia nazionale per le nuove tecnologie, l'energia e lo sviluppo economico sostenibile, ENEA), 2016.
[33] M. Marefati, M. Mehrpooya, M. Behshad, Optical and thermal analysis of a parabolic trough solar collector for production of thermal energy in different climates in Iran with comparison between the conventional nano fluids, J. Clean. Prod. 175 (2018) 294—313.
[34] P.H. Wagner, Thermodynamic Simulation of Solar Thermal Power Stations with Liquid Salt as Heat Transfer Fluid, Diploma thesis, Technical University of Munich, 2012. Available from: http://elib.dlr.de/83921/.
[35] A. Zaaoumi, M. Asbik, H. Hafs, A. Bah, M. Alaoui, Thermal performance simulation analysis of solar field for parabolic trough collectors assigned for ambient conditions in Morocco, Renew. Energy 163 (2021) 1479—1494, https://doi.org/10.1016/j.renene.2020.08.151.
[36] F. Burkholder, C.F. Kutscher, Heat Loss Testing of Schoot's 2008 PTR70 Parabolic Trough Receiver, NREL, 2009. Technical Report NREL/TP-550-45633.
[37] R. Forristall, Heat Transfer Analysis and Modeling of a Parabolic Trough Solar Receiver Implemented in Engineering Equation Solver, NREL, 2003. Technical Report NREL/TP-550-34169.
[38] V. Dudley, G. Kolb, M. Sloan, D. Kearney, SEGS LS2 solar collector-test results, Tech. Rep.; Report of Sandia National Laboratories (1994) (SANDIA94-1884).
[39] M. Geyer, E. Lüpfert, R. Osuna, A. Esteban, W. Schiel, A. Schweitzer, E. Zarza, P. Nava, J. Langenkamp, E. Mandelberg, Eurotrough - parabolic Trough collector developed for cost efficient solar power generation, in: 11th Int. Symposium on Concentrating Solar Power and Chemical Energy Technologies, September 4-6, 2002 (Zurich, Switzerland).
[40] G. Morin, J. Dersch, W. Platzer, M. Eck, A. Haberle, Comparison of linear Fresnel and parabolic trough collector power plants, Sol. Energy 86 (1) (2012) 1—12, https://doi.org/10.1016/j.solener.2011.06.020.
[41] A. Giostri, M. Binotti, M. Astolfi, P. Silva, E. Macchi, Comparison of different

solar plants based on parabolic trough technology, Sol. Energy 86 (5) (2012) 1208–1221, https://doi.org/10.1016/j.solener.2012.01.014.

[42] L. Valenzuela, R. López-martín, E. Zarza, Optical and thermal performance of large-size parabolic-trough solar collectors from outdoor experiments: a test method and a case study, Energy 70 (2014) 456–464, https://doi.org/10.1016/j.energy.2014.04.016.

[43] N. Fraidenraich, C. Oliveira, A.F. Vieira, J.M. Gordon, O.C. Vilela, Analytical modeling of direct steam generation solar power plants, Sol. Energy 98 (2013) 511–522, https://doi.org/10.1016/j.solener.2013.09.037.

[44] M. Larcher, M. Rommel, A. Bohren, E. Frank, S. Minder, Characterization of a parabolic trough collector for process heat applications, Energy Procedia 57 (2014) 2804–2811, https://doi.org/10.1016/j.egypro.2014.10.313.

[45] H. Schenk, T. Hirsch, J.F. Feldhoff, M. Wittmann, Energetic comparison of linear Fresnel and parabolic trough collector systems, J. Sol. Energy Eng. 136 (4) (2014), https://doi.org/10.1115/1.4027766.

[46] PTMx Parabolic Trough Collector – Technical Data Sheet, Soltigua, 2014.

[47] M.J. Montes, Análisis y propuestas de sistemas solares de alta exergía que emplean agua como fluido calorífero, PhD Thesis, Escuela Técnica Superior de Ingenieros Industriales, Madrid, 2008.

[48] A. Giostri, M. Binotti, P. Silva, E. Macchi, G. Manzolini, Comparison of two linear collectors in solar thermal plants: parabolic trough vs FRESNEL, in: Proceedings of the ASME 2011 5th International Conference on Energy Sustainability ES2011 August 7-10, 2011 (Washington, DC, USA).

[49] H. Yang, Q. Wang, X. Huang, J. Li, G. Pei, Performance study and comparative analysis of traditional and double-selective-coated parabolic trough receivers, Energy 145 (2018) 206–216, https://doi.org/10.1016/j.energy.2017.12.126.

[50] G. Najafi, B. Ghobadian, T. Tavakoli, D.R. Buttsworth, T.F. Yusaf, M. Faizollahnejad, Performance and exhaust emissions of a gasoline engine with ethanol blended gasoline fuels using artificial neural network, Appl.

[51] B. Khoshnevisan, S. Rafiee, M. Omid, H. Mousazadeh, Development of an intelligent system based on ANFIS for predicting wheat grain yield on the basis of enrgy inputs, Information Processing in Agriculture 1 (1) (2014) 14–22, https://doi.org/10.1016/j.inpa.2014.04.001.

[52] M. Karamirad, M. Omid, R. Alimardani, H. Mousazadeh, S.N. Heidari, ANN based simulation and experimental verification of analytical four-and five-parameters models of PV modules, Simulat. Model. Pract. Theor. 34 (2013) 86–98, https://doi.org/10.1016/j.simpat.2013.02.001.

[53] Ö.A. Dombaycı, M. Gölcü, Daily means ambient temperature prediction using artificial neural network method: a case study of Turkey, Renew. Energy 34 (4) (2009) 1158–1161, https://doi.org/10.1016/j.renene.2008.07.007.

[54] M. Imran, S.A. Alsuhaibani, A Neuro-Fuzzy Inference Model for Diabetic Retinopathy Classification, Intelligent Data Analysis for Biomedical Applications (2019) 147–172, https://doi.org/10.1016/B978-0-12-815553-0.00007-0. Academic Press.

[55] W. Yaïci, E. Entchev, Performance prediction of a solar thermal energy system using artificial neural networks, Appl. Therm. Eng. 73 (1) (2014) 1348–1359, https://doi.org/10.1016/j.applthermaleng.2014.07.040.

[56] S.A. Kalogirou, Artificial neural networks in renewable energy systems applications: a review, Renew. Sustain. Energy Rev. 5 (2000) 373–401.

[57] S. Haykin, Neural Networks: A Comprehensive Foundation, second ed., Prentice-Hall, New Jersey, 1999.

[58] S. Haykin, Neural Networks and Learning Machines, third ed., Prentice Hall, New Jersey, 2009.

[59] B. Ihya, a. Mechaqrane, R. Tadili, M.N. Bargach, Prediction of hourly and daily diffuse solar fraction in the city of Fez (Morocco), Theor. Appl. Climatol. 120 (2015) 737–749, https://doi.org/10.1007/s00704-014-1207-y.
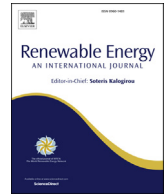
Energy 86 (5) (2009) 630–639, https://doi.org/10.1016/j.apenergy.2008.09.017.

Thermal performance simulation analysis of solar field for parabolic trough collectors assigned for ambient conditions in Morocco

Anass Zaaoumi[*], Mohamed Asbik, Hajar Hafs, Abdellah Bah, Mohammed Alaoui

Center of Energy, ERTE, Ecole Normale Supérieure de l'Enseignement Technique, Mohammed V University in Rabat, BP 6207, Rabat, 10100, Morocco

ARTICLE INFO

ABSTRACT

This paper aims to assess thermal performances of the solar field of the Integrated Solar Combined Cycle (ISCC) power plant at Aïn Beni Mathar (ABM) in Morocco for the year of 2015. Thus, mathematical modeling of the Schott PTR-70 2008 solar receiver consists of energy balance equations which were solved using COMSOL Multiphysics software. Next, the model was validated with empirical data from the literature, so the comparison is satisfactory. Results analyze daily and annual thermal performances of the plant, and also comparison between simulated and actual plant operating results. Indeed, for selected typical days, it was concluded that the model's predictions seem to be adequate except at the beginning and end of each day. On the other hand, the estimates of cumulative thermal productions for selected ten days of each season were also carried out. Accordingly, the actual operating thermal energy is very close to simulated one for all chosen days since the relative error does not exceed 3.27% in the worse case. Unlike summer season (25.86 GWh in July), the monthly average thermal production is low in winter (about 6.0 GWh), as expected. In conclusion, the annual operating thermal production is about 172.5 GWh/year versus 176.3 GWh/year estimated value.

© 2020 Elsevier Ltd. All rights reserved.

1. Introduction

Concentrating solar power (CSP) plants are one of the most promising technologies to produce electric power [1]. Four technologies were developed, including the parabolic trough, solar tower, solar dish and linear Fresnel systems. Among them, the parabolic trough collectors (PTCs) which are actually the most commercialized and mature solar technology for solar harvesting [2,3]. They are usually used for solar steam generation due to their relatively high temperatures (up to 400 °C). Also, this technology can be employed in other industrial applications at low temperatures such as: desalination and sterilization processes.

Solar field of PTCs is the key component of a CSP plant. Many research works have been carried out to study the thermal performances and heat transfer characteristics of PTCs. Generally, published studies could be divided into two main categories: testing models and performance models [4]. Performance models are usually used to estimate the thermal power or the thermal efficiency of a single module, or a parabolic solar collector loop or the entire solar field. Well know specific PTC parameters such as optical

and thermal properties are required to simulate its thermal behavior. Those parameters information could be determined by performing a testing model.

Reviews existing literature show that PTC performance models can be either steady state models or dynamic models. S. A. Kalogirou [5] developed a detailed thermal model of solar parabolic trough collector that would have been installed in Cyprus University of Technology, to determine its performances. In his analysis, the author took into account all modes of heat transfer between the elements of the modeled receiver. The model equations have been solved by using Engineering Equation Solver (EES), and then the proposed model was validated by experimental results conducted in Sandia National Laboratories (SNL). Accordingly, he concluded that the comparison was satisfactory. Yılmaz et al. [6] referred to the same subject when they developed a thermo-mathematical modeling of a parabolic trough solar collector to simulate its thermal performance under different operating conditions. Indeed, as previous several works, all modeled equations were solved using EES, and compared to available SNL data. The comparison seems reasonable. Moreover, the proposed model was then applied to an existing parabolic trough solar collector module to highlight its thermal performances. Bouhal et al. [7] assessed the thermal performance of a PTC under six climatic regions in Morocco. A steady state physical model is developed to determine flow parameters

---

* Corresponding author.
E-mail addresses: a.zaaoumi@gmail.com, anass.zaaoumi@um5s.net.ma
(A. Zaaoumi).

Nomenclature

A	Cross sectional area, (m^2)
A_c	Aperture area in a loop, (m^2)
b	Interaction coefficient, $(-)$
Bi	Biot number, $(-)$
c	Accommodation coefficient, $(-)$
C_p	Heat capacity, (J/kg.K)
D	Tube diameter, (m)
fr	Friction factor, $(-)$
f	Focal distance of the collector, (m)
f_1	Factor between 0 and 1 to account for any additional reduction in energy absorption by the solar field loops, $(-)$
f_{clean}	Mirror cleanliness factor, $(-)$
$f_{dustEnv}$	Factor related to the light absorption of dust on the receiver glass cover, $(-)$
$f_{EndLoss}$	End effect loss, $(-)$
$f_{RowShad}$	Row shading, $(-)$
h	Heat transfer coefficient, (W/m^2K)
H	Height of the parabolic trough (m)
HL	Heat loss, (W/m)
I_b	Direct normal irradiation, (W/m^2)
k	Thermal conductivity, (W/mK)
L	Length, (m)
m	Mass in segment, (kg)
Nu	Nusselt number, $(-)$
P	Pressure, (Pa)
Pr	Prandlt number, $(-)$
Q_x	Heat flow coming to the segment, (W)
$Q_{x+\Delta x}$	Heat flow leaving the segment, (W)
Q	Heat flow for receiver segment, (W)
Ra	Rayleigh number, $(-)$
Re	Reynolds number, $(-)$
T	Temperature, (K)
t	Time, (s)
V	velocity, (m/s)
W	Width, (m)
w	hour angle, $(°)$

Abbreviations

DNI	Direct normal irradiation

HCE	Heat Collector Element
HTF	Heat transfer fluid
ISCC	Integrated Solar Combined Cycle
SCA	Solar Collector Assemblies

Greek letters

α	Absorptance
γ	Ratio of specific heats for the annulus gas
δ	Molecular diameter of annulus gas (cm) or Declination $(°)$
ε	Emissivity
$\eta_{opt,0}$	Peak optical efficiency
λ	mean-free-path between collisions of a molecule, (cm)
ρ	Density, (kg/m^3)
ρ_{cl}	Clean mirror reflectance
σ	Stefan-Boltzmann constant $(5.67*10^{-8} W/m^2K^4)$
τ	Transmittance
θ	Incidence angle, $(°)$
θ_z	Zenith angle, $(°)$
$k(\theta)$	Incident angle modifier
$\dot{m}$	Mass flow rate, (kg/m^3)

Subscripts

a	Absorber
ai	Absorber interior diameter
ae	Absorber exterior diameter
amb	Ambient
an	Annulus
av	Average
conv	Convection
diff	Diffusion
g	Glass envelope
Loop	Loop
Space	Space between rows in the solar field
sky	Sky
sol	Solar radiation
std	Standard
rad	Radiation
u	useful
w	Wind
x	length

and heat transfer applied to PTC technology. They deduced that the installation location and weather conditions are determinant parameters in controlling the global performance of the parabolic trough solar collectors. The obtained results show also that the selection of thermal heat transfer fluid plays a crucial role in increasing CSP efficiency and cost-effectiveness. Additionally, Zaharil et al. [8] performed an energetic and exergetic study that aims to evaluate and compare performances of 6 different heat transfer fluids (HTFs) (Pressurized water, Therminol VP-1, Syltherm 800, Solar salt, Hitec XL and liquid sodium) under various inlet temperature values (300K–900K) and climatic conditions (based on Malaysian climatic condition). 1D mathematical model has been developed and written in MATLAB programming language. It has been highlighted that the Liquid sodium at the temperature level of 700K showed the highest exergetic gain for any potential implementation of PTSC power plant in Malaysia. For a large scale power plant, Patnode [9] developed a model for the solar field using the TRNSYS simulation tool. The steady-state power cycle performance was regressed in terms of heat transfer fluid mass flow rate, the heat transfer fluid temperature and condensing pressure. The model was validated with measured temperature and flow rate data from the Nine Electric Generation Systems VI plant (California, USA) from 1998 to 2005. This work includes heat loss effect by broken glass annulus, vacuum loss and very low hydrogen permeation between glass cover to absorber surface. It was concluded that very low hydrogen permeation (1 torr) increases heat loss from 400 W/m to 1200 W/m in heat collecting element (HCE) from perfect vacuum annulus. For broken glass cover, heat loss was 600 W/m at 400 °C HTF temperature. Manzolini et al. [10] published a steady state model to predict performance and preliminary CSP plant sizing at normal nominal conditions for different plant layouts. The model was based on energy balance equations applied along the length of the HCE of the solar field and validated with experimental indoor tests from national renewable energy laboratory (NREL). Abutayeh [11] presented a detailed model of a real solar thermal power plant developed from steady state power plant simulation software. In this numerical model, the parabolic trough collectors track the sun movement on a single axis.

Simulation results matched well with plant data including data collected during warm up and cool down transient operations.

Because of the intermittency of solar energy, the solar field needs to be studied as a dynamic system to predict accurately its operating conditions. M. Ouagued et al. [12] and Y. Marif et al. [13] examined thermal performances of a parabolic trough collector under Algerian climate conditions. In reference [12], the study was simultaneously focused on the potential of direct solar irradiation of Algeria, and the estimation of temperature, heat gain and heat loss of a PTC in terms of various thermal oils. To reach this last objective, they undertook a heat transfer model subject to a solar tracking system. The solar absorber was divided into several segments and then energy conservation principle has been applied to each of them over a section of the heat collector element (solar receiver). Modified Euler Method allowed solving the obtained differential equations system. The results show that an increase in temperature of heat transfer fluid and absorber tube generates the augmentation of heat loss as well as the reduction of heat gain. As for the reference of Marif et al. [13], it dealt with numerical simulation of solar parabolic through collector. Their work was based on one dimensional energy balance approach solved using implicit numerical finite difference scheme, after meshing the absorber pipe, glass envelope and the HTF. Afterwards, the established algebraic systems were simultaneously solved by Gauss-Seidel iterative method. Note that two fluids were used as HTF: TherminolVP-1™ synthetic oil and liquid water. Numerical simulation results were validated by experimental data obtained from SNL, and it was found that the thermal efficiency varies from 69.73 to 72.24%. The research team of PROMES laboratory [14] has benefited from 1D thermal model to obtain performances of its pilot PTC during transient mode. Furthermore, it describes the thermal behavior of the HTF, the absorber tube and the glass cover all the more so a uniform solar irradiation is considered too. The results of the model have been firstly compared with those of two different experimental setups, in steady-state conditions. Secondly, for comparison purpose during two periods of time with varying inlet conditions, experimental and numerical results were combined. As a result, it was found that the model is capable of predicting the thermal behavior of the parabolic trough collector with changeable climate and environment conditions (DNI, mass flow, inlet temperature). In the worst case, the relative standard error value is of 9.6%. García et al. [15] proposed a detailed performance model of a 50 MWe parabolic trough solar thermal power plant with two thermal storage molten salt tanks using Wolfram's Mathematica 7 software. The solar field is composed of 156 loops, of which each contains four solar collector assemblies (SCA) that consists of 12 solar collector elements (SCE). Empirical correlations obtained from the NREL for different types of commercial HCEs were implemented in the simulation program. The simulation results compared with measurements resulting from experiments for 42 days in summer at the Andasol2 power plant in Spain showing good agreement for clear days. Tähtinen et al. [16] developed a dynamic model of power plant. Two models of solar field have been implemented using the Advanced Process Simulation Software (APROS) which is based on parabolic cylindrical and linear Fresnel reflector technologies. Both solar field models use water as a heat transfer fluid. Based also on APROS, a full scale dynamic model of the solar power plant (Andasol II, Spain) was presented by Al-Maliki et al. [17]. The comparison between simulation results and measured data showed a reliable prediction of the real behavior of the investigated solar power plant. Rohani et al. [18] used ColSimCSP tool developed at Fraunhofer ISE to assess performance parameters of solar field (thermal power and net electrical energy yield) associated with the commercial PTC power plant Andasol 3 (Spain) for ten consecutive days of three different months (July, September and November). Special attention was given to storage strategy and start time operation. Results of simulation showed that the lowest mean

deviation of solar field thermal power and net electrical energy yield are 0.59% and 2.29% respectively.

The purpose of this study is to demonstrate the daily and annual behavior of the sole CSP plant. This paper, by the way, presents operating data of thermal production and efficiency of the solar field of the Integrated Solar Combined Cycle (ISCC) power plant of Aïn Beni Mathar site (Morocco) during 2015. Those operating data will be compared with the proposed thermal model. This will allow us to better analyze the thermal performances of the considered solar field. To this end, numerical simulation is performed using COMSOL Multiphysics software.

2. Thermal analysis of the parabolic trough collector

2.1. Description of the system

The considered system is among the most important part of a parabolic trough collector. It is a solar receiver (Fig. 1) or HCE which is known as Schott PTR 70 type. Its specific characteristics are presented in Table 1. Usually, it is installed at the focal axis of a PTC to receive the reflected direct solar irradiation coming from a parabolic reflector. The solar receiver is mainly composed of the stainless-steel surrounded by an evacuated glass envelope to decrease heat losses, an absorber tube, and heat transfer fluid (HTF). The role of the absorber is to transmit the heat energy to the HTF (Therminol VP-1), whose temperature can reach 391 °C. Note that, the cylindrical coordinates (r, x) are adopted in this study.

2.2. Hypotheses

The thermal model of the parabolic trough collector is based on energy balance inside the main elements of solar receiver (glass envelope, absorber tube and HTF) which are coupled with appropriate boundary conditions. In order to simplify this mathematical model, the following assumptions are taken into account:

- 1D transient heat balance regime is considered,
- there is the vacuum in the annular between absorber and glass cover,
- there is no radial heat conduction within the glass envelope, the absorber tube and the HTF,
- thermo-physical properties of the heat transfer fluid depend on the temperature,
- the HTF flow is turbulent and its mass flow rate is assumed to be constant.

2.3. Mathematical formulation

Considering the previous hypotheses, energy balance equation of each medium (element) is given below.

2.3.1. Governing equations for the HTF

The heat balance of the HTF could be expressed by temperature differential equation [22]:

$$m_{HTF}.\frac{\partial(C_{p_{HTF}}.T_{HTF})}{\partial t} = Q_x - Q_{(x+\Delta x)} + Q_{HTF,diff} + Q_{HTF,conv} \qquad (1)$$

The heat balance per unit of length is as follows.
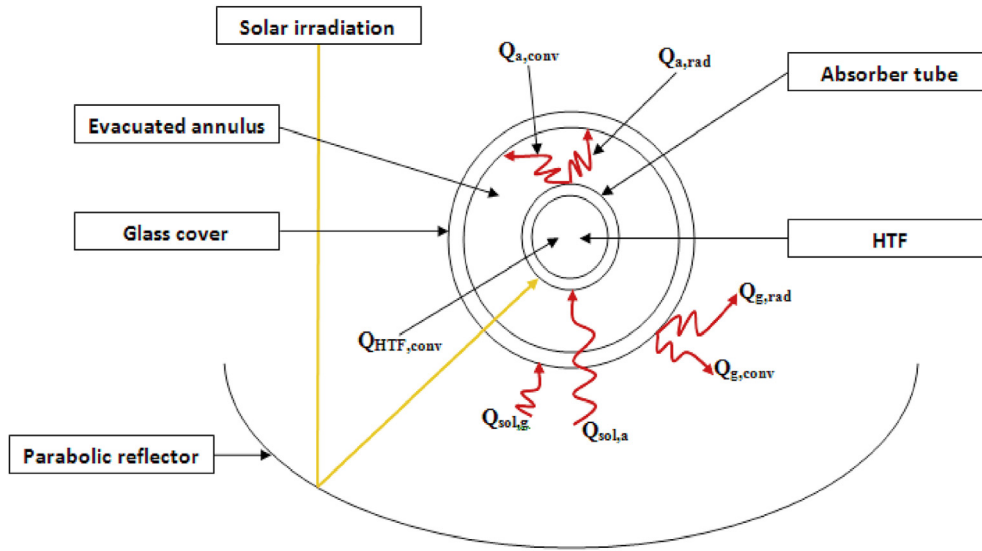
(a)
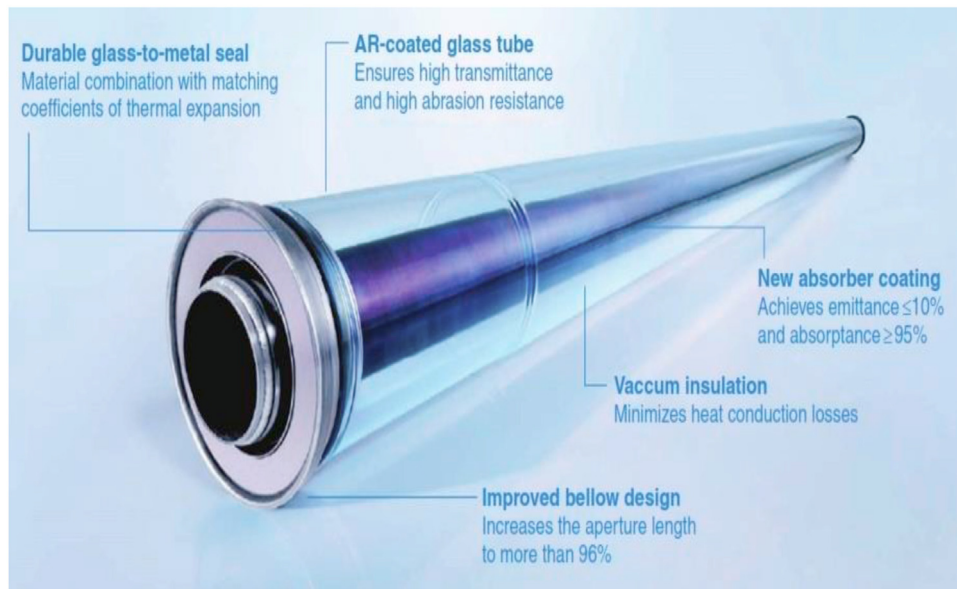
(b)

Fig. 1. Schematic view of the solar receiver.
(a) Schematic and heat transfer process of the receiver.
(b) The solar receiver tube [19].

$$A_{HTF}\frac{\partial(\rho_{HTF}.C_{p_{HTF}}T_{HTF})}{\partial t} = -\dot{m}_{HTF}.\frac{\partial(C_{p_{HTF}}T_{HTF})}{\partial x}$$
$$+ A_{HTF}.\frac{\partial}{\partial x}\left(k_{HTF}\frac{\partial T_{HTF}}{\partial x}\right) \qquad (2)$$
$$+ h_{HTF}..D_{ai}.(T_a - T_{HTF})$$

with

$$A_{HTF} = \left(\pi D_{ai}^2\right)\Big/4 \qquad (3)$$

2.3.2. Energy balance in the absorber tube

The heat balance associated to the absorber tube is expressed by Ref. [22]:

$$m_a.C_{p_a}.\frac{\partial T_a}{\partial t} = Q_{sol,a} + Q_{a,diff} - Q_{HTF,conv} - Q_{a,conv} - Q_{a,rad} \qquad (4)$$

and then

Table 1
Characteristics of the solar receiver [5,20–22].

Designation	Characteristics
Receiver type	Schott PTR-70 2008
Absorber material type	304L
HTF type	Therminol VP-1
HTF density (kg/m^3)	$-0.90797*T(°C)+0.00078116*T^2(°C)-2.367*10^{-6}*T^3(°C)+ 1083.25$
HTF specific heat (kJ/kgK)	$0.002414*T(°C)+5.9591*10^6*T^2(°C)-2.9879*10^{-8}*T^3(°C) +1.498$
HTF thermal conductivity (W/mK)	$-8.19477*10^{-5}*T(°C)-1.92257*10^{-7}*T^2(°C)+2.5034*10^{-11} *T^3(°C) +0.137743$
HTF kinematic viscosity (mm^2/s)	$e^{([544.149/(T(°C)+114.43)]-2.59578)}$
Thermal conductivity of the absorber pipe (W/mK)	$0.013*T_a+15.2$
Density of the absorber pipe (kg/m^3)	8020
Specific heat of glass envelope (J/kgK)	1090
Density of glass envelope (kg/m^3)	2230
Radiation emissivity of glass envelope (ε_g)	0.89
Radiation emissivity of absorber	$0.062 + 2*10^{-7}* T_a^2$
Absorber internal diameter (m)	0.066
Absorber external diameter (m)	0.07
Glass cover internal diameter (m)	0.114
Glass cover external diameter (m)	0.12

$$\rho_a.A_a.C_{p_a}\frac{\partial T_a}{\partial t}=\frac{Q_{sol,a}}{L}+A_a.k_a\frac{\partial^2 T_a}{\partial x^2}-h_{HTF}.\pi.D_{ai}.(T_a-T_{HTF})$$
$$-h_{an}.\pi.D_{ae}.(T_a-T_g)-\frac{\sigma\pi D_{ae}\left(T_a^4-T_g^4\right)}{\frac{1}{\varepsilon_a}+\frac{(1-\varepsilon_g)D_{ae}}{\varepsilon_g D_{gi}}}\tag{5}$$

with

$$A_a=\frac{\pi\left(D_{ae}^2-D_{ai}^2\right)}{4}\quad and$$
$$\varepsilon_a=0.000327(T_a+273.15)-0.06597\tag{6}$$

2.3.3. Energy balance in the glass envelope

For this main component, we get the following heat balance [22]:

$$m_g.C_{p_g}.\frac{\partial T_g}{\partial t}=Q_{sol,g}+Q_{g,diff}+Q_{a,conv}+Q_{a,rad}-Q_{g,conv}-Q_{g,rad}\tag{7}$$

Consequently,

$$\rho_g.A_g.C_{p_g}\frac{\partial T_g}{\partial t}=\frac{Q_{sol,g}}{L}+A_g.k_g\frac{\partial^2 T_g}{\partial x^2}+h_{an}.\pi.D_{ae}.(T_a-T_g)$$
$$+\frac{\sigma.\pi.D_{ae}\left(T_a^4-T_g^4\right)}{\frac{1}{\varepsilon_a}+\frac{(1-\varepsilon_g)D_{ae}}{\varepsilon_g D_{gi}}}-h_{amb}.\pi.D_{ge}.(T_g-T_{amb})$$
$$-\sigma.\pi.D_{ge}\left(T_g^4-T_{sky}^4\right)\tag{8}$$

with

$$A_g=\frac{\pi\left(D_{ge}^2-D_{gi}^2\right)}{4}\quad and\quad T_{sky}=0.0553T_{amb}^{1.5}\tag{9}$$

2.4. Estimation of convective heat transfer coefficients

This study requires knowledge of various convective heat transfer coefficients which will be deduced from appropriate empirical correlations. These correlations are those of Nusselt numbers that depend on several main parameters, especially flow regime (laminar or turbulent) and convection type (free or forced).

2.4.1. Convective heat transfer coefficient between the HTF and the absorber tube

At typical operating conditions, the flow of HTF inside the absorber tube is considered to be turbulent and transitional, and the following correlation was chosen [23]:

$$Nu_{HTF}=\frac{\left(\frac{fr}{8}\right)(Re_{HTF}-1000)(Pr_{HTF})}{1+12.7\sqrt{\frac{fr}{8}}(Pr_{HTF}^{2/3-1)}}\ with\ 2300\le Re_{HTF}\le 5\times 10^6\ and\ 0.5\le Pr_{HTF}\le 2000\tag{10}$$

where

$$fr=(1.82\log(Re_{HTF})-1.64)^{-2}\tag{11}$$

So, the convective heat transfer coefficient, hHTF, between HTF the internal pipe wall is estimated by.

$$h_{HTF}=Nu_{HTF}\frac{k_{HTF}}{D_{ai}}\tag{12}$$

2.4.2. Convective heat transfer coefficient between the absorber tube and the glass envelope

To determine the convective heat transfer coefficient between the absorber and the glass envelope, we suppose that the HCE annulus is under vacuum ($P_{an}\le 100$ mmHg). The convective heat transfer between the absorber and the glass envelope is due to free-

molecular convection [5]. Thus,

$$h_{an} = \frac{k_{std}}{\frac{D_{ae}}{2\ln\left(\frac{D_{gi}}{D_{ae}}\right)} + b\lambda\left(\frac{D_{ae}}{D_{gi}} + 1\right)} \quad \text{for} \quad Ra_{an} < \left(\frac{D_{gi}}{D_{gi} - D_{ae}}\right)^4$$

(13)

This correlation includes the Rayleigh number (Ra_{an}) and others parameters defined below:

$$b = \frac{(2 - ac)(9\gamma - 5)}{2ac(\gamma + 1)}, \lambda = 2.33 \times 10^{-20} \frac{T_{av}}{P_{an}\delta^2} \text{ and } T_{av} = \frac{T_a + T_g}{2}$$

(14)

2.4.3. Convective heat transfer coefficient between the glass envelope and the ambient

In taking into account the presence of the wind (forced convection), the convective heat transfer coefficient, h_{amb}, between the external surface of the glass envelope and the ambient is deduced from the expression as follows [23]:

$$h_{HTF} = Nu_{amb}\frac{K_{amb}}{D_{ge}}$$

(15)

with

$$Nu_{amb} = Re_{D_{ge}}^m \Pr_{amb}^n \left(\frac{\Pr_{amb}}{\Pr_{ge}}\right)^{1/4} \quad \text{for } 1.0 < Re_{D_{ge}} < 10^6 \text{ and } 0.7 < \Pr_{amb} < 500$$

(16)

The constant values of C and m are given in Table 2 [5], and the exponent n was taken equal to 0.37 for $\Pr_{ge} \leq 10$ and 0.36 in the case where $\Pr_{ge} > 10$.

2.5. Estimation of solar power absorption

2.5.1. Solar power absorbed by the absorber pipe

The portion of solar power absorbed by the absorber pipe is obtained by Ref. [17].

$$Q_{sol,a} = I_b A_c \eta_{opt,0} K(\theta) f_{RowShad} f_{EndLoss} f_{Clean} f_{DustEnv} \eta_{track} f_1$$

(17)

where A_c is the mirror aperture area in a loop, I_b is the direct normal irradiation and $\eta_{opt,0}$ is the peak optical efficiency (the optical efficiency at zero angle of incidence) and is expressed as follow [24]:

$$\eta_{opt,0} = \rho_{Cl}\tau_g\alpha_a\gamma$$

(18)

$K(\theta)$ is the incident angle modifier and can be evaluated for ET150 collectors by Ref. [25].

Table 2
Constant values of C and m with respect to Reynolds number range.

Re_{Dg}	C	m
1–40	0.75	0.4
40–1000	0.51	0.5
1000–200000	0.26	0.6
200000–10^6	0.076	0.7

$$K(\theta) = \cos(\theta) - 2.859621*10^{-5}\theta^2 - 5.25097*10^{-4}\theta$$

(19)

θ is the incident angle, which can be calculated for a plane in rotation around the horizontal North-South axis with a single axis tracking by the relation [6]:

$$\theta = \cos^{-1}\left(\sqrt{\cos^2\theta_z + \cos^2\delta\sin^2 w}\right)$$

(20)

θ_z, δ, and w are respectively the zenith angle, the declination angle and the hour angle.

$f_{EndLoss}$ is the end loss factor and is defined by Ref. [15].

$$f_{EndLoss} = 1 - \frac{m_2 f}{L_{SCA}}\tan(\theta) + \left(\frac{(m_2 - 1)}{L_{SCA}}\right)\max[0, f\tan(\theta) - d_2]$$
$$+ \left(\frac{(m_1 - 1)}{m_1 L_{SCA}}\right)\max[0, f\tan(\theta) - d_1]$$

(21)

where L_{SCA} is the tube length, f the focal distance, d_1 is the spacing between consecutive SCAs in a row, d_2 is the spacing between consecutive SCEs in a SCA, m_1 is the number of SCAs in a row and m_2 is the number of SCEs within a SCA,. More details about those parameters could be found in Ref. [15].

$f_{RowShad}$ is the row shadowing factor due to the shadows of collectors on one another. This factor is given by the following equation [17]:

$$f_{RowShad} = \frac{L_{Space}}{w_{SCA,total}}.\frac{\cos(\theta_z)}{\cos(\theta)}$$

(22)

where L_{Space} is the space between rows in the solar field and $w_{SCA,total}$ is the total aperture width of a single SCA. Table 3 shows dimensions and optical parameters of the ET-150 collector and its corresponding values.

Table 3
Spatial dimensions and optical parameters of PTC [15,21].

Parameter	value	Unit
A_c	3462	m²
d_1	1.5	m
d_2	0.25	m
f	1.71	m
f_1	1	–
$f_{DustEnv}$	0.98	–
f_{Clean}	0.97	–
H	0.61	m
L_{SCA}	142.8	m
L_{Space}	17.2	m
m_1	2	–
m_2	12	–
$W_{SCA, total}$	5.77	m
α_a	0.96	–
α_g	0.02	–
γ	0.94	–
η_{track}	0.99	–
ρ_{Cl}	0.94	–
τ_g	0.96	–
Geometric concentration	82	–
Rim angle	80	–

2.5.2. Solar power absorbed by the glass envelope

The portion of solar power absorbed by the glass envelope is discussed by Ref. [21] and evaluated here as:

$$Q_{sol,g} = I_b A_c \frac{\alpha_g}{\tau_g \alpha_a} \eta_{opt,0} K(\theta) f_{RowShad} f_{EndLoss} f_{Clean} f_{DustEnv} \eta_{track} f_1 \tag{23}$$

2.6. Initial and boundary conditions

To solve the system of governing equations (2), (5) and (8), the HTF, the absorber pipe and the glass cover are assumed to have a uniform initial temperature:

$$T_{HTF}(t = 0, x) = T_a(t = 0, x) = 293\ °C \tag{24a-b}$$

$$T_g(t = 0, x) = T_{amb} \tag{24c}$$

Regarding the boundary conditions, they are as follows.

- Among the operation conditions of Aïn Beni-Mathar ISCC power plant, the inlet operating temperature (set-point HTF inlet temperature) at which the solar field operates is 293 °C. That's why we assumed that:

$$T_{HTF}(t, x = 0) = 293\ °C \tag{25a}$$

To justify this order of magnitude, the schematic diagram of an identical CSP plant, called Noor 1 (160 MW) and localized at Ouarzazate city (Morocco), is shown in Fig. 2 below. According to this figure, we can observe that the inlet operating temperature of HTF is $T_{HTF,in} = 289.75$ °C whereas its exit operating temperature (set-point HTF exit temperature) takes the value of 394.74.

As for the boundary condition at x = L, it was considered that:

$$\left.\frac{\partial T_{HTF}}{\partial x}\right|_{x=L} = 0 \tag{25b}$$

- Thermal insulation at the absorber ends

$$\left.\frac{\partial T_a}{\partial x}\right|_{x=0} = \left.\frac{\partial T_a}{\partial x}\right|_{x=L} = 0 \tag{26a-b}$$

- The heat flux at the inlet and outlet of the glass equal to 0 (Thermal insulation at the glass ends)

$$\left.\frac{\partial T_g}{\partial x}\right|_{x=0} = \left.\frac{\partial T_g}{\partial x}\right|_{x=L} = 0 \tag{27a-b}$$

- The outer surface of the glass envelope was defined with a mixed boundary with convection and radiation.
- The absorber tube and the heat transfer fluid were defined as coupled fluid—solid interfaces in which the energy is conserved and the temperature is the same ($T_{HTF} = T_a$).

3. Description of Aïn Beni-Mathar ISCC power plant

ISCC power plants are composed of a CSP plant and a natural gas-fired combined cycle power plant [26]. The main components of the ISCC power plant installed in ABM town (Morocco) are sketched in Fig. 3. It uses an integrated solar system combined with a system that run on natural gas to generate electricity continuously even in the absence of the sun. The solar section is equipped
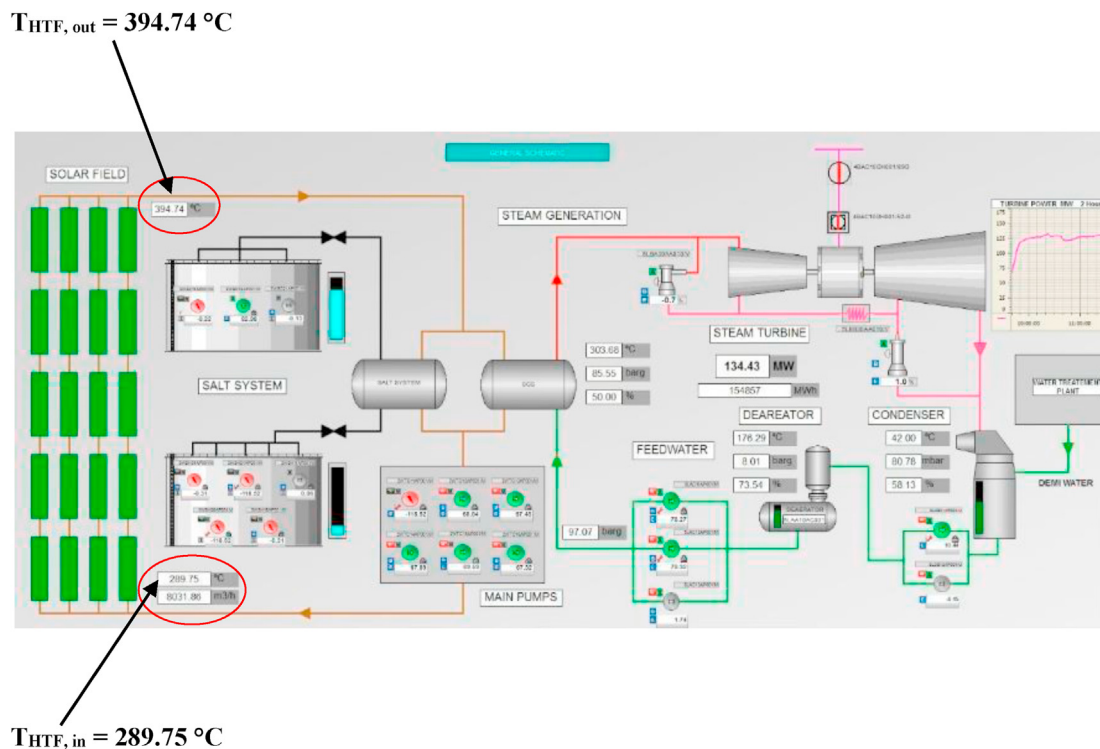
T$_{\text{HTF, out}}$ = 394.74 °C

T$_{\text{HTF, in}}$ = 289.75 °C

Fig. 2. Schematic diagram of a parabolic trough solar thermal power plant (Noor 1: 160 MW) localized at Ouarzazate (Morocco).
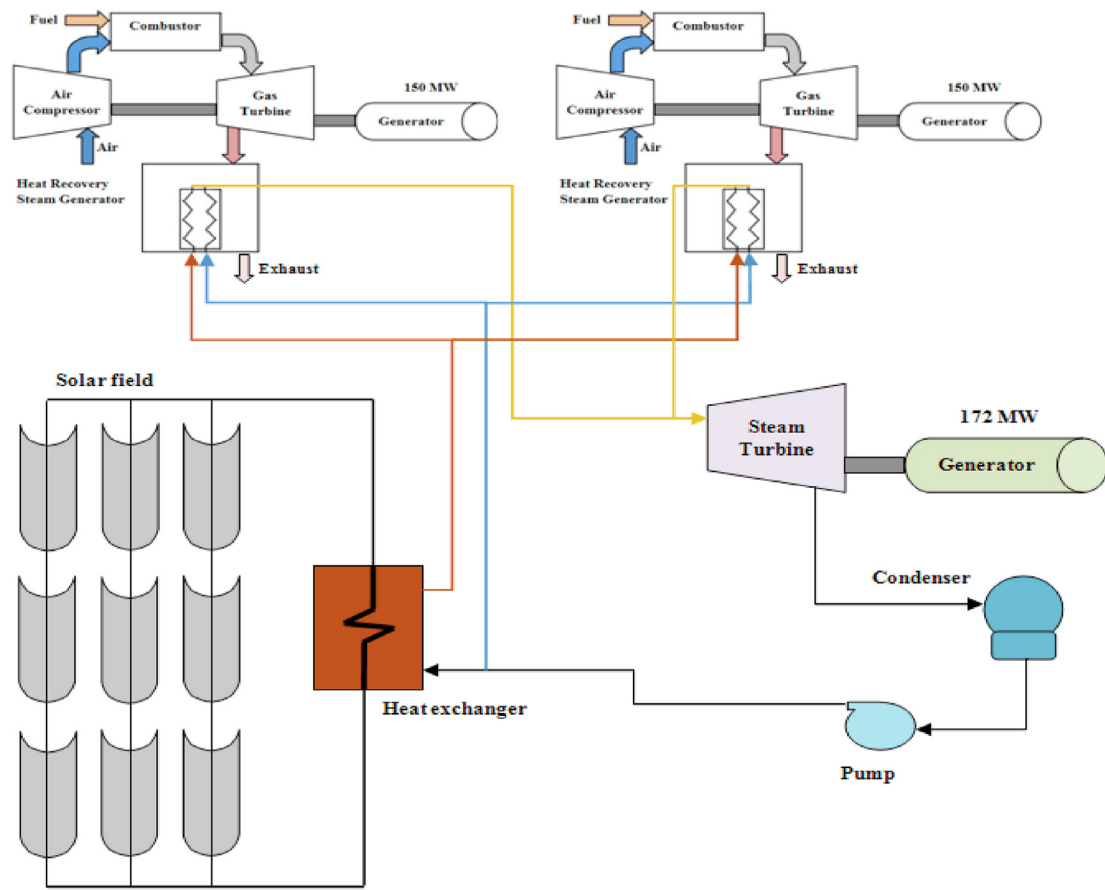
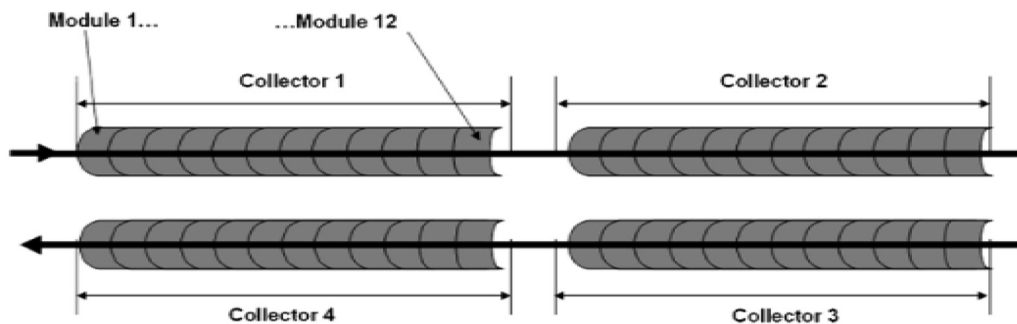**Fig. 3.** Components of the integrated solar combined cycle power plant.

Fig. 4. The receiver loop [25].

with a solar field of parabolic trough collectors (ET-150 type), a solar heat exchanger, two gas turbines and a steam turbine. The solar field consists of 224 parabolic trough solar collectors classified in 56 parallel loops; each of which consists of 4 collectors and has a total length of about 600 m (Fig. 4). The two heat recovery steam generators (HRSG) receive exhaust heat from the gas turbines and they are also fed with water vapor produced by the solar heat exchanger via the circulating HTF inside the absorber pipe. The created steam by HRSG is delivered to the steam turbine which sends its energy to the generator where it is converted into electricity.

In order to calculate the useful thermal power supplied to the HTF, the heat losses of the receiver tubes $Q_{loss,HCE}$ and the of the pipes $Q_{loss, pipes}$ have to be determined and subtracted from the absorbed power. It can be calculated for a loop as [21]:

$$Q_u = Q_{sol,a} - \left(Q_{loss,HCE} + Q_{loss,pipes} \right) \tag{28}$$

To calculate the heat losses of the absorber tubes, an empirical correlation reported by NREL [21] was used since Schott's 2008 PTR70 receiver tubes are part of the solar field design. For evacuated receiver tubes, the linear heat loss per HCE length (W/m) can be calculated by the following correlation:
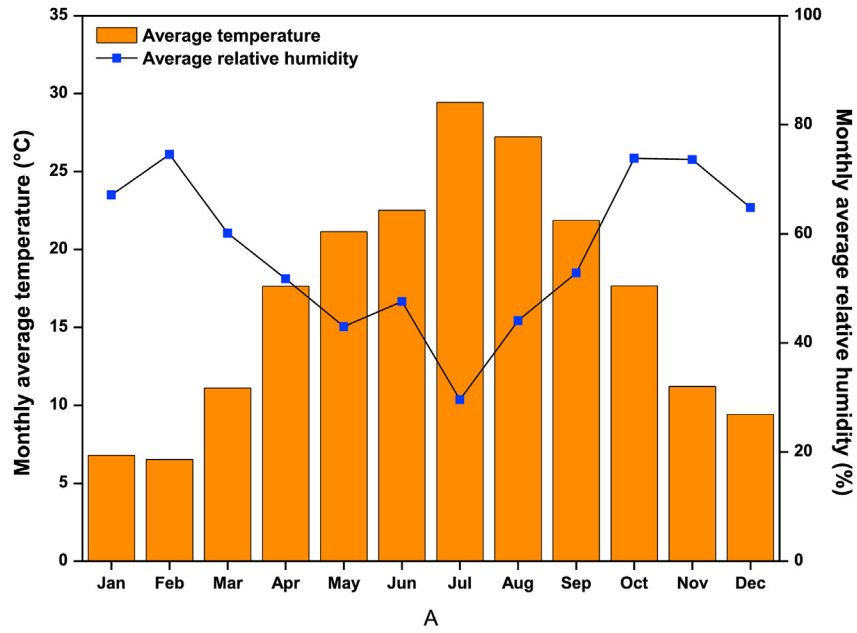
Fig. 5. Monthly averages of the ambient temperature and relative humidity at ISCC site (year of 2015).

$$HL_{PTR70-2008} = 4.05 + 0.247(T_{HTF} - T_{amb}) - 0.00146T_{HTF}^2$$
$$+ 5.65 \times 10^{-6}T_{HTF}^3 + 7.62 \times 10^{-8} I_b K(\theta)T_{HTF}^2$$
$$+ sqrt(V_w)[-1.70 + 0.0125(T_{HTF} - T_{amb})]$$
$$(29)$$

The final heat loss for HCE is given as follows:

$$Q_{loss,HCE} = HeatLossFactor \frac{HL_{PTR70-2008}}{W_{SCA,total}}A_c \qquad (30)$$

where the heat loss factor value is 1.

Thermal losses from the piping leading to and from the loop in the solar field are accounted by the following empirical equation

[9]:

$$Q_{loss,pipes} = \left[0.01693(T_{av,HTF} - T_{amb})\right.$$
$$- 1.683 \times 10^{-4}(T_{av,HTF} - T_{amb})^2$$
$$\left. + 6.780 \times 10^{-7}(T_{av,HTF} - T_{amb})^3\right]A_c$$
$$(31)$$

where $T_{av,HTF}$ is the HTF average temperature. More details about the model of the heat losses could be found in Ref. [9]. Also, the thermal efficiency which is the net gain to the HTF on the amount of solar power that reaches the aperture area of the solar field is described by Ref. [27], and evaluated here as:

Fig. 6. Monthly averages of DNI and wind speed at the ISCC site (year of 2015).

Table 4
Input parameters [21].

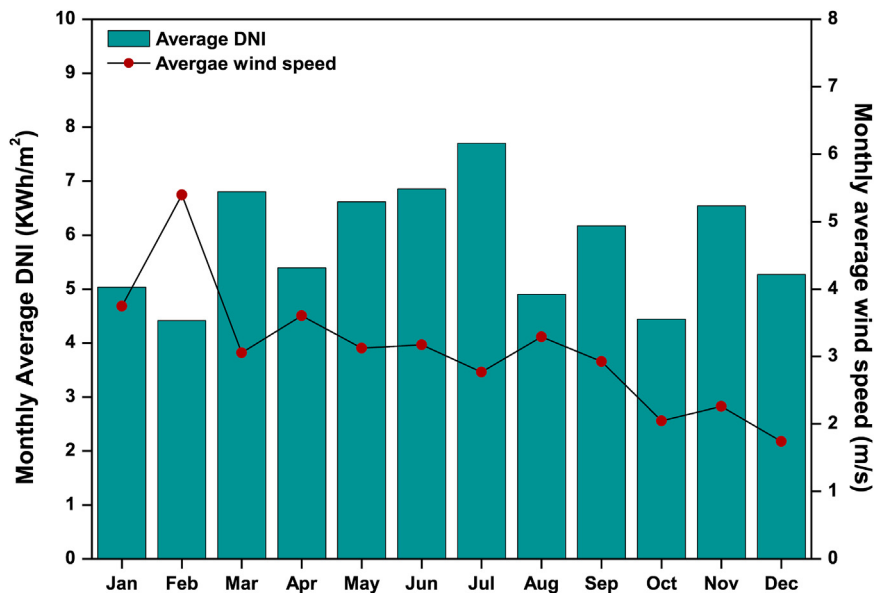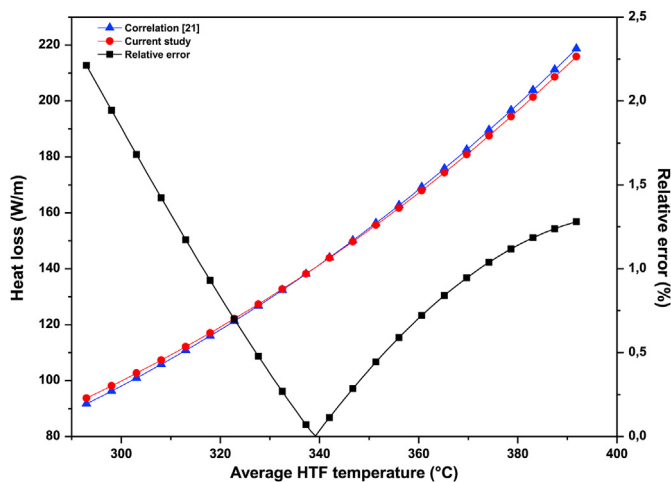| Total loop length (m)	588
Mass flow rate (kg/s)	9
$I_b(W/m^2)$	950
Incidence angle, θ (deg)	20
Wind speed (m/s)	2
Ambient temperature (°C)	30

Fig. 7. Comparison between numerical and empirical results [21] of the receiver linear thermal loss.

$$\eta_{th} = \frac{Q_u}{Q_{sol}} \quad \text{with} \quad Q_{sol} = I_b A_c \tag{32}$$

4. Mesh generation

Comsol Multiphysics is a commercial solver and simulation software used to solve time-dependant one-dimensional partial differential equations (PDEs) system described above (Equations (2), (5) and (8)) associated with appropriate boundary and initial conditions. It is based on the finite element method and has suitable criteria to generate the best-suited mesh and it provides the discretization in the considered domain. The most adequate mesh, ensuring the convergence of numerical solutions, was taken for this simulation study. Details of this software are given in reference [28].

5. Results and discussion

5.1. Weather conditions

The site of ABM power plant is located in the Eastern part of Morocco (34°00′35″N, 2°01′29″W) at about 560 km from the Capital (Rabat). It is the first Moroccan solar thermal power plant. The climate in this region is classified as "Csa", according to Köppen-Geiger climate classification. The climatic data used in this study were taken from the weather station in situ. As a result, monthly averages of ambient temperature, relative humidity of air, wind speed and Direct Normal Irradiation (DNI), will be presented here, for the year of 2015.

Indeed, the ambient temperature presents significant seasonal changes as indicated in Fig. 5, and as usual the summer season is hotter than the other seasons. This important parameter influences the heat losses in the solar field of PTCs. The average of the monthly minimum value of temperature of the coldest month (February) is 6.5 °C while the average of the monthly maximum temperature of the hottest month (July) is about 30 °C. Besides, as expected, the relative humidity depends strongly on the ambient temperature since they vary in an opposite way as shown in Fig. 5, too. Moreover, the ambient air is quite dry when it gets very hot during summer; the minimum average relative humidity recorded on July is 29.6%. Conversely, air is over-humidified in winter; with a maximum of 74.6% recorded in February 2015.

Let us now examine the wind speed which is manifestly one of decisive parameters on the CSP plant efficiency. So, Fig. 6 depicts monthly averages of wind speed for the year of 2015. It shows that average values are almost ranging from 1.74 m/s to 5.4 m/s. Note that the maximum average value (5.4 m/s) was recorded in February 2015. In an energy point of view, the area of the power plant is well exposed to sunlight with an average of daily DNI of
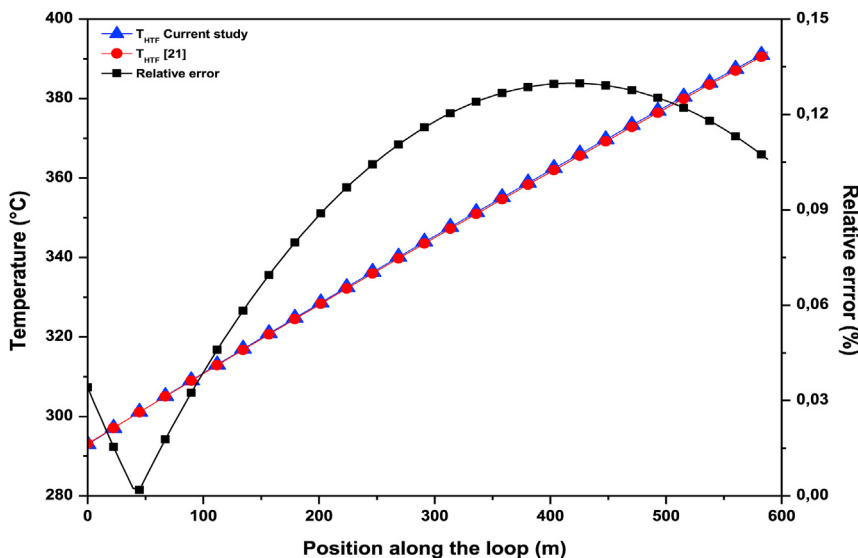

Fig. 8. Comparison between numerical and empirical correlation results [21] corresponding to HTF temperatures along a single loop.
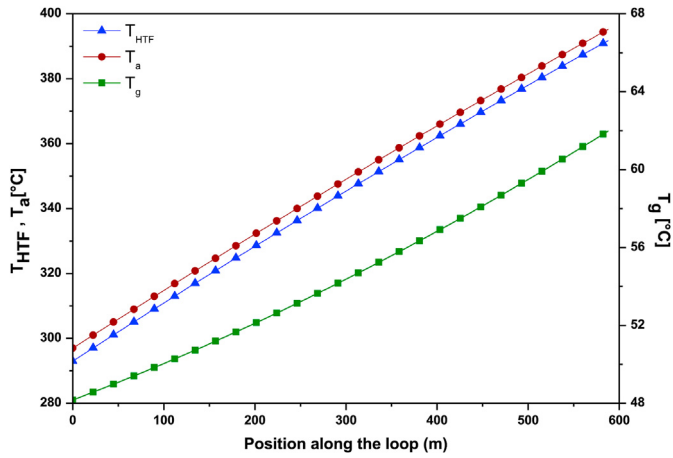
Fig. 9. Variation of temperature along position in one loop for the HTF, the absorber and the glass envelope.

5.85 kWh/m², and the monthly averages are also presented in Fig. 6. The maximum and minimum values of DNI are 7.7 kWh/m² and 4.41 kWh/m², respectively, and they recorded in July and February 2015. This parameter is considered as the most relevant factor influencing the energy production of a solar power plant.

5.2. Model validation and temperature profiles

As usual in this type of study, model validation is quite often recommended. But before starting this task, it is important to point out that databases of DNI, ambient temperature and wind speed were obtained from the operators of Ain Beni Mathar ISCC power plant. The HTF system is designed for a HTF mass flow of Solutia's VP1 of 440 kg/s at 100% load (about 7.86 kg/s per loop). The inlet and the outlet HTF temperatures are about 293 °C and 391 °C respectively, which are the operation conditions of the solar field.

As to the model validation, it will be conducted later in this section by comparing numerical results and correlations available in the literature [21]. Indeed, thermal performances of the PTR-70 2008 solar receiver have been estimated numerically and then compared with results of NREL [21]. The input parameters of the simulation are taken from Refs. [21] and presented in Table 4. The simulation was done for an interval of 1h and the results are presented at t = 1h when the steady state is maintained.

Fig. 7 depicts the linear heat loss against average HTF temperature, and compares also the results of the current study with the empirical correlation given above (Equ. 25). It's obviously clear that the trends marked by the two curves are roughly the same. After that, we could conclude that the simulation results are in good agreement with those of the aforementioned correlation since the relative error does not exceed 2.5% in the worse case.

Additionally, for an increase in the HTF temperature from 293 °C to 391 °C the linear heat loss increases from 92 W/m to 219 W/m for the empirical correlation and from 94 W/m to 216 W/m for the numerical results. On average, every 10 °C increase in the HTF temperature generates an increase of about 12.7 W/m in thermal loss. Furthermore, during the simulation process, it has been observed that the rate of increase in HTF temperature varies between 0.18 °C and 0.16 °C/m at the inlet and the exit of the loop, respectively. It also noted that the net gain of energy decreases with the fluid flow inside the loop because of the increasing of heat losses.

To confirm the model validation, HTF temperature profiles were compared in Fig. 8. Similar to the previous comparison (Fig. 7), it is
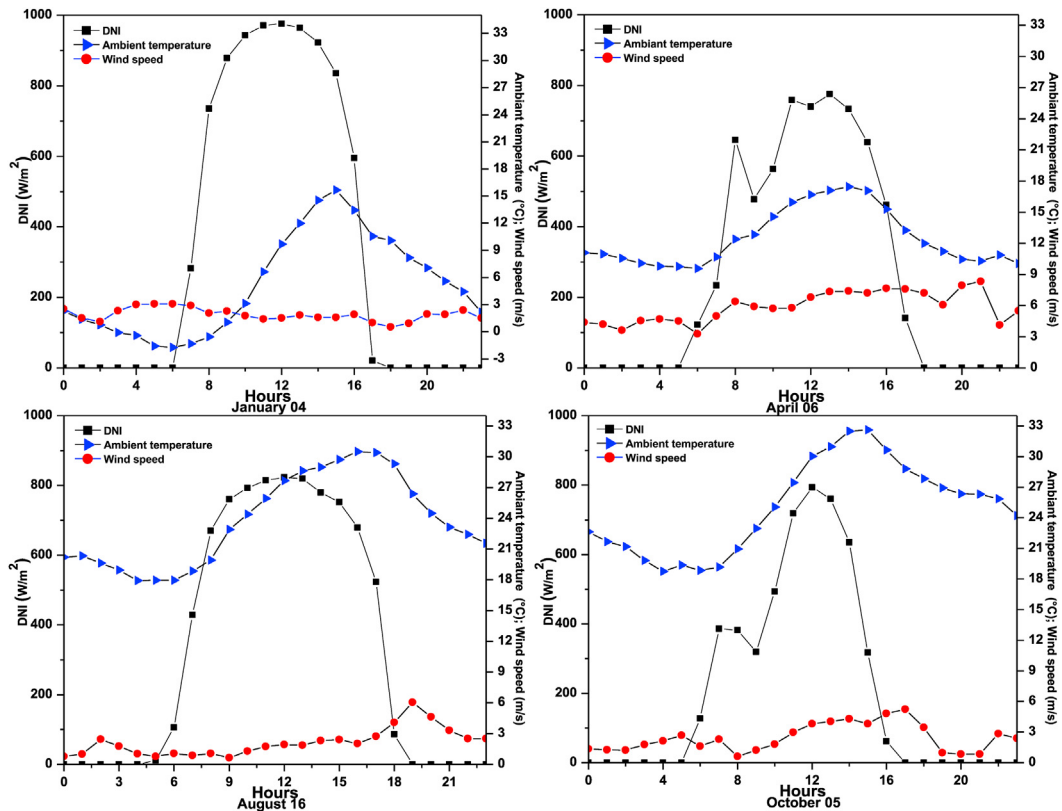

Fig. 10. Hourly DNI, ambient temperature and wind speed for the four different typical days.

evident that the two curves of HTF temperature, which appear to be linear, are nearly the same and hence the model validation is affirmed again since the relative error between these results is less than 0.15%.

Now we move on to discussing thermal behavior of the main components of the receiver namely, HTF, absorber pipe and glass envelope, whose temperatures are exhibited in Fig. 9. These profiles are almost linear and temperature values rise along the tube length. Due to these thermal properties, the absorber gets significant amount of the solar energy, so its temperature is higher than that of the two other elements (HTF and glass envelope) along the loop. The mean deviation from the HTF temperature is about 3.7 °C while it is about 292 °C from the glass envelope temperature. These differences could be explained by the disparity of thermal resistances of the three components of the solar receiver.

5.3. Thermal performances of Ain Beni Mathar ISCC power plant

In this part of work, daily and annual thermal performances of the solar field of Ain Beni Mathar ISCC power plant are discussed. For this purpose, daily data of the year 2015 were used to validate the capability of the model to estimate the thermal energy production and the thermal efficiency of the solar field. The HTF system is designed for a HTF mass flow of Solutia's VP1 of 440 kg/s at 100% load (about 7.86 kg/s per loop).

5.3.1. Daily performance of the solar field of ABM - ISCC power plant (year of 2015)

To highlight the daily performance of the solar field of ABM power plant for the year of 2015, the daily average of DNI, ambient temperature and energy production for each season, were carried out. This procedure aims to choose a typical day during each season. Consequently, January 4th, April 06th, August 16th, and October 5th, have been selected as typical days. The variation of DNI, ambient temperature and wind speed are depicted in Fig. 10.

It should be noted that due to the variation of the amount of DNI received by the solar field of the ABM power plant over the seasons of the year, the operation of the power plant confronts some technical constraints. This means that operating hours of thermal production vary from a season to another. In fact, in winter (December 21st − March 20th), and autumn (September 21st − December 20th), the solar field of PTCs operates 8 h/day in average by supplying hot HTF at 391 °C to the power block. For spring (March 21st − June 20th) and summer (June 21st − September 20th), the power block produces electricity for an average of 10 and 11 h/day, respectively.

For typical days (January 04th, April 06th, October 05th and August 16th), Fig. 11 compares operating thermal energy and efficiency obtained from ABM plant and those numerically simulated. Indeed, maximum values of operating thermal energy, their associated efficiencies and recording time are given in Table 5.

As seen in the figure below (Fig. 11), it can be noticed that the trends and variations marked by the two curves are roughly the same. However, abrupt variations in energy production are difficult to model, whatever the type of model considered. The only situations where predictions are less accurate are those of low values of the produced thermal power that are normally associated to low values of DNI (especially the hours at the start and end of typical days). These overestimations can be explained by the fact that thermal inertia phenomena are not considered at the start-up
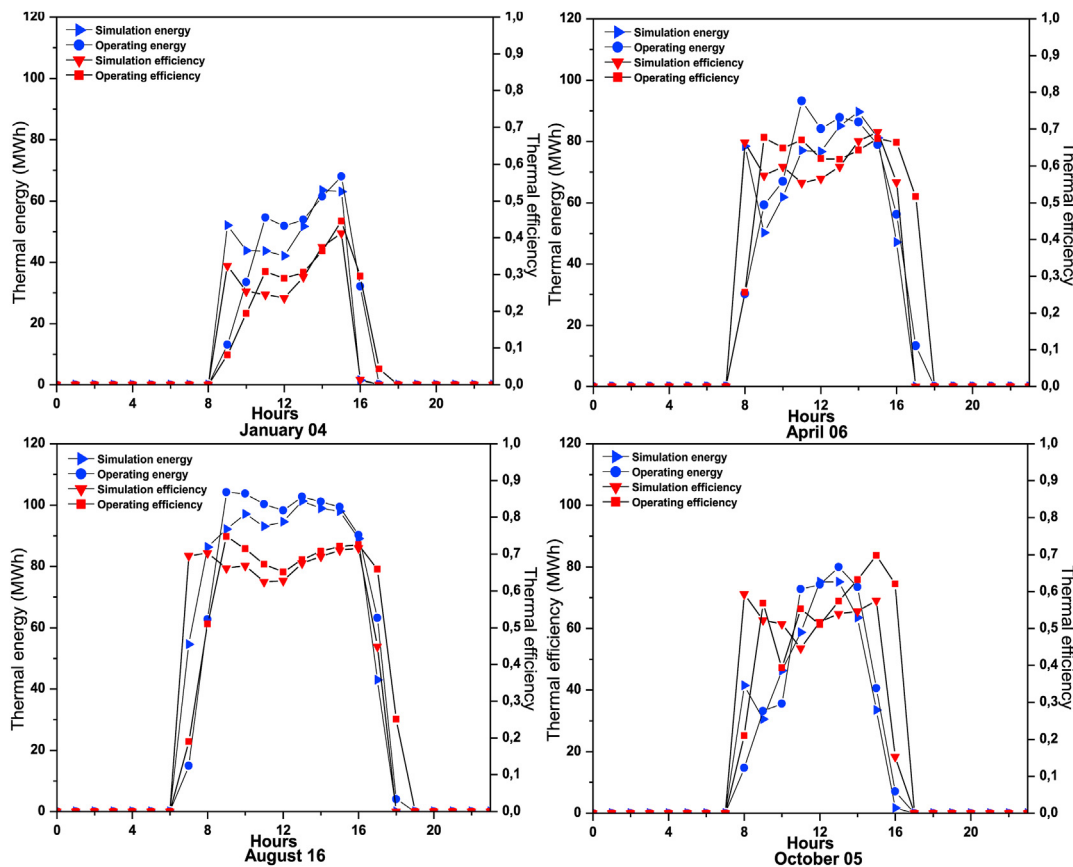

Fig. 11. Hourly experimental and estimated thermal performances for the four different typical days.

Table 5
Highest values of operating thermal energy as well as their associated efficiencies.

Typical day	Peak operating thermal energy (MWh)	Efficiency (%)	Recording time
January 04th	68	44	15h
April 06th	93	67	11h
October 05th	104	74	9h
August 16th	80	57	13h

period. As for the underestimations at the end of the day, they are mainly due to the low value of the shadow loss factor.

In Fig. 12, the model predictions of the outlet HTF temperature of one loop, for the four studied typical days, are presented. After the sunrise, the DNI increases during the daylight hours. As a result, the HTF temperature starts from 293 °C at the loop inlet to reach the selected temperature setpoint (391 °C) at the outlet which is often used to calculate the heat losses from the HCEs and piping in the model.

The estimates of thermal productions are more accurate in daily cumulative as shown in Fig. 13. A comparison of daily net thermal energy production between the simulation results and operating data was done for ten days of each season. The chosen ten days are: ($1^{st} - 10^{th}$) January for winter, ($1^{st} - 10^{th}$) April for spring, ($1^{st} - 10^{th}$) July for summer and ($3^{rd} - 12^{th}$) November for autumn. In this graphical representation, red and blue dots are the amount of delivered thermal energy from the solar field to the power block at each specific day, whereas histograms present the daily cumulative DNI. It is obvious from these curves that the experimental thermal energy is very close to simulated one for all considered days. Individual deviations in daily thermal energy production are less important and obtained results are highly correlated with operating data. More details about thermal energy, heat losses, efficiency and their corresponding deviations are presented in Table 6. The latter presents the cumulative thermal energy, DNI, heat losses and also overall thermal efficiency obtained for ten days of each season. Accordingly, the highest and lowest values of thermal energy production were respectively recorded in summer and winter. Thermal efficiency follows the same logic as thermal energy. Indeed, the operating cumulative thermal energy production is

about 8.07 GWh for the first ten days of July with a corresponding thermal efficiency of 64.79%. The difference between this last result and that of the simulation is estimated at 1.47%. Regarding the lowest thermal efficiency (22.83%), it is reached in January with about 2.8 GWh with a relative error of 1.46%. So, it can be concluded that the proposed model is more appropriate when the daily cumulative analysis is considered.

5.3.2. Annual performance of the solar field of ABM - ISCC power plant (year of 2015)

After dealing with daily performances of the solar field of ABM - ISCC power plant during 2015, we believe that it is useful to have a more accurate idea about its annual performances. Thus, Table 7 and Fig. 14 offer a comparison of performances between the simulation and operating data.

Due to the variation of DNI during the year, the monthly average thermal production varies greatly. As expected, it is low in winter unlike summer season where the peak production is around 25.86 GWh in July, for which the model underestimates the production with about 0.48%. Additionally, the highest efficiency was recorded in June with about 64.38%, and a relative error of 2.98%. As for the month of February, it has the lowest thermal energy production and the largest deviation (41.21%) between operating data and simulation results since the ABM plant was operating for only sixteen days (see Fig. 15).

According to Fig. 15 associated with the month of February, it is evident that the model better estimates thermal energy production under normal operating conditions. There are, however, some days whose production appears to have overestimated because of various causes, especially maintenance days or high wind speed
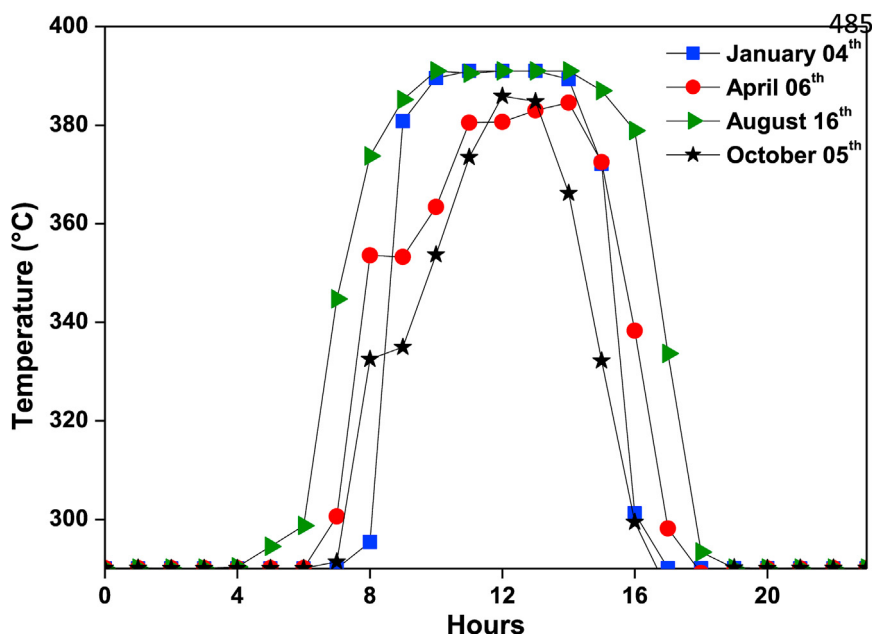

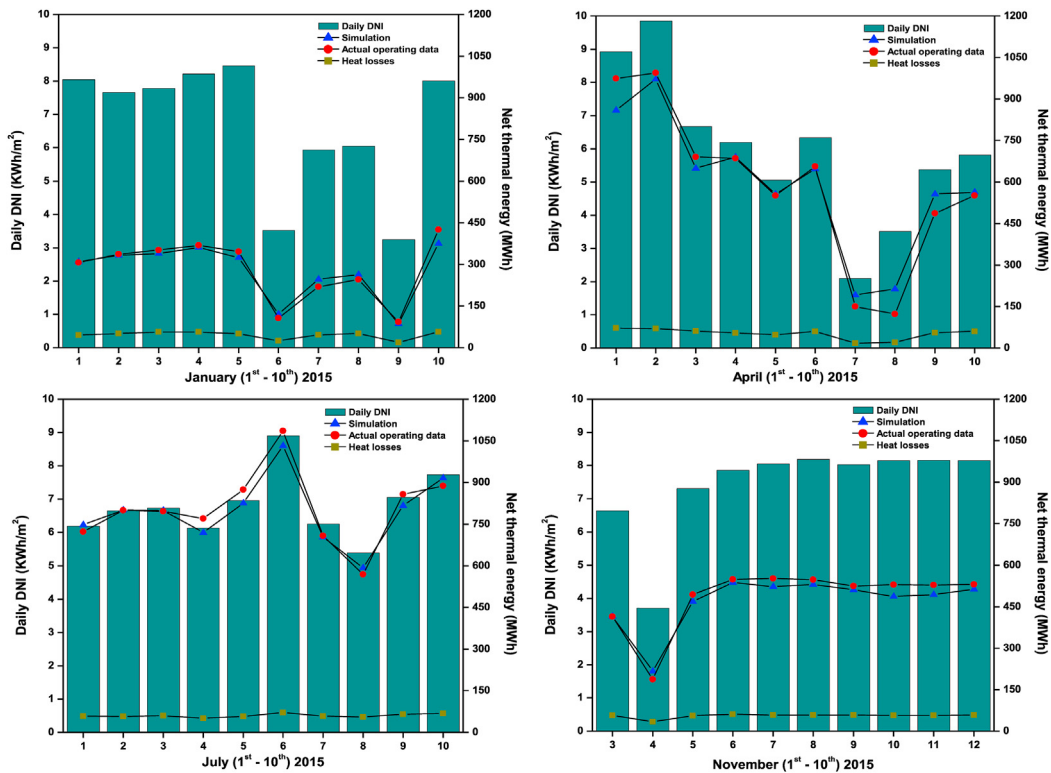**Fig. 12.** Variation of outlet HTF temperature of one loop.

Fig. 13. Daily net energy production for the ten days of each season: comparison of the experimental data and simulated results.

Table 6
Cumulative thermal energy and efficiency of the solar field: comparison of operating and simulated results for the ten days of each season.

		DNI (kWh/m²-ten days)	Heat losses (MWh)	Thermal energy (MWh)	Efficiency (%)
January	Operating	66.96		2799.42	22.83
	Simulated	_	457.40	2758.44	22.50
	Relative error (%)	_		1.46	
April	Operating	59.87		5859.57	53.44
	Simulated	_	519.25	5897.44	53.79
	Relative error (%)	_		0.65	
July	Operating	68.03		8071.32	64.79
	Simulated	_	605.10	7952.44	63.83
	Relative error (%)	_		1.47	
November	Operating	74.29		4852.90	35.67
	Simulated	_	550.97	4694.31	34.51
	Relative error (%)	_		3.27	

Table 7
Performances of the ABM solar field during 2015.

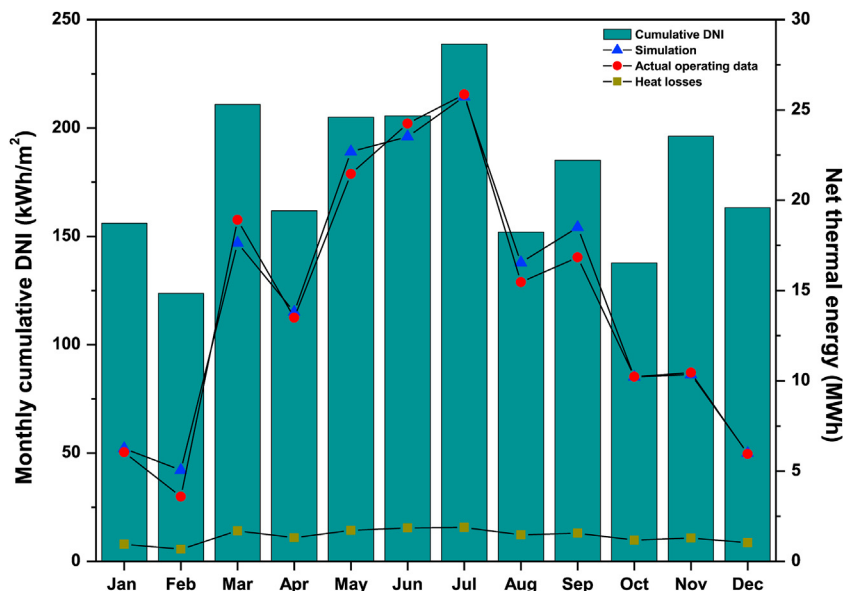| Month	DNI (kWh/m²/month)	Solar field thermal output		Solar field thermal efficiency		Heat losses (GWh)	Relative error (%)
		Operating output (GWh)	Estimated output (GWh)	Operating efficiency (%)	Estimated efficiency (%)		
January	156.04	6.05	6.25	21.17	21.89	0.95	3.40
February	123.65	3.58	5.06	15.82	22.34	0.67	41.21
March	210.90	18.91	17.63	48.96	45.65	1.69	6.77
April	161.83	13.49	13.81	45.53	46.60	1.31	2.36
May	205.07	21.45	22.68	57.13	60.39	1.72	5.70
June	205.61	24.24	23.52	64.38	62.46	1.85	2.98
July	238.71	25.86	25.73	59.15	58.86	1.88	0.48
August	152.00	15.46	16.55	55.55	59.45	1.47	7.02
September	185.09	16.83	18.51	49.66	54.61	1.56	9.96
October	137.81	10.23	10.21	40.52	40.48	1.18	0.11
November	196.21	10.45	10.34	29.10	28.78	1.30	1.10
December	163.29	5.95	5.99	19.89	20.05	1.03	0.80
Annual	2136.21	172.51	176.29	44.10	45.07	16.61	2.19

Fig. 14. Monthly net thermal energy production for the year of 2015: comparison of the experimental data and simulated results.
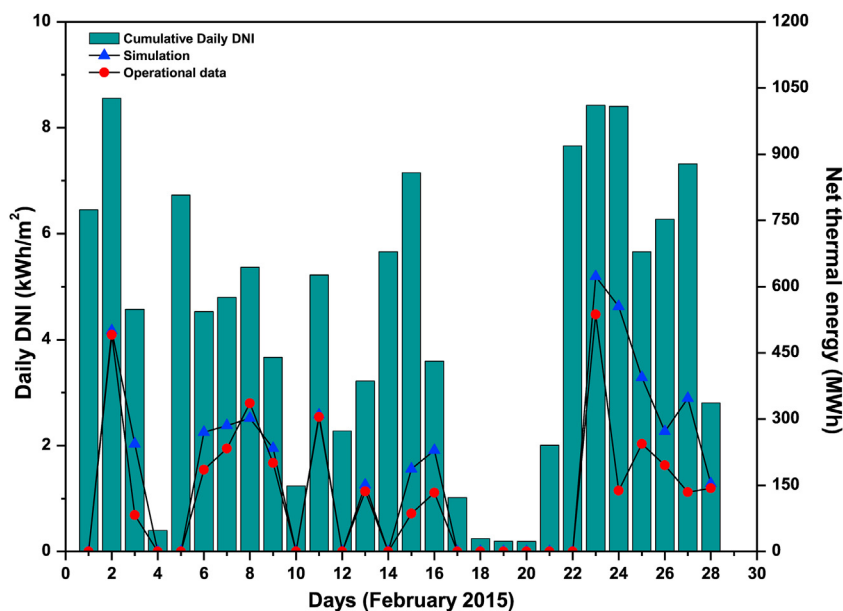

Fig. 15. Daily net energy production for February: comparison of the experimental data and simulated results.

values (see Fig. 6). As an illustration, if the particular days of 3rd, 15th, 24th and 27th February, for which the thermal energy is overestimated, are not considered, the relative error will be reduced from 41.21% to only 18.5%. After all, it is always interesting and helpful to have more information on different operation such as maintenance or others to better simulate ABM plant performances.

The annual operating thermal production is about 172.5 GWh versus 176.3 GWh estimated from the simulation, which represents an overestimation of only 2.2%. The annual heat losses were about 16.6 GWh. Before concluding this work, it is important to emphasize that performances of ABM plant could be improved if heat storage system were used [29—32].

6. Conclusions

In this work, thermal performances of the solar field of Aïn Beni Mathar ISCC power plant were analyzed for the year 2015. Firstly, the solar receiver Schott PTR-70 2008 was modeled and simulated using Comsol Mutiphysics software. Next, the model was validated with empirical data from NREL, so the comparison is satisfactory. It should be noted that main results have been focused on daily and annual thermal performances, as well as comparison between simulated results and actual plant operating ones.

For selected typical days, it was concluded that the model's predictions seem to be adequate except at the beginning and end of each day. On the other hand, the estimates of cumulative thermal productions for selected ten days of each season were also carried out. As a result, the actual operating thermal energy is very close to

simulated one for all chosen days. As an illustration, actual energy output and its corresponding thermal efficiency, for the first ten days of July, are respectively 8.07 GWh and 64.79% with a relative error of 1.47% compared to simulation result. Conversely and with a relative error of 1.46%, the month of January recorded the lowest production (about 2.8 GWh) with a thermal efficiency of 22.83%. So, it can be concluded that the proposed model is more appropriate when the daily cumulative analysis is considered.

As expected, the monthly average thermal production is low in winter unlike summer season where the peak production is around 25.86 GWh in July, for which the model underestimates the production with about 0.48%. Additionally, the highest efficiency was recorded in June with about 64.38%, and a relative error of 2.98%. As for the month of February, it has the lowest thermal energy production and the largest deviation (41.21%) between operating data and simulation results since the ABM plant was operating for only sixteen days.

CRediT authorship contribution statement

Anass Zaaoumi: Conceptualization, Methodology, Numerical Simulation, Data analysis, Writing - original draft, Writing - review & editing. **Mohamed Asbik:** Work Supervision, Project administration, Formal analysis, Results interpretation and analysis, Writing - original draft, Writing - review & editing. **Hajar Hafs:** Methodology, Numerical Simulation. **Abdellah Bah:** Work supervision, Project administration. **Mohammed Alaoui:** Work Supervision.

Declaration of competing interest

The authors declare that they have no known competing financial interests or personal relationships that could have appeared to influence the work reported in this paper.

Acknowledgment

References

[1] S.A. Kalogirou, Solar thermoelectric power generation in Cyprus: selection of the best system, Renew. Energy 49 (2013) 278—281, https://doi.org/10.1016/j.renene.2012.01.014.

[2] A. Mwesigye, H. Yılmaz, J.P. Meyer, Numerical analysis of the thermal and thermodynamic performance of a parabolic trough solar collector using SWCNTs-Therminol®VP-1 nanofluid, Renew. Energy 119 (2018) 844—862, https://doi.org/10.1016/j.renene.2017.10.047.

[3] S. Marrakchi, Z. Leemrani, H. Asselman, A. Aoukili, H. Asselman, Temperature distribution analysis of parabolic trough solar collector using CFD, collector using CFD, Procedia Manufact. 22 (2018) 773—779, https://doi.org/10.1016/j.promfg.2018.03.110.

[4] J.H.M. Neto, M.A. Pessoa, E.B. Borges, F.R.S. Lima, Experimental test of the parabolic trough solar collectors of the first demonstration testing facility of Brazil using the QDT model, Appl. Therm. Eng. 163 (2019), https://doi.org/10.1016/j.applthermaleng.2019.114405.

[5] S.A. Kalogirou, A detailed thermal model of a parabolic trough collector receiver, Energy 48 (1) (2012) 298—306, https://doi.org/10.1016/j.energy.2012.06.023.

[6] H. Yılmaz, M.S. Söylemez, Thermo-mathematical modeling of parabolic trough collector, Energy Convers. Manag. 88 (2014) 768—784, https://doi.org/10.1016/j.enconman.2014.09.031.

[7] T. Bouhal, Y. Agrouaz, T. Kousksou, A. Allouhi, T. El Rhafiki, A. Jamil, M. Bakkas, Technical feasibility of a sustainable Concentrated Solar Power in Morocco through an energy analysis, Renew. Sustain. Energy Rev. 81 (2018) 1087—1095, https://doi.org/10.1016/j.rser.2017.08.056.

[8] H.A. Zaharil, M. Hasanuzzaman, Modelling and performance analysis of parabolic trough solar concentrator for different heat transfer fluids under Malaysian condition, Renew. Energy 149 (2020) 22—41, https://doi.org/10.1016/j.renene.2019.12.032.

[9] A.M. Patnode, Simulation and Performance Evaluation of Parabolic Trough Solar Power Plants, Ph.D. thesis, University of WisconsinMadison. Department of Mechanical Engineering, 2006.

[10] G. Manzolini, A. Giostri, C. Saccilotto, P. Silva, E. Macchi, Development of an innovative code for the design of thermodynamic solar power plants part A: code description and test case, Renew. Energy 36 (2011) 1993—2003, https://doi.org/10.1016/j.renene.2010.12.027.

[11] M. Abutayeh, Y.D. Goswami, E.K. Stefanakos, Solar thermal power plant simulation, Environ. Prog. Sustain. Energy 32 (2013) 417—424, https://doi.org/10.1002/ep.11636.

[12] M. Ouagued, A. Khellaf, L. Loukarfi, Estimation of the temperature, heat gain and heat loss by solar parabolic trough collector under Algerian climate using different thermal oils, Energy Convers. Manag. 75 (2013) 191—201, https://doi.org/10.1016/j.enconman.2013.06.011.

[13] Y. Marif, H. Benmoussa, H. Bouguettaia, M.M. Belhadj, M. Zerrouki, Numerical simulation of solar parabolic trough collector performance in the Algeria Saharan region, Energy Convers. Manag. 85 (2014) 521—529, https://doi.org/10.1016/j.enconman.2014.06.002.

[14] T. Fasquelle, Q. Falcoz, P. Neveu, F. Lecat, G. Flamant, A thermal model to predict the dynamic performances of parabolic trough lines, Energy 141 (2017) 1187—1203, https://doi.org/10.1016/j.energy.2017.09.063.

[15] I.L. García, D. Blanco, A. Luis, Performance model for parabolic trough solar thermal power plants with thermal storage : comparison to operating plant data, Sol. Energy 85 (2011) 2443—2460, https://doi.org/10.1016/j.solener.2011.07.002.

[16] M. Tahtinen, L. Kannari, R. Weiss, H. Mikkonen, Dynamic modelling of concentrated solar power and power plant integration, in: 4th Solar Integration Workshop. Berlin.Germany, 2014.

[17] W.A.K. Al-Maliki, F. Alobaid, V. Kez, B. Epple, Modelling and dynamic simulation of a parabolic trough power plant, J. Process Contr. 39 (2016) 123—138, https://doi.org/10.1016/j.jprocont.2016.01.002.

[18] S. Rohani, T.P. Fluri, F. Dinter, P. Nitz, Modelling and simulation of parabolic trough plants based on real operating data, Sol. Energy 158 (2017) 845—860, https://doi.org/10.1016/j.solener.2017.10.023.

[19] B. Hoffschmidt, S. Alexopoulos, J. Göttsche, M. Sauerborn, O. Kaufhold, 3.06 - high concentration solar collectors, in: Ali Sayigh (Ed.), Comprehensive Renewable Energy, Elsevier, 2012, pp. 165—209, https://doi.org/10.1016/B978-0-08-087872-0.00306-1.

[20] Solutia technical bulletin, Available at: https://www.therminol.com/products/Therminol-VP1. Accessed 30.04.2020.

[21] F. Burkholder, C.F. Kutscher, Heat Loss Testing of Schott's 2008 PTR70 Parabolic Trough Receiver, NREL, 2009. Technical Report NREL/TP-550-45633.

[22] A. Benidir, F. Khaldi, A. H Benmachiche, F. Bouras, Numerical thermal analysis of schott 2008 PTR70 solar receiver under hassi R 'Mel power plant operation conditions, J. Eng. Technol. 13 (1) (2018) 122—140.

[23] Incropera P. Frank, DeWitt P. David, Bergman L. Theodore, Lavine S. Adrienne, Fundamentals of Heat and Mass Transfer, sixth ed., John Wiley & Sons, US, 2007.

[24] L. Valenzuela, R. López-Martín, E. Zarza, Optical and thermal performance of large-size parabolic-trough solar collectors from outdoor experiments : a test method and a case study, Energy 70 (2014) 456—464, https://doi.org/10.1016/j.energy.2014.04.016.

[25] M.J. Montes, A. Abánades, J.M. Martínez-Val, M. Valdés, Solar multiple optimization for a solar-only thermal power plant. using oil as heat transfer fluid in the parabolic trough collectors, Sol. Energy 83 (2009) 2165—2176, https://doi.org/10.1016/j.solener.2009.08.010.

[26] B.J. Alqahtani, D. Patiño-Echeverri, Integrated solar combined cycle power plants: paving the way for thermal solar, Appl. Energy 169 (2016) 927—936, https://doi.org/10.1016/j.apenergy.2016.02.083.

[27] T.A. Yassen, N.D. Mokhlif, M.A. Eleiwi, Performance investigation of an integrated solar water heater with corrugated absorber surface for domestic use, Renew. Energy 138 (2019) 852—860, https://doi.org/10.1016/j.renene.2019.01.114.

[28] COMSOL Multiphysics Reference Manual, COMSOL Multiphysics® V. 5.5, COMSOL AB, Stockholm, Sweden, 2019.

[29] K. El Alami, M. Asbik, H. Agalit, N. Zari, S. Rachidi, A literature review of igneous Moroccan rocks for thermal energy storage in CSP plants, AIP Confer. Proc. 2126 (2019) 200015, https://doi.org/10.1063/1.5117730.

[30] K. El Alami, M. Asbik, N. Zari, S. Rachidi, Thermocline thermal storage using a packed bed of Moroccan rocks. IOP Conference Series: Earth and Environmental Science, IOP Publishing, 2018, 012016.

[31] K. El Alami, M. Asbik, H. Agalit, Identification of natural rocks as storage materials in Thermal Energy Storage (TES) system of Concentrated Solar Power (CSP) plants - A review, Solar Energy Mater. Solar Cells (2020). SOLMAT-D-19-01426R1.

[32] Y. Jemmal, N. Zari, M. Asbik, M. Maâroufi, Thermal performance investigation of an air-rock packed bed storage system: experimental characterization and thermal performance comparison of six Moroccan rocks, J. Energy Storage 30 (2020) 101—513, https://doi.org/10.1016/j.est.2020.101513.

Energy production estimation of a parabolic trough solar power plant using artificial neural network

Anass Zaaoumi, Zahra Bouramdane, Abdellah Bah, Mohammed Alaoui
Thermal and Energy Research Team,
ENSET, Mohammed V University,
Rabat, Morocco
anass.zaaoumi@um5s.net.ma, zahra.bouramdane@um5s.net.ma,
a.bah@um5s.net.ma, m.alaoui@um5s.net.ma

Abdellah Mechaqrane
Laboratory of Renewable Energies and Smart Systems,
FST, SMBA University,
Fez, Morocco
a.mechaqrane@usmba.ma

Abstract— The aim of the present study is the use of Artificial Neural Networks (ANN) modeling to estimate the hourly based electric energy generation of a Parabolic Trough Solar Thermal Power Plant (PTSTPP), located in Eastern Morocco. Data covering 4 years are used in order to train and validate a three Multi-Layers Perceptron (MLP) model. In order to choose the best architecture, several statistical criteria are used such as: Coefficient of Correlation (R), Root Mean Squared Error (RMSE), Relative Root Mean Squared Error (RRMSE), Relative Mean Bias Error (RMBE) and Mean Absolute Error (MAE). The back propagation learning algorithm is used to train different ANN architectures. Predicted results indicates that the total electric energy accumulated for the validation year was about 42.6 GWh/year, representing an underestimation less than 5% from the recorded energy. The results indicate that the ANN model can successfully estimate the energy production of a solar power plant with parabolic trough collectors.

Keywords— *Artificial Neural Networks, Multi-Layers Perceptron, Energy production, Parabolic Trough Solar Thermal Power Plant, Back propagation.*

I. INTRODUCTION

In the world, several developing countries that have great potential of Direct Normal Irradiation (DNI) are moving to Concentrating Solar Power (CSP) technology for electricity generation and especially in Morocco, which imports around 91 % of its energy needs to face the demands that increase progressively [1].

CSP plants are one of the most promising technologies to produce electric power [2]. It aims to transform the solar radiation to heat at high temperature, then to mechanical and electrical energy through a thermodynamic cycle. The accurate estimation of the production of a solar power plant is a subject of great interest, because of the important fluctuations of the meteorological parameters like solar radiation, ambient temperature, wind speed and humidity, which cause fluctuations in production and generate problems on the electricity grid caused by the non-uniform production.

Different researchers used different solar power plant simulation tools such as Green Energy System Analysis Tool (GRRENIUS) developed by the German Aerospace Center (DLR) [3] and System Advisor Model (SAM) developed by the National Renewable Energy Laboratory (NREL) [4] to determine the power output and feasibility of the renewable energy systems for a given location ([5]; [6]). Other researchers used artificial intelligence like artificial neural networks [7].

Thanks to the results achieved over the last two decades, ANN modeling becomes increasingly successful and proved its effectiveness in several areas like: meteorological applications especially for solar irradiation forecasting ([8]; [9]; [10]), energy control and optimization ([11]; [12]) and prediction of solar system performance ([13]; [14]; [15]; [16]). Thus, this subject has attracted the attention of a large number of researchers in the field of solar energy systems, and in particular for the estimation of energy production of solar systems.

Many studies applied ANN method to estimate solar systems production. For photovoltaic applications, there have been several studies that use ANN [17]; [18]; [19]; [20]). The study of [17] explored the capability of artificial intelligence techniques such feed-forward and Elman neural networks. Mellit et al [18] studied a large-scale grid connected photovoltaic plant. Three distinct ANN models were used for short-term forecasting of the power produced by the photovoltaic plant located in Southern Italy in order to be applied to three different types of day (sunny, overcast and partly cloudy). The inputs of the ANN-models were the future values of solar cell temperature, in-plane solar irradiance, and the present value of the produced power, whereas the output was represented by the future value of the produced power. Izgi et al [19] applied ANN methodology to predict solar power of a small scale PV panel at different time horizons. An ANN model is used in [20] to obtain the power provided by a photovoltaic installation. The architecture of the neural network was composed by two input variables: temperature and solar irradiance.

Despite the capability of ANN to predict and optimize different solar energy systems, the application of ANN to estimate the electric energy production of PTSTPP is very limited. According to the best knowledge of the authors, single study [7] was reported in the literature based on the following input data: ambient temperature, direct normal radiation, solar multiple, row spacing between parallel collectors and the total number of desired storage hours.

The aim of the present study is to estimate the hourly based energy production of a PTSTPP by using ANNs. As input data we considered the present time step climatic data beside the previous time step energy production. The electric energy production of the PTSTPP was determined by establishing relationships among input-output variables through a feed forward ANN with back propagation algorithm.

II. MATERIALS

A. Location of the power plant and climate data

The site of Ain Beni Mathar (ABM) power plant is located in the Eastern part of Morocco (34°00'35"N, 2°01'29"W) at about 88 km from the city of Oujda. It is the first Moroccan solar thermal plant.

The climate in the region of the plant is Csa (under the Köppen climate classification). The climatic data used in this study were taken from the meteorological station available at the power plant site. The measurements were taken every hour during 1522 days from 01 November 2011 to 31 December 2015. Fig.1 and Fig.2 present respectively the monthly averages of direct normal irradiation and ambient temperature at the region of the power plant over 4 years (2012-2015).
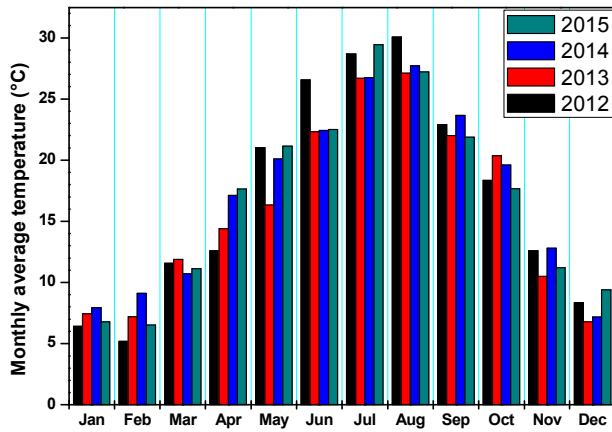

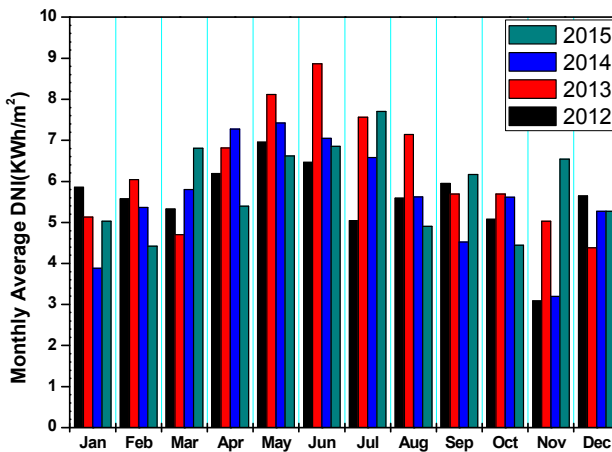Fig.1.Monthly averages of ambient temperature at the power plant location for 4 years (2012-2015)

Fig.2.Monthly averages of DNI for 4 years

B. Description of the power plant

The principle scheme of the ABM power plant is presented in Fig.3. The power plant is a PTSTPP integrated in a combined cycle and composed of two natural gas turbines, a steam turbine, two recovery boilers, a solar field of parabolic trough and a solar-steam heat exchanger.
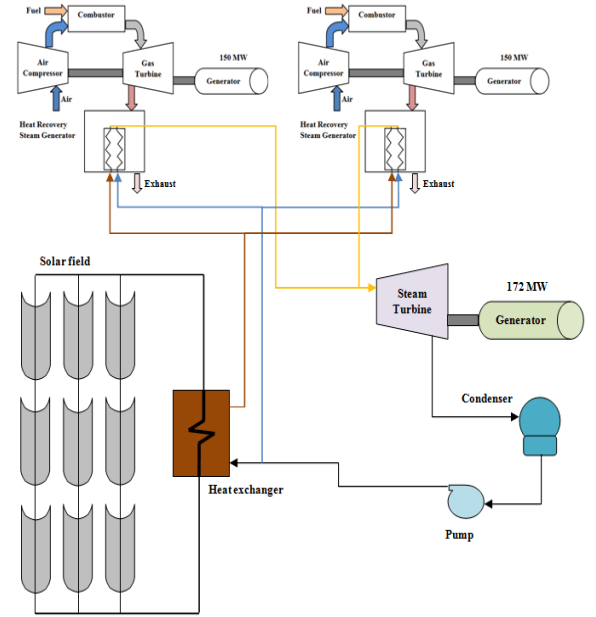
Fig.3.Components of the integrated solar combined cycle power plant

Table 1 illustrates some technical characteristics of the solar field of the power plant.

TABLE I.   TECHNICAL CHARACTERISTICS OF THE SOLAR FIELD [21]

Characteristics	Value	U.M.
Solar Collector Assemblies (SCA) Manufacturer (Model)	Abengoa Solar (ASTR-Ø)	-
Number of Loops	56	-
Number of SCA per Loop	4	-
Number of SCA	224	-
SCA Length	150	m
Mirror Manufacturer	Rioglass	-
Solar-Field Aperture Area	183,120	m²
Solar-Field Outlet Temp	393	°C
Heat Collector Elements Manufacturer (Model)	Schott (PTR70)	-
Number of Heat Collector Elements	8064	-
Heat-Transfer Fluid Type	Therminol VP-1	-

The thermal power at the heat exchanger is calculated as:

$$Q_{th} = \dot{m}_{HTF}.C_{p,HTF}.\Delta T \qquad (1)$$

Where $\dot{m}_{HTF}$ is the mass flow rate of the HTF [kg/s], $C_{p,HTF}$ is the heat capacity of the HTF [J/kg K], ΔT is the HTF temperature difference measured between the inlet and the

outlet at the heat exchanger [K]. More details about the HTF can be found in [22].

The contribution of this thermal power in the total electrical power produced by the steam turbine is determined considering the global efficiency of the heat conversion into electricity $\eta_g = 0.26$:

$$Q_{ele} = \eta_g . Q_{th} \qquad (2)$$

In this work, we focus on the electrical energy produced by the solar field of the power plant. This electrical energy production will be predicted with the ANN modeling. Fig.4 shows the electrical energy production from the solar part of the power plant over 4 years (2012-2015).

The produced energy is about 38.9 GWh for the year 2012, 41.9 GWh for the year 2013 and 39.8 GWh in 2014, while for the year 2015 was recorded the highest production that was about 44.7GWh.
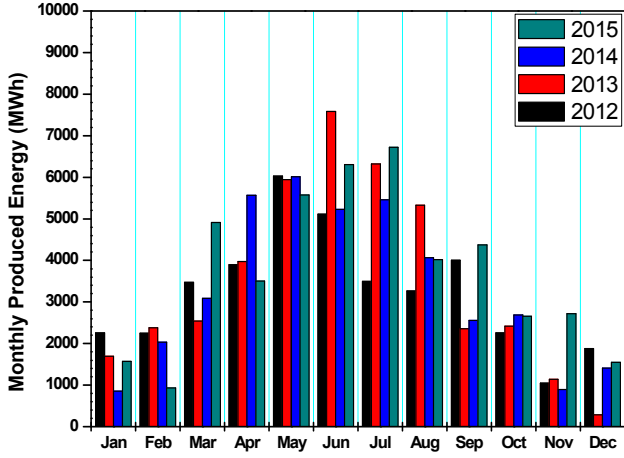

Fig.4. Monthly electrical energy production for 4 years
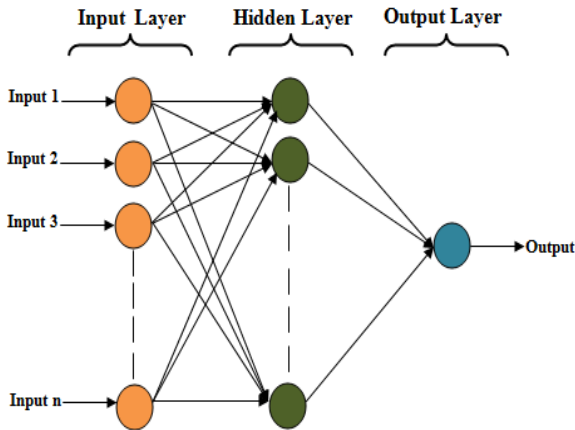
III. METHOD

A. Artficial Neural Networks

Fig.5. Structure of a MLP

ANNs are one of the concepts of artificial intelligence, which is inspired from the working mechanisms of the biological neural system. The MLP are the most popular type of ANNs. The majority of MLP models developed are three layers MLP as indicated in Fig.5.

The first layer is defined as the input layer which receives the input information and unto its communication ability with other neurons, transfers the input signal to next layer [23]. The second layer corresponds to the hidden layer that allows the inputs to be processed using the transfer functions. The third layer is the output layer, which consists of the output unit of the network.

B. Statistical analysis

In this research, several statistical criteria such as coefficient of determination (R), the root mean square error (RMSE), the relative root mean square error (RRMSE), the relative mean bias error (RMBE) and the mean absolute error (MAE) have been used for evaluation of each tested model and to select the best one. Equations used for calculating the criteria are mentioned below.

$$R = \frac{\sum_{k=1}(y_k - \bar{y}).(t_k - \bar{t})}{\sqrt{\sum_{k=1}(y_k - \bar{y})^2 . \sum_{k=1}(t_k - \bar{t})^2}} \qquad (3)$$

$$RMSE = \sqrt{\frac{1}{N}.\sum_{k=1}(t_k - \bar{t})^2} \qquad (4)$$

$$RRMSE = \frac{100}{\bar{t}}\sqrt{\frac{1}{N}.\sum_{k=1}(t_k - y_k)^2} \qquad (5)$$

$$RMBE = 100.\frac{\sum_{k=1}(t_k - y_k)}{\sum_{k=1}(y_k)} \qquad (6)$$

$$MAE = \frac{1}{N}.\sum_{k=1}\left|(t_k - y_k)\right| \qquad (7)$$

Where: t_k is the predicted output and y_k is the real value. $\bar{y}$ and $\bar{t}$ are respectively the mean values of real and the predicted output. N is the number of observations.

C. Implementation of the ANN models

In this study, ANN model was implemented on hourly scale to estimate the hourly electric energy production.

ANN model uses as inputs meteorological data covering period of 4 years. These data are separated into two sets: the training set formed by data from 01 November 2011 to 31 December 2014 and the validation set formed by data of the year 2015.

Relevant input variables, which have a significant influence on energy production (the output), have been selected. In this analysis, several combinations of input variables (direct normal irradiation (DNI_h), hour of the year ($\tau_{h,y}$), hour of the day ($\tau_{h,d}$), ambient temperature (t_h), relative humidity (φ_h), wind speed

(w_h), ambient pressure (p_h), previous hourly energy production (E_{h-1})) have been tested to estimate the hourly energy production (E_h). Fig.6 shows the proposed model.
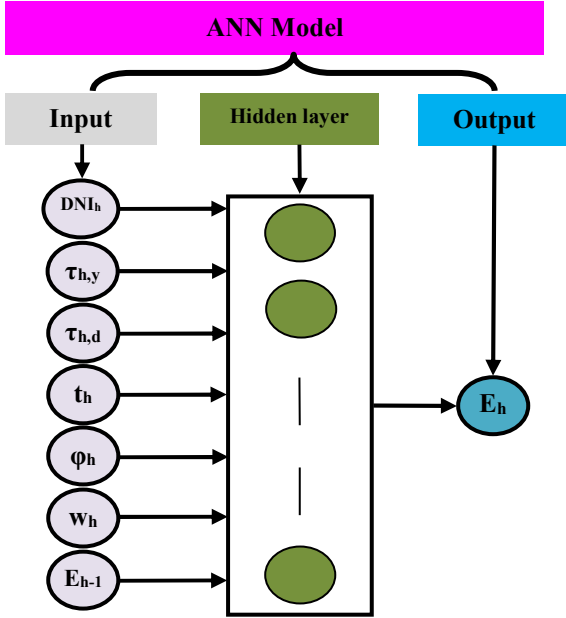

Fig.6. Proposed model for the ANN model

It is worth mentioning that the number of input variables and the number of neurons in the hidden layer was varied in order to find the best combination that gives the best results within reasonable time. The network was trained for 1000 epochs using the Levenberg-Marquardt learning algorithm.

IV. RESULTS AND DISCUSSION

The input parameters selection is the first step in developing the ANN model. In this process, we chose to evaluate the average performance of each input variable for 10 runs. We suggested an incremental method by combining progressively the inputs regarding their individual performances. For all tested ANN models the best architecture will be the one that yield to the best generation results for the validation dataset. Table 2 summarizes the average performances obtained on the hourly dataset for 10 runs. It is well noticed that the combination [DNI_h, τ_{h,y}, τ_{h,d}, t_h, φ_h, w_h, E_{h-1}] gives the best performances in term of R, RMSE, RRMSE, RMBE and MAE values. The performance values are respectively 0.9609, 2.69 MWh 17.36%, -5.67% and 1.95 MWh. Therefore, this combination was considered as the best input combination. In order to find the best architecture that represents accurately the relationship between the inputs and the output, a choice of the number of hidden neurons is mandatory.

TABLE II.   AVERAGE PERFORMANCES OBTAINED FOR VALIDATION DATASET

Input variables							Performances indicators				
DNI_h	τ_{h,y}	τ_{h,d}	t_h	φ_h	w_h	E_{h-1}	R	RMSE [MWh]	RRMSE [%]	RMBE [%]	MAE [MWh]
x							0,7148	6,1373	41,4195	-0,8459	5,0266
x	x						0,8793	4,6481	29,9655	-9,9152	3,7104
x	x	x					0,9330	3,6424	23,4822	-9,3830	2,8414
x	x	x	x				0,9344	3,5878	23,1297	-9,1666	2,7879
x	x	x	x	x			0,9373	3,5242	22,7200	-9,0641	2,7659
x	x	x	x	x	x		0,9397	3,4609	22,3118	-8,9186	2,6982
x	x	x	x	x	x	x	0,9609	2,6931	17,3618	-5,6709	1,9536
x	x	x				x	0,9565	2,8446	18,3385	-6,1117	2,0885
x	x	x	x			x	0,9575	2,8049	18,0828	-5,9752	2,0326
x	x	x	x	x		x	0,9579	2,7796	17,9197	-5,7268	1,9849
x	x	x		x		x	0,9576	2,7995	18,0481	-5,9441	2,0207
x	x	x			x	x	0,9593	2,7760	17,8962	-6,0935	2,0652

TABLE III.   AVERAGE PERFORMANCES OBTAINED FOR DIFFERENT NUMBER OF HIDDEN NEURONS FOR THE VALIDATION DATASET

Number of hidden neurons	R	RMSE [MWh]	RRMSE[%]	RMBE [%]	MAE [MWh]	Number of hidden neurons	R	RMSE [MWh]	RRMSE [%]	RMBE [%]	MAE [MWh]
1	0,9133	3,8247	24,6573	-5,2272	2,8624	16	0,9683	2,4215	15,6108	-5,0855	1,7005
2	0,9300	3,5151	22,6610	-6,1702	2,6297	17	0,9688	2,4138	15,5616	-5,2510	1,7036
3	0,9501	3,0418	19,6102	-6,1369	2,3220	18	0,9688	2,3886	15,3989	-4,7914	1,6702
4	0,9586	2,7591	17,7875	-5,3168	2,0538	19	0,9688	2,3868	15,3876	-4,7691	1,6359
5	0,9609	2,6931	17,3618	-5,6709	1,9536	20	0,9688	2,4151	15,5694	-5,2919	1,7001
6	0,9632	2,5983	16,7510	-5,3001	1,8394	21	0,9683	2,4072	15,5189	-4,8154	1,7071
7	0,9653	2,5653	16,5382	-5,8037	1,8599	22	0,9692	2,3725	15,2949	-4,7345	1,6272
8	0,9656	2,5108	16,1864	-5,0667	1,7622	23	0,9683	2,4174	15,5844	-4,9795	1,7175
9	0,9659	2,5125	16,1976	-5,3309	1,7774	24	0,9681	2,4170	15,5822	-4,8369	1,6753
10	0,9673	2,4624	15,8749	-5,2187	1,7283	25	0,9687	2,4017	15,4834	-4,8838	1,6832
11	0,9670	2,4629	15,8782	-5,0174	1,7310	26	0,9677	2,4428	15,7481	-5,1084	1,7266
12	0,9681	2,4399	15,7300	-5,3390	1,7256	27	0,9682	2,4149	15,5687	-4,8676	1,6988
13	0,9683	2,4209	15,6070	-5,0588	1,6995	28	0,9682	2,4113	15,5454	-4,7894	1,6716
14	0,9688	2,4086	15,5278	-5,1475	1,6947	29	0,9678	2,4328	15,6836	-4,9793	1,7429
15	0,9688	2,3867	15,3869	-4,7438	1,6592	30	0,9677	2,4293	15,6611	-4,8673	1,7000

As for the choice of input variables, several experiments have been performed in the current study, by varying the number of neurons in the hidden layer using a constructive approach. Indeed, the procedure consists in starting with single neuron and then adding, accumulatively, additional neurons. Obviously, the variables [DNI_h, $\tau_{h,y}$, $\tau_{h,d}$, t_h, φ_h, w_h, E_{h-1}] have been taken as inputs in all runs.

For all tested architectures, the average performances in term of R, RMSE, RRMSE, RMBE and MAE values are presented in Table 3. It is noticed that the best R, RMSE, RRMSE, RMBE, MAE values are obtained with 22 hidden neurons architecture. So, we can consider the combination [DNI_h, $\tau_{h,y}$, $\tau_{h,d}$, t_h, φ_h, w_h, E_{h-1}] with 22 hidden neurons as a good architecture for estimating the energy production of our PTSTPP in an hourly scale.

The regression plots of measured and predicted ANN model energy production for the training and validation dataset are presented in Fig.7.
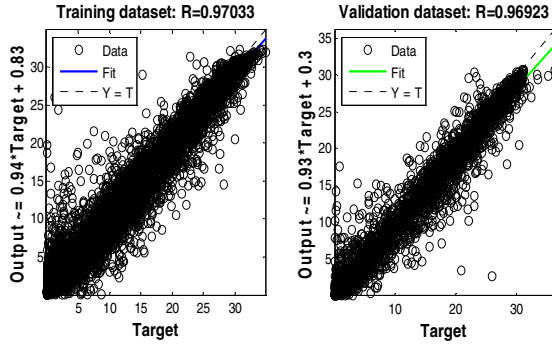

Fig.7. Regression plots of hourly measured and predicted outputs of training and validation datasets.

Table 4 summarizes the best statistical performances on 10 runs obtained for the training and validation datasets by considering the ANN model with [DNI_h, $\tau_{h,y}$, $\tau_{h,d}$, t_h, φ_h, w_h, E_{h-1}] as input variables and 22 hidden neurons. The performances in term of R, RRMSE and MAE on 10 runs for the training phase are respectively 0.9703, 14.63% and 1.36 MWh. For the validation dataset, these values are 0.9692, 15.29% and 1.63 MWh.

TABLE IV.   BEST PERFORMANCES OBTAINED FOR TRAINING AND VALIDATION DATASETS FOR THE BEST ANN MODEL

	R	RMSE [MWh]	RRMSE [%]	MAE [MWh]
Training dataset	0,9703	2,1593	14,6308	1,3645
Validation dataset	0,9692	2,3725	15,2949	1,6272

A comparison between experimental and ANN predicted results for validation year is presented in Fig.8. The trend of the variation of the monthly energy is close to the measured one. The total measured electric energy production is about 44.7 GWh/year, while the predicted one is 42.6 GWh/year, representing an underestimation less than 5%. This underestimation is noticed in the RMBE value, which equals to -4.73%.
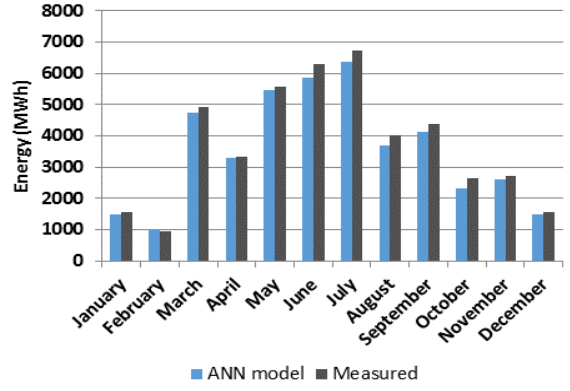

Fig.8.Comparison between measured and ANN predicted energy production

Fig.9 shows the relative difference between measured and ANN predicted energy production of the PTSTPP. The highest relative difference value was about 12.8%, noticed in October and the lowest value was about 0.84% and was noticed in April.
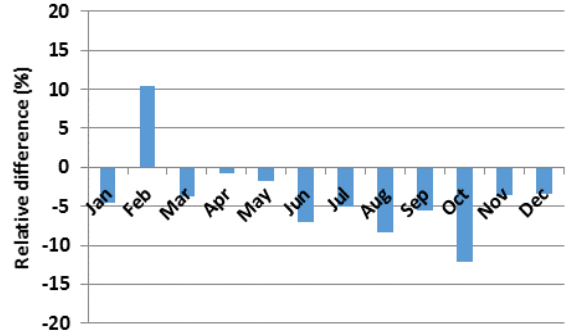

Fig.9. Relative difference between measured and ANN predicted energy production.

V.   CONCLUSION

In this study, ANN method has been applied to model a PTSTPP in the goal to predict the electric energy production at the output of the generator. Very limited studies of this type were reported in literature.

We tested the performance of ANN MLP to predict hourly energy production.

In order to choose the best architecture, several models were developed by using different input variables and by varying the number of neurons in the hidden layer.

This approach shows that the predicted values were very close to the measured values with regression values of about 0.97 for the training and validation data sets. Results of the validation dataset prove that the RRMSE, RMBE and MAE are respectively about 16.2 %, -4.65 % and 1.68 MWh. Also, it was found that the ANN model underestimates the annual energy production with -4.73%.

On the basis of the results obtained, it can be concluded that the ANN model can successfully estimate the energy production in a PTSTPP. This study can help assess the

performance of a similar solar power plant, in particular Morocco.

REFERENCES

[1] Z. Aqachmar, A. Allouhi, A. Jamil, and B. Gagouch, "Parabolic trough solar thermal power plant Noor I in Morocco," *Energy*, vol. 178, pp. 572–584, 2019.

[2] A. Zaaoumi, A. Bah, M. Alaoui, A. Mechaqrane and M. Berrehili, "Application of artificial neural networks and adaptive neuro-fuzzy inference system to estimate the energy generation of a solar power plant in Ain Beni-Mathar (Morocco)," 2018 *10th International Conference on Electronics, Computers and Artificial Intelligence (ECAI)*, Iasi, Romania, 2018, pp. 1-6.

[3] Dersch, J., *Greenius User Manual. Tech. rep.*, DLR, Koln, Germany. 2010.

[4] System Advisor Model. National Renewable Energy Laboratory. Golden, CO. https://sam.nrel.gov/download.html. [Accessed: 09-Apr-2020]

[5] H. A. L. Ouali, A. A. Merrouni, M. A. Moussaoui and A. Mezrhab, "Electricity yield analysis of a 50 MW solar tower plant under Moroccan climate," *2015 International Conference on Electrical and Information Technologies (ICEIT)*, Marrakech, 2015, pp. 252-256.

[6] Wagner, M. J. and Zhu, G., "A Direct-Steam Linear Fresnel Performance Model for NREL's System Advisor Model," *Proceedings of the ASME 2012 6th International Conference on Energy Sustainability & 10th Fuel Cell Science, Engineering and Technology Conference*, San Diego, CA.2012.

[7] T. E. Boukelia, O. Arslan, and M. S. Mecibah, "ANN-based optimization of a parabolic trough solar thermal power plant," *Appl. Therm. Eng.*, vol. 107, pp. 1210–1218, 2016.

[8] F. Gutierrez-corea and M. Manso-callejo, "ScienceDirect Forecasting short-term solar irradiance based on artificial neural networks and data from neighboring meteorological stations," *Sol. Energy*, vol. 134, pp. 119–131, 2016.

[9] B. Ihya, a. Mechaqrane, R. Tadili, and M. N. Bargach, "Prediction of hourly and daily diffuse solar fraction in the city of Fez (Morocco)," *Theoretical and Applied Climatology*, vol. 120, no. 3–4, pp. 737–749, 2014.

[10] A. Ouammi, D. Zejli, H. Dagdougui, and R. Benchrifa, "Artificial neural network analysis of Moroccan solar potential," *Renew. Sustain. Energy Rev.*, vol. 16, no. 7, pp. 4876–4889, 2012.

[11] M. Jamma, M. Barara, A. Bennassar, et M. Akherraz, « Intelligent Control Strategy of a Three-Phase PWM Rectifier Based on Artificial Neural Networks Approach and Fuzzy Logic Controller », *Proceedings of the 16th International Conference on Hybrid Intelligent Systems (HIS 2016), Advances in Intelligent Systems and Computing.* vol. 552, pp. 329-339. 2017.

[12] M. M. Elkholy and A. Fathy, "Optimization of a PV fed water pumping system without storage based on teaching-learning-based optimization algorithm and artificial neural network," *Sol. Energy*, vol. 139, pp. 199–212, 2016.

[13] A. F. Mashaly, A. A. Alazba, A. M. Al-awaadh, and M. A. Mattar, "ScienceDirect Predictive model for assessing and optimizing solar still performance using artificial neural network under hyper arid environment," *Sol. Energy*, vol. 118, pp. 41–58, 2015.

[14] W. Yaïci and E. Entchev, "Performance prediction of a solar thermal energy system using artificial neural networks," *Appl. Therm. Eng.*, vol. 73, no. 1, pp. 1348–1359, 2014.

[15] A. Mellit, S. A. Kalogirou, L. Hontoria, and S. Shaari, "Artificial intelligence techniques for sizing photovoltaic systems: A review," *Renew. Sustain. Energy Rev.,* vol. 13, no. 2, pp. 406–419, 2009.

[16] S. A. Kalogirou and S. Panteliou, "Thermosiphon solar domestic water heating systems: long-term performance prediction using artificial neural networks," *Sol. Energy*, vol. 69, no. 2, pp. 163–174, 2000.

[17] C.-D. Dumitru, A. Gligor, and C. Enachescu, "Solar Photovoltaic Energy Production Forecast Using Neural Networks," *Procedia Technology*, vol. 22, pp. 808–815, 2016.

[18] A. Mellit, A. M. Pavan, and V. Lughi, "Short-term forecasting of power production in a large-scale photovoltaic plant," *Sol. Energy*, vol. 105, pp. 401–413, 2014.

[19] Izgi, E., Oztopal, A., Yerli, B., Kaymak, M.K. and Sahin, A.D., "Short – mid-term solar power prediction by using artificial neural networks," *Sol. Energy*, vol. 86, pp. 725–733, 2012.

[20] F. Almonacid, C. Rus, P. J. Pérez, and L. Hontoria, "Estimation of the energy of a PV generator using artificial neural network," *Renew. Energy*, vol. 34, no. 12, pp. 2743–2750, 2009.

[21] ISCC Ain BeniMathar. National Renewable Energy Laboratory (https://solarpaces.nrel.gov/iscc-ain-beni-mathar). [Accessed: 09-Apr-2020]

[22] Solutia, "Therminol VP-1," *Solutia*, pp. 1–5, 2014.

[23] M. Vakili, S. Sabbagh-yazdi, K. Kalhor, and S. Khosrojerdi, "Using Artificial Neural Networks for Prediction of Global Solar Radiation in Tehran Considering Particulate Matter Air Pollution," *Energy Procedia*, vol. 74, pp. 1205–1212, 2015.

Application of artificial neural networks and adaptive neuro-fuzzy inference system to estimate the energy generation of a solar power plant in Ain Beni-Mathar (Morocco)

A.Zaaoumi, A.Bah, M.Alaoui
Research Team in Thermal and Energy
ENSET, Mohammed V University
Rabat, Morocco
a.zaaoumi@gmail.com

A.Mechaqrane
Laboratory of Renewable
Energies and Smart Systems
FST Street Immouzar, B.P. 2202
Fez, Morocco

M.Berrehili
Office National de l'Electricité
et de l'Eau Potable
Oujda, Morocco

Abstract— **Currently, concentrated solar power (CSP) plant has gained large importance due to its good environmental aspect. However, the process of the CSP power production presents important variability, as it relied on meteorological conditions, which gives new challenges to power system operators. To handle these challenges, it is significant to be able to anticipate and observe production levels. The present paper presents a comparison between two artificial intelligence models artificial neural networks (ANN) and adaptive neuro-fuzzy inference system (ANFIS), to estimate the daily electric energy generation of a solar power plant in Ain Beni-Mathar (34°00'35"N, 2°01'29"W) in Eastern Morocco. Six input variables (daily direct normal irradiation, day of the month, daily mean ambient temperature, mean wind velocity, relative humidity and previous daily electric production) served as the inputs of the ANN and ANFIS models. The results showed that both the ANN and ANFIS models performed similarly in terms of prediction accuracy.**

Keywords— CSP; Energy generation; ANN; ANFIS; Prediction;

I. INTRODUCTION

Today, the concern from the problem of climate change is global and worries the citizens of the whole world. Solar energy is considered as the most suitable and interesting energy solution for the greenhouse gases. Many technologies are developed in order to benefit from this energy. The best and most promising of these technologies is the CSP plant, which allows to transform the energy radiated by the sun into heat at high temperature, then into mechanical and electrical energy through a thermodynamic cycle [1]. However, the exploitation of solar energy raises some technical challenges. Like wind energy, it is an energy called intermittent and random: its availability varies greatly without possibility of control. The integration of such sources on the electricity grid generates problems for maintaining the balance between consumption and production.

Two main avenues are used to overcome this limitation. The first one is Storage: the storage of energy would stabilize the production of electricity by storing thermal power during periods of high production to restore it during production falls [2]. However, storing large amounts of energy remains a challenge at the moment especially in term of cost and technology. The second tool is Forecasting: forecasting the production of intermittent energies would make it possible to anticipate the availability of generation sources and thus facilitate the management of the grid. In the last two decades, artificial intelligence had been used widely to forecast the energy production. Many studies with artificial neural networks and fuzzy logic, genetic algorithm, or the combination of two techniques shows their powerful ability to predict the energy production with suitable accuracy.

In [3] the authors use a MLP neural network with two inputs, temperature and irradiance, to predict the power produced by a PV installation. An ANFIS with an echo state network (ESN) for short term PV power prediction was developed and compared in [4]. The artificial intelligence techniques capability such feed-forward and Elman neural network for forecasting the energy production of a photovoltaic resource was explored in [5].

For solar thermal energy systems (STES), W. Yaïci and E. Entchev [6, 7] predict the performance parameters of a STES under different weather conditions in Canada by the application of ANN and ANFIS models.

Many other works using ANN and ANFIS models in the field of predicting the energy generation from different nature like solar, wind, hydraulic can be found in [8-10].

The present work focused on predicting the daily electric production of a solar power plant in Ain Beni-Mathar (eastern Morocco) by ANN and ANFIS models. For this purpose a large amount of data (01 November 2011 - 31 December 2015) was used to train and test the models. . A comparison between the two techniques was done in order to define their prediction ability and accuracy.

ST: Steam Turbine   GT: Gas Turbine   RB: Recover Boiler   AC: Air Condenser

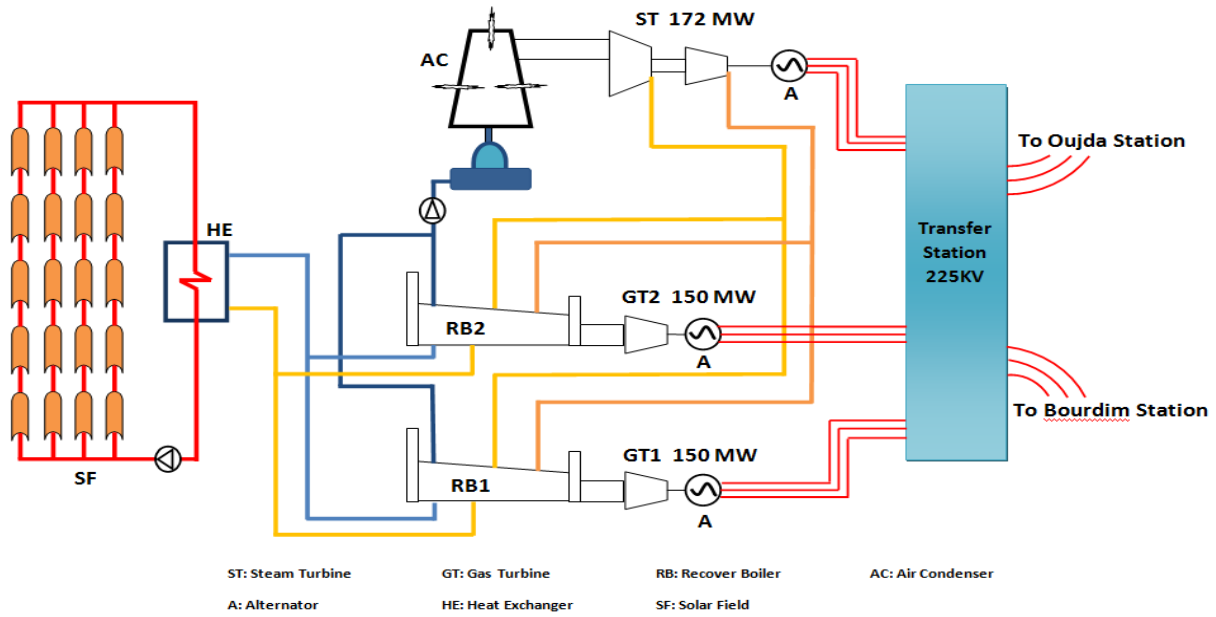A: Alternator   HE: Heat Exchanger   SF: Solar Field

Fig. 1 Components of the Integrated Solar Combined Cycle Power Plant used in Ain Beni-Mathar

The paper is structured as follows. Section II presents the characteristics of the solar power plant which is followed by a description of the site weather in section III. The section IV will be devoted to the energy generation of the CSP plant. In section V we present the methodology of data normalization. Section VI shows the characteristics of ANN and ANFIS models. The section VII is interested to the study results. Finally, conclusions are presented.

II. SYSTEM DESCRIPTION

Ain Beni-Mathar Integrated Solar Combined Cycle Power Plant (ISCC) (Fig.1) is constituted of a CSP plant and a Natural Gas-Fired Combined Cycle (NGCC) power plant. The whole plant consists of two gas turbines fueled by natural gas, a steam turbine, two recovery boilers, a solar field and heat exchanger. The solar energy collected at the parabolic troughs participates in increasing the flow of steam produced in the recovery boilers [11]. The steam generated in the two recovery boilers is expanded in the three body steam turbine (High, Medium and Low Pressure). Solar radiation contributes to increase the total power of the plant up to 20 MW. Table 1 illustrates some technical characteristics of the ABM power plant [12].

TABLE1: TECHNICAL CHARACTERISTICS OF THE AIN BENI MATHAR POWER PLANT

Site Area	160 ha (including 88 ha for the solar field)
Total installed power	472 MW of which 20 MW of solar origin
Solar field heating surface	183200 m²
Solar heat	58.7 MJ / s
Specific consumption Combined Cycle Power plant (including solar)	6912.5 kJ / kWh; 6588.8 kJ / kWh
Cooling Mode	Dry (air condenser: annual water consumption 850 000 m³)
Availability: Combined Cycle	93%
Solar field	95%

III. WEATHER CHARACTERISTICS OF SITE

The climate in Ain Beni-Mathar is Mediterranean with a mild to cold and rainy winter and a hot summer. The temperature of the region of Ain Beni Mathar presents a very great seasonal variability (Fig 2). The summers are hot and the winters cold.

The average minimum temperature of the coldest month (February) is 5.2 °C while the average maximum temperature of the hottest month (August) is 30 ° C.

The monthly evolution of the average wind speed in the region of Ain Beni Mathar is characterized by great variability (Fig.3): maximum average speed recorded in February is 5.4 m/s.

The relative humidity in the region of Ain Beni Mathar varies seasonally (Fig.4). The ambient air is very dry in summer, the minimum average relative humidity recorded in August is 21.8%, and humid in winter, the average maximum relative humidity recorded in December is 77%.

The area of Ain Beni Mathar is quite sunny with an average daily DNI of 5.2 KWh/m². It is sunny throughout the year (Fig.5). The maximum average irradiation value was recorded in June (8.86 KWh/m²) and the mean minimum value in November (3.08 KWh/m²). The data used in this study are taken from the meteorological station available at the power plant site.

IV. ENERGY GENERATION

Since solar energy is not very dense, it is necessary to concentrate it, via reflecting mirrors, to obtain exploitable temperatures for the production of electricity. Parabolic trough plants are currently considered to be the most mature and sustainable technology of CSP plants.
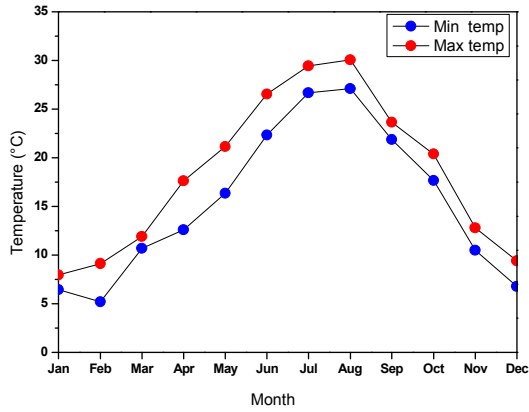
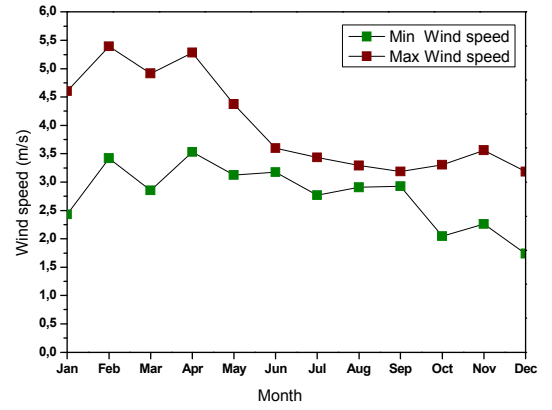Fig.2 Average min and max temperature at the work site

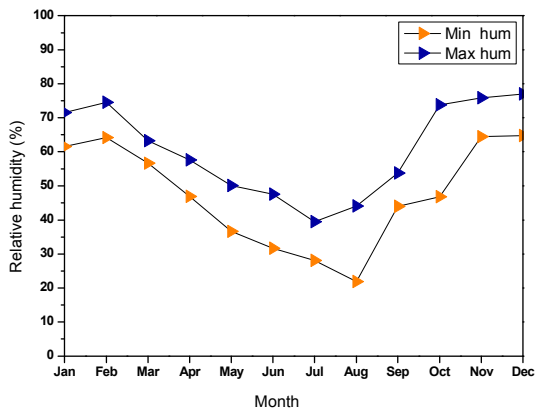Fig.3 Average min and max wind speed at the work site

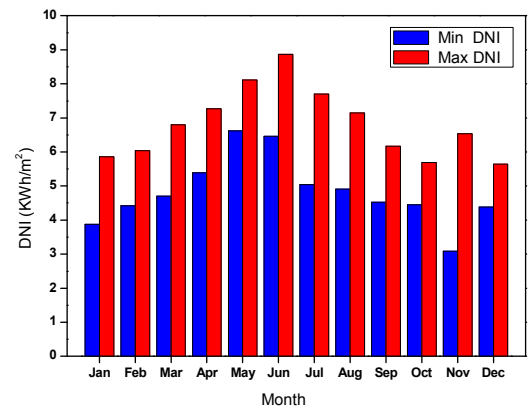Fig.4 Average min and max relative humidity at the work site

Fig.5 Daily sum of DNI

The CSP plant is composed of parallel alignments of long hemi-cylindrical reflector mirrors, which rotate around a horizontal axis. The solar radiation is concentrated on a tubular absorber, located on the focal axis. The absorber absorbs the energy reflected by the mirrors and transfers it to the thermodynamic fluid called heat transfer fluid (HTF) whose temperature generally reaches 400 °C. This fluid is then pumped through the heat exchanger to produce superheated steam that operates a turbine and then by an alternator to convert mechanical energy into electrical energy [13].

The energy collected at the heat exchanger is given by the following equation:

$$Q = \dot{m}_{HTF}.C_{p,HTF}.\Delta T$$
$$= \dot{m}_{HTF} (C_{p,HTFin} .T_{HTF,in} - C_{p,HTFout} T_{HTF,out}) \quad (1)$$

with $\dot{m}_{HTF}$ is the mass flow rate [kg/s], $C_{p,HTFin}$ and $C_{p,HTFout}$ are the input and output heat capacities [J/kg K] of the HTF, respectively, $T_{HTF,in}$ and $T_{HTF,out}$ are respectively the HTF temperature measured at the inlet and the outlet at the heat exchanger [K]. It's worth mentioned that because of the higher working temperature of the HTF, its properties change with temperature [14].

The electrical energy collected at the output of the alternator is given by:

$$E=0.26*Q \quad (2)$$

It's this electrical energy that we will predict with the ANN and ANFIS modeling.

V. NORMALIZATION OF DATA

In this study, direct normal irradiation, ambient temperature, relative humidity and wind speed values, collected at Ain Beni-Mathar station located in Eastern of Morocco, were used for the prediction of electric energy using ANN and ANFIS models. To enhance the network prediction processing, the data was normalized between 0 and 1 according to the following equation [10].

$$X_i = \frac{X_{ki} - \min(X_k)}{\max(X_k) - \min(X_k)} \quad (3)$$

where X_i is the ith normalized value and X_{ki} is the ith input of the vector $X_k = (X_{k1},...,X_{kn})$ that we will normalize.

VI. APPLICATION OF ARTIFICIAL NEURAL NETWORKS AND ADAPTIVE NEURO-FUZZY INFERENCE SYSTEM

A. Artificial neural networks:

Artificial neural network is a method inspired by the working mechanism of the human brain. It operates like a black box that understands/models the relation between some excitations of a system and their corresponding responses. The most used ANN architecture is the feed forward Multi-Layers Perceptron (MLP) with one hidden layer (Fig.6). In this model, the information spreads forward one layer to another.

Before their use, ANNs require to be well trained to anticipate connection parameters. Training is a gradual process, iterative or recursive, in which the weights of the network are modified several times according to a defined goal before reaching their final values. Among the methods of training a network, the algorithm of back propagation (BP) of the gradient is most often used [15, 16].

The main benefit of using ANNs is that they can exploit the information related with the problem, without having knowledge of the existing relationships linking the different variables and sources of information.
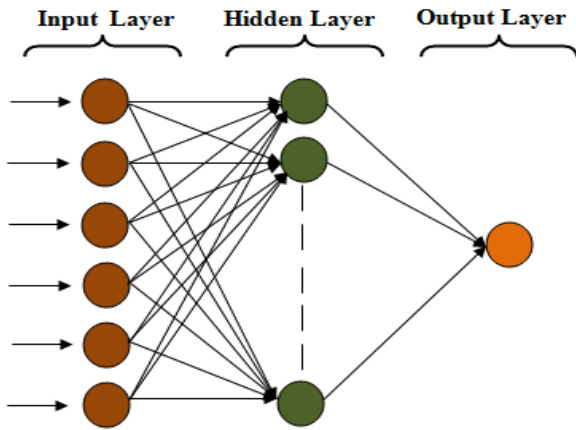

Fig.6 Structure of ANN selector for six inputs

B. Adaptative neuro-fuzzy inference system:

Adaptive neuro-fuzzy inference system (ANFIS) is a combination of artificial intelligence methods which allows the application of ANN and fuzzy logic together [17].The advantage of this method is that it uses the benefit of both methods. It is capable of solving nonlinear and complex problems. ANFIS architecture is an adaptive network that uses supervised learning, which has a function similar to the model of Takagi–Sugeno fuzzy inference system and has a five layered architecture (Fig.7).

Analyzing the mapping relation between the input and output data, ANFIS can establish the optimal distribution of membership functions using either a back propagation gradient descent algorithm alone or in combination with a least-squares method.
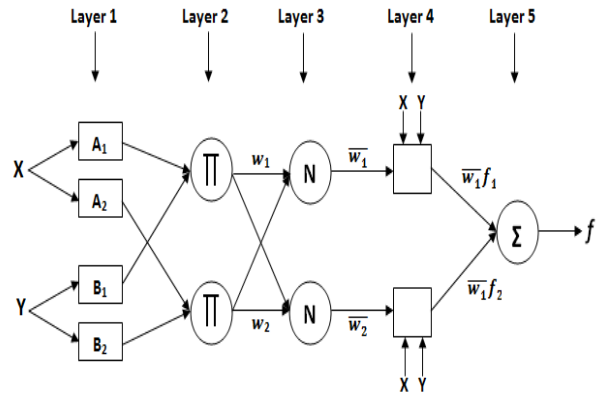

Fig.7 Adaptive neuro-fuzzy inference system structure.

C. Selection of the best model:

To compare and test the constructed models and select the best one, the models performance were evaluated using regular comparison tools in modeling involving the coefficient of determination (R), root mean square error (RMSE) and mean absolute error (MAE).

$$R = \frac{\Sigma_{k=1}(y_k - \overline{y})(t_k - \overline{t})}{\sqrt{\Sigma_{k=1}(y_k - \overline{y})^2 \, \Sigma_{k=1} \, (t_k - \overline{t})^2}} \quad (4)$$

$$RMSE = \sqrt{\frac{1}{N} \cdot \Sigma_{k=1} \, (t_k - y_k)^2} \quad (5)$$

$$MAE = \frac{1}{N} \cdot \Sigma_{k=1} \left| (t_k - y_k) \right| \quad (6)$$

y_k and t_k denote, respectively, the network output and the measured value for the k_{th} element.

VII. RESULTS AND DISCUSSION

The ANN and ANFIS models used in this work have six inputs and one output. Day of the month (D_m), daily direct normal irradiation (DNI), daily ambient temperature (T), daily relative humidity (H_r), daily wind speed (W_s) and daily previous production (E_{t-1}) are served as the input variables, whilst the electric energy production is the output variable. To train and test the models, MATLAB platform was used.

The data set used in this study covers a period of more than 4 years between 01 November 2011 and 31 December 2015 (Fig.8). The data between 01 November 2011 and 31 December 2014 were used for training phase and the data of the year 2015 were used for the validation procedure. It is well noted that the data used in this study have undergone a fine processing, and it has been taken into account only the data where there is energy production. It is to notice that there are days where there is no solar energy production because of the maintenance of solar components or no enough solar irradiation. So we eliminated those data to have a model that links the variation of the input parameters with the variation of energy generation.
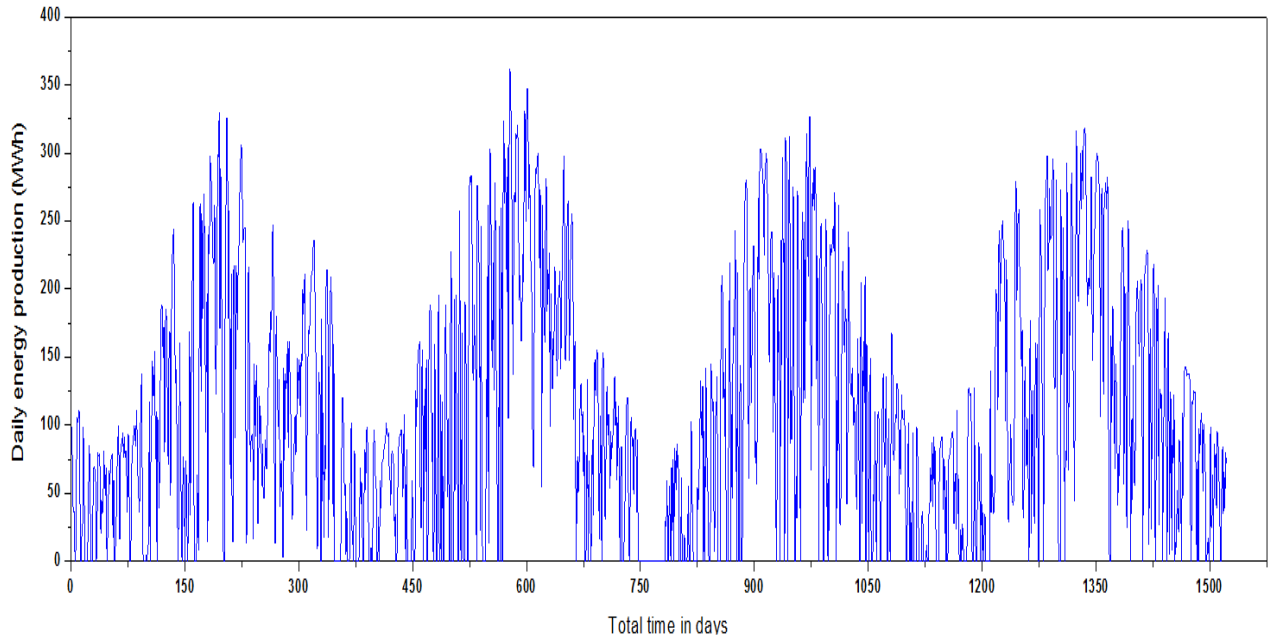
Fig.8 Chronological energy production.

For ANN model, the network was trained and tested using Levenberg-Marquardt back propagation algorithm (Table 2). We choose this algorithm because it was performed the best in the predicting procedure. The number of neurons in the hidden layer was varied from 1 to 10.

For the ANFIS model and in order to find the smallest architecture that represents accurately the relationship between the inputs and the output, we select the Subtractive Clustering as FIS generation method. Various numbers of radius between 0.5 and 1 have been tested in the current study to see who performed the best in term of R, RMSE and MAE. Of course the variables [DNI D_m T_a H_r W_s E_{t-1}] have been taken as inputs in all runs. More informations and details about the ANFIS model are given in Table 3.

TABLE2: PARAMETERS OF THE NEURAL NETWORKS

ANN info	Parameters
Number of hidden layers	1
Number of epochs	1000
Training algorithm of network	Back propagation
Type of activation functions	Logsig, Tansig

TABLE3: PARAMETERS OF THE ANFIS

ANFIS info	Characteristics
Fuzzy structure	Sugeno-type
Initial FIS for training	Genfis2
Epoch	50
Output membership function	Linear
Training algorithm	Hybrid

Table 4 shows for each tested architecture, the average performances in term of R, RMSE and MAE for 10 runs. It is found that the architecture that yielded to the best generalization results is the architecture with 4 hidden neurons.

Table 5 shows for each tested ANFIS architecture, the average performances in term of R, RMSE and MAE for different numbers of radius. It is noticed that the best architecture for the testing phase is obtained

with radius = 0.9.

Figure 9 and 10 show the plots for the best regression values obtained for the validation phases and its corresponding value of the training phase respectively for the ANN and ANFIS models.

TABLE4: Average performances obtained for different numbers of hidden neurons

Number of hidden neurons	Training phase			Testing phase		
	R	RMSE	MAE	R	RMSE	MAE
1	0,9224	0,0868	0,0634	0,9203	0,0972	0,0716
2	0,9330	0,0809	0,0600	0,9304	0,0943	0,0697
3	0,9396	0,0769	0,0570	0,9386	0,0925	0,0701
4	0,9451	0,0735	0,0539	0,9408	0,0899	0,0662
5	0,9465	0,0725	0,0531	0,9362	0,0906	0,0684
6	0,9494	0,0706	0,0509	0,9389	0,0896	0,0654
7	0,9503	0,0699	0,0508	0,9369	0,0907	0,0661
8	0,9516	0,0691	0,0501	0,9335	0,0912	0,0658
9	0,9536	0,0676	0,0490	0,9380	0,0901	0,066
10	0,9554	0,0663	0,0484	0,9330	0,0925	0,0685

TABLE5: Average performances obtained for different numbers of radius

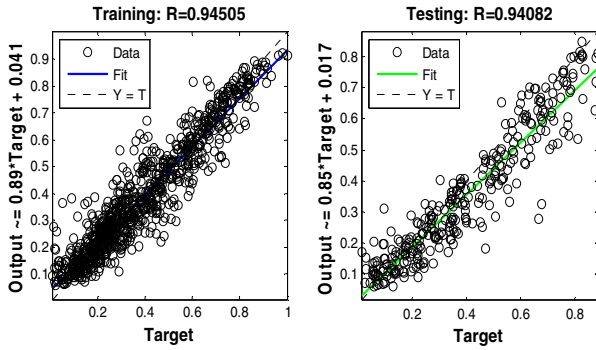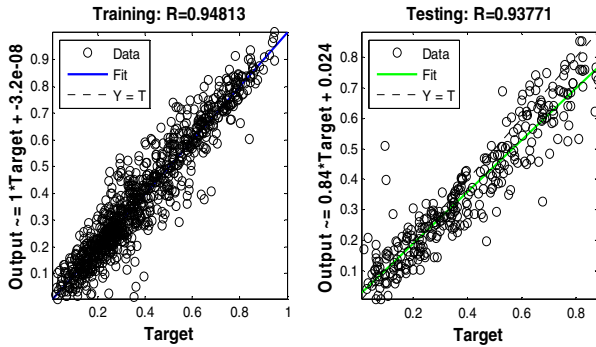| Number of Radius	Training phase			Testing phase		
	R	RMSE	MAE	R	RMSE	MAE
0,50	0,9672	0,0571	0,0415	0,9099	0,1028	0,0759
0,55	0,9650	0,0590	0,0431	0,9139	0,0975	0,0717
0,60	0,9619	0,0615	0,0443	0,9218	0,0974	0,0721
0,65	0,9553	0,0664	0,0480	0,9213	0,0984	0,0741
0,70	0,9534	0,0678	0,0484	0,9355	0,0912	0,0686
0,75	0,9531	0,0680	0,0488	0,9361	0,0916	0,0685
0,80	0,9519	0,0688	0,0497	0,9299	0,0963	0,0703
0,85	0,9483	0,0713	0,0513	0,9375	0,0895	0,0668
0,90	0,9481	0,0714	0,0514	0,9377	0,0893	0,0664
0,95	0,9427	0,0749	0,0551	0,9373	0,0903	0,0670
1.00	0,9426	0,0750	0,0553	0,9368	0,0907	0,0677

Fig.9 Regression plot of ANN.

Fig.10 Regression plot of ANFIS.

In this part of work, we will compare the best performance of the ANN and ANFIS models. Table 6 shows the best performance of the ANN and ANFIS models in term of R, RMSE and MAE. It is clear that both ANN and ANFIS models gives the same accuracy for training and testing phase, with a negligible difference.

TABLE6: Performance comparison between the best ANN and ANFIS models.

Model	Training phase			Testing phase		
	R	RMSE	MAE	R	RMSE	MAE
ANN	0,9451	0,0735	0,0539	0,9408	0,0899	0,0662
ANFIS	0,9481	0,0714	0,0514	0,9377	0,0893	0,0664

VIII. CONCLUSION

In this study, ANN and ANFIS methods have been applied to predict the alternator energy generation of a solar power plant composed from a CSP plant and a Natural Gas-Fired Combined Cycle power plant. The ANN and ANFIS models were developed considering six inputs [DNI D_m T_a H_r W_s E_{t-1}] and one output data. The predicted values with the ANN and ANFIS models are very close to the experimental ones. Coefficients were R=0.9450 and R=0.9408 for ANN, and R=0.9481 and R=0.9377 for ANFIS for training and validation phases. So, it is clear that ANN and ANFIS models perform similarly and can successfully forecast the electric energy generation of a solar power plant.

REFERENCES

[1] G. Cac, "Concentrated solar power plants : Review and design methodology," Renewable and Sustainable Energy Reviews, vol. 22, pp. 466–481, 2013.

[2] M. S. Guney, "Solar power and application methods," Renewable and Sustainable Energy Reviews, vol. 57, pp. 776–785, 2016.

[3] F. Almonacid, C. Rus, P. J. Pérez, and L. Hontoria, "Estimation of the energy of a PV generator using artificial neural network," Renewable Energy, vol. 34, no. 12, pp. 2743–2750, 2009.

[4] I. Jayawardene and G. K. Venayagamoorthy, "Comparison of adaptive neuro-fuzzy inference systems and echo state networks for PV power prediction," Procedia Computer Science, vol. 53, no. 1, pp. 92–102, 2015.

[5] C.-D. Dumitru, A. Gligor, and C. Enachescu, "Solar Photovoltaic Energy Production Forecast Using Neural Networks," Procedia Technology, vol. 22, pp. 808–815, 2016.

[6] W. Yaïci and E. Entchev, "Performance prediction of a solar thermal energy system using artificial neural networks," Applied Thermal Engineering, vol. 73, no. 1, pp. 1348–1359, 2014.

[7] W. Yaïci and E. Entchev, "Performance prediction of a solar thermal energy system using artificial neural networks," Applied Thermal Engineering, vol. 73, no. 1, pp. 1348–1359, 2014.

[8] C. D. Dumitru and A. Gligor, "Daily Average Wind Energy Forecasting Using Artificial Neural Networks," Procedia Engineering, vol. 181, pp. 829–836, 2017.

[9] B. Ihya, a. Mechaqrane, R. Tadili, and M. N. Bargach, "Prediction of hourly and daily diffuse solar fraction in the city of Fez (Morocco)," Theoretical and Applied Climatology, vol. 120, no. 3–4, pp. 737–749, 2014.

[10] A. T. Hammid, M. H. Bin Sulaiman, and A. N. Abdalla, "Prediction of small hydropower plant power production in Himreen Lake dam (HLD) using artificial neural network," Alexandria Engineering Journal, vol. 57, pp. 211-221, 2018.

[11] B. J. Alqahtani and D. Patiño-Echeverri, "Integrated Solar Combined Cycle Power Plants: Paving the way for thermal solar," Applied Energy, vol. 169, pp. 927–936, 2016.

[12] Office National de l'Electricite "Centrale Thermo-Solaire À Cycle Combine Integre D ' Ain Beni Mathar," (www.one.ma).

[13] H. Price et al., "Advances in Parabolic Trough Solar Power Technology," Journal of Solar Energy Engineering, vol. 124, no. 2, p. 109, 2002.

[14] Solutia, "Therminol VP-1," Solutia, pp. 1–5, 2014.

[15] H. Esen, F. Ozgen, M. Esen, and A. Sengur, "Artificial neural network and wavelet neural network approaches for modelling of a solar air heater," Expert Systems with Applications, vol. 36, no. 8, pp. 11240–11248, 2009.

[16] M. A. Costa, A. de P. Braga, and B. R. de Menezes, "Improving generalization of MLPs with sliding mode control and the Levenberg-Marquardt algorithm," Neurocomputing, vol. 70, no. 7–9, pp. 1342–1347, 2007.

[17] J. R. Jang, "ANFIS : Adaptive-Network-Based Fuzzy Inference System," IEEE Transactions on Systems, Man and Cybernetics, vol. 23, no. 3, 1993.

Effect of the Nanofluid (Brackish water/Al₂O₃) on the Passive Solar Still Desalination Performance with Heat Storage System

H. Hafs, A.Zaaoumi
Research Team in Thermal and
Energy
ENSET, Mohammed V University
Rabat, Morocco
hajar.hafs@um5s.net.ma

O.Ansari, A.Bah
Research Team in Thermal and
Energy
ENSET, Mohammed V University
Rabat, Morocco

M.Asbik, M.Malha
Research Team in Thermal and
Energy
ENSET, Mohammed V University
Rabat, Morocco

Abstract - **A numerical simulation is investigated to enhance the freshwater productivity of the modified solar still desalination system. A phase change material (PCM) is incorporated under the absorber plat as a thermal energy storage medium. Nanoparticles (Al₂O₃) have been added to the saline water and the whole system is covered by a transparent glass. Energy conservation equations were solved numerically by using Comsol software. Calculations have been done for three nanoparticle concentration values (0.02%, 0.1% and 0.2%) and several PCM quantities (10kg, 15kg, 20kg and 25kg). The model considered is validated and the influence of these two last parameters on the freshwater productivity is highlighted. the results indicated that the daily freshwater reached a maximum value of *7.74kg/m²* with m_{pcm}=20kg, compared to *6.67kg/m²* for the modified solar still with nanofluid and without PCM, and to *5.23kg/m²* for the conventional solar still.**

Keywords- Passive Solar Still; Nanofluid; Heat Storage System; Nanoparticles.

I. INTRODUCTION

Solar desalination is one of various technologies developed for water purification; it is an effective and an ecological technology, but the low productivity of freshwater is the mean and essential problem to solve for solar stills.

Several researchers have studied the performance of solar stills. Thus, Badran et al.[1] developed experimentally a sun tracking system and they used it to a fixed solar still to enhance its performance. They founded that the water productivity increased by 22%. Rajaseenivasan et al.[2]investigated experimentally and theoretically a glass basin solar still with preheated water and integrated with different storing materials (sand charcoal, and metal scrap). They concluded that the maximum value of fresh water productivity (3.61 kg/day) is obtained by using charcoal in fins.

Ansari et al.[3] Conducted a numerical study which highlighted the improvement of passive solar still performances by using separately three kinds of phase change materials (Paraffine C18, Paraffin52–54, Paraffin wax) as a storage medium. They reported that using heat energy storage enhances both the productivity and the efficiency of the distillation system. Furthermore, this last research work was undertaken by Asbik et al.[4] To determine the exergy losses during the charging/discharging periods. They deduced that the use of the latent heat storage process allows the increasing of the water productivity but it also reduces the exergy efficiency of the system. For the same goals mentioned above, Panchal et al.[5]tested different approaches to reach the productivity enhancement of up to 100 l/day. Indeed, they transformed the passive solar still into an active multi-stage solar still all the more so as the basin surface was coated by appropriate absorbing materials to increase the temperature of the still. Besides, fins have been used to increase convective heat transfer coefficient and hence to maximize the system productivity.

Sahota et al.[6][7]studied firstly the impacts of different concentrations of Al₂O₃ nanoparticles on thermal properties of the passive double slope solar still (DSSS) with 35kg and 80kg of basefluid, Moreover, they investigated the effect of three different nanoparticles (Al₂O₃,TiO₂ and CuO)on the performance of passive double slope solar still, this study showed that the thermal energy efficiency was higher for nanofluids compared to basefluid. Also, Incorporation of AL₂O₃ nanoparticles in saline water (Water/Al₂O₃) gives more productivity than others nanofluids (Water/TiO₂ and Water/CuO).

Kabeel et al.[8] highlighted numerically the effect of integrating different ranges of nanoparticles on modified solar still with external condenser, the simulation results showed that the efficiency of the

modified still is 84.16% and 73.85% respectively when using Cu_2O and Al_2O_3 nanoparticles.

Rashidi et al.[9]examined the effect of nanofluids on productivity of cascade solar still (22% enhancement); also they used the Response Surface Method (RSM) to optimize height and length of the steps. Prasher et al.[10] Studied the direct solar absorption by the mixed metallic nanoparticles in base fluid (Figure 1).They used the radiative transport to define the intensity attenuation as the radiation penetrates through the fluid. Moreover they studied the influences of nanoparticles size and volume fraction.
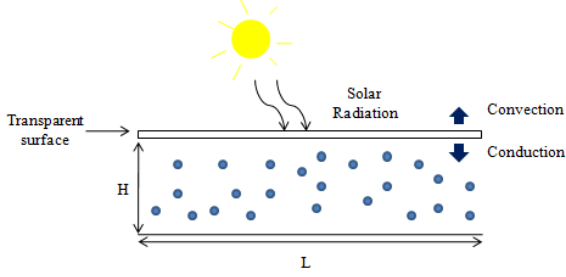

Figure 1.   Nanofluid based direct absorption solar receiver[10].

The main objective of this study is to improve the productivity of solar still by using Al_2O_3 nanoparticles in the base fluid (Brackish Water) combined with a phase change material (PCM) storage system.

II.   SYSTEM DESCRIPTION

A schematic diagram of the developed solar still is shown in Figure 2. The system is mainly composed of the basin area of 1m²(1m x 1m) insulated from sides and bottom walls with fiber glass (5cm thickness) to reduce thermal losses between the system and the ambient.

A phase change material (PCM) is incorporated under the absorber plat as a thermal energy storage medium. Nanoparticles have been added to the saline water to obtain a nanofluid whose thermal and optical properties will be enhanced. The whole system is covered by a transparent glass with a thickness of (3mm) and inclination angle of 34°. The solar still is south facing in order to have a maximum solar radiation and it is localized at Rabat city (Morocco) whose geographical coordinates are: Latitude: 34°00′47″ N, Longitude: 6°49′57″ W.
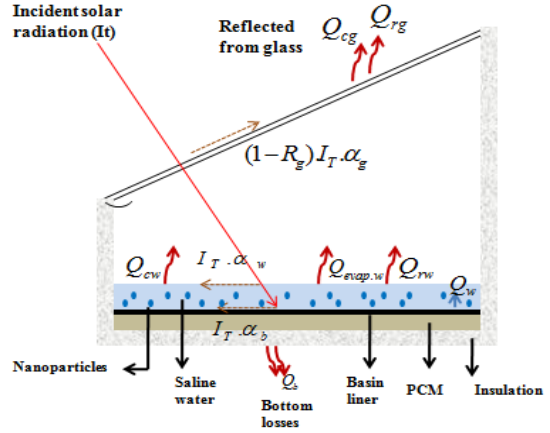

Figure 2.   Shematic diagram of modified solar desalination system with PCM and nanofluids

TABLE I.   THERMO PHYSICAL PROPERTIES OF NANOFLUID (WATER/AL2O3).

Correlations	Expressions
[11]	$\rho_{nf} = (1-\varphi_p).\rho_{bf} + \varphi_p.\rho_p$
[11]	$Cp_{np} = \dfrac{(1-\varphi_p).\rho_{bf}.Cp_{bf} + \varphi_p.Cp_p}{\rho_{bf}}.$
[12]	$K_{nf} = K_{bf}.\left[\begin{array}{c} 1+1.0112.\varphi_p + 2.4375.\varphi_p.\left(\dfrac{47}{d_p}\right) \\ -0.0248.\varphi_p\left(\dfrac{K_p}{0.613}\right) \end{array} \right]$
[13]	$\mu_{nf} = -0.4491 + \dfrac{28.837}{T_{nf}} + 0.547.\varphi_p - 0.163\varphi_p^2$ $+23.653\left(\dfrac{\varphi_p}{T_{nf}}\right)^2 + 0.0132\varphi_p^2 - 23547.\left(\dfrac{\varphi_p}{T_{nf}^2}\right)$ $+23.498\left(\dfrac{\varphi_p}{d_p}\right)^2 - 3.018\left(\dfrac{\varphi_p^2}{d_p^2}\right)$
[14], [15]	$\beta_{nf} = (1-\varphi_p).\beta_{bf} + \varphi_p.\beta_p$

III.   MATHEMATICAL MODELING

The governing equations of thermal model are deduced from the energy balance relative to each component of the solar still. They are written in taking into account the following assumptions:

- Heat losses from the sides and bottom of the solar still are negligible.
- Water temperature is considered homogenous in the absorber surface.
- The phase change material (Paraffin wax) is in perfect contact with the absorber.

- All processes in the system are in steady state.
- There is no deposition of nanoparticles.

A. Glass cover

$$m_g.Cp_g.\frac{dT_g}{dt} = I(t).A_g.\alpha_g + Q_{bf-g} - Q_{c,g-a} - Q_{r,g-s} \quad (1)$$

Where:

$$Q_{bf-g} = Q_{e,bf-g} + Q_{c,bf-g} + Q_{r,bf-g}$$

B. Base fluid

$$m_{bf}.Cp_{bf}.\frac{dT_{bf}}{dt} = I(t).A_{bf}.\tau_g.\alpha_{bf} + Q_{c,b-bf} - Q_{bf-g} \quad (2)$$

C. Absorber

$$m_b.Cp_b.\frac{dT_b}{dt} = I(t).A_b.\tau_g.\tau_{bf}.\alpha_b - Q_{c,b-bf} - Q_{cd,b-pcm} \quad (3)$$

D. Phase change material (PCM)

$$m_{eq}.\frac{dT_{pcm}}{dt} = Q_{cd,b-pcm} - Q_{cd,pcm-ins} \quad (4)$$

E. Insulation material

$$m_{ins}.Cp_{ins}.\frac{dT_{ins}}{dt} = Q_{cd,pcm-ins} - Q_{c,ins-a} - Q_{r,ins-soil} \quad (5)$$

All the terms in energy equations are defined in Tables (II and III).

TABLE II.   HEAT FLUX DEFINITIONS[3][16]

Heat flux(Q_i)	Expression	Heat transfer mode
$Q_{c,g-a}$	$h_{c,g-a}.A_g.(T_g - T_a(t))$	Convection
$Q_{r,g-a}$	$h_{r,g-sky}.A_g.(T_g - T_{sky}(t))$	Radiation
$Q_{e,bf-g}$	$h_{e,bf-g}.A_{bf}.(T_{bf} - T_g)$	Evaporation
$Q_{c,bf-g}$	$h_{c,bf-g}.A_{bf}.(T_{bf} - T_g)$	Convection
$Q_{r,bf-g}$	$h_{r,bf-g}.A_{bf}.(T_{bf} - T_g)$	Radiation
$Q_{c,b-bf}$	$h_{c,b-bf}.A_b.(T_b - T_{bf})$	Convection
$Q_{cd,b-pcm}$	$\frac{K_b}{x_b}.A_b.(T_b - T_{pcm})$	Conduction
$Q_{cd,pcm-ins}$	$\frac{K_{pcm}}{x_{pcm}}.A_{pcm}.(T_{pcm} - T_{ins})$	Conduction
$Q_{c,ins-a}$	$h_{c,ins-a}.A_{ins}.(T_{ins} - T_a(t))$	Convection
$Q_{r,ins-soil}$	$h_{r,ins-soil}.A_{ins}.(T_{ins} - T_{soil}(t))$	Radiation

TABLE III. TECHNICAL SPECIFICATIONS AND NUMERICAL CONSTANTS OF THE SOLAR STILL [3] [6] [8]

Thermal Properties	value	Numerical constants	value
Glass		σ	5.67×10^{-8} (W/m^2.K^4)
λ_g	0.78(W/m.K)		
ρ_g	2800(kg/m^3)	x_g	0.003(m)
Cp_g	840(J/kg.°C)	x_b	0.002(m)
ε_g	0.88	x_{ins}	0.05(m)
Water		α_g	0.05
λ_{bf}	0.64(W/m.K)	τ_g	0.09
ρ_{bf}	1000(kg/m^3)	Ag	1(m^2)
Cp_{bf}	4190(J/kg.°C)	V	2.5(m/s)
ε_{bf}	0.9	α_w	0.05
β_{bf}	5.5E-4(K^{-1})	α_b	0.9
Absorber		μ_{bf}	0.469.10^{-3} (N.s/m^2)
λ_b	73(W/m.K)		
ρ_b	7897(kg/m^3)	d_p	14(nm)
Cp_b	452(J/kg.°C)	L_{bf}	2350(kJ/kg.K)
Paraffin wax			
T_m	56(°C)		
λ_{pcm}	0.24(W/m.K)		
Cp_{pcms}/Cp_{pcml}	2950/2510(J/kg°C)		
ρ_{pcms}/ρ_{pcml}	818/760(kg/m^3)		
L_{pcm}	169(kJ/kg)		
Al$_2$O$_3$			
ρ_p	3900(kg/m^3)		
Cp_p	880(J/kg.°C)		
λ_p	46(W/m.K)		
β_p	8.1E-6(K^{-1})		

IV.   VALIDATION OF THE NUMERICAL MODEL

Energy balance equations (Equs. 1 to 5) are numerically solved by Comsol Multiphysics software which using the finite element method and via ODE global equations. Results are performed for climatic conditions of Rabat city (Latitude: 34°00′47″ N, Longitude: 6°49′57″ W) on a typical day of 15/06/2017. Thus, the hourly variations of ambient temperature Ta (t) and solar radiation I (t) relative to this specific day are plotted in the Figure3.
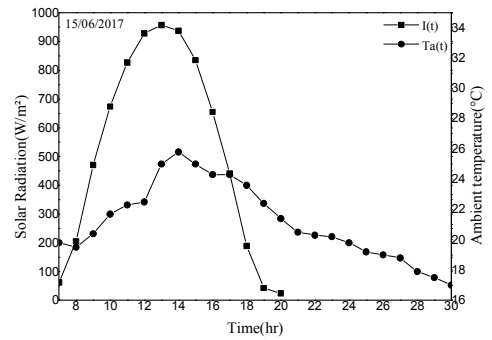

Figure 3.   Hourly variations of solar radiation and ambient temperature, 15-06-2017.

To validate the current model, we proceeded by comparing the numerical results with those of Kabeel et al.[8]. Indeed, Figure 4 shows the hourly temperature variation of nanofluid with 0.2% as a concentration of nanoparticles integrated in base fluid. It can be seen that the numerical results are in good
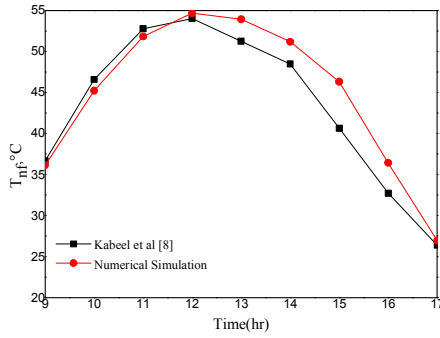
agreement with those of the reference [8].

Figure 4. Hourly temperature variation of modified solar still with cuprous oxide nanoparticles.

V. RESULTS AND DISCUSSION

Firstly, numerical simulations have been carried out for modified solar still by using the nanofluid based on the aluminum oxide (Al_2O_3) nanoparticles without a storage medium. Then, this desalination device has been supported by a layer of specific PCM as storage medium under the absorber plat. The performance parameters of solar still such as evaporation coefficient and hourly productivity are predicted for five different quantities of PCM.

1. Brackish water/Al2O3 without PCM:

As shown in Figure 5 temperature of nanofluid increases with nanoparticles concentration (φ). The viscosity correlation (see Table 1), as known, is a function of diameter and volume fraction as well as nanofluid temperature and therefore the Nusselt number varies with those two parameters. Figure6 highlights the hourly variations of evaporative heat transfer coefficient ($h_{e,w-g}$) for different concentrations of nanoparticles (0.02% 0.1%, and 0.2%) and with a fixed mass of water (50 kg). A significant increase of h_{evap} is observed for $\varphi=0.2\%$, during the sunny period of the specific day, compared to the conventional solar still ($\varphi=0\%$).
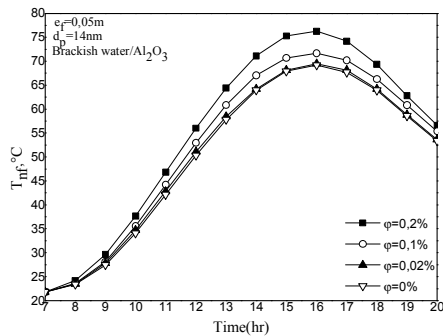

Figure 5. Hourly variations of nanofluid temperature for different concentrations (0.2%,0.1% ,0.02% and 0%)
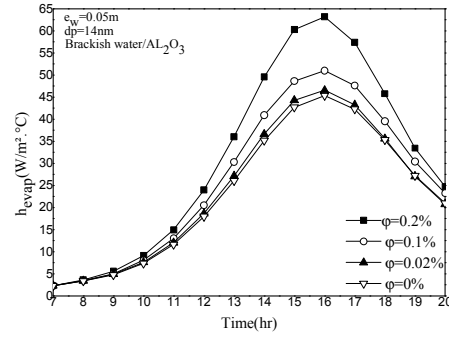

Figure 6. Evaporative heat transfer coefficient.

Besides, the hourly productivity is defined using the following equation[16].

$$P_h = \frac{Q_{e,bf-g}.3600}{L_{bf}}$$

It is seen from the results of Figure7 that the hourly variations of the yield increase over time as both increase of solar radiation increase and nanoparticles concentration.
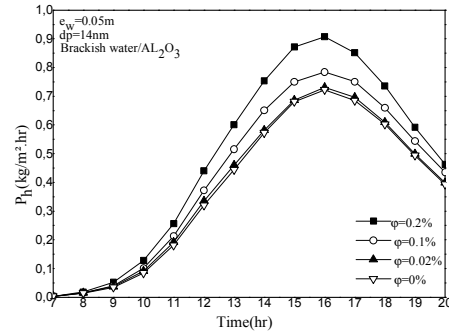

Figure 7. Hourly freshwater productivity with respect to nanofluid concentrations.

2. Brackish water /Al2O3 with PCM:

In this second part of results, paraffin wax was added to act as heat source for basin water during night. So, Figure 8 shows temperature variations of nanofluid for different values of PCM masses when $\varphi=0.2\%$ compared to the case where the heat storage system is not considered. During the morning period, the heat transfer by conduction between absorber and PCM increase as solar radiation increase, a part of energy is stored in PCM as sensible heat. By time, PCM reaches its melting temperature where energy is stored as latent heat. After sunset (20h), the absorber receives the amount of energy from PCM medium during discharging process and from absorber to brackich water until solidification of PCM.

From the results of Figure 9, it is clear that the hourly fresh water productivity with nanofluid and without PCM ($m_{pcm}=0kg$) is important compared to the case of with thermal energy storage. It can be explained by the fact that solar energy is used directly

to evaporate saline water however for the second case with PCM a large energy is absorbed by the paraffin wax to restitute it later.

It is also obvious from Figure 10 that the daily fresh water productivity increase with increasing m_{pcm} to reach a maximum value of *7.74kg/m²* for m_{pcm} =20kg and after that decrease slightly with increasing m_{pcm}.

TABLE IV. AVERAGE VALUES FOR VARIOUS HEAT TRANSFER COEFFICIENTS FOR MODIFIED SOLAR STILL WITH NANOFLUID (BRACKISH WATER/AL2O3) AND PCM.

PCM (Kg)	$h_{c,b-w}$ (W/m².°C)	$h_{e,w-g}$ (W/m².°C)	h_1 (W/m².°C)
10	360,84	18,98	21,19
15	378,60	19,35	21,56
20	379,63	19,54	21,73
25	378,57	19,49	21,68

Table IV shows the average values of different heat transfer coefficients for modified solar still with nanofluid (Brackish water/Al$_2$O$_3$ and φ=0.2%) and with PCM.
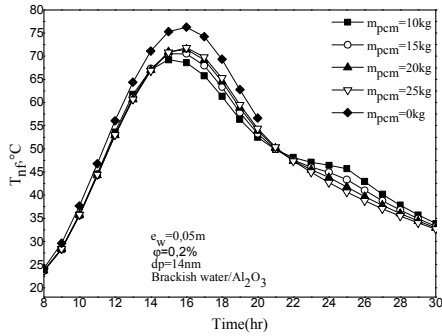

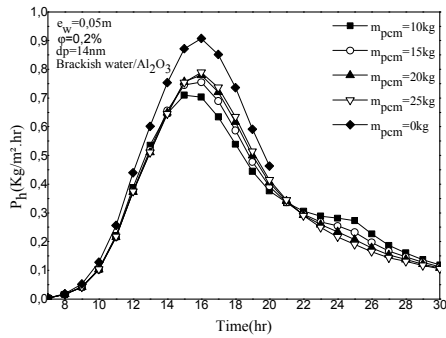Figure 8. Nanofluid temperature variations with different masses of PCM.

Figure 9. Hourly distillate water productivity with nanofluid and PCM.

The daily productivity is calculated using the present formula:
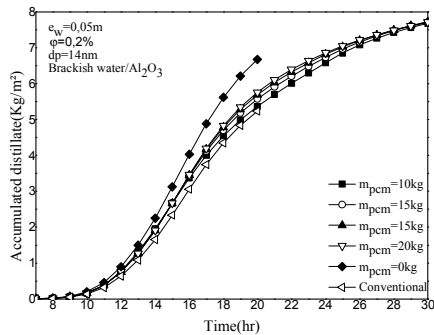
$$P_d = \sum_{24h} P_h$$

Figure 10. Accumulated daily productivity for different masses of PCM with nanofluid on typical day of 15-06-2017.

I. CONCLUSION

A developed solar still with nanofluid (Brackish water/Al$_2$O$_3$) and integrated PCM is studied numerically to improve the fresh water productivity, in the first step a comparison between modified solar still with different concentrations of aluminum oxide are carried out with the conventional solar still, the second step we integrated a phase change materiel (PCM) in the modified solar still under the same climatic conditions of Rabat city (Morocco). From the results it was observed that the daily productivity increase by 27 % for the modified solar still without PCM and by 48 % with PCM (φ=0.2%, m_{pcm}=20kg) than that for conventional solar still.

NOMENCLATURE

A	Surface Area, m²
Cp	Specific heat, J/Kg. °K
h	Heat transfer coefficient, W m^{-2} K^{-1}
I	Incident solar power, W m^{-2}
L	Latent heat, J/Kg
m	Masse, Kg
P_h	Distillation mass flow rate, Kg/m².h
Q	Heat flux density, W
T	Temperature, °C
t	Time, hour
x	Thickness, m

GREEK LETTERS

λ	Thermal conductivity, W/m. K
μ	Viscosity, N.s/m²
ρ	Density, Kg/m³
ε	Emissivity
φ	Nanoparticles concentration
σ	Stefan–Boltzmann constant, W/m².K⁴
α	Absoptivity
β	Thermal expansion coefficient of nanoparticle, K^{-1}

SUBSCRIPTS

a	Ambient
b, abs	Absorber
bf	Base fluid
conv, c	Convection
cd	Conduction
d	Daily
e	Evaporation
g	Glass

h	Hourly
i	Internal
ins	Insulation
nf	nanofluid
pcm	Phase change Material
r	Radiation
s	Sky

References

[1] S. Abdallah and O. O. Badran, "Sun tracking system for productivity enhancement of solar still," vol. 220, pp. 669–676, 2008.

[2] T. Rajaseenivasan, A. P. Tinnokesh, G. R. Kumar, and K. Srithar, "Glass basin solar still with integrated preheated water supply ??? Theoretical and experimental investigation," *Desalination*, vol. 398, pp. 214–221, 2016.

[3] O. Ansari, M. Asbik, A. Bah, A. Arbaoui, and A. Khmou, "Desalination of the brackish water using a passive solar still with a heat energy storage system," *Desalination*, vol. 324, pp. 10–20, 2013.

[4] M. Asbik, O. Ansari, A. Bah, N. Zari, A. Mimet, and H. El-ghetany, "Exergy analysis of solar desalination still combined with heat storage system using phase change material (PCM)," *Desalination*, vol. 381, pp. 26–37, 2016.

[5] H. Panchal and I. Mohan, "Various methods applied to solar still for enhancement of distillate output," *Desalination*, vol. 415, no. January, pp. 76–89, 2017.

[6] L. Sahota and G. N. Tiwari, " Effect of Al $_2$ O $_3$ nanoparticles on the performance of passive double slope solar still," *Sol. Energy*, vol. 130, pp. 260–272, 2016.

[7] L. Sahota and G. N. Tiwari, "Effect of nano fl uids on the performance of passive double slope solar still : A comparative study using characteristic curve," *Desalination*, vol. 388, pp. 9–21, 2016.

[8] A. E. Kabeel, Z. M. Omara, and F. A. Essa, "nanofluids and external condenser," *J. Taiwan Inst. Chem. Eng.*, vol. 0, pp. 1–10, 2017.

[9] S. Rashidi, M. Bovand, N. Rahbar, and J. Abolfazli, "Steps optimization and productivity enhancement in a nano fl uid cascade solar still," *Renew. Energy*, vol. 118, pp. 536–545, 2018.

[10] R. Prasher, "Predicted Efficiency of a Nanofluid-Based Direct Absorption Solar Receiver," pp. 1–8, 2016.

[11] P. Taylor, "Experimental Heat Transfer : Hydrodynamic and heat transfer study of dispersed fluids with submicron metallic oxide," A Journal of Thermal Energy Generation , Transport , Storage , and Conversion, no. January 2013, pp. 37–41.

[12] O. A. Alawi, N. Azwadi, C. Sidik, H. Wei, T. Hao, and S. N. Kazi, " Transfer Thermal conductivity and viscosity models of metallic oxides nanofluids," International Journal of Heat and Mass ,*Int. J. Heat Mass Transf.*, vol. 116, pp. 1314–1325, 2018.

[13] K. Khanafer and K. Vafai, " Transfer A critical synthesis of thermophysical characteristics of nanofluids," International Journal of Heat and Mass ,*Int. J. Heat Mass Transf.*, vol. 54, no. 19–20, pp. 4410–4428, 2011.

[14] K. S. Hwang, J. Lee, and S. P. Jang, "Buoyancy-driven heat transfer of water-based Al 2 O 3 nanofluids in a rectangular cavity," vol. 50, pp. 4003–4010, 2007.

[15] C. J. Ho, M. W. Chen, and Z. W. Li, "Numerical simulation of natural convection of nanofluid in a square enclosure : Effects due to uncertainties of viscosity and thermal conductivity," vol. 51, pp. 4506–4516, 2008.

[16] A. A. El-Sebaii, A. A. Al-Ghamdi, F. S. Al-Hazmi, and A. S. Faidah, "Thermal performance of a single basin solar still with PCM as a storage medium," *Appl. Energy*, vol. 86, no. 7–8, pp. 1187–1195, 2009.

Numerical analysis of acoustic field in standing wave thermoacoustic engine with different stack lengths

Zahra BOURAMDANE[a], Anass ZAAOUMI[a],
Abdellah BAH[a],
[a]Equipe de Recherche en Thermique et Energie
(ERTE) - Centre de Recherche Energie, ENSET
Mohammed V University in Rabat, Morocco
zahra.bouramdane@um5s.net.ma

Nadia MARTAJ[b,c], Mohammed ALAOUI[a]
[b]EPF-Ecole d'Ingénieur-e-s 2, rue Fernand Sastre
10430 Rosières-près-Troyes, France
[c]GRESPI EA 4694, University of Reims
Champagne-Ardenne Reims, France

Abstract – **This paper deals with a CFD (Computational Fluid Dynamics) simulation of standing wave thermoacoustic engine composed of tube (resonator) and stack placed between two heat exchangers. Theoretical models are developed based on coupled compressible Navier-Stokes and heat transfer equations that govern the working gas.**

The study is performed to investigate the influence of stack length on the acoustic wave. The thermoacoustic effect has been firstly validated using numerical results obtained by using Ansys fluent in order to be used in the present investigation. It is found that the variation of stack length not only influences the acoustic pressure and frequency of the system, but also affects the acoustic field along the tube.

Keywords-Thermoacoustic engine; CFD simulation; Stack length;

I. INTRODUCTION

The thermoacoustic effect is a phenomenon that concerns the conversion of acoustic energy into thermal energy or vice versa. The manifestations of the thermoacoustic effect have been known for a long time. The emission of sound by a heated tube has been observed for centuries by glassblowers.

The heat-excited acoustic oscillation was first studied by Byron Higgins [1], who observed that sound can be generated when moving a flame in a wide and open tube at both ends. In 1850, Sondhauss [2] carried out the first quantitative study on the thermoacoustic phenomenon. He conducted the experiments in an open tube at one end and closed at the other end by a glass bulb. Once the bulb is heated, a sound is created, Sondhauss observed that its frequency depends on the size of the tube (diameter, length, volume). This experimental device is today called the Sondhauss tube. Almost at the same time, Rijke [3] performed another experiment with a vertical tube open at both ends. A grid is placed inside the tube, and this grid is heated with a flame. Rijke observed the generation of sound in the tube, and noted that the frequency of sound depends on the length of the tube. The oscillations in the Rijke tube have been widely studied for more than 100 years, especially for their importance in the field of combustion.

In 1887, Lord Rayleigh qualitatively explained the thermoacoustic phenomenon in his book The Theory of Sound [4]: if an oscillating gas absorbs heat during the compression phase and gives up heat during the relaxation phase, then the oscillation is amplified. On the contrary, if the oscillating gas absorbs heat during the expansion phase, and gives up heat during the compression phase, then the oscillation is damped.

Swift has developed a linear theory that predicts the operation of a thermoacoustic system under the assumption of small amplitude oscillations. The difference between the experiment and the prediction becomes important when the amplitude of the oscillations is stronger. It is then necessary to study the nonlinear and multidimensional effects [5]. As a result of Swift's work, most efforts in the field of thermoacoustics have been devoted to the development and understanding of stationary-wave thermoacoustic systems [6, 7, 8, 9, 10, 11, 12, 13, 14]. However, the efficiency of this type of machine remains low because of the imperfection of the thermal contact between the fluid particle and the stack. At the end of the 1990s, the development of annular traveling wave systems [15, 16] significantly increased the efficiency of thermoacoustic motors.

Several recent researches were also devoted for more understanding the phenomenon of the thermoacoustic effect. For example, Hariharan et al. [17] showed the influence of stack parameters such as plate thickness and plate spacing on the performance of thermoacoustic engine. In 2016, Dragonetti et al. [18] established a modeling energy conversion in a tortuous stack for thermoacoustic application, a study of the performance of a thermoacoustic engine in which a tortuous porous material was used as stack was presented. In terms of stack geometry, Abd El-Rahman et al. [19] presented a 3D investigation of

thermoacoustic fields in a square stack and Zolpakar et al. [20] studied the performance of a 3D-printed stack in a standing wave thermoacoustic refrigerator.

This study focuses on numerical investigation of a thermoacoustic engine with different stack lengths. It aims to provide some guidelines on the influence of stack design on the acoustic oscillation. This numerical resolution is based on the finite element method to solve the coupled compressible Navier-Stokes and heat transfer equations that govern the working gas. The results show that the length of the stack influences the acoustic field along the resonator, which can lead to the damping of the wave oscillation.

II. NUMERICAL MODELING OF THE THERMOACOUSTIC ENGINE

A. Model design

A simple standing-wave thermoacoustic engine is composed of an acoustic resonator tube, stack (that is the main core of the machine because it synchronizes the exchanges between the fluid and the solid to achieve the thermodynamic cycle at the thermal boundary layer) and tow heat exchangers placed at the extremities of the stack, as illustrated in Fig. 1. The device of our study is the model used in [21]. Table I shows the geometrical and physical parameters of the device and lists the physical properties of the air at ambient pressure and temperature.
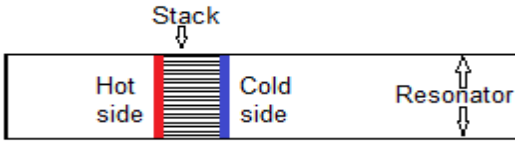

Figure 1. Schematic of thermoacoustic engine model.

TABLE I. THERMOACOUSTIC ENGINE PARAMETERS.

Parameters	Values
Tube	
Tube length L	150 mm
Tube wide	12 mm
Stack	
Number of plates	12
Plate thickness	0.5 mm
Gap between plates	0.5 mm
Left end position	30 mm
Right end position	40 mm
Air	
Model	Ideal gas
Density	1.1768 Kg/m^3
Viscosity	1.847 x 10^{-5} Kg/(sm)
Specific heat ratio	1.4
Specific gas constant	287 J/(Kg.K)
Speed of sound c	348 m/s
Thermal conductivity k	0.0263 W/(m.K)
Isobaric specific heat C_P	1006 J/(Kg.K)

The evolution of the physical parameters of the fluid (pressure, temperature, velocity and density) is governed by the Navier-Stokes equations:

$$\partial\rho/\partial t + \nabla . (\rho u) = 0 \qquad (1)$$

$$\rho(\partial u/\partial t + (u.\nabla)u) = \nabla . [- pI + \mu (\nabla u + (\nabla u)T - (2/3) \mu (\nabla .u) I] + F \qquad (2)$$

The energy equation:

$$\rho C_P (\partial T/\partial t + u.\nabla T) = \nabla . (K\nabla T) + Q_{vh} + W_P \qquad (3)$$

$$W_P = \alpha_p T (\partial p/\partial t) \qquad (4)$$

$$\alpha_p = - 1/\rho (\partial p/\partial T)\big|_P \qquad (5)$$

$$Q_{vh} = \tau : \nabla u \qquad (6)$$

Where W_P is the pressure work, α_p is thermal expansion coefficient and Q_{vh} is the contribution of viscous heating. To solve the system of equations described above, we provide the ideal gas equation for the working gas to link the physical parameters of the fluid:

$$\rho = P/R_S T \qquad (7)$$

B. Boundary conditions

The stack is made up of parallel plates and placed near of the closed end of the tube. The heat transfer coefficient between the stack walls and the working gas is set to be 50 W/m^{2}K [14] and the temperature distribution on the surface of the horizontal walls of the stack along was determined as following [22]:

$$T(x) = 1100 – (500 + 300 \cos(x/L_{st})) \qquad (8)$$

The temperature distribution causes that the maximum value of temperature for the hot side is 700 K, and it decreases along the length of the stack to the value of 300 K the cold side. Table II presents the basic data adopted for the analysis of the thermoacoustic engine.

TABLE II. PARAMETERS ADOPTED FOR THE NUMIRICAL ANALYSIS.

Parameters	Values
Initial temperature	300 K
Ambient pressure	101325 Pa
Heat transfer coefficient	50 W/m²K
Initial pressure	10 Pa
Pressure outlet	0 Pa gauge
Mesh	30.000 triangular cell

We used a mesh based on triangular elements with a total cell number of 30000. The mesh was refined near walls in the boundary viscous layer of the stack.

III. RESULTS AND DISCUSSION

A. Model validation

The performance of the model has been developed numerically using the finite element method with Comsol Multiphysics. To validate the theoretical estimates, a series of simulations were executed and the performance of the thermoacoustic engine was characterized in terms of the oscillating frequency and the pressure amplitudes of the working gas at the entrance of the stack.
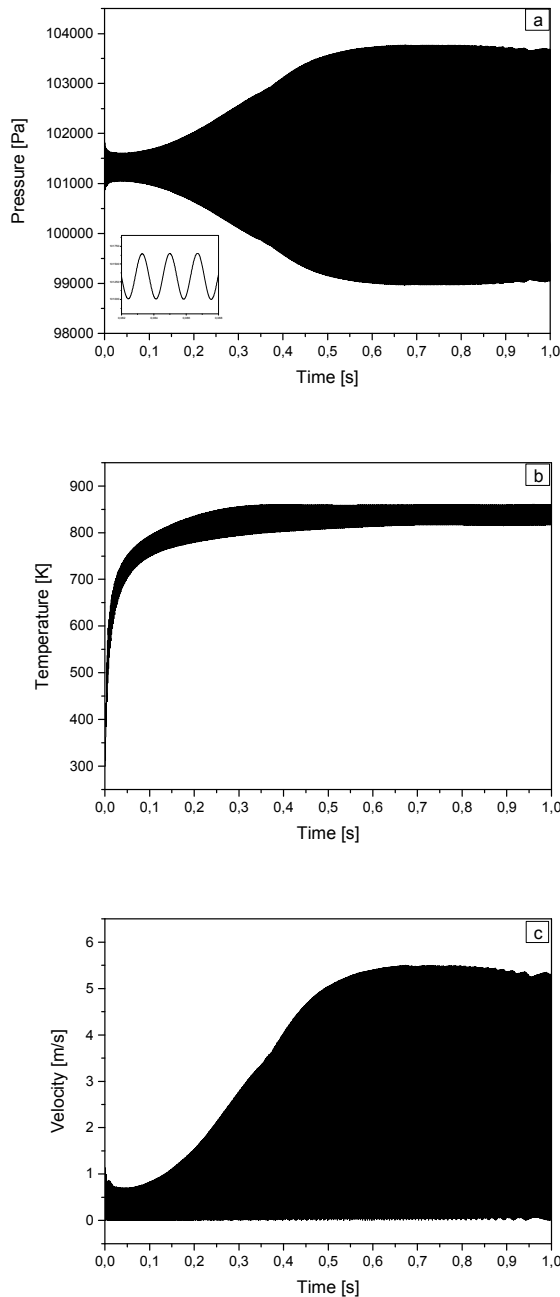

Figure 2. Pressure (a), temperature (b) and velocity (c) of the working gas at the entrance of the stack.
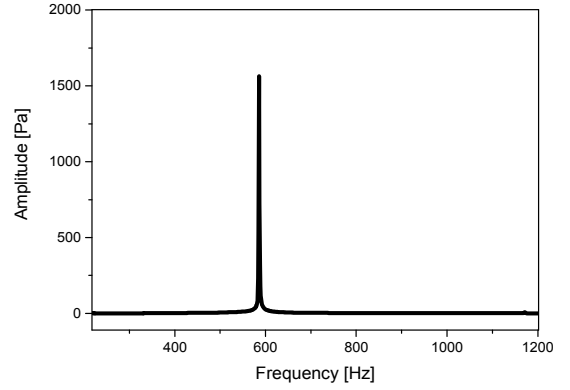

Figure 3. Fast Fourier Transform (FFT) of the acoustic pressure.

We plot the evolution of the pressure, temperature and velocity at the entrance of the stack. Fig. 2 and 3 show the process of the working gas parameters and FFT (Fast Fourier Transform) analysis of the acoustic wave excitation.

The progression of the acoustic wave can be divided into three stages: first, the instability occurs because the temperature gradient across the stack reaches the onset value. The second stage, the system is upcoming equilibrium between the various energy losses from viscous and thermal losses to the surrounding environment; the amplitude of the acoustic pressure continues to increase gradually. Finally, after heating the stack for around 0.6 s, the limit-cycle oscillation occurs and the fluid parameters reach the steady state.

The FFT analysis confirms that the results obtained with Comsol Multiphysics are the same as [21], in which the same frequency is obtained. This frequency corresponds well with the theoretical operating frequency of an engine with a total length of:

$$L = 0.15 \text{ m} = \lambda/4 \quad ; \lambda = 0.6 \text{ m}$$

$$f = C/\lambda = 348/0.6 = 580 \text{ s}^{-1} = 580 \text{ Hz}$$

Where C and L are the speed of sound and the wavelength respectively.

B. Stack length and intensity of the thermoacoustic effect

In this following, we applied a modified length of the stack (2.5, 5, 10, 12.5 and 15mm). The initial and the boundary conditions remained constant to ensure the same resonance conditions. As a result, the variation of the thermodynamic parameters of working gas are a result of the variation of the stack length.
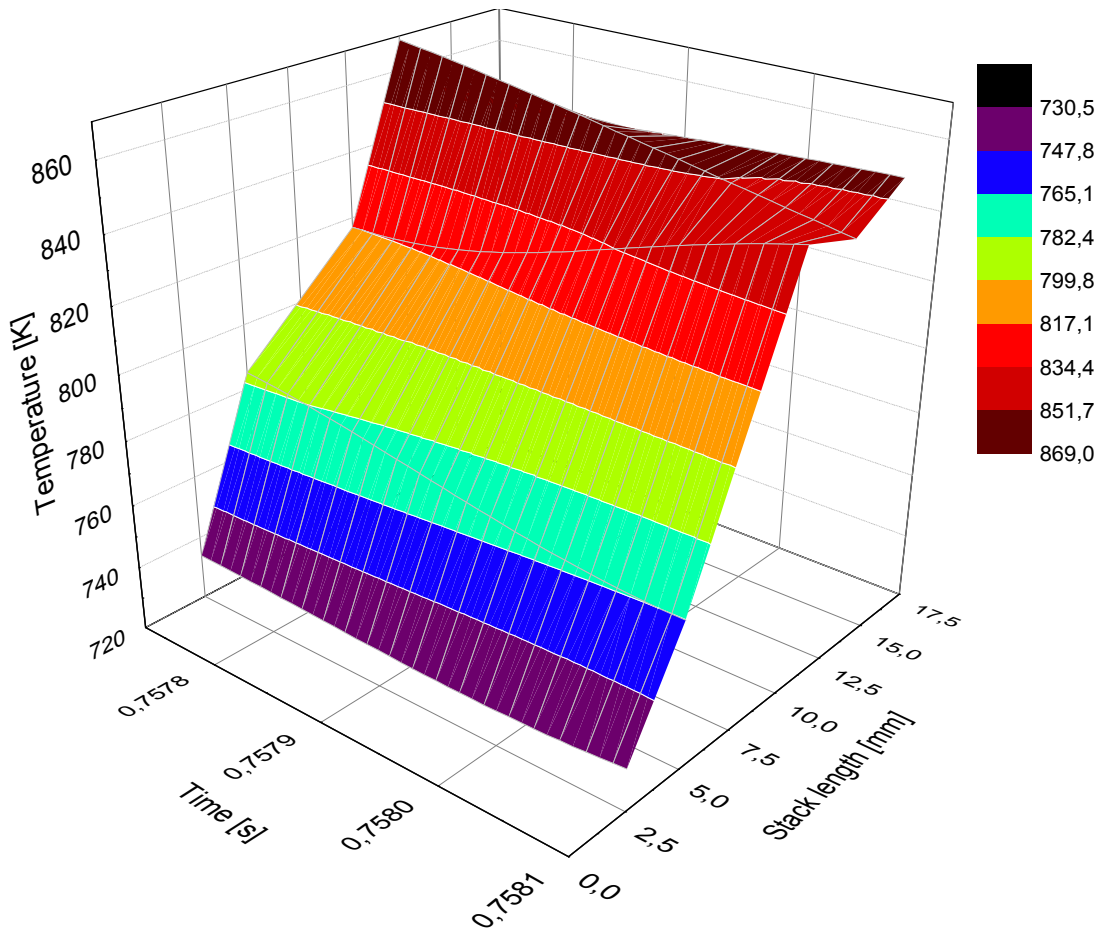
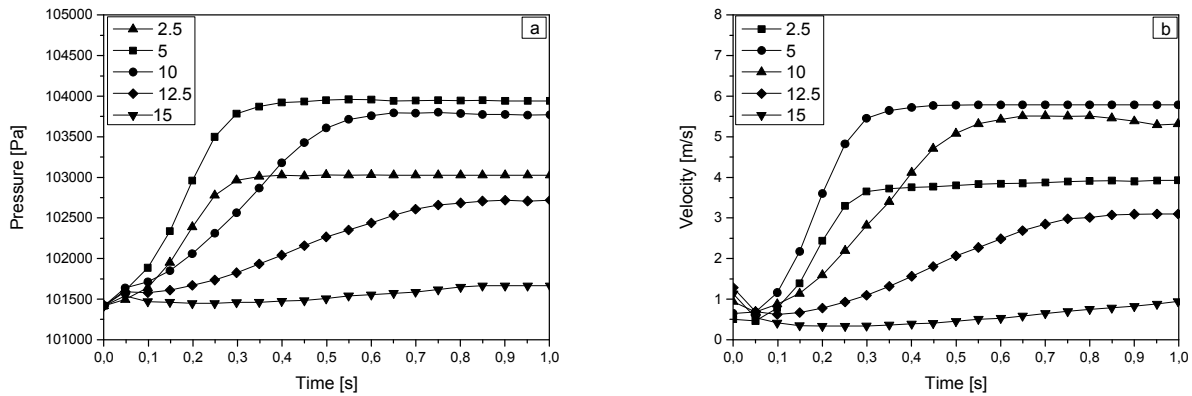Figure 4. Temperature for different stack lengths at the steady state.

Figure 5. Pressure (a) and velocity (b) for different stack lengths.

The flow variables of interest in thermoacoustics are the velocity and temperature, and, as a result, the heat transfer between the solid and gas inside the stack. We plot the evolution of the temperature, pressure and velocity at the entrance of stack. Fig. 4 shows the resulting temperature behavior at the steady state for different stack lengths. It is clear that, the working gas temperature is affected by the variation of stack length. Temperature evolution is established due to thermoacoustic heat pumping from the hot side to the working gas, but according to the stack length

variation the increase of the length causes a significant heat transfer between the stack and the gas; the temperature of the surrounding gas sloping upward. The pressure and velocity evolution is shown in fig. 5 over a course of 1 second. It can be observed that the velocity inside the stack is influenced by the variation of stack length. A clear difference between the evolutions become apparent. This is caused by the reversal of flow and fluid interacting with the stack walls.
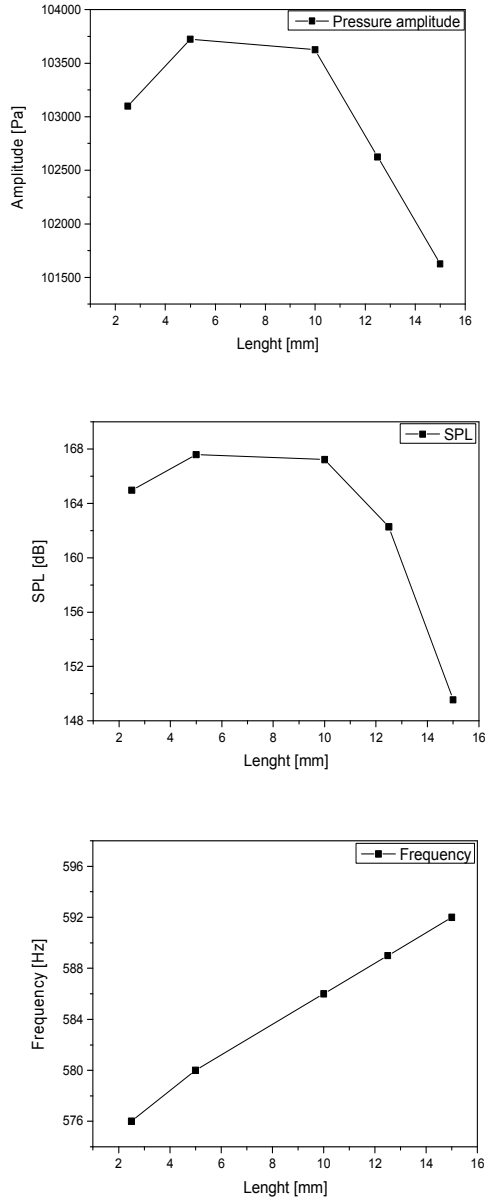
Figure 6. Amplitude, SPL and frequency of the acoustic wave

Above, we discussed the effect of stack length on the temperature, pressure and velocity throughout the stack. Next, we must discuss the effect of stack length on the frequency and SPL (sound pressure level) behavior of the thermoacoustic engine, as the sound output is the primary metric in the characterization of thermoacoustic devices. Fig.6 shows the pressure amplitude, SPL and frequency against the stack length. The results showed conclusive evidence that, unsurprisingly, stack length negatively influenced the thermoacoustic effect.

IV. CONCLUSION

In this work, we have applied a 2D model of thermoacoustic engine using the finite element method with Comsol Multiphysics to explore the effect of the stack length on the thermoacoustic effect. As a conclusion, this investigation shows that the variation of stack length not only influence the

acoustic pressure and frequency of the system, but also affect the acoustic field along the tube. The theoretical method in this study provide useful guidelines for the design of thermoacoustic engines for potential energy harvesting systems.

The numerical simulation in COMSOL Multiphysics can be a first step for other researches to enhance the performance of thermoacoustic devices; a thermal model can be predicted with different parameters for the design optimization.

Nomenclature

T   Temperature [K]
P   Pressure [Pa]
u   Velocity components [m.s^{-1}]
K   Thermal conductivity [W.m^{-1}.K^{-1}]
L_{st} Length of the stack [m]
C_p Heat capacity at p=cte [J.kg-1.K^{-1}]
Q   Heat source, power density [W.m^{-3}]
Q_{vh} Heating by viscous dissipation [W.m^{-3}]
W_p Pressure force work [W.m^{-3}]
SPL Sound pressure level [dB]
FFT Fast Fourier Transform
CFD Computational fluid dynamics

Greek letters

ρ   Density [Kg.m^{-3}]
μ   Dynamic viscosity [Pa.s]
α   Coefficient of thermal expansion [K^{-1}]

REFERENCES

[1]   Beyer, R. T. Sounds of Our Times: Two Hundred Years of Acoustics. Edition 1999th. Springer, 1999.
[2]   Feldman, K. T. Review of literature on Sondhauss thermoacoustic phenomena. J. Sound. Vib. 7 (1968), 71–82.
[3]   Feldman, K. T. Review of literature on Rijke thermoacoustic phenomena. J. Sound. Vib. 7 (1968), 83–89.
[4]   Rayleigh, L. Theory of sound. Second Edition. 1894.
[5]   Atchley, A. A. Analysis of the initial buildup of oscillations in a thermoacoustic prime mover. J. Acoust. Soc. Am. 95 (1993), 1661–1664. 174
[6]   Arnott, W. P., Bass, H. E., and Raspet, R. General formulation of thermoacoustics for stacks having arbitrarily shaped pore cross section. J. Acoust. Soc. Am. 90 (1991), 3228–3237.
[7]   Arnott, W. P., Bass, H. E., and Raspet, R. Specific acoustic impedance measurements of an air filled prime mover. J. Acoust. Soc. Am. 92 (1992), 3432–3434.
[8]   Arnott, W. P., Belcher, J. R., Raspet, R., and Bass, H. E. Stability analysis of a helium-filled thermoacoustic engine. J. Acoust. Soc. Am. 96 (1994), 370–375.
[9]   Arnott, W. P., Sabatier, J. M., and Raspet, R. Sound propagation in capillary-tube-type porous media with small pores in the capillary walls. J. Acoust. Soc. Am. 90 (1991), 3299–3306.
[10] Atchley, A. A. Standing wave analysis of a thermoacoustic prime mover below onset of self-oscillation. J. Acoust. Soc. Am. 92 (1992), 2907–2914.

[11] Atchley, A. A., and Kuo, F. M. Stability curves for a thermoacoustic prime mover. J. Acoust. Soc. Am. 95 (1993), 1401–1404.

[12] Atchley, A. A., Bass, H. E., Hofler, T. J., and Lin, H. T. Study of a thermoacoustic prime mover below onset of self-oscillation. J. Acoust. Soc. Am. 91 (1992), 734–743.

[13] Olson, J. R., and Swift, G. W. A loaded thermoacoustic engine. J. Acoust. Soc. Am. 98 (1995), 2690–2693

[14] Yu, Z. B., Jaworski, A. J., and Abduljalil, A. S. Impact of viscous and heat relaxation loss on the critical temperature gradients of thermoacoustic stacks. International Journal of Engineering and Applied Sciences 5(3) (2009), 152–156.

[15] Backhaus, S., and Swift, G. W. A thermoacoustic-stirling heat engine : detailed study. J. Acoust. Soc. Am. 107 (2000), 3148–3166.

[16] Yazaki, T., Iwata, A., and Maekewa, T. and Tominaga, A. Traveling wave thermoacoustic engine in a looped tube. Phys. Review Letters 81(15) (1998), 3128–3131.

[17] N.M.Hariharan, P.Sivashanmugam, S.Kasthurirengan. : Influence of stack geometry and resonator length on the performance of thermoacoustic engine, Applied Acoustics, Volume 73, Issue 10, Pages 1052-1058 (2012).

[18] Raffaele Dragonetti, Marialuisa Napolitano, Sabato Di Filippo, Rosario Romano.: Modeling energy conversion in a tortuous stack for thermoacoustic applications, Applied Thermal Engineering 103: 233–242 (2016).

[19] Ahmed I. Abd El-Rahman, Waleed A. Abdelfattah, Mahmoud A. Fouad.: A 3D investigation of thermoacoustic fields in a square stack. International Journal of Heat and Mass Transfer 108 292–300 (2017).

[20] Nor Atiqah Zolpakara, Normah Mohd-Ghazalia, Robiahn Ahmadb, Thierry Maré.: Performance of a 3D-printed stack in a standing wave thermoacoustic refrigerator. Energy Procedia 105: 1382 – 1387 (2017).

[21] Florian Zink, Jeffrey S. Vipperman, Laura A. Schaefer.: Advancing thermoacoustic technology through CFD simulation using FLUENT, in Proceedings of the International Mechanical Engineering Congress and Exhibition (2008).

[22] Garrett, S. L.: Reinventing the engine. Nature, 339 (1999).